

# **Advanced Hybrid Laser Welding of Pipeline Steels Using Novel Technologies**

by

**Hanwen Yang**

A thesis

presented to the University of Waterloo

in fulfillment of the

thesis requirement for the degree of

Doctor of Philosophy

in

Mechanical and Mechatronics Engineering

Waterloo, Ontario, Canada, 2024

© Hanwen Yang 2024

## **Examining Committee Membership**

The following served on the Examining Committee for this thesis. The decision of the Examining Committee is by majority vote.

External Examiner                      NAME: Michel Guillot  
Professor, Dept. of Mechanical Engineering, Laval  
University

Supervisor                                NAME: Adrian Gerlich  
Professor, Dept. of Mechanical and Mechatronics  
Engineering, University of Waterloo

Internal Member                        NAME: Hamid Jahed Motlagh  
Professor, Dept. of Mechanical and Mechatronics  
Engineering, University of Waterloo

Internal Member                        NAME: Peng Peng  
Assistant Professor, Dept. of Mechanical and  
Mechatronics Engineering, University of Waterloo

Internal-external Member              NAME: William Wong  
Professor, Dept. of Electrical and Computer  
Engineering, University of Waterloo

## **Author's Declaration**

This thesis consists of material all of which I authored or co-authored: see Statement of Contributions included in the thesis. This is a true copy of the thesis, including any required final revisions, as accepted by my examiners.

I understand that my thesis may be made electronically available to the public.

## Statement of Contribution

This thesis consists of a literature review (Chapter 2) and five research data chapters written in the manuscript format (Chapters 5-9). At the time of submission, 3 papers (first author) had been published. Two manuscripts (first author) are under review by refereed journals. All manuscripts are modified to fit the style of the thesis. I am the primary author of all the manuscripts. Dr. Adrian Gerlich is the corresponding author and has reviewed each chapter. Several co-authors on these manuscripts have been shown in this thesis. Their contributions are described below.

### Chapter 5

Hanwen Yang, James Chen, Nazmul Huda, Xiaoye Zhao, Adrian Gerlich. “Effect of wire preheat and feed rate in X80 steel laser root welds: Part 1 - Microstructure”, *Welding Journal* 4 (2024): 95s-106s.

Hanwen Yang, James Chen, Nazmul Huda, Xiaoye Zhao, Adrian Gerlich. “Effect of wire preheat and feed rate in X80 steel laser root welds: Part 2 – Mechanical properties”, *Welding Journal* 4 (2024): 107s-116s.

Dr. James Chen helped with the Charpy tests and edited the manuscript. Dr. Nazmul Huda performed arc welding, tensile tests, and SEM characterization. Dr. Xiaoye Zhao performed SEM characterization. Dr. Adrian Gerlich provided suggestions on the experiments, reviewed and edited the manuscript.

### Chapter 6

Hanwen Yang, James Chen, Nazmul Huda, Adrian Gerlich. “Effect of beam wobbling on microstructure and hardness during laser welding of X70 pipeline steel”, *Science and Technology of Welding & Joining* 27, 5 (2022): 326-338.



Dr. James Chen provided suggestions on the experiments and edited the manuscript. Dr. Nazmul Huda performed SEM characterization. Dr. Adrian Gerlich provided suggestions on the experiments, reviewed and edited the manuscript.

## Chapter 7

Hanwen Yang, James Chen, Xiaoye Zhao, Nazmul Huda, Adrian Gerlich. “Effect of beam wobbling and welding speed in X80 steel wire-fed laser welds”, *Journal of Materials Processing Technology* 327 (2024): 118383.

Dr. James Chen provided suggestions on the experiments and edited the manuscript. Dr. Xiaoye Zhao performed SEM characterization. Dr. Nazmul Huda and Dr. Abdelbaset R.H. Midawi helped with the instrumented indentation. Dr. Adrian Gerlich provided suggestions on the experiments, reviewed and edited the manuscript.

## Chapter 8

Hanwen Yang, James Chen, Xiaoye Zhao, Adrian Gerlich. “A study in hot-wire-fed laser welding of X80 steel using beam wobbling”, Submitted.

Dr. James Chen provided suggestions on the experiments and edited the manuscript. Dr. Xiaoye Zhao performed SEM characterization. Dr. Adrian Gerlich provided suggestions on the experiments, reviewed and edited the manuscript.

## Chapter 9

Hanwen Yang, James Chen, Xiaoye Zhao, Nazmul Huda, Adrian Gerlich. “Effect of filler wire composition on weld metal in X80 steel laser welds”, Under review by *The International Journal of Advanced Manufacturing Technology*. (JAMT-D-24-01498)

Dr. James Chen helped with the Charpy tests and edited the manuscript. Dr. Xiaoye Zhao and Dr. Nazmul Huda performed SEM characterization. Dr. Adrian Gerlich provided suggestions on the experiments, reviewed and edited the manuscript.

Dr. Paulo Costa Assuncao helped with weld specimen preparation and performing GMAW. Fred Bakker at the machine shop in the University of Waterloo helped with base material preparation.

Charlie Boyle at the machine shop in the University of Waterloo helped with Charpy samples extraction.

Garrett Larrimore at IPG Photonics Corporation helped with performing bead-on-plate laser welding experiments.

## Abstract

Laser beam welding using a high energy density source is a promising method for joining thick plates due to its deep penetration and high productivity, although there are drawbacks such as poor gap-bridging ability, and fast cooling which can lead to weld metal brittleness in more hardenable carbon steels. These limitations can be overcome by adding a filler wire into the weld pool. Meanwhile, novel technologies including beam wobbling and hot-wire feeding have shown the potential to improve the mechanical properties of laser welds. The aim of the present work is to pursue the development of a state-of-art hybrid laser welding process as a root pass for the welding of high strength low-alloy pipeline steels with improved weld quality, mechanical properties, and increased productivity.

The first part of the current research focused on the effect of hot-wire feeding ER70S-6 wire on the microstructure and mechanical properties of API X80 steel laser welds. A high wire feed rate along with preheating of the wire limited the formation of brittle microconstituents such as bainite and martensite in the weld metal, leading to an acicular-ferrite-dominated microstructure. The weld metal strength and toughness met the industrial requirement, although the hardness exceeded the maximum value allowed.

Further study was conducted utilizing a wobble laser during wire-fed laser welding process. Beam wobbling technique provided the potential to increase the gap-bridging ability. However, increased amount of bainite was found due to the dilution effect with more melted base material in the fusion zone, and this led to an increase in the hardness and strength of the weld metal.

Utilizing a hot-wire feed together with a wobble laser with a small spot size improved the fusion zone microstructure homogeneity and reduced the weld metal hardness. The preheating of the substrates reduced the cooling rate and resulted in the formation of more ferrite. Heat-affected zone hardness was also reduced with the preheating. A larger root gap was found to limit the dilution of alloying elements from the filler material, providing sufficient nucleation

sites for the formation of acicular ferrite.

The influence of wire chemistry was then investigated with the optimized welding parameters. Introducing an ER70S-2 wire with a lower carbon equivalent into the weld pool led to a coarser weld metal microstructure, and resulted in a lower hardness and a sufficient toughness which met the API standard. Considering the high productivity and satisfactory mechanical properties of the laser welds, the welding procedure proposed by this work indicates strong potential for utilizing laser welding for more applications in the pipeline industry.

## **Acknowledgements**

Before I started my PhD study, I never thought that my PhD carer could go so smooth. I am incredibly grateful to my supervisor Dr. Adrian Gerlich, who gave me the opportunity to pursue PhD under his supervision and always provides effective guidance on the research. I am extremely lucky to have a supervisor who supports a lot not only in the research but also in my daily life. Our ongoing, meticulous interaction helps me a lot during my study in University of Waterloo.

I want to express my gratitude to NSERC, CFI and Natural Resources Canada for funding the project. I would like to thank Dr. James Chen at CanmetMATERIALS for his support and guidance in the project. I am grateful for Dr. Nazmul Huda, Dr. Abdelbaset R.H. Midawi, Dr. Paulo Costa Assuncao and Dr. Yuquan Ding for their help and suggestions in the lab. I would like to appreciate the technical staffs Fred Bakker and Charlie Boyle at the machine shop in the University of Waterloo for helping throughout my PhD study. Also, I would like to express my thanks to my warm-hearted colleges and professors in CAMJ, who supported me in the critical period of my research.

I want to express my deep gratitude to my wife Dr. Xiaoye Zhao, who makes me a better version of myself, for her lasting companionship and support. I want to thank our lovely daughter Natalie, whose birth started all the joy in my life. Also, I would like to appreciate my parents, Mrs. Lixin Wu and Mr. Jinyun Yang, for their endless love and care.

## Dedication

*To my dear wife Xiaoye and our daughter Natalie.*

*You light up my world.*

## Table of Contents

Author's Declaration.....	iii
Statement of Contribution.....	iv
Abstract.....	vii
Acknowledgements.....	ix
Dedication.....	x
List of Figures.....	xv
List of Tables.....	xxvi
Nomenclature.....	xxvii
Chapter 1: Introduction.....	1
Chapter 2: Literature review.....	5
2.1 Pipeline steels.....	5
2.1.1 The classification of pipeline steels.....	5
2.1.2 Alloying elements in pipeline steels.....	6
2.1.3 Thermo-mechanically controlled processing.....	8
2.1.4 Transformation products in HSLA steels.....	9
2.1.5 Heat-affected zone in HSLA steels.....	12
2.2 Laser and laser welding techniques.....	13
2.2.1 The principle of laser.....	13
2.2.2 Autogenous laser welding.....	16
2.2.3 Wire-fed laser welding.....	17
2.2.4 Hybrid laser arc welding.....	20
2.2.5 Wobble laser welding.....	24
2.3 Industrial requirements for pipeline steel welds.....	35
2.4 Summary.....	36

Chapter 3: Objectives and scope.....	38
Chapter 4: Materials and experimental methodology .....	40
4.1 Materials .....	40
4.2 Welding and monitoring equipment.....	41
4.3 Elements and microstructural analysis.....	42
4.4 Mechanical tests.....	43
4.4.1 Microhardness .....	43
4.4.2 Instrumented indentation .....	44
4.4.3 Tensile test .....	44
4.4.4 Charpy impact test .....	45
4.4.5 Bend test .....	45
Chapter 5: Effect of wire preheat and feed rate in X80 steel laser welds .....	46
5.1 Introduction.....	46
5.2 Experimental procedures .....	46
5.3 Weld morphologies .....	50
5.4 FZ microstructure.....	51
5.5 HAZ microstructure .....	56
5.6 Microhardness.....	60
5.7 Tensile behavior .....	61
5.8 Charpy impact toughness and fracture surfaces.....	63
5.9 Bend test results .....	67
5.10 Summary .....	68
Chapter 6: Penetration and microstructural study during bead-on-plate laser welding with beam wobbling.....	70
6.1 Introduction.....	70



6.2 Experimental procedures .....	70
6.3 Surface morphologies .....	72
6.4 Weld penetration .....	73
6.5 FZ microstructure.....	74
6.6 Grain structure .....	76
6.7 Summary.....	77
Chapter 7: Effect of beam wobbling and welding speed in X80 steel wire-fed laser welds ...	79
7.1 Introduction.....	79
7.2 Experimental procedures .....	80
7.3 Weld morphologies .....	82
7.4 Alloying element distributions in fusion zones .....	85
7.5 Microstructure.....	86
7.6 Role of beam wobbling and travel speed on microhardness distribution .....	93
7.7 Local yield strength estimation.....	96
7.8 Summary.....	98
Chapter 8: Study on hot-wire-fed laser welding of X80 steel using beam wobbling.....	99
8.1 Introduction.....	99
8.2 Experimental procedures .....	99
8.3 Cross-sectional morphologies.....	101
8.4 Elements distribution .....	103
8.5 Microstructure.....	103
8.6 Microhardness.....	108
8.7 Conclusions.....	111
Chapter 9: Effect of filler wire composition on weld metal in X80 steel laser welds .....	113
9.1 Introduction.....	113

9.2 Experimental procedures .....	114
9.3 Effect of feeding pure iron and nickel wires .....	115
9.3.1 Cross-sectional morphologies.....	115
9.3.2 Filler material distribution and FZ microstructure .....	116
9.3.3 FZ hardness.....	120
9.4 Effect of feeding ER70S wires with different carbon equivalents.....	122
9.4.1 FZ microstructure .....	122
9.4.2 FZ hardness.....	123
9.4.3 Charpy impact toughness and fracture surfaces .....	124
9.5 FZ hardness comparison of the laser welds obtained in this work .....	125
9.6 Summary.....	127
Chapter 10: Conclusions.....	129
Recommendations and opportunities for future work .....	131
Letters of Copyright Permission .....	133
References.....	159

## List of Figures

Figure 2-1. Generalized CCT diagram for low carbon steel. Reprinted with permission [45]. Copyright 2020, John Wiley and Sons. ....	10
Figure 2-2. A schematic correlating the temperature ranges for HAZ sub-zones in carbon steel welds. Reprinted with permission [58]. Copyright 1992, Elsevier. ....	13
Figure 2-3. Schematic of a typical laser system. Reprinted with permission [61]. Copyright 2017, Elsevier. ....	14
Figure 2-4. A Gaussian laser beam diverging from its waist. Reprinted with permission [65]. Copyright 2021, The author(s). ....	15
Figure 2-5. Schematic of laser welding modes. Reprinted with permission [69]. Copyright 2023, The author(s). ....	17
Figure 2-6. Experimental set-up for hot-wire laser welding. Reprinted with permission [76]. Copy right 2020, Elsevier. ....	19
Figure 2-7. Schematic of hybrid laser arc welding process. Reprinted with permission [27]. Copy right 2018, Elsevier. ....	20
Figure 2-8. (a) Patterns of weld formation during arc welding, laser welding and hybrid laser arc welding; (b) cross-sectional view of a hybrid laser arc weld. Reprinted with permission [27]. Copy right 2018, Elsevier. ....	22
Figure 2-9. Cross-section morphologies of joints welded with different arc types: (a) GMA pulse; (b) GMA normal; (c) modified spray arc. Reprinted with permission [28]. Copyright 2014, SAGE Publications. ....	23
Figure 2-10. Cross-section morphologies of joints welded with different laser/arc energy ratio: (a) 1.49; (b) 0.87; (c) 0.58. Reprinted with permission [30]. Copyright 2008, SAGE Publications. .....	23
Figure 2-11. Experimental set-up for laser hybrid welding with pre-placed cut-wire fragments.	

Reprinted with permission [87]. Copyright 2016, Elsevier. ....24

Figure 2-12. Experimental set-up of wobble laser welding, with common wobble patterns presented. Reprinted with permission [88]. Copyright 2022, SAGE Publications.....25

Figure 2-13. Effects of wobble amplitude  $A$  and frequency  $f$  on weld surface morphologies: laser power  $P = 2$  kW; welding speed  $v = 3$  m/min. Reprinted with permission [10]. Copyright 2015, Elsevier.....27

Figure 2-14. Process of bubble formation and absorption by keyhole during LBW recorded with X-ray imaging technique. Reprinted with permission [21]. Copyright 2018, The author(s). .....29

Figure 2-15. EBSD results of FZ microstructure produced with varying wobbling conditions: (a, c, e, g) cross-section of welds without wobbling, with transversal wobbling, with longitudinal wobbling and with circular wobbling; (b, d, f, h) horizontal section of welds without wobbling, with transversal wobbling, with longitudinal wobbling and with circular wobbling; (i)-(l) grain size distribution of welds without wobbling, with transversal wobbling, with longitudinal wobbling and with circular wobbling. Reprinted with permission [90]. Copyright 2016, Elsevier. ....30

Figure 2-16. Formation mechanism of the microstructure in FZ produced with varying wobbling conditions: (a, b) without wobbling; (c, d) with transversal wobbling; (e, f) with longitudinal wobbling; (g, h) with circular wobbling. Reprinted with permission [90]. Copyright 2016, Elsevier. ....32

Figure 2-17. EDS results of FZ in dissimilar materials welds produced with varying wobbling conditions: (a) linear scanning result of FZ of static-spot laser welded joint; (b) linear scanning result of FZ of the wobble laser welded joint; (c) map scanning result of FZ of static-spot laser welded joint; (d) map scanning result of FZ of the wobble laser welded joint. Reprinted with permission [26]. Copyright 2020, Elsevier. ....34

Figure 2-18. Schematic of solute transfer in laser arc hybrid Al-Si welds: (a) without wobbling; (b)  $A = 0.2 \text{ mm}$ ,  $f = 300 \text{ Hz}$ ; (c)  $A = 1 \text{ mm}$ ,  $f = 300 \text{ Hz}$ . Reprinted with permission [96]. Copyright 2020, Elsevier. ....35

Figure 3-1. Flow chart summarizing the research work in this thesis .....39

Figure 4-1. Groove design for X80 steel laser welding, showing the inside diameter (ID) side .....40

Figure 4-2. A typical experimental set-up for laser welding process.....42

Figure 5-1. Laser welding experimental set-up with wire feed. ....47

Figure 5-2. (a) Schematic diagram showing the extraction position of tensile and Charpy samples; (b) dimensions of sub-size tensile coupon; (c) dimensions of sub-size Charpy sample. ....49

Figure 5-3. Weld surfaces morphologies: (a) and (b) top and bottom surfaces of autogenous laser weld; (c) and (d) top and bottom surfaces of cold-wire laser weld with a WFR of 4 m/min; (e) and (f) top and bottom surfaces of cold-wire laser weld with a WFR of 6 m/min; (g) and (h) top and bottom surfaces of hot-wire laser weld with a WFR of 6 m/min; (i) and (j) top and bottom surfaces of cold-wire laser weld with a WFR of 12 m/min; (k) and (l) top and bottom surfaces of hot-wire laser weld with a WFR of 12 m/min; (m) top surface of cap arc weld...50

Figure 5-4. Cross-section morphologies: (a) autogenous laser weld; (b) cold-wire laser weld,  $WFR = 4\text{m/min}$ ; (c) cold-wire laser weld,  $WFR = 6\text{m/min}$ ; (d) hot-wire laser weld,  $WFR = 6\text{m/min}$ ; (e) cold-wire laser weld,  $WFR = 12\text{m/min}$ ; (f) hot-wire laser weld,  $WFR = 12\text{m/min}$ ; (g) final joint with root laser weld and filler GMAW welds.....51

Figure 5-5. Microstructure of the X80 base metal: (a) optical micrograph; (b) SEM micrograph with locations of ferrite (F) and martensite/austenite (MA) indicated. ....52

Figure 5-6. Optical micrographs showing the microstructure and locations of acicular ferrite (AF), bainite (B) and grain-boundary ferrite (GBF) in the upper region of the FZ: (a)

autogenous laser weld; (b) cold-wire laser weld,  $WFR = 4$  m/min; (c) cold-wire laser weld,  $WFR = 6$  m/min; (d) hot-wire laser weld,  $WFR = 6$  m/min; (e) cold-wire laser weld,  $WFR = 12$  m/min; (f) hot-wire laser weld,  $WFR = 12$  m/min. ....53

Figure 5-7. Optical micrographs showing the microstructure and locations of acicular ferrite (AF), bainite (B) and grain boundary ferrite (GBF) in the lower region of the FZ; (b) cold-wire laser weld,  $WFR = 4$  m/min; (c) cold-wire laser weld,  $WFR = 6$  m/min; (d) hot-wire laser weld,  $WFR = 6$  m/min; (e) cold-wire laser weld,  $WFR = 12$  m/min; (f) hot-wire laser weld,  $WFR = 12$  m/min. ....54

Figure 5-8. SEM micrographs indicating the presence of bainite (B) and acicular ferrite (AF) in: (a) and (b) upper region of the FZ in autogenous laser weld; (c) and (d) lower region of the FZ in autogenous laser weld; (e) and (f) upper region of the FZ in hot-wire laser weld with a  $WFR$  of 12 m/min; (g) and (h) lower region of the FZ in hot-wire laser weld with a  $WFR$  of 12 m/min. ....55

Figure 5-9. (a) Sub-zones in the HAZ of laser weld; (b) optical micrograph of CGHAZ, cold-wire laser weld,  $WFR = 6$  m/min; (c) optical micrograph of FGHAZ, cold-wire laser weld,  $WFR = 6$  m/min; (d) optical micrograph of ICHAZ, cold-wire laser weld,  $WFR = 6$  m/min. ....57

Figure 5-10. SEM micrographs of HAZ of cold-wire laser weld with a  $WFR$  of 12 m/min: (a) and (b) CGHAZ; (c) and (d) FGHAZ; (e) and (f) ICHAZ. ....58

Figure 5-11. (a) Optical micrograph of CGHAZ of arc weld; (b) optical micrograph of ICRCGHAZ of arc weld; (c) and (d) SEM micrographs of ICRCGHAZ of arc weld; (e) optical micrograph of CGHAZ of cold-wire laser weld with a  $WFR$  of 6 m/min; (f) optical micrograph of ICRCGHAZ of cold-wire laser weld with a  $WFR$  of 6 m/min; (g) and (h) SEM micrograph of ICRCGHAZ of cold-wire laser weld with a  $WFR$  of 6 m/min. ....59

Figure 5-12. (a) Macrograph showing the hardness mapping location; (b) hardness mapping results of autogenous laser weld; (c) hardness mapping results of cold-wire laser weld with a

WFR of 6 m/min; (d) hardness mapping results of cold-wire laser weld with a WFR of 12 m/min; (e) hardness mapping results of hot-wire laser weld with a WFR of 12 m/min.....	61
Figure 5-13. (a) Top side hardness distribution of the laser root weld; (b) Weld metal hardness distribution of the laser root weld along the through-thickness direction. ....	61
Figure 5-14. (a) Tensile coupon of cold-wire laser weld with a WFR of 6 m/min, showing the fracture in the base metal; (b) DIC strain maps with different welding parameters; (c) local strain distribution of cold-wire laser weld with a WFR of 6 m/min; (d) stress-strain curve of cold-wire laser weld with a WFR of 6 m/min.....	62
Figure 5-15. Ultimate tensile strength obtained from the transverse tensile tests. ....	63
Figure 5-16. Force-displacement curves of Charpy samples at different testing temperatures: (a) 0 °C; (b) -20 °C; (c) -45 °C.....	64
Figure 5-17. Charpy impact toughness of weld metal at different temperatures. ....	64
Figure 5-18. SEM images of Charpy fracture surfaces of samples tested at 0 °C: (a) autogenous laser weld, near the notch; (b) autogenous laser weld, towards the middle; (c) cold-wire laser weld with a WFR of 12 m/min, near the notch; (d) cold-wire laser weld with a WFR of 12 m/min, towards the middle. ....	66
Figure 5-19. SEM images of Charpy fracture surfaces of samples tested at -20 °C: (a) autogenous laser weld, near the notch; (b) autogenous laser weld, towards the middle; (c) cold-wire laser weld with a WFR of 12 m/min, near the notch; (d) cold-wire laser weld with a WFR of 12 m/min, towards the middle. ....	66
Figure 5-20. (a) SEM image of Charpy fracture surface showing the presence of inclusions in the weld metal of cold-wire laser weld with a WFR of 12 m/min, tested at 0 °C; (b) SEM image of Charpy fracture surface showing the EDS scanning area and the presence of inclusion in the weld metal of cold-wire laser weld with a WFR of 12 m/min, tested at -20 °C; (c) EDS spectrum and chemical composition of the inclusion.....	67

Figure 5-21. Root surfaces of the samples after bend tests, with the root pass of: (a) autogenous laser weld; (b) hot-wire laser weld with a WFR of 12 m/min. ....68

Figure 6-1. Schematic diagram of wobble laser welding: (a) experimental set-up; (b) laser wobble patterns. ....71

Figure 6-2. Weld surface morphologies with different wobble parameters: (a) without wobble,  $v = 1.0$  m/min; (b) circular wobble,  $A = 0.5$  mm,  $v = 1.0$  m/min; (c) circular wobble,  $A = 1.0$  mm,  $v = 1.0$  m/min; (d) figure-eight wobble,  $A = 0.5$  mm,  $v = 1.0$  m/min; (e) without wobble,  $v = 1.5$  m/min; (f) circular wobble,  $A = 0.5$  mm,  $v = 1.5$  m/min; (g) circular wobble,  $A = 1.0$  mm,  $v = 1.5$  m/min; (h) figure-eight wobble,  $A = 0.5$  mm,  $v = 1.5$  m/min. ....73

Figure 6-3. Cross-section morphologies with different wobble parameters: (a) without wobble,  $v = 1.0$  m/min; (b) circular wobble,  $A = 0.5$  mm,  $v = 1.0$  m/min; (c) circular wobble,  $A = 1.0$  mm,  $v = 1.0$  m/min; (d) figure-eight wobble,  $A = 0.5$  mm,  $v = 1.0$  m/min; (e) without wobble,  $v = 1.5$  m/min; (f) circular wobble,  $A = 0.5$  mm,  $v = 1.5$  m/min; (g) circular wobble,  $A = 1.0$  mm,  $v = 1.5$  m/min; (h) figure-eight wobble,  $A = 0.5$  mm,  $v = 1.5$  m/min. ....74

Figure 6-4. Microstructure of the X70 base metal: (a) optical micrograph; (b) SEM micrograph. ....75

Figure 6-5. Microstructure of weld metal, indicating presence of grain-boundary ferrite (GBF), upper bainite (UB) and martensite (M) in: (a) optical micrograph of static spot laser welded joint at a welding speed of 1.0 m/min; (b) and (c) SEM micrograph of 0.5 mm amplitude wobble laser welded joint at a welding speed of 1.0 m/min with different magnifications; (d) SEM micrograph of 0.5 mm amplitude wobble laser welded joint at a welding speed of 1.5 m/min. ....75

Figure 6-6. Schematics diagram of melt flow and top surface grain structure morphology with different wobble patterns: (a) without wobble; (b) circular wobble; (c) figure-eight wobble. 77

Figure 7-1. Experimental set-up for wire-fed laser welding with beam wobbling, showing



wobble pattern and groove design. ....	81
Figure 7-2. Laser travel path and radiation area with varying parameters: (a) $v = 1.0$ m/min, $A = 0.5$ mm; (b) $v = 1.0$ m/min, $A = 1.0$ mm; (c) $v = 1.5$ m/min, $A = 0.5$ mm; (d) static-spot laser welding.....	83
Figure 7-3. Weld surface morphologies on top and back of the welds: (a) static-spot laser weld, $v = 1.0$ m/min; (b) wobble laser weld, $v = 1.0$ m/min, $A = 0.5$ mm; (c) wobble laser weld, $v = 1.0$ m/min, $A = 1.0$ mm; (d) static-spot laser weld, $v = 1.5$ m/min; (e) wobble laser weld, $v = 1.5$ m/min, $A = 0.5$ mm. ....	84
Figure 7-4. Cross-sectional morphologies: (a) static-spot laser weld, $v = 1.0$ m/min; (b) wobble laser weld, $v = 1.0$ m/min, $A = 0.5$ mm; (c) wobble laser weld, $v = 1.0$ m/min, $A = 1.0$ mm; (d) static-spot laser weld, $v = 1.5$ mm; (e) wobble laser weld, $v = 1.5$ m/min, $A = 0.5$ mm. ....	85
Figure 7-5. EPMA maps showing the Si distribution in the weld metal: (a) static-spot laser weld, $v = 1.0$ m/min; (b) wobble laser weld, $v = 1.0$ m/min, $A = 1.0$ mm; (c) static-spot laser weld, $v = 1.5$ m/min; (d) wobble laser weld, $v = 1.5$ m/min, $A = 0.5$ mm.....	86
Figure 7-6. (a) EPMA line-scan results showing the Si distribution in the weld metal, with the ‘best-fit’ curves obtained by Lowess fitting highlighted; (b) the comparison between original data and the ‘best-fit’ curve.....	86
Figure 7-7. Optical micrographs showing the microstructure of upper region of the FZ, indicating the presence of acicular ferrite (AF), grain boundary ferrite (GBF) and bainite (B): (a) static-spot laser weld, $v = 1.0$ m/min; (b) wobble laser weld, $v = 1.0$ m/min, $A = 1.0$ mm; (c) static-spot laser weld, $v = 1.5$ m/min; (d) wobble laser weld, $v = 1.5$ m/min, $A = 0.5$ mm. ....	87
Figure 7-8. Optical micrographs showing the microstructure of lower region of the FZ, indicating the presence of acicular ferrite (AF), grain boundary ferrite (GBF), bainite (B) and martensite (M): (a) static-spot laser weld, $v = 1.0$ m/min; (b) wobble laser weld, $v = 1.0$ m/min, $A = 1.0$ mm; (c) static-spot laser weld, $v = 1.5$ m/min; (d) wobble laser weld, $v = 1.5$ m/min, $A$	

= 0.5 mm. ....	88
Figure 7-9. Volume fraction of microconstituents within the fusion zone: (a) upper region; (b) lower region. ....	88
Figure 7-10 SEM micrographs indicating the presence of acicular ferrite (AF) and bainite (B) in the upper region of the fusion zone: (a) and (b) static-spot laser weld, $v = 1.0$ m/min; (c) and (d) wobble laser weld, $v = 1.0$ m/min; $A = 1.0$ mm; (e) and (f) static-spot laser weld, $v = 1.5$ m/min. ....	90
Figure 7-11. SEM micrographs indicating the presence of acicular ferrite (AF), bainite (B) and martensite (M) in the lower region of the fusion zone: (a) and (b) static-spot laser weld, $v = 1.0$ m/min; (c) and (d) wobble laser weld, $v = 1.0$ m/min; $A = 1.0$ mm; (e) and (f) static-spot laser weld, $v = 1.5$ m/min. ....	91
Figure 7-12. SEM micrographs showing the presence of bainite (B) and ferrite (F) in the HAZ, and the ferrite grain size was evaluated by average grain intercept (AGI) method: (a) CGHAZ of the static-spot laser weld with a welding speed of 1.0 m/min; (b) CGHAZ of the wobble laser weld with a welding speed of 1.0 m/min and a wobble amplitude of 1.0 mm; (c) CGHAZ of the static-spot laser weld with a welding speed of 1.5 m/min; (d) FGHAZ of the static-spot laser weld with a welding speed of 1.0 m/min; (e) FGHAZ of the wobble laser weld with a welding speed of 1.0 m/min and a wobble amplitude of 1.0 mm; (f) FGHAZ of the static-spot laser weld with a welding speed of 1.5 m/min. ....	92
Figure 7-13. SEM micrographs showing the ICHAZ microstructure, indicating the presence of martensite-austenite (MA) island: (a) and (b) static-spot laser weld with a welding speed of 1.0 m/min; (c) and (d) wobble laser weld with a welding speed of 1.0 m/min and a wobble amplitude of 1.0 mm; (e) and (f) static-spot laser weld with a welding speed of 1.5 m/min. ....	93
Figure 7-14. Microhardness mapping results: (a) static-spot laser weld, $v = 1.0$ m/min; (b) wobble laser weld, $v = 1.0$ m/min, $A = 1.0$ mm; (c) static-spot laser weld, $v = 1.5$ m/min; (d)	

wobble laser weld, $v = 1.5$ m/min, $A = 0.5$ mm. ....	94
Figure 7-15. (a) Weld metal hardness distribution along the through-thickness direction; (b) Top side hardness distribution. ....	95
Figure 7-16. Load - depth curves obtained through indentation tests, showing the load when the highest plastic strain is concentrated at the edge of the indenter ( $F_s$ ). The indenter profile and indentation location were also presented. ....	97
Figure 7-17. Local yield strength estimation of the FZ in the laser welds. The error bars represent a 95% confidence interval from the mean yield strength value of 5 tests.....	97
Figure 8-1. Schematics of laser-base metal interactions with different root gaps and wobbling conditions: (a) wobble laser, 0.4 mm gap; (b) wobble laser, 0.8 mm gap; (c) static laser, 0.8 mm gap.....	102
Figure 8-2. Cross-sectional morphologies of laser welds with varying gaps and preheat temperatures.....	102
Figure 8-3. (a) EPMA map showing the distribution of Si in the weld with a 0.4 mm gap (without preheating); (b) EPMA map showing the distribution of Si in the weld with a 0.8 mm gap (without preheating); (c) EPMA line-scan results showing the distribution of Si in the welds without preheating. ....	103
Figure 8-4. SEM images showing the microstructure in the FZ, indicating the presence of acicular ferrite (AF), bainite (B), polygonal ferrite (PF) and gran boundary ferrite (GBF): (a) and (b) 0.4 mm gap, without preheating; (c) and (d) 0.8 mm gap, without preheating; (e) and (f) 0.8 mm gap, with a preheat temperature of 120 °C; (g) and (h) 0.8 mm gap, without preheating, indicating the presence of inclusions. ....	105
Figure 8-5. OM images showing the microstructure in the FZ, indicating the presence of acicular ferrite (AF), bainite (B), polygonal ferrite (PF) and gran boundary ferrite (GBF): (a) and (b) 0.4 mm gap, without preheating; (c) and (d) 0.8 mm gap, without preheating; (g)-(i) 0.8	

mm gap, with a preheat temperature of 120 °C. ....	106
Figure 8-6. Volume fraction of microconstituents in weld metal produced using different preheats and gaps. ....	107
Figure 8-7. Cooling curves in the FZ with varying preheat temperatures, showing the $t_{8/5}$ values. ....	107
Figure 8-8. SEM images showing the HAZ microstructure, indicating the presence of ferrite (F), bainite (B) and martensite-austenite (MA) islands: (a) CGHAZ, 0.4 mm gap, without preheating; (b) CGHAZ, 0.4 mm gap, with a preheat temperature of 120 °C; (c) FGHAZ, 0.4 mm gap, without preheating; (d) FGHAZ, 0.4 mm gap, with a preheat temperature of 120 °C; (e) ICHAZ, 0.4 mm gap, without preheating; (f) ICHAZ, 0.4 mm gap, with a preheat temperature of 120 °C. ....	108
Figure 8-9. Microhardness maps of the welds with varying root gaps and preheat temperatures. ....	110
Figure 8-10. FZ hardness changes with preheat temperature: (a) welds with a 0.4 mm gap; (b) welds with a 0.8 mm gap. ....	110
Figure 8-11. FZ hardness changes with root gap: (a) welds without preheating; (b) welds with a preheat temperature of 80 °C; (c) welds with a preheat temperature of 120 °C. ....	111
Figure 8-12. HAZ hardness distribution of the welds with a 0.4 mm root gap: (a) CGHAZ; (b) FGHAZ. ....	111
Figure 9-1. Cross-section morphologies: (a) autogenous laser weld; (b) laser weld with ER70S wire; (c) laser weld with pure iron wire; (d) laser weld with nickel wire. ....	116
Figure 9-2. (a) top surface of the laser weld with pure nickel wire, showing the presence of crack; (b) and (c) SEM images of cross-sectional morphology of the laser weld with pure nickel wire, showing the presence of crack in the upper region of the FZ. ....	116
Figure 9-3. EDS results showing the distribution of Ni and Fe in the laser weld with pure nickel	

wire. ....	117
Figure 9-4. SEM images showing the microstructure and locations of acicular ferrite (AF), ferrite (F), bainite (B), austenite and martensite (M) in: (a) upper region of the FZ in autogenous laser weld; (b) lower region of the FZ in autogenous laser weld; (c) upper region of the FZ in the laser weld with ER70S wire; (d) lower region of the FZ in the laser weld with ER70S wire; (e) upper region of the FZ in the laser weld with pure iron wire; (f) lower region of the FZ in the laser weld with pure iron wire; (g) upper region of the FZ in the laser weld with pure nickel wire; (h) lower region of the FZ in the laser weld with pure nickel wire .....	119
Figure 9-5. Volume fraction of microconstituents within the fusion zone: (a) upper region; (b) lower region. ....	120
Figure 9-6. Hardness mapping results of: (a) autogenous laser weld; (b) laser weld with ER70S wire; (c) laser weld with pure iron wire; (d) laser weld with nickel wire.....	121
Figure 9-7. Weld metal hardness distribution along the through-thickness direction.....	121
Figure 9-8. SEM images showing the FZ microstructure, indicating the presence of acicular ferrite (AF), ferrite (F) and bainite (B): (a) with ER70S-6 wire, upper region; (b) with ER70S-2 wire, upper region; (c) with ER70S-6 wire, lower region; (d) with ER70S-2 wire, lower region. ....	123
Figure 9-9. Microhardness maps of the welds made with: (a) ER70S-6 wire; (b) ER70S-2 wire. ....	124
Figure 9-10. (a) Charpy impact toughness of weld metal with ER70S wires addition at different temperatures; (b) force-displacement curves of Charpy samples with ER70S-2 wire addition at different testing temperatures. ....	125
Figure 9-11. SEM images of Charpy fracture surfaces of ER70S-2-wire-fed weld samples tested at: (a) 0 °C; (b) -20 °C. ....	125
Figure 9-12. FZ hardness comparison of the welds obtained in this work.....	127

## List of Tables

Table 2-1. Comparison of different high strength pipeline steels.....	5
Table 2-2. Different groups of additional elements in HSLA steels.....	8
Table 4-1. Chemical compositions of base materials (wt.).....	40
Table 4-2. Chemical compositions of filler wires (wt.).....	40
Table 5-1. Welding parameters during static-spot laser welding.....	48
Table 6-1. Welding parameters during bead-on-plate laser welding.....	72
Table 7-1. Welding parameters during static-spot and wobble laser welding with cold-wire feeding.....	81
Table 7-2. Average hardness of the weld metal with different welding speeds and wobble conditions.....	95
Table 8-1. Welding parameters during hot-wire-fed laser welding with beam wobbling.....	100
Table 8-2. Mean hardness values in the FZ with different preheat temperatures and root gaps (HV).....	109
Table 8-3. Mean hardness values in the HAZ with different preheat temperatures (HV).....	109
Table 9-1. Welding parameters during static-spot laser welding with different wires.....	115
Table 9-2. Average hardness in different locations of the joints.....	122

## Nomenclature

AF	Acicular ferrite
AGI	Average grain intercept
API	American Petroleum Institute
ASM	American Society for Metals
BPP	Beam parameter product
CCT	Continuous-cooling transformation
CGHAZ	Coarse-grained heat affected zone
CSA	Canadian Standards Association
CVN	Charpy V Notch
DIC	Digital Image Correlation
EBS	Electron Backscatter Diffraction
EDS	Energy dispersive X-ray spectroscopy
EPMA	Electron probe microanalysis
FGHAZ	Fine-grained heat affected zone
FZ	Fusion zone
GMAW	Gas metal arc welding
HAZ	Heat affected zone
HLAW	Hybrid laser arc welding
HSLA	High strength low alloy
ICHAZ	Inter-critical heat affected zone
ICRCGAZ	Inter-critically reheated coarse-grained heat affected zone
IIW	International Institute of Welding
LBW	Laser beam welding
LM	Lath martensite

MA	Martensite-austenite
NGLW	Narrow gap laser welding
NMI	Non-metallic inclusions
PF	Proeutectoid ferrite
SAW	Submerged arc welding
SCHAZ	Sub-critical heat affected zone
SEM	Scanning electron microscope
SMAW	Shield metal arc welding
TMCP	Thermo-mechanically controlled processing
WFR	Wire feed rate



## Chapter 1: Introduction

The rapid expansion of industrial activities has brought about a continual increase in energy demand. Despite energy sources such as wind, hydro, tidal and nuclear energy being developed in recent years, fossil fuels such as petroleum, natural gas and coal are still major sources of the world's energy supply. It is reported that fossil fuels accounted for 82% of the primary energy use in 2021, with natural gas consumption growing remarkably by 5.3% [1]. Among all the methods for oil and gas transportation, pipeline systems are the most used due to their high efficiency and economy. Long-distance transportation between source and storage areas requires high integrity pipelines with excellent strength and toughness. In the modern energy industry, pipes are made of high strength low alloy (HSLA) steels due to their superior performance [2].

Considering the growing demand of energy as well as the need to reduce costs, development of higher strength pipelines is always an important issue. By utilizing higher-strength-level pipeline steels, oil and gas pipeline infrastructure can be used under higher pressures, and the diameter of pipes can be made larger to increase the efficiency, which can thus significantly reduce the costs [2]. In addition, transportation costs of pipe material during construction can be significantly reduced using thinner walled steels with higher strength [3]. Thermo-mechanically controlled processing (TMCP) is a steel production technique that can improve both strength and toughness through grain refinement, and it has become the main strategy for modern HSLA steel production. Pipeline steels with a yield strength over 830 MPa can be produced through TMCP with carefully selected alloying elements and processing [4].

Welding is common and very important for the processing of pipeline construction, since the reliability of completed assemblies depends on the quality of welding joints. Welding processes in pipeline industry include longitudinal welding, field girth welding of pipe sections as well as repair welding. The commonly used techniques are arc welding methods, including

manual shield metal arc welding (SMAW), automatic gas metal arc welding (GMAW) and submerged arc welding (SAW). As for repair welding, SMAW is more popular due to the increased flexibility and simplicity for complicated repair joints [5,6]. These traditional welding methods usually require long processing time and skilled labor, which limit the productivity and weld quality [7].

In recent years, the cost and size of high-power solid-state laser welding systems have dropped considerably. Laser and hybrid laser welding, which combines a laser with another heat source, have gained popularity due to their potential on improving productivity and weld quality. Laser welding is a high energy-density beam welding method which offers deep penetration, high welding speed, narrow heat affected zone (HAZ), excellent surface quality, and high weld metal strength compared to conventional arc welding methods [8,9]. However, autogenous laser welding also has drawbacks, for example, poor gap bridging ability [10], porosity formation at high speeds [11], and high fusion zone (FZ) hardness which may lead to weld metal brittleness [12]. In recent years, researchers have developed novel technologies such as hot-wire laser welding [13], hybrid laser arc welding (HLAW) [7], dual-beam laser welding [14], vacuum laser welding [15] and wobble laser welding [16] to improve the performance of conventional laser welding.

Laser welding with a filler wire, i.e. wire-fed laser welding, is a common way to improve the gap bridging ability of laser beam welding [17]. Another significant benefit of feeding wire is to modify the chemical composition and the resulting microstructure of the weld metal [18,19]. To improve the deposition rate, hot-wire laser welding which utilizes electrical current for resistive pre-heating of the filler wire was developed. The use of an external power source to heat the wire leads to a higher deposition rate and energy efficiency [20]. Another strategy to improve the gap tolerance is by laser beam wobbling. In recent years, the invention of the high-precision galvanometer scanner and integrated wobble welding head promoted further

research and development of wobble laser welding. Laser beam wobbling is also reported to have the ability of reducing porosity [21,22] and refining grains in the fusion zone [23,24]. The effect of stirring molten pool by laser beam wobbling also has the potential to provide better intermixing of elements in the weld metal. However, this has been mostly investigated in dissimilar material welding process up to now [25,26].

HLAW is another newly developed technology and there is a rising interest in hybrid welding of pipeline steels over the recent years [7]. During HLAW, a laser beam and an electrical arc heat in the same molten pool. This combines the advantages of the two heat sources and eliminates the drawbacks of a single one. HLAW shows remarkable increase in gap tolerance, penetration depth, welding speed and welding process stability [27]. One of the most challenging technical difficulties in HLAW of thick steel is the insufficient intermixing of the filler material and base metal in the root laser zone of the weld metal. This promotes the formation of hard and brittle microstructure in the laser zone which results in a deterioration of toughness. It appears that filler material penetration and its homogeneous distribution play an important role in achieving high toughness because filler material tends to concentrate in the upper arc zone rather than in the laser zone. A method reported to alleviate this problem involves utilizing pulse spray arc with a short arc length to enhance the transport of filler material into the root [28]. Other researchers studied the influence of parameters including laser to arc power ratio, welding speed as well as the gap width on the filler material penetration [29,30].

The aim of the present work is to pursue the development of a state-of-art hybrid laser welding process as a root pass for the welding of HSLA pipeline steels with improved weld quality, mechanical properties, and increased productivity. Novel technologies including hot-wire feeding and laser beam wobbling were applied to enhance filler material transportation and elements homogeneity. The influence of parameters including wire feed rate, welding

speed, preheat temperature, root gap width, as well as beam wobbling were investigated. The elements distribution was analyzed with electron probe microanalysis (EPMA) and energy dispersive X-ray spectroscopy (EDS). The microstructure in the weld metal and HAZ were examined using a scanning electron microscope (SEM), and the volume fractions of acicular ferrite, bainite and martensite microconstituents in the weld metal were evaluated. The mechanical properties including hardness, tensile strength and toughness were tested, and the process-microstructure-properties relationship was then discussed. A detailed explanation of the objectives and scope of this work will be provided in chapter 3.

## Chapter 2: Literature review

### 2.1 Pipeline steels

#### 2.1.1 The classification of pipeline steels

Several international agencies have developed manufacturing standards for pipeline materials, among which the standards by American Petroleum Institute (API) are favored by researchers and accepted globally, which specify a designation system for pipeline steels according to different specified minimum yield strength levels. For example, X70 grade pipeline steel has a yield strength over 70 ksi, which is 485 MPa [31]. According to the American Society for Metals (ASM), high strength steels generally refer to the ones with yield strength over 290 MPa [32]. Based on this criterion, pipeline steels of grade X42 to X120 in API standards can be considered as high strength pipeline steels. Table 2-1 shows the year of invention and major mechanical properties of high strength pipeline steels [31,33].

Table 2-1. Comparison of different high strength pipeline steels.

Grade	Year of invention	Minimum yield strength (MPa)	Maximum yield strength (MPa)	Minimum tensile strength (MPa)	Maximum tensile strength (MPa)
X42	1948	290	495	415	655
X46	1953	320	525	435	655
X52	1953	360	530	460	760
X56	-	390	545	490	760
X60	1966	415	565	520	760
X65	1967	450	600	535	760
X70	1973	485	635	570	760
X80	1985	555	705	625	825
X90	1985	625	775	695	915
X100	1985	690	840	760	990
X120	1998	830	1050	915	1145

API X70 grade pipes are widely used nowadays, and X80 steels have been developed in the 1980s and used in many projects [34]. The applications of X100 and X120 steels are still under investigation, which are mainly limited by their weldability [35].

A strain-based design approach is commonly applied in the pipeline industry instead of the historically applied stress-based design for most structures, since it is anticipated that some plastic deformation will occur in the pipeline, as sometimes the stress in pipelines may exceed the limit under some loads such as ground movement and landslides, and yet safe operation can still be ensured [36]. Compared to the pipe body which exhibits a high toughness with a superior crack arresting ability, the weld metal and HAZ are always the weaker region in a welded pipe and their microstructure and mechanical properties need to be carefully controlled.

### **2.1.2 Alloying elements in pipeline steels**

The strength of pure iron is too low to be used in most engineering structural applications. The alloying elements in steels play a very important role in achieving high strength through solution hardening and precipitation strengthening, and can also contribute to grain refinement. However, poor control of excessive alloying elements could deteriorate the weldability and increase the cold cracking sensitivity [37], so it is essential to strictly control alloying to achieve the desired mechanical properties.

Carbon is typically used as the predominant strength controlling element from the initial development of steels. A small amount of carbon addition, for instance, 0.1wt.%, can notably improve the strength [5]. The strengthening effect is mainly due to the strong solution hardening as well as precipitation strengthening through the formation of  $Fe_3C$ . The main drawback of adding a large amount of carbon for strengthening is the deterioration of weldability and toughness. The weldability of steel is often evaluated by the carbon equivalent. There are two widely accepted formulas for calculating carbon equivalent, which depend on the overall carbon fraction. One is given by Dearden et al. [38] and recommended by the

International Institute of Welding (IIW), and is commonly used for steels with a carbon addition greater than 0.18 wt. %:

$$CE_{IIW} = C + \frac{Mn}{6} + \frac{Cr+Mo+V}{5} + \frac{Cu+Ni}{15} \quad (2-1)$$

The other formula is given by Ito and Bessyo [39] and is more applicable for steels with less than 0.18 wt. % carbon content:

$$P_{CM} = C + \frac{Si}{30} + \frac{Mn+Cu+Cr}{20} + \frac{Ni}{60} + \frac{Mo}{15} + \frac{V}{10} + 5B \quad (2-2)$$

The carbon content tends to be reduced for modern high strength steels to preserve low temperature toughness, and so it becomes a common practice to use other additional elements to retain strength, while also achieving more acceptable weldability and reducing cold cracking sensitivity. In modern HSLA pipeline steel, carbon can be limited to a rather low level typically below 0.09 wt. % [37].

Except for carbon, there are other macro- and micro-alloying elements presented in HSLA steel, according to the relative percentage added. Macro-alloying elements refer to manganese, nickel, chromium, and molybdenum. Meanwhile, micro-alloying elements have a relatively low percentage and mainly include boron, aluminum, vanadium, titanium, niobium etc. These elements have their influence on the microstructure and the resulting mechanical properties such as strength and toughness. With respect to the effect on phase transformation in steels, they can also be classified to two groups: austenite stabilizers and ferrite stabilizers [5], as shown in Table 2-2. Ferrite stabilizers expand the temperature range for ferrite formation during austenite-ferrite transformation. In contrast, austenite stabilizers lower the austenite-ferrite transformation temperature and as a result promote the formation of acicular ferrite or other low temperature transformation products such as bainite and martensite. Bainite and martensite typically have a relatively high dislocation density which contributes to high strength; however, the toughness could be lower when a larger amount of upper bainite or martensite is presented.

Table 2-2. Different groups of additional elements in HSLA steels.

Austenite stabilizers	Ferrite stabilizers
carbon	chromium
nickel	aluminum
manganese	molybdenum
nitrogen	silicon
cobalt	niobium
	tungsten
	vanadium

Some micro-alloying elements such as niobium, vanadium and titanium play a key role in modern HSLA steel manufacturing strategy, i.e., TMCP. The addition of these alloying elements can help generate fine carbide, nitride or carbonitride particles. During the heating process, these precipitates are pinned at the grain boundaries to prevent the growth of austenite grains, which leads to the refinement of grains and promotes the formation of ferrite rather than bainite or martensite. These particles also contribute to strength by precipitation hardening [40].

### 2.1.3 Thermo-mechanically controlled processing

TMCP is the main strategy for producing modern HSLA steel with superior mechanical properties combining high strength and toughness. It involves two major stages, as controlled rolling and controlled cooling [41]. Grain refinement and microstructure control in the controlled cooling stage are the key mechanisms during TMCP.

Grain refinement is an important strengthening mechanism for metals. In the 1950s, Hall and Petch [42] studied the relationship between grain size and yield strength of carbon steels, and established the famous Hall-Petch relation:

$$\sigma_s = \sigma_0 + kd^{-1/2} \quad (2-3)$$

where  $\sigma_0$  and  $k$  are constants, and  $d$  represents the effective grain size. It indicates that the yield



strength increases with decreasing grain size. The grain boundaries can also hinder the crack propagation so that low temperature toughness can be improved. Petch also presents the relationship between the ductile-to-brittle transition temperature  $T_k$  and grain size  $d$  [42]:

$$T_k = a - bd^{-1/2} \quad (2-4)$$

where  $a$  and  $b$  are constants. Based on these findings, grain refinement improves both the strength and toughness of steel.

Controlled rolling process occurs in two separate temperature ranges, i.e., recrystallization and non-recrystallization region. To obtain fine-grain microstructure, microalloying elements such as niobium are added [40]. In the recrystallization region, the recrystallization of deformed austenite occurs repeatedly. In the subsequent non-recrystallization region, these grains are pancaked, and a large amount of deformation bands are created, while niobium-containing particles precipitate due to induced deformation. These precipitates pin at the grain boundaries to prevent austenite grains from growing. Niobium can also increase the recrystallization temperature to retard the austenite recrystallization [43].

After the controlled cooling stage, a large amount of crystal defects is induced. These defects such as ledges and deformation bands provide additional nucleation sites for phase transformation in the controlled cooling stage, which help to achieve grain refinement. Furthermore, the niobium precipitates can also contribute to the increase of yield strength by precipitation strengthening [40]. By applying different cooling conditions in the controlled cooling stage, various microstructures can be tailored to include varying fractions of ferrite, bainite or martensite, which offers control of mechanical properties.

#### **2.1.4 Transformation products in HSLA steels**

Modern HSLA steels usually have a carbon fraction below 0.1 wt.% and are classified as hypoeutectoid steels. When solidified at a sufficiently low cooling rate from liquid state (equilibrium solidification), the liquid iron is first transformed to  $\delta$ -ferrite and then fully

transforms to austenite. When the temperature decreases to  $A_{r3}$ ,  $\alpha$ -ferrite begins to precipitate from austenite. This process is driven by carbon diffusion, where carbon is rejected from prior austenite to the surrounding grain structure. When the temperature further decreases to  $A_{r1}$ , the carbon content in the remaining austenite reaches 0.77 wt.%, and a eutectoid transformation occurs where austenite transforms to pearlite. Pearlite is a lamellar compound with thin alternating layers of ferrite and cementite. A small amount of tertiary cementite ( $Fe_3C_{III}$ ) also precipitates from proeutectoid ferrite. In summary, proeutectoid ferrite and pearlite are the main transition products of hypoeutectoid steel under equilibrium solidification. Ferrite in this case has a morphology of equiaxed grains and is called polygonal ferrite [44].

The degree of supercooling is defined as the difference between the theoretical phase transformation temperature and the actual transformation temperature. A high degree of supercooling can be achieved by applying a fast cooling, which leads to non-equilibrium solidification and promotes the formation of low temperature transformation products such as bainite and martensite. The generalized continuous-cooling transformation (CCT) diagram for low carbon steel is shown in Fig. 2-1, which can explain the development of microstructure in low carbon steels.

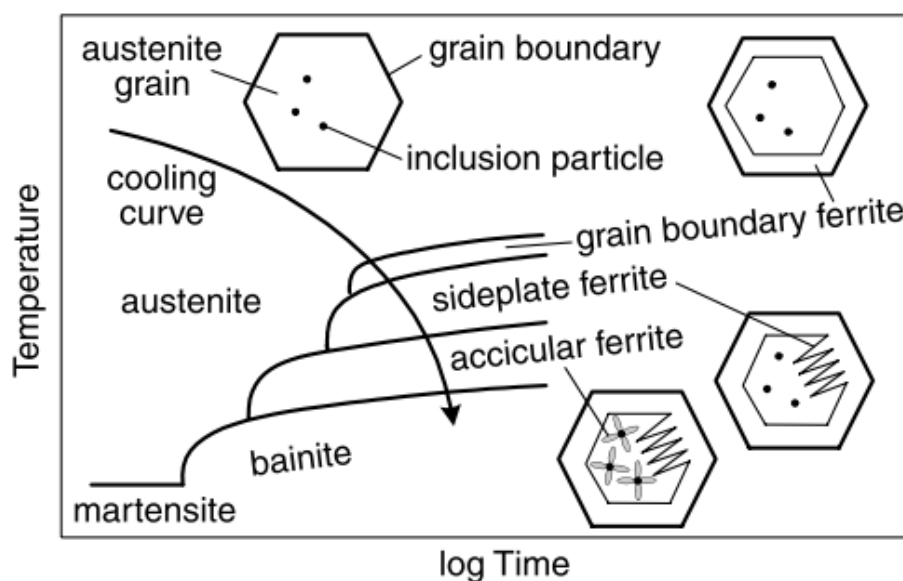


Figure 2-1. Generalized CCT diagram for low carbon steel. Reprinted with permission [45]. Copyright 2020, John Wiley and Sons.

Acicular ferrite (AF) forms at a temperature close to  $A_{r1}$ . It forms within original austenite grains and contains fine needle shaped laths that are interlocking or interlaced. Due to this fine interlocking structure, AF has a good ability to prevent the crack propagation so that high toughness can be achieved [46]. AF is the preferred microstructure in the steel welds due to its superior properties combining a high strength and toughness. Non-metallic inclusions (NMIs) play an important role in promoting the formation of AF by providing favorable nucleation sites at the inclusion surface [29,47]. Zhang and Farrar [48] reported that Si, Mn, and Ti-based oxides can promote the formation of AF in a low alloy weld metal. Evans [49] reported that a very small amount of Ti (0.001 wt.%) can promote significant metallurgical changes and generate 60% AF in a C-Mn steel weld. There has been a considerable number of studies to determine the elements most effective in promoting AF microstructures, and Gregg et al. [50] found that TiO and  $Ti_2O_3$  inclusions acted as the effective nucleation sites for AF in low alloy steel.

At a temperature below  $A_{r1}$ , bainite transformation occurs. Depending on the different temperature ranges, upper bainite and lower bainite may be obtained. Upper bainite forms at a relatively higher temperature and has a feather-like shape with sheaves of bainitic ferrite and continuous or semi-continuous layers of carbides under an optical microscope. In contrast, lower bainite is produced at a lower temperature and has a needle-like shape with bainitic ferrite and intra-ferritic carbides [37]. Another common form of bainite is the granular bainite, where the Martensite-austenite (MA) constituents dispersed in the bainitic ferrite matrix [51]. Bainite usually has a fine microstructure which contributes to a high strength [44]. However, the presence of upper bainite could deteriorate toughness by providing favorable propagation path for cracks.

Martensite transformation occurs at a temperature below martensite start temperature  $M_s$  at a critical fast cooling rate. Martensite has a body centered tetragonal lattice which is a

supersaturated solid solution with carbon atoms in a body centered cubic iron lattice. The transformation temperature is typically 400 to 500 °C for low carbon steels [52]. The diffusion of carbon atoms is thus rather slow at these temperatures, so that carbon atoms in austenite cannot diffuse out of the lattice. Hence, martensite forms through shear transformation other than diffusion-based transformation. Compared to ferrite or bainite, martensite has a higher dislocation density and normally a higher strength [37].

MA constituents can also be present in HSLA steels, which prefer to form in the temperature range with a peak temperature between  $A_{r1}$  and  $A_{r3}$  where partial austenization occurs. Upon cooling from this temperature range, some carbon-enriched austenite was retained to room temperature or partially transformed to martensite below the martensite start temperature ( $M_s$ ), which led to the formation of blocky MA [53,54]. These MA constituents usually appear as small islands in the base metal, FZ and HAZ and can initiate brittle fracture.

### **2.1.5 Heat-affected zone in HSLA steels**

The heat-affected zone adjacent to the FZ is heated up to temperatures just below the melting point of the base material. The HAZ sub-regions exhibit different grain sizes and microstructures resulting from various peak temperatures and cooling rates, as illustrated in Fig. 2-2. The coarse-grained heat affected zone (CGHAZ) adjacent to the FZ experiences a high peak temperature (above  $A_{r3}$ ) that promotes the growth of prior austenite grains, which aids the formation of low-temperature transformation products like bainite or martensite [55]. The peak temperature in the fine-grained heat affected zone (FGHAZ) is still higher than the full austenization temperature ( $A_{r3}$ ), but lower than the dissolution temperature of most precipitates existing in the HSLA steels produced through TMCP [56]. The pinning effect of the precipitates would retard the growth of austenite grains, which provides more grain boundaries as favorable nucleation sites for ferrite [55]. The inter-critical heat affected zone (ICHAZ) exhibits a peak temperature between  $A_{r1}$  and  $A_{r3}$  where partial austenization occurred

and could contain MA islands [57]. Sub-critical heat affected zone (SCHAZ) experiences a temperature lower than  $A_{r1}$  and no obvious microstructural change occurs but strain aging can happen [5].

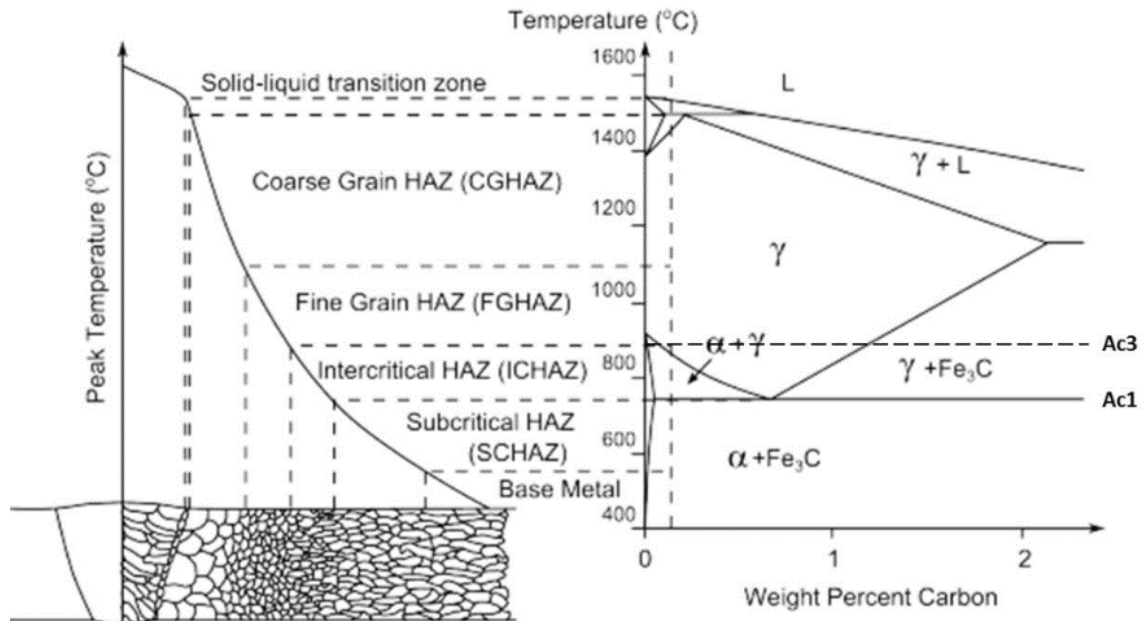


Figure 2-2. A schematic correlating the temperature ranges for HAZ sub-zones in carbon steel welds. Reprinted with permission [58]. Copyright 1992, Elsevier.

In the case of multi-pass welding, the second thermal cycle leads to the formation of multiple reheated HAZs, of which the inter-critically reheated (ICR) CGHAZ is often considered the weakest or most brittle region in a multi-pass weldment of pipeline steel due to the bainitic microstructure, large bainite packet size, along with the presence of second phase such as MA [57].

## 2.2 Laser and laser welding techniques

### 2.2.1 The principle of laser

The term ‘laser’ is the acronym of ‘light amplification by stimulated emission of radiation’. As the name implies, a laser is an enhanced photon beam produced by electron transitions during atoms stimulating [59]. Stimulated emission is a process that an incoming photon with a certain wavelength causes an excited-state atom to return to its ground-state and releases a

new photon [60]. A typical laser system includes an optical resonator containing the laser active medium within two parallel mirrors, an external pump energy source, and the cooling system [61], as shown in Fig. 2-3. The emitted photons are bounced back by the mirrors and re-enter the laser medium to stimulate the release of more photons. The photon beam that is released through the semi-transmissive mirror becomes the output laser beam [61–63].

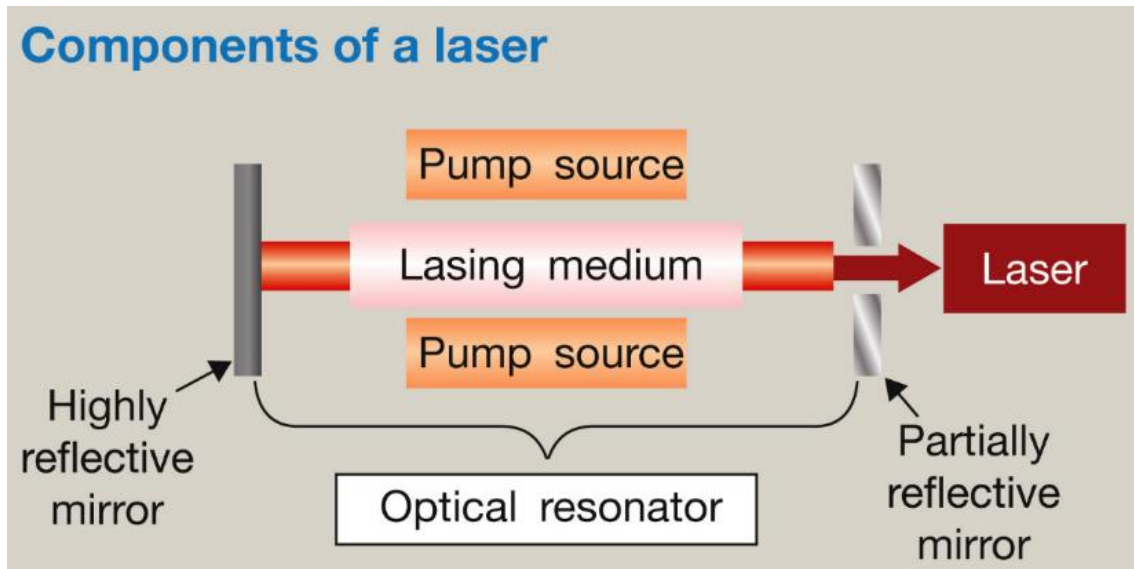


Figure 2-3. Schematic of a typical laser system. Reprinted with permission [61]. Copyright 2017, Elsevier.

The features of laser beam include monochromaticity, polarization and coherency. Monochromaticity indicates that the laser has a single wavelength, which leads to a high spectra power density. Polarization refers that laser beam has very low divergence and can be focused over a long distance, which is important for the delivery of laser through fiber optic systems. Coherency also allows the laser beam to be focused to a very tiny spot over an extreme long distance [60,63]. A Gaussian laser beam diverging from its waist is illustrated in Fig. 2-4. The beam parameter product (BPP) is an important parameter that can qualify the laser beam, which is defined as the product of the divergence half angle ( $\theta/2$ ) and the beam radius at the waist ( $w_0$ ). BPP represents how well the laser beam can be focused and a smaller BPP indicates a finer focused spot and a consequently higher power density [64].

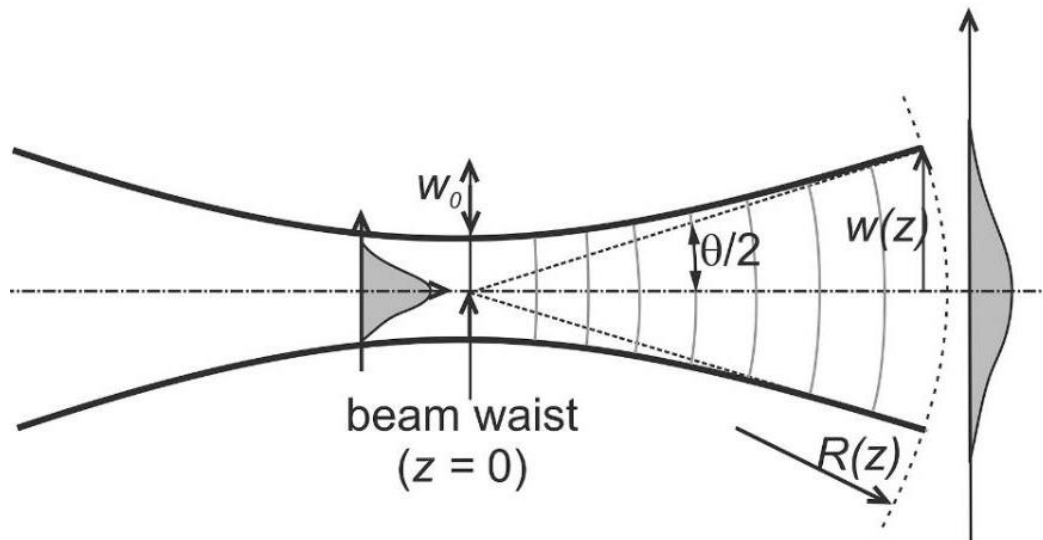


Figure 2-4. A Gaussian laser beam diverging from its waist. Reprinted with permission [65]. Copyright 2021, The author(s).

The concept of laser can be traced back to Einstein's prediction of stimulated emission [66]. In 1960, Theodore H. Maiman, a scientist at Hughes Research Laboratory in California, announced the acquisition of a laser beam with a wavelength of 0.6943 microns, which was the first functioning laser beam ever obtained [67]. Maiman thus became the first scientist to introduce laser beam into the practical field in the world. Since then, various types of industrial lasers including CO<sub>2</sub> lasers, Argon lasers, Nd: YAG lasers, and diode pumped Nd: YAG lasers have been developed, based on different active media. Among these, CO<sub>2</sub> and Nd: YAG laser systems are well established and widely used in industrial fields such as automobile and aerospace industries [9]. Nd: YAG lasers with fiber optic delivery can be integrated into flexible manufacturing systems and is thus more favorable in three-dimensional processing applications. Also, most metals have higher absorption ability to Nd: YAG lasers than to CO<sub>2</sub> lasers. This is beneficial to welding process, especially for the welding of highly reflective materials. In contrast, CO<sub>2</sub> lasers are also preferred in some cases due to its lower initial and operation cost [68], however over the long term they may require more maintenance and service costs.

### 2.2.2 Autogenous laser welding

With the invention of kilowatt-level high power laser systems, laser welding has become an important manufacturing technology, and has been widely used and researched by related companies and researchers. Compared to conventional arc welding technologies, laser beam welding (LBW) is often considered to have following advantages [8,9]:

- (1) Relatively low heat input, deep penetration, narrow HAZ and small distortion of the workpiece.
- (2) High welding speed and productivity.
- (3) Good surface quality.
- (4) Good continuity and repeatability.
- (5) Flexibility to access remote positions which are difficult for other methods.

However, there are some shortcomings to LBW [8,9]:

- (1) High precision demand for workpiece assembly and laser beam position adjustment.
- (2) High initial and operation cost.
- (3) Formation of defects like cracks, pores, and undercuts.
- (4) High hardness and brittleness of the weld metal.

The laser beam is highly focused and can reach an energy intensity between  $10^5$  to  $10^7$  W/cm<sup>2</sup>. Based on the power intensity, LBW can be divided into two primary categories, i.e., conduction and keyhole mode welding [69], as shown in Fig. 2-5. With a power density lower than  $10^6$  W/cm<sup>2</sup>, the energy absorbed by the workpiece is not enough to vaporize the metal, and instead, the melting of metal originates from the absorption and conduction of laser radiation energy. This process is known as laser conduction welding, during which only a shallow penetration can be achieved due to the low laser intensity and lack of vapor pressure. However, with a sufficiently high energy density (typically higher than  $10^6$  W/cm<sup>2</sup>), the laser keyhole welding mode can be realized. This occurs when vaporization of metal causes the



molten metal to be pushed away by the high vapor pressure, inducing a keyhole in the weld pool where the laser is internally reflected in a narrow cavity. The laser induced plasma presents on the top of the workpiece and in the keyhole, which could affect the absorption of laser energy. Deep penetration can be obtained during laser keyhole welding process, which leads to a high productivity and makes the keyhole mode more attractive for practical applications in industry [70].

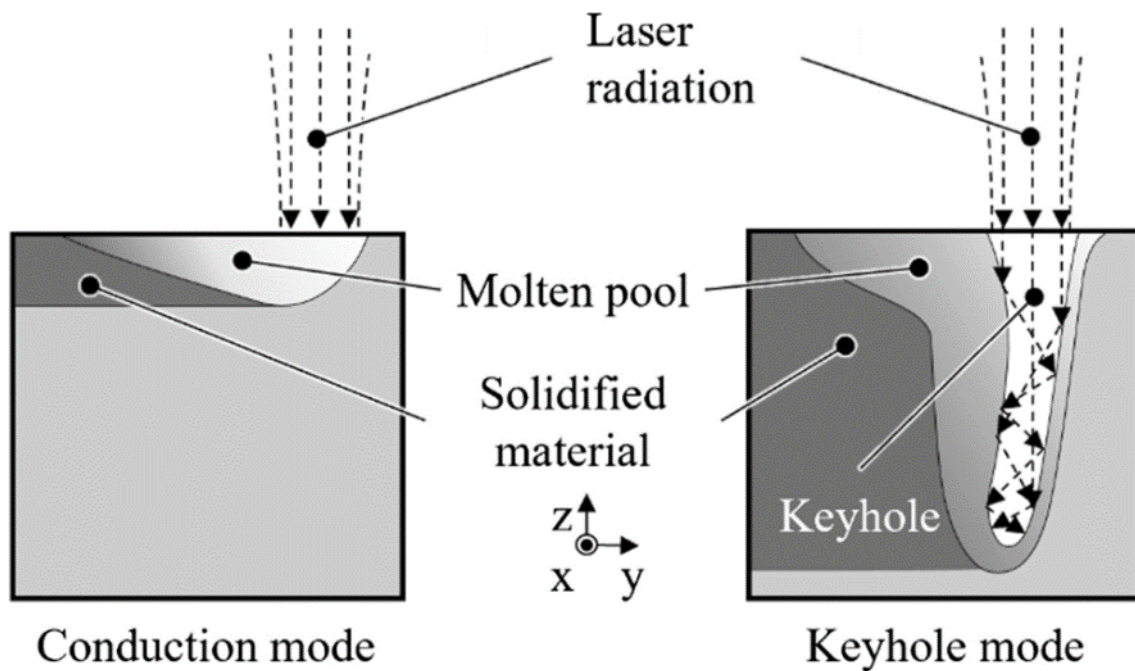


Figure 2-5. Schematic of laser welding modes. Reprinted with permission [69]. Copyright 2023, The author(s).

### 2.2.3 Wire-fed laser welding

#### Cold-wire laser welding

One of the main weaknesses of autogenous laser welding is the poor gap bridging ability. The laser beam is highly focused to a spot typically smaller than 1 mm in diameter, so good edge preparation and precise assembly are required during laser welding. Several researchers found that the acceptable gap for autogenous laser welding is less than 10% of the sheet thickness [17,71,72]. Feeding an additional wire during laser welding process is an effective way to improve the acceptable gap tolerance, usually with the laser in a conduction mode. Also,

the welding of thick-section plates becomes more efficient by multi-pass laser welding with filler wires, as Tsukamoto et al. [73] successfully achieved the joining of 150 mm-thick carbon steel plates by multi-pass narrow gap laser welding (NGLW) with a filler wire.

Due to the excellent penetration of the laser, the groove can be very narrow, thus reducing the number of total weld passes and the amount of required filler material, which is beneficial to improve the productivity in comparison with arc welding [74]. Guo et al. [75] compared multi-pass ultra narrow gap laser welding with the GMAW process during the welding of an 8-mm-thick S960 high strength steel and found that the total heat input and required filler material using GMAW was 6 times that of NGLW; meanwhile, the travel speed of NGLW was 1.5 times that of GMAW. Besides these, the feeding of welding wires can also optimize the chemical composition of the fusion zone and the resulting microstructure of the weld metal [18,19]. This could lead to better mechanical properties, for example, improved toughness for steels by promoting the formation of acicular ferrite [19].

### **Hot-wire laser welding**

Researchers also investigated the potential advantages of pre-heating wires. Fig. 2-6 shows a typical experimental set-up of hot-wire laser welding. The pre-heating of the welding wire is achieved by running an electrical current through it, and the filler material can be preheated to a temperature near the melting point [76]. Since an external power source is applied to heat the wire, the efficiency of laser welding and the deposition rate can be improved [20]. Nurminen et al. [77] found that the deposition rate of hot-wire laser cladding was 2 to 4 times that of cold-wire cladding. Wei et al. [13] proposed that the preheating of the filler wire increased the welding stability and improved the weld seam formation, while reducing the total heat input needed from the laser, with a maximum energy saving of 16% over laser cold wire welding process. Ohnishi et al. [78] obtained sound, fully penetrated welds over a range of gaps from 0 to 0.4 mm when performing hot wire laser welding with a 16 kW laser power on 12 mm thick

carbon steels. Sun et al. [79] reported that the distribution of wire elements was uniform from the top to the bottom of a 3-mm-thick hot-wire laser welded butt joint. Metzbower et al. [80] reported that during laser welding of HY80 steel, instead of obtaining an untempered martensitic microstructure in the autogenous welds, the introduction of a hot-wire feed could modify the weld metal microstructure depending on the feed rate. A slow wire feed resulted in a mixed martensite-bainite structure, whereas a fast feed resulted in a microstructure with primarily acicular ferrite. They also suggested that the addition of a hot wire had an effect equivalent to using a preheated substrate during welding, which would reduce the cooling rate in the fusion zone (FZ). Phillips et al. [19] found that hot-wire feed during laser welding of HY80 and HY100 steel reduced the weld metal hardness while also increasing the Charpy V-notch toughness by promoting the formation of acicular ferrite instead of martensite in the fusion zone.

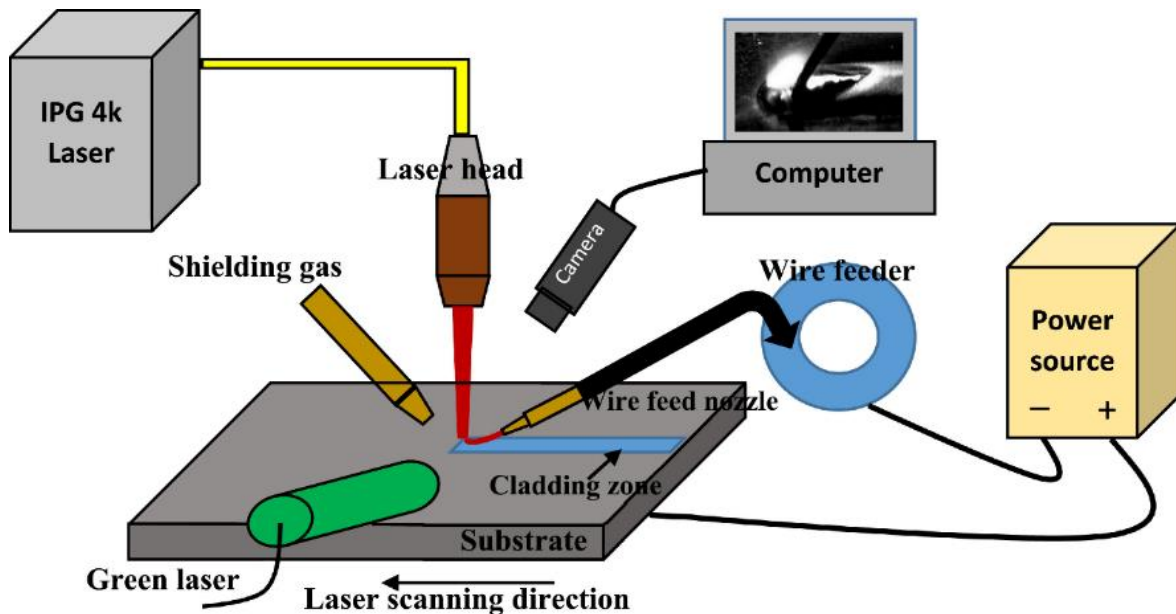


Figure 2-6. Experimental set-up for hot-wire laser welding. Reprinted with permission [76]. Copy right 2020,

Elsevier.

## 2.2.4 Hybrid laser arc welding

Hybrid laser arc welding is a combined-energy-sources welding technique during which a laser beam and an electrical arc heat in the same molten pool, as illustrated in Fig. 2-7 [27]. HLAW was first performed by Steen et al. [81] in 1980s, and the first industrial laser-MIG hybrid welding system was put into use by Fraunhofer ILT in the year 2000 [82]. HLAW combines the advantages of both energy sources, and eliminates the drawbacks of the welding with a single heat source. Deep penetration, high welding speed and good gap-bridging ability are achieved at the same time [83], which lead to a high productivity. The use of the arc reduces the total operation cost due to less laser power needed during the welding process. Compared to autogenous laser welding, a relatively lower cooling rate helps avoid the formation of brittle phases in the weld metal. Furthermore, the welding of highly reflective materials is easier compared to laser beam welding, with the assist of an arc heat source [84].

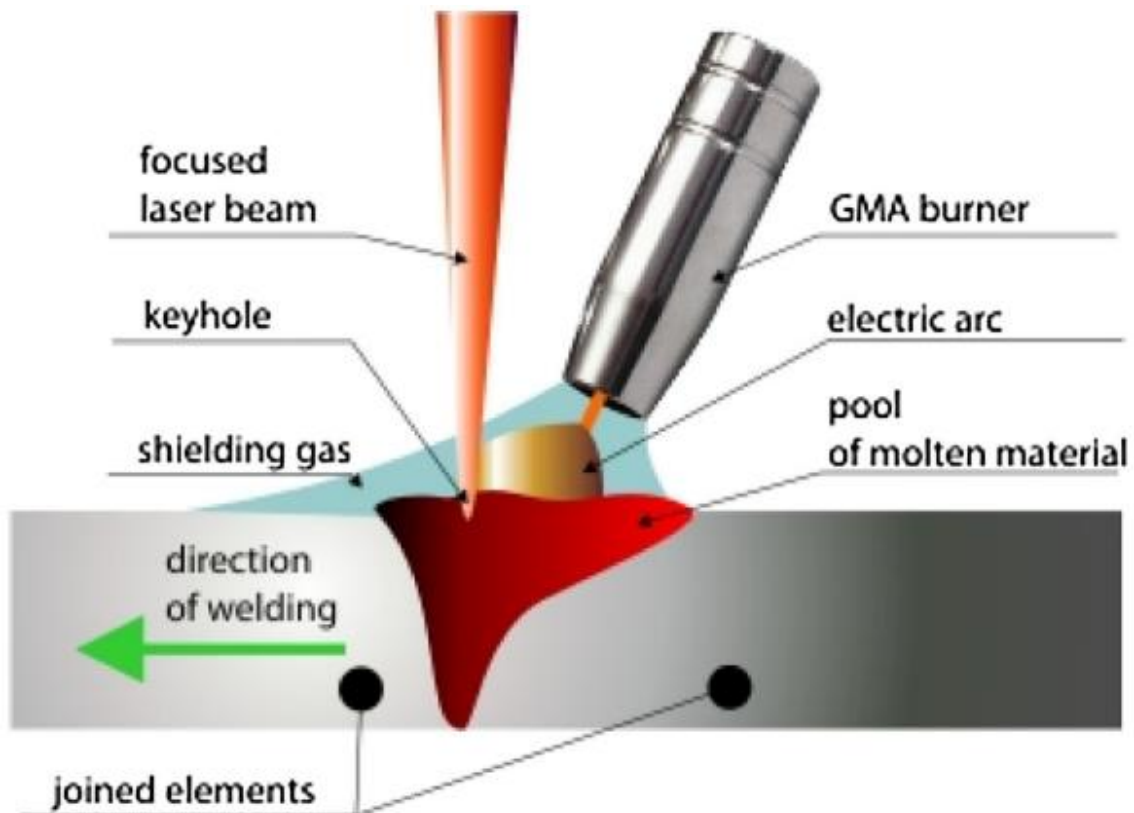


Figure 2-7. Schematic of hybrid laser arc welding process. Reprinted with permission [27]. Copy right 2018,

Elsevier.

It is reported that the arc is stabilized due to the presence of laser induced plasma [81,85]. Steen et al. [81] indicated that the hybrid-welding arc was attracted to the laser irradiation spot and the arc root was constricted. The laser-induced plasma caused by the ionization of metal vapor provided a large number of charged particles, which increase the electrical conductivity and reduce the electrical resistance at the laser irradiation spot. Since the arc always operates at the lowest potential, it tends to be attracted to the laser irradiation spot. The charged particles also increase the density of welding current and the resulting self-induction electromagnetic force of the arc, which causes the electromagnetic constriction of the arc root [81,85].

One shortcoming of HLAW is that a large number of parameters are involved and need to be evaluated and optimized, which not only include the parameters of individual welding processes, but also some new parameters like laser to arc power ratio, and laser to electrode distance [27]. This increases the difficulty of obtaining a stable welding process.

A typical HLAW joint has two distinctive regions in the FZ, which are upper 'arc zone' and lower 'laser zone', as presented in Fig. 2-8. The shape of arc zone is like a cup, while the laser zone has a finger-like shape [27,86]. During HLAW, a filler wire is utilized to fill the gap, and more importantly, optimize the chemical composition and the resulting microstructure to provide enhanced mechanical properties. However, the arc welding process normally leads to poor penetration depth, and the delivery of filler metal along the through-thickness direction during HLAW becomes problematic [28,29,87]. For HLAW of pipeline steels, filler wires are introduced to the weld pool, to promote the formation of acicular ferrite with high strength and toughness. However, insufficient mixing of filler wire and base metal may occur at the root laser zone, which leads to the formation of hard and brittle microstructure instead of acicular ferrite, and deteriorates the fracture toughness of the weld.

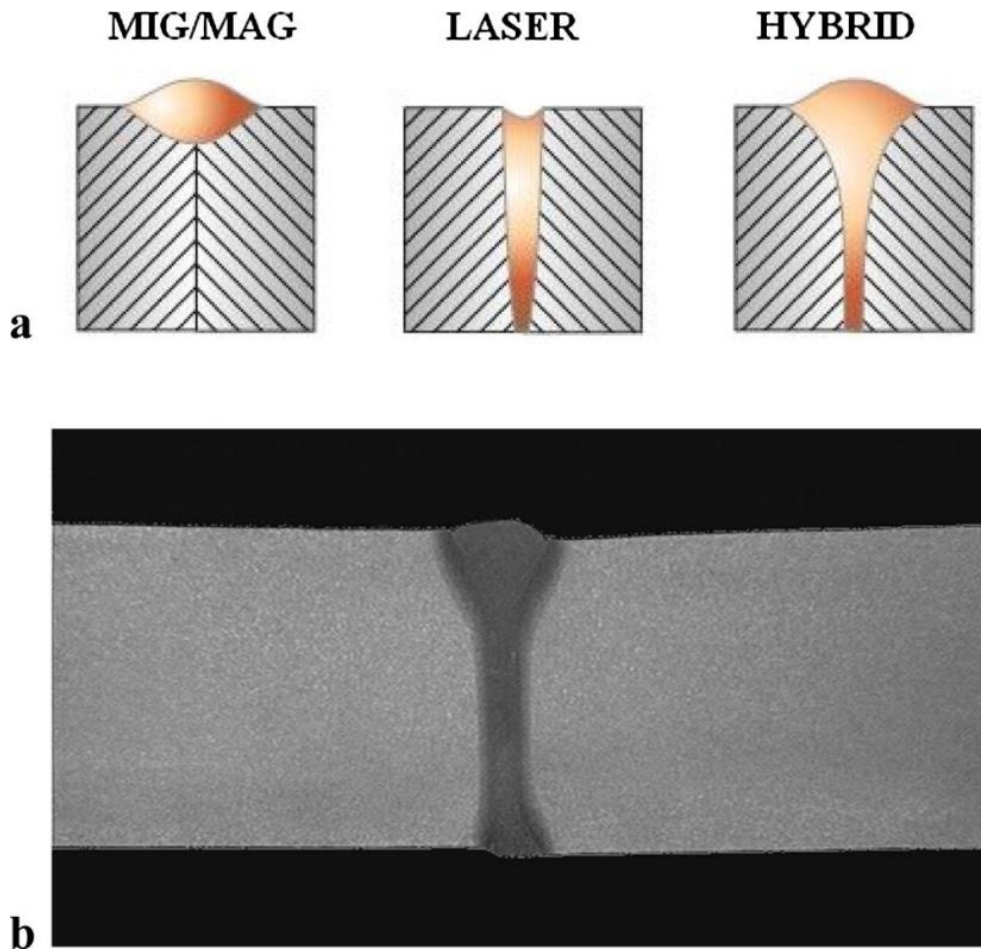


Figure 2-8. (a) Patterns of weld formation during arc welding, laser welding and hybrid laser arc welding; (b) cross-sectional view of a hybrid laser arc weld. Reprinted with permission [27]. Copy right 2018, Elsevier.

Gook et al. [28] utilized a modified pulsed spray arc with a very short arc length of 3.1 mm to enhance the transport of filler material into the root region of FZ in an arc leading configuration during hybrid welding of HSLA steel. The cross-sections of joints welded with different types of arcs are shown in Fig. 2-9. The areas with a homogenous Ni (as a ‘tracer’ element of the wire) distribution (defined as 0.59%-0.63%) extended up to 3.7 mm for normal and pulsed arc, whereas this reaches around 5.0 mm for modified spray arc. The modified spray arc with a short arc length had extremely high directional stability which resulted in a high plasma pressure acting on the molten pool and helped deliver the filler material to the root bottom.

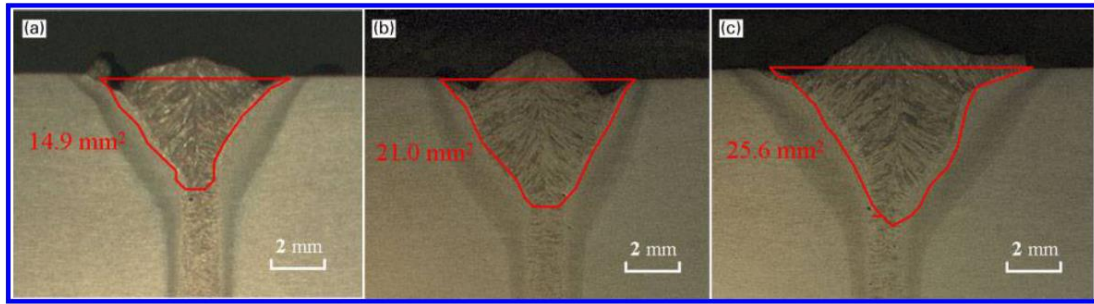


Figure 2-9. Cross-section morphologies of joints welded with different arc types: (a) GMA pulse; (b) GMA normal; (c) modified spray arc. Reprinted with permission [28]. Copyright 2014, SAGE Publications.

Gao et al. [30] investigated the influence of the laser to arc power ratio and root gap on the filler material delivery during hybrid welding of medium carbon steel. The weld shapes with different laser/arc energy ratios are shown in Fig. 2-10. The filler material penetration was increased by 3.0 mm when the laser/arc energy ratio decreased from 1.49 to 0.58. The increase in arc power led to stronger arc force and energy density, which could drive more arc heat to the root and enhance the transportation of filler material. It is also reported that an increase of groove gap from 0 to 0.6 mm improved the filler material penetration by 1.0 mm since the gap provided a channel for the melted material to the root and reduce the flowing resistance. Bunaziv et al. [29] also found that an increase air gap enhanced the filler material transportation to the root area during HLAW of HSLA steel. However, they claimed that the filler metal penetration was still low at welding speeds higher than 1.0 m/min.

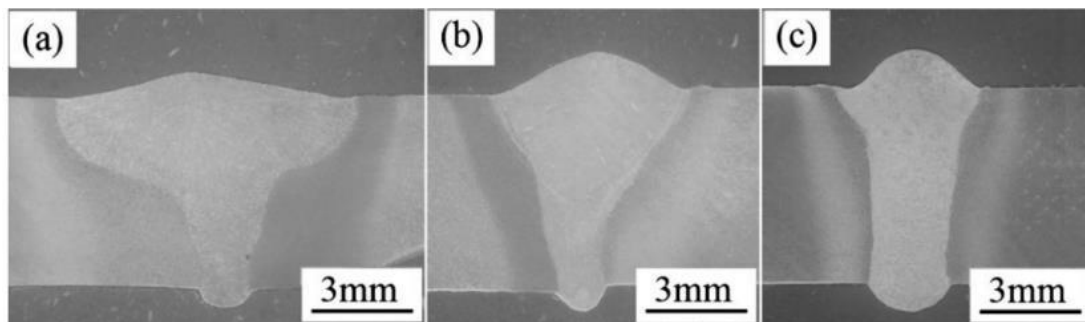


Figure 2-10. Cross-section morphologies of joints welded with different laser/arc energy ratio: (a) 1.49; (b) 0.87; (c) 0.58. Reprinted with permission [30]. Copyright 2008, SAGE Publications.



Wahba et al. [87] used pre-placed wire in the joint gap to improve the microstructure homogeneity during HLAW of SM490A steel. The experimental set-up is shown in Fig. 2-11. Pre-cut wire fragments were placed into a square groove with an air gap of 2.5 mm before welding. The use of pre-placed wire fragments provided a homogenous filler metal distribution along the through-thickness direction, with both the arc- and laser- dominated fusion zone consisting of acicular ferrite and grain boundary ferrite. Due to a lower heat input and a higher cooling rate, the laser zone exhibited a higher strength and toughness resulting from a finer microstructure.

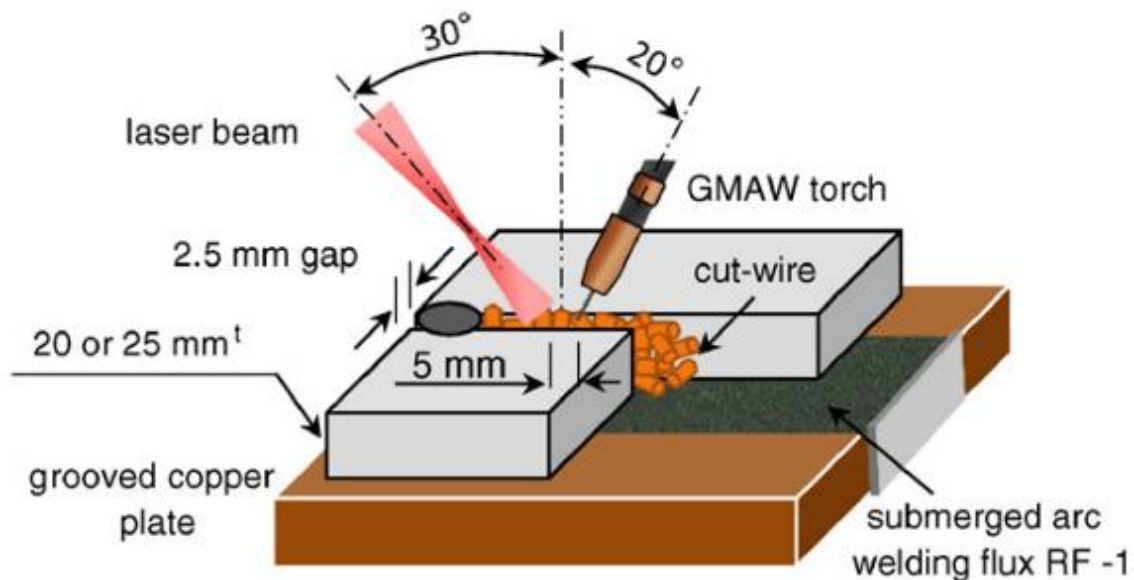


Figure 2-11. Experimental set-up for laser hybrid welding with pre-placed cut-wire fragments. Reprinted with permission [87]. Copyright 2016, Elsevier.

## 2.2.5 Wobble laser welding

### Characteristics of laser beam wobbling

Rather than use a simple linear motion for the beam in the case of conventional laser welding, a wobble mechanism can move the spot in different repeating patterns hundreds of times per second. Fig. 2-12 illustrates the components of a wobble welding head and a typical experimental set-up for wobble laser welding, with the most common wobble patterns presented. Beam oscillation is controlled by the galvanometer scanners integrated inside the



wobble head. Various wobble patterns including linear, circular, figure-eight and infinity paths can be achieved by the precise motion of the galvanometer scanners [88].

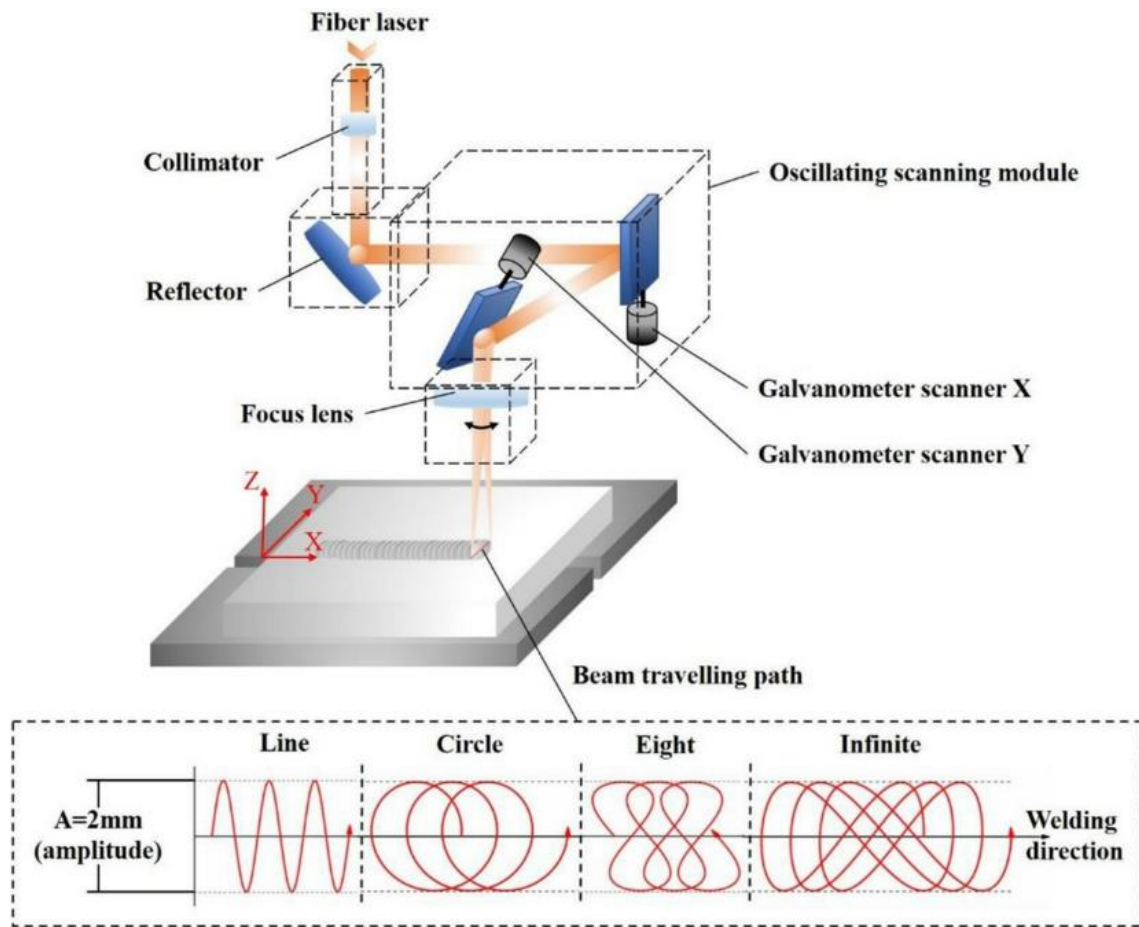


Figure 2-12. Experimental set-up of wobble laser welding, with common wobble patterns presented. Reprinted with permission [88]. Copyright 2022, SAGE Publications.

With beam wobbling, the laser spot position can be expressed by following equation:

$$\begin{cases} x(t) = x_0 + vt + A_x \sin(2\pi f_x t + \varphi_x) \\ y(t) = y_0 + A_y \sin(2\pi f_y t + \varphi_y) \end{cases} \quad (2-5)$$

Where  $x(t)$  and  $y(t)$  define the laser spot position after a welding time  $t$ ,  $x_0$  and  $y_0$  are the initial positions,  $v$  is welding speed,  $A_x$  and  $A_y$  are the wobble amplitudes along the  $x$ - and  $y$ - directions, respectively.  $f_x$  and  $f_y$  are the wobbling frequencies along  $x$ - and  $y$ - directions, respectively.  $\varphi_x$  and  $\varphi_y$  are the initial phase angles. The shape of wobble pattern is determined by these parameters. For example, when the wobble amplitudes and frequencies

along two directions are equal and the phase shift is equal to  $\pi/2$ , a circular wobble pattern is achieved [90,91].

By taking the derivative of the equation (2-5), an expression for the laser spot velocity can be obtained, which is shown by following equation:

$$\begin{cases} v_x = v + 2A_x\pi f_x \cos(2\pi f_x t + \varphi_x) \\ v_y = 2A_y\pi f_y \cos(2\pi f_y t + \varphi_y) \\ v_r = \sqrt{v_x^2 + v_y^2} \end{cases} \quad (2-6)$$

where  $v_x$  and  $v_y$  are the velocities along  $x$ - and  $y$ -direction, respectively.  $v_r$  is the actual velocity of the laser spot [90].

The laser irradiation area, melt flow behavior, temperature distribution, the resulting microstructure and mechanical properties are all modified with laser beam wobbling, which provides the potential to overcome the shortages of conventional LBW. Beam wobbling is reported to have the ability to improve the gap-bridging ability with a larger laser irradiation area [10], suppress porosity by stabilizing the keyhole [21,22], promote grain refinement by affecting the solidification process [24,90,92], and improve the microstructure homogeneity by enhancing materials mixing with the stirring effect [26].

### **Improving gap-bridging ability with beam wobbling**

Laser beam wobbling offers the potential to accommodate larger gaps, because the laser irradiates a larger area so that a wider fusion zone can be obtained. Rubben et al. [16] first applied beam wobbling technique during laser welding and claimed that it increased the gap tolerance of tailed blanks to 25% of the sheet thickness. Hao et al. [10] investigated the effects of wobble parameters during laser welding of AISI304 steel, with the weld surface morphologies shown in Fig. 2-13. With a very low wobble frequency (10 Hz), zigzag-line-shaped weld beads formed (Fig. 2-13a, e, i and m). With an increasing wobble frequency, the overlapping region of the melted metal along the laser traveling path was enlarged, and smooth weld beads were obtained (Fig. 2-13d, h, l and p) at a sufficiently high wobble frequency (500

Hz). At a constant frequency of 100 Hz, the weld width increased by 212.5%, from 1.6 mm to 5.0 mm with the wobble amplitude increased from 0.5 mm to 2.5 mm, which indicates that the gap-bridging ability can be improved with beam wobbling [10]. With a constant welding speed, either a larger wobble amplitude or a higher frequency led to a faster local laser spot velocity, which resulted in the reduction of penetration. Therefore, in order to increase the gap-bridging ability while maintaining a sufficient penetration, the total heat input need to be increased when increasing the wobbling amplitude and frequency [10].

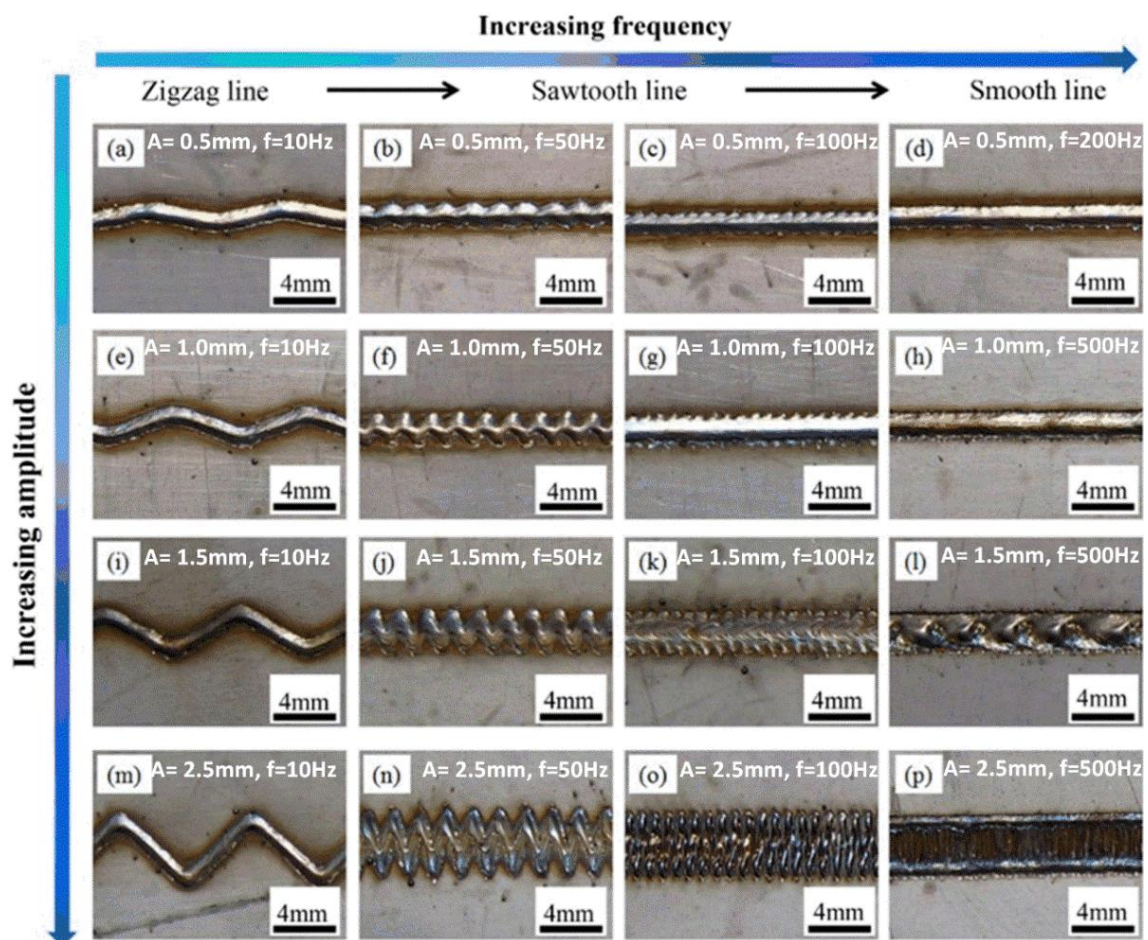


Figure 2-13. Effects of wobble amplitude  $A$  and frequency  $f$  on weld surface morphologies: laser power  $P = 2$  kW; welding speed  $v = 3$  m/min. Reprinted with permission [10]. Copyright 2015, Elsevier.

### Reducing porosity by beam wobbling

The formation of pores can be a serious problem during laser welding, especially for metals like aluminium and copper, etc. Fast cooling during LBW in addition to high thermal

conductivity of these metals lead to severe pores formation. Typically, two types of pores could be produced during laser welding. The hydrogen pores are generated due to the presence of contamination on the sheet surface, chemical component of the weld material or the impurity of the shielding gas. The other type is related to keyhole instability during the laser welding process [93]. Li et al. [23] pointed out that beam wobbling suppressed porosity during laser welding because the enlarged molten pool and the reduced cooling rate provided more time for the bubbles to diffuse out from the molten pool. Liu et al. [94] found that a wobble laser enlarged the keyhole diameter and improved keyhole stability, which was helpful to suppress porosity. Zhang et al. [22] pointed out that a high laser spot speed during wobble laser welding was also beneficial to suppress porosity, which helped avoid local excessive evaporation and led to a more stable keyhole.

Fetzer et al. [21] and Zhang et al. [22] explained the mechanism of reducing porosity by the stirring effect of beam wobbling and keyhole-bubbles interaction during wobble laser welding. As shown in Fig. 2-14, a bubble was generated at a quarter of the wobbling period ( $1/4 T$ ). At  $3/4 T$ , the bubble met the keyhole again and was absorbed by it. During traditional LBW, the formed bubbles will be left behind such that they will not interact with the keyhole. With a circular wobble pattern, a vortex flow is generated by the vapor recoil pressure, which drove the bubbles rotating with it. If the bubbles do not escape from the vortex flow, they would inevitably meet the keyhole and be absorbed by it, thus suppressing pores formation [21].

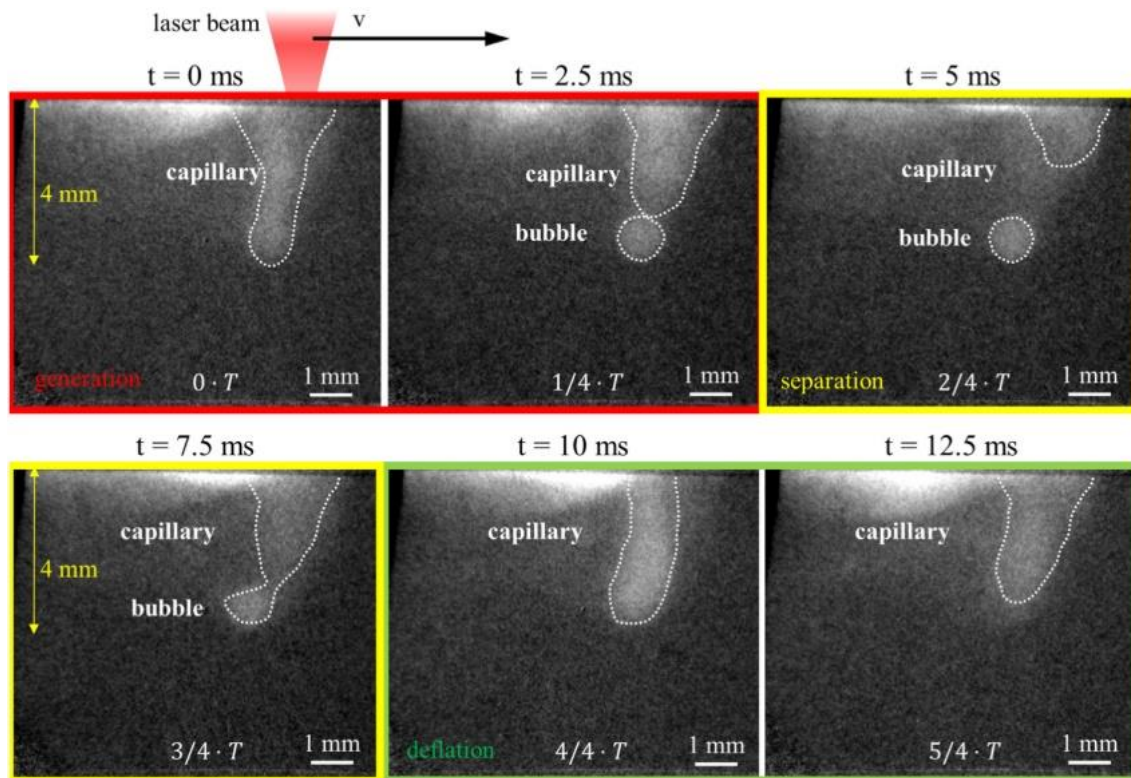


Figure 2-14. Process of bubble formation and absorption by keyhole during LBW recorded with X-ray imaging technique. Reprinted with permission [21]. Copyright 2018, The author(s).

### Refining grains by beam wobbling

Since beam wobbling considerably affects the flow of molten pool and the temperature gradient, it helps achieve a fine-grained microstructure with improved mechanical properties. Jiang et al. [24] found that grain refinement was achieved by beam wobbling during laser welding of Invar alloy. They indicated that with increasing wobble amplitude, a larger molten pool with a lower peak temperature and a shallower temperature gradient was obtained, which promoted the formation of finer equiaxed grains, based on the constitutional supercooling theory. Li et al. [23] found that the growth of columnar grains was interrupted and the microstructure was refined by beam wobbling during laser welding of 304 stainless steel.

Wang et al. [90] investigated the influence of wobble patterns on the microstructure and mechanical properties during laser welding of AA6061-T6 aluminium alloy. Fig. 2-15 shows the Electron Backscatter Diffraction (EBSD) maps of FZ microstructure with varying wobble



conditions. In Fig. 2-20a and b, the static-spot laser weld mainly consisted of columnar dendrites growing from the fusion line to the weld center, and the axial grains growing along the center line. For the wobble laser welds, the grains in the center zone evolved from axial shape to equiaxed shape. The circular-wobble-laser weld contained the most equiaxed grains (52%) with the smallest average grain size compared to the transversal- and longitudinal-wobble-laser welds (27% and 38%, respectively). The highest hardness was also found in the circular-wobble-laser weld [90].

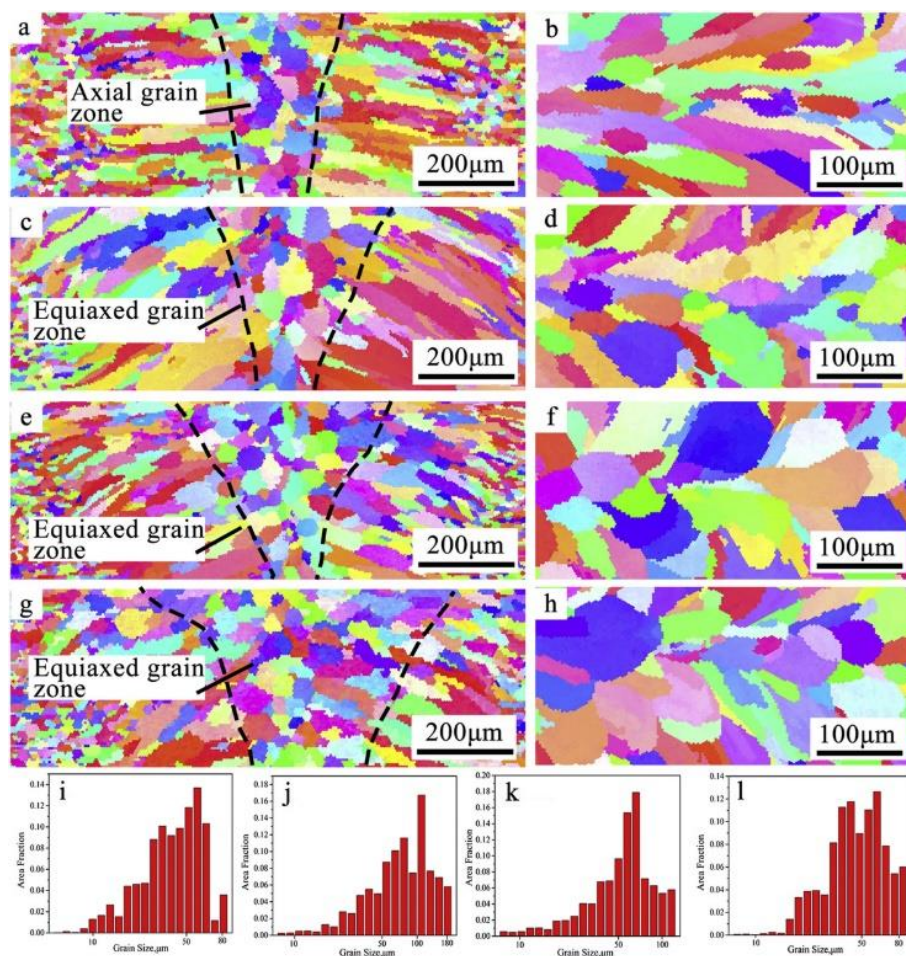


Figure 2-15. EBSD results of FZ microstructure produced with varying wobbling conditions: (a, c, e, g) cross-section of welds without wobbling, with transversal wobbling, with longitudinal wobbling and with circular wobbling; (b, d, f, h) horizontal section of welds without wobbling, with transversal wobbling, with longitudinal wobbling and with circular wobbling; (i)-(l) grain size distribution of welds without wobbling, with transversal wobbling, with longitudinal wobbling and with circular wobbling. Reprinted with permission [90]. Copyright

The formation mechanism of the FZ microstructure is illustrated in Fig. 2-16. As shown in Fig. 2-16a-b, the molten pool formed during static-spot laser welding presented the smallest size which resulted in the highest temperature gradient that promoted the formation of columnar dendrite based on solidification theory [95]. In contrast, the molten pool was enlarged due to a larger laser irradiation area with beam wobbling. The larger molten pool led to a smaller temperature gradient which promoted the formation of equiaxed grains. A circular wobble laser generated the largest molten pool such that the FZ contained the most equiaxed grains. Due to the high frequency oscillation of the laser beam, small melt flow turbulences formed at the trailing edge of molten pool during wobble laser welding. These turbulences would penetrate the mushy zone which contained both the growing dendrites and the liquid metal. The solidifying dendrites were remelted and broken into small pieces. A circular wobble laser led to the highest local laser spot velocity and thus the strongest stirring effect, which produced the strongest turbulence and contributed to the formation of most equiaxed grains [90].

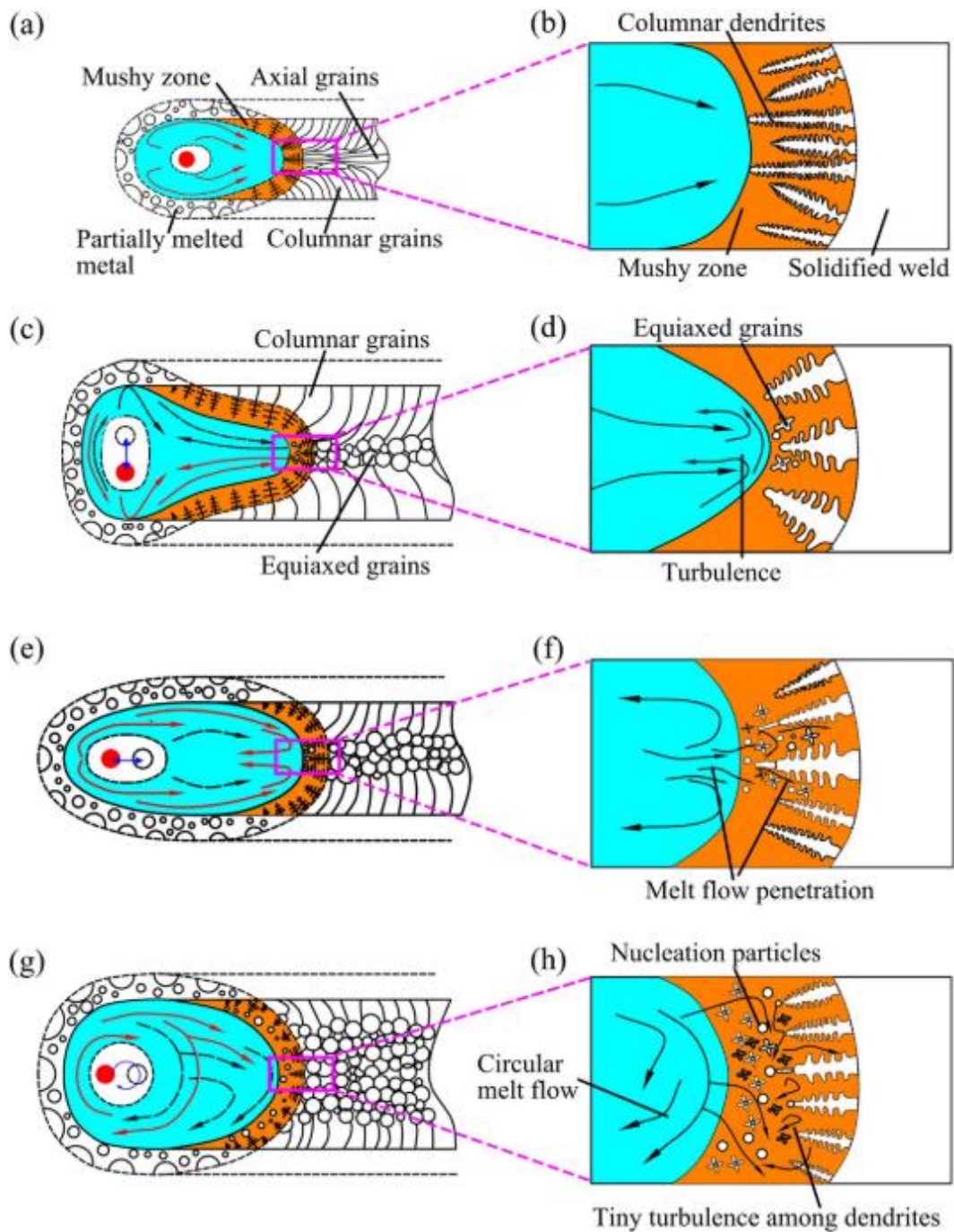


Figure 2-16. Formation mechanism of the microstructure in FZ produced with varying wobbling conditions: (a, b) without wobbling; (c, d) with transversal wobbling; (e, f) with longitudinal wobbling; (g, h) with circular wobbling. Reprinted with permission [90]. Copyright 2016, Elsevier.

### Enhancing materials mixing by beam wobbling

The effects of stirring molten pool and adjusting temperature gradient by laser beam wobbling have the potential to provide uniform materials intermixing in the FZ, and this has



gained interest in applications for dissimilar materials welding and HLAW. Due to the differences in physical properties and chemical compositions during dissimilar materials welding, it can be challenging to produce a sound weld joint with good mechanical properties. One serious problem is the macro-segregations due to the high temperature gradient during laser welding and the difference between melting points of the phases in two substrates. For dissimilar metals welding, some base metals consist of high melting point phases which might not be completely melted but just partially dissolved in the FZ. This inhomogeneous microstructure causes reduction and deterioration of the mechanical properties such as toughness, strength and corrosion resistance [26].

Jiang et al. [26] investigated the effect of laser beam wobbling on the FZ microstructure during Ni-Cr-Mo and Cu-Cr-Zr dissimilar metals welding. Fig. 2-17 shows the EDS maps of the welds produced with and without laser beam wobbling, indicating that a wobble laser produced a more homogeneous FZ microstructure with the uniform distribution of nickel, copper, and molybdenum. Beam wobbling provided a more even temperature distribution and the high-frequency beam wobbling allowed sufficient intermixing of the melted metals, both of which resulted in a homogeneous distribution of elements [26].

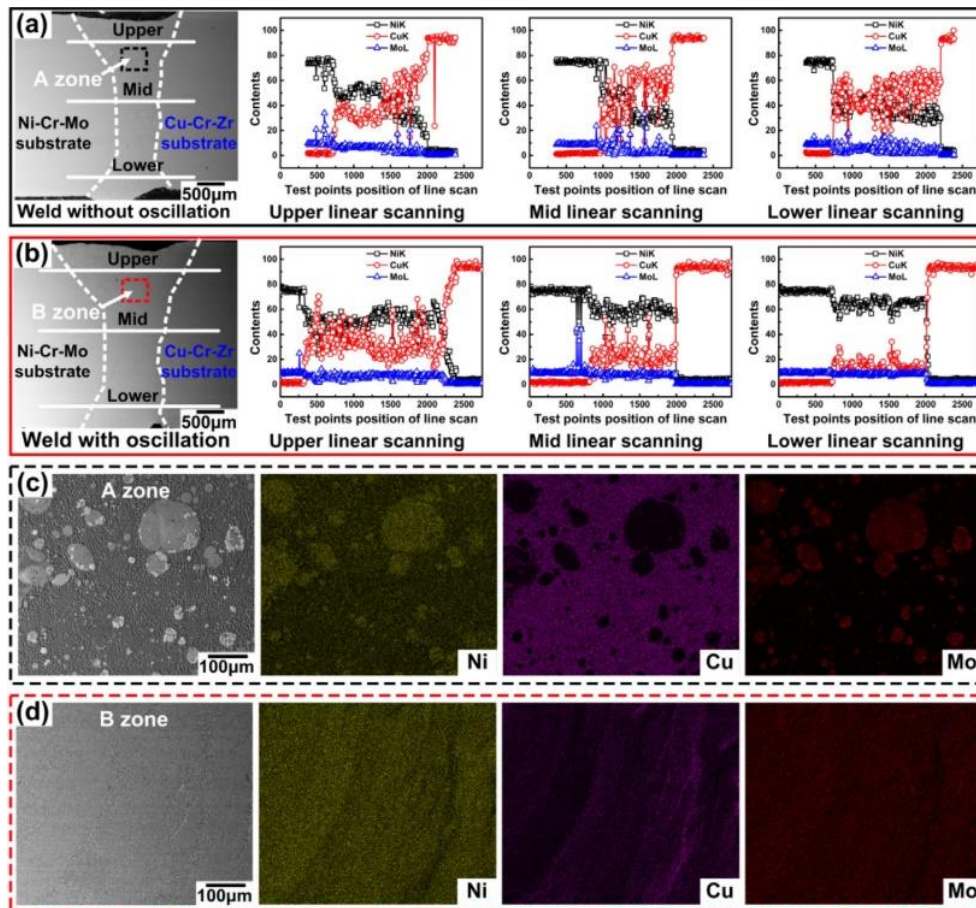


Figure 2-17. EDS results of FZ in dissimilar materials welds produced with varying wobbling conditions: (a) linear scanning result of FZ of static-spot laser welded joint; (b) linear scanning result of FZ of the wobble laser welded joint; (c) map scanning result of FZ of static-spot laser welded joint; (d) map scanning result of FZ of the wobble laser welded joint. Reprinted with permission [26]. Copyright 2020, Elsevier.

Wang et al. [96] found that beam wobbling promoted the solute transfer, mitigated the macro-segregation, and improved the microstructure homogeneity in laser arc hybrid Al-Si welds. As shown in Fig. 2-18, a larger wobble amplitude of 1 mm enlarged the transaction angle between the upper and lower molten pool, and thus promoted the diffusion of the elements from the filler material to the root bottom region of the keyhole. In addition, the stronger stirring effect created by the larger Renold number ( $R_e$ , which increases with wobble amplitude and frequency) also helped migrate the Si-rich particles from the filler material, leading to a more homogenous distribution of the elements.

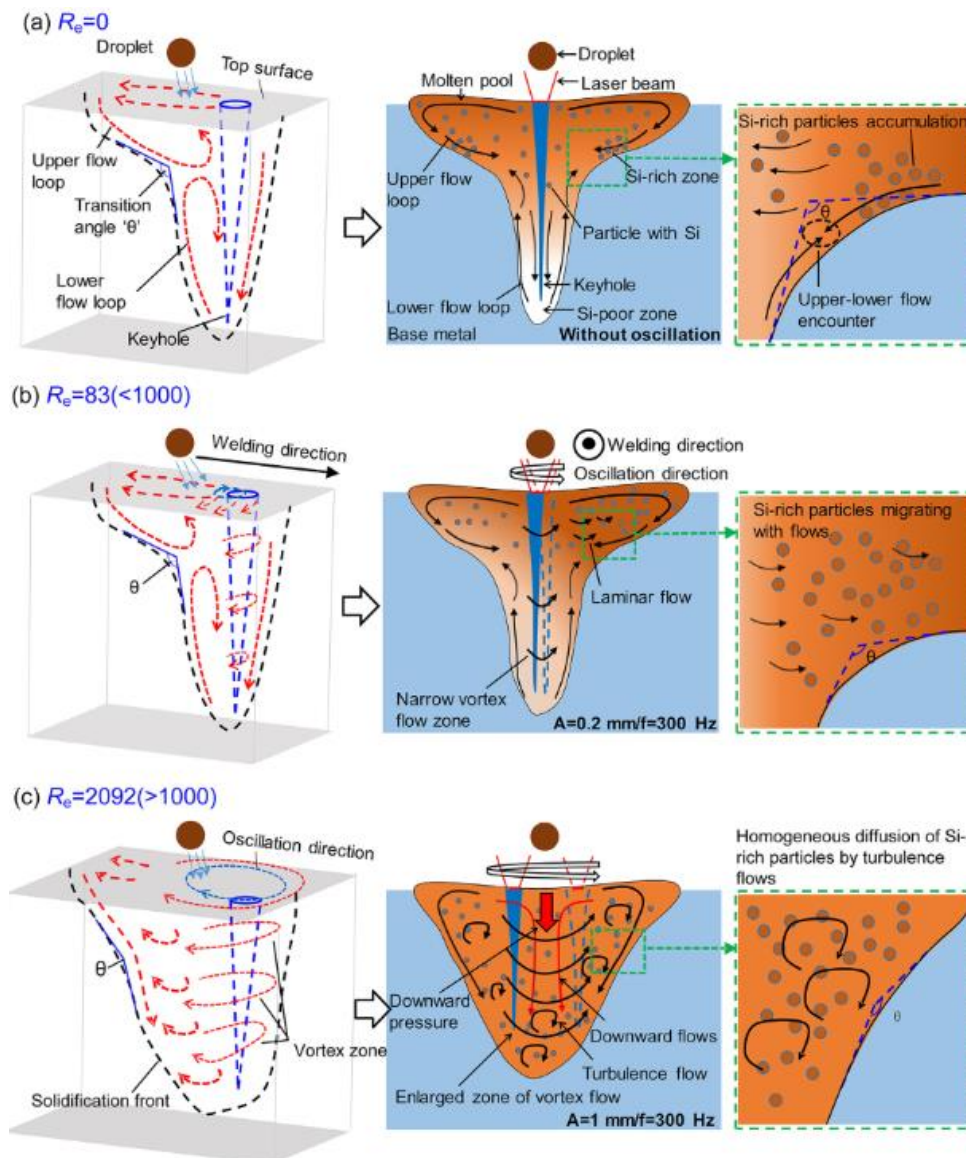


Figure 2-18. Schematic of solute transfer in laser arc hybrid Al-Si welds: (a) without wobbling; (b)  $A = 0.2 \text{ mm}$ ,  $f = 300 \text{ Hz}$ ; (c)  $A = 1 \text{ mm}$ ,  $f = 300 \text{ Hz}$ . Reprinted with permission [96]. Copyright 2020, Elsevier.

### 2.3 Industrial requirements for pipeline steel welds

The current pipeline standards are developed based on conventional GMAW technologies. API 5L and CSA Z662 (by Canadian Standards Association) both require that the tensile strength of the weld metal should reach the specified minimum tensile strength of the pipe material. Meanwhile, CSA Z662 also points out that the strength of the weld metal should overmatch that of the base material, to avoid failure happen in the FZ.

The API 5L standard requires that the average full-size CVN (i. e., Charpy V Notch)

absorbed energy for a pipe weld test should reach 27 J for pipes with a diameter smaller than 1422 mm in grades up to X80, and 40 J for pipes with a diameter larger than 1422 mm. If sub-size test pieces are used, the required minimum average absorbed energy should correspond to the values for full-size samples (with a width of 10 mm) times the ratio of the specified width of the sub-size sample to that of the full-size sample.

API 5L states that the hardness of the FZ and HAZ in an X80 steel weld should not exceed 275 HV for pipes designed for sour service. As a higher hardness often indicates the presence of more carbides which could act as initiation sites for cracks, and low temperature transformation products like upper bainite and lath martensite which provide favorable propagation path for the cracks. For non-sour service pipes, the weld metal hardness limit can be relaxed, which can be 300 HV. A British standard (BS 4515) points out that the FZ hardness should not exceed 275 HV, and the HAZ hardness should not reach 350 HV for non-sour service pipes.

API 5L requires that no cracks shall occur in any portion of a test piece in a bend test, and no opening of the weld shall occur. CSA Z662 states that no cracks or other imperfections exceeding the lesser of 3 mm and 0.5 times the nominal wall thickness in any direction shall occur in the weld after the sample is bent.

## **2.4 Summary**

HSLA steels are optimized with carefully selected micro-alloying elements and TMCP in order to achieve a combination of high strength and toughness, and are thus widely used for oil and gas pipelines, cranes, bridges, automotive components, and so on. In most of these applications, welding is a common and important process, since the reliability of completed assemblies depends on the quality of the welded joints. Laser welding is a high energy density beam welding technique which has gained popularity by offering high productivity, low heat input, deep penetration, and small HAZ which can offer superior mechanical properties to arc

welding methods. In the pipeline industry, replacing the conventional welding methods like SAW and GMAW with hybrid laser welding can significantly increase the productivity and reduce the total operation cost due to its high welding speed and deep penetration. However, the limitations for laser welding of thick carbon steel include the poor gap-bridging ability, and the fast cooling in the FZ that could generate hard and brittle weld metal. In the literature, the weld metal hardness of an X80 steel laser weld typically reaches 290 HV to 360 HV even with wire addition [7,97–100], which exceeds the maximum values required by API. HLAW is a more effective technique, with one major technical difficulty related to poor microstructure homogeneity in the weld metal, which is caused by the lack of filler material penetration. In prevailing literature, several solutions such as utilizing pulse spray arc with a short arc length, optimizing laser to arc power ratio, and modifying joint configuration offered limited effect to improve the performance of HLAW joints. Novel technologies such as the feeding of hot-wires and the addition of beam wobbling help overcome some critical limitations of conventional laser beam welding, offering higher deposition rate, slower cooling, better gap-bridging ability, and improved mixing in the FZ, which could help improve the quality of pipe laser welds.

Currently, there is a research gap on combining beam wobbling and hot-wire feeding techniques during a laser keyhole welding process of pipeline steels. The effect of beam wobbling on the filler material distribution, weld metal microstructure, and mechanical properties has yet to be studied. As the commercial welding wires and industrial standards are developed based on arc welding processes, the mechanical properties of the laser welds obtained with these novel techniques need to be evaluated. By optimizing the groove design, filler material chemistry and preheating conditions, it may be possible to develop laser welding procedures that meet the weld metal hardness, strength, and toughness requirements.

### **Chapter 3: Objectives and scope**

The aim of this work is to develop a state-of-art hybrid laser welding process as a root pass for the welding of HSLA pipeline steels with improved weld quality, mechanical properties, and increased productivity. The research on laser welding and HLAW technologies of pipeline steels has been ongoing for several years. Replacing conventional arc welding methods with hybrid laser welding can significantly increase productivity and reduce the total construction costs. In past literature, filler materials with different chemistry from the base metal have been used to promote the formation of a tough weld metal microstructure with mainly acicular ferrite. One major technical difficulty in HLAW of thick pipeline steels is the microstructure inhomogeneity in the weld metal caused by the poor filler material transportation. Brittle bainitic microstructures may form in the laser zone, which deteriorates the toughness of the weld. Novel technologies like hot-wire fed and laser beam wobbling have provided the potential to overcome some limitations of conventional laser welding. In this work, these techniques were applied to improve the performance of the pipe laser welds. The relationship between the welding parameters and the elements distribution, microstructure as well as the mechanical properties were investigated.

The scope of this work can be divided into sections as follows:

- Investigation on the effect of wire feed rate (WFR) and the preheat of the wire on the microstructure and mechanical properties such as microhardness, tensile strength, and Charpy V-notch impact toughness during wire-fed laser keyhole welding of pipeline steel.
- Investigation on the effect of laser beam wobbling on the filler material distribution, fusion zone microstructure, and mechanical properties including hardness and yield strength in pipe laser welds. Bead-on-plate wobble laser welding was first performed

for penetration and microstructural study. Beam wobbling was then applied to Y-groove laser welding process.

- Utilizing a wobble laser in combination with a hot-wire feed during laser welding of pipeline steel. Investigation on the effect of root gaps and substrate preheating on the cooling rate, FZ and HAZ microstructure, and the corresponding hardness properties.
- Investigation on the influence of filler wire chemistry on the microstructure and hardness in pipe laser welds. Laser welding was evaluated using different filler wires: ER70S-6 steel, ER70S-2 steel, commercially pure iron, and pure nickel filler, in the context of welding X80 pipeline steel.

The flow chart shown in Fig 3-1 summarized the research work that has been done to achieve above objectives. The effect of hot-wire feeding and laser beam wobbling in X80 steel laser welds were studied respectively. A wobble laser was then combined with a hot-wire feed during laser welding X80 steel. Finally, the effect of wire chemistry was studied with the optimized welding procedures.

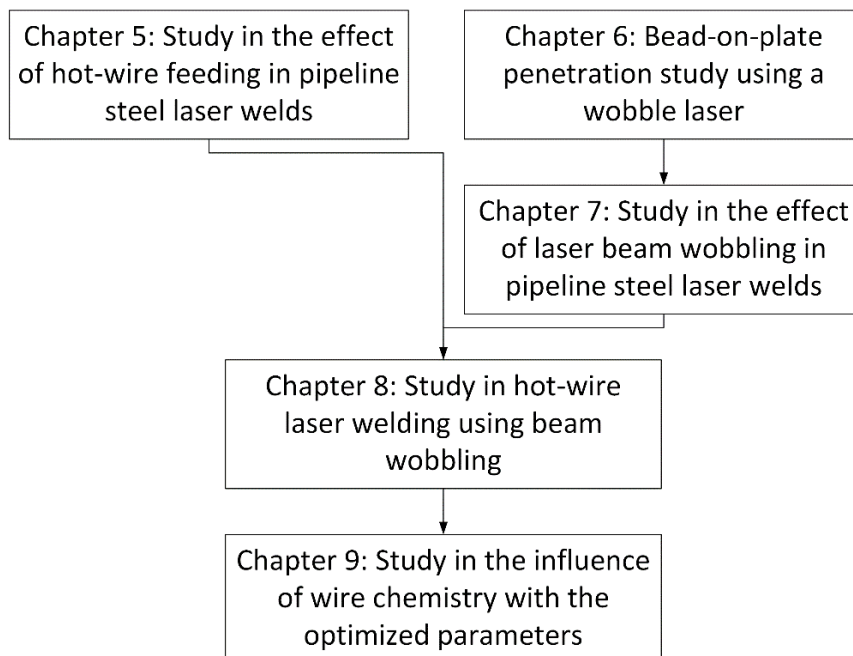


Figure 3-1. Flow chart summarizing the research work in this thesis

## Chapter 4: Materials and experimental methodology

### 4.1 Materials

X70 and X80 HSLA pipeline steels were used as the base material in this work, with the chemical compositions given in Table 4-1. A 16-mm-thick X70 steel was used for bead-on-plate laser welding tests, whereas the X80 steel was mainly used for Y-shaped groove welding. The X80 substrates had dimensions of 250 mm × 120 mm × 14 mm and an internal radius of 470 mm, with the edge of the plates machined with a 30-degree bevel and a 6 mm root height, as shown in Fig. 4-1. Before welding, the oxides on the plate surfaces were removed by sandblasting, and the plates were tack welded together to ensure accurate positioning and minimize distortion during welding. ER70S-6 (provided by Prostar) and ER70S-2 (provided by Lincoln Electric and also named as L52 wire) carbon steel welding wires with a diameter of 0.9 mm were used, with the typical wire chemistry provided in Table 4-2. Commercially pure iron (99.95% purity) and nickel (99% purity) wires were also utilized to study the effect of chemical composition.

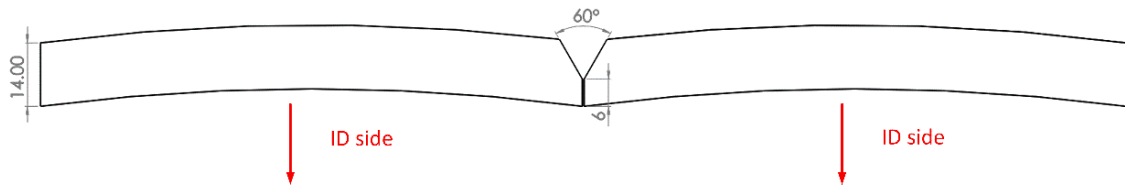


Figure 4-1. Groove design for X80 steel laser welding, showing the inside diameter (ID) side

Table 4-1. Chemical compositions of base materials (wt.%).

	C	Mn	Cr	Si	Ni	Cu	Mo	Ti	Nb	Fe	$P_{cm}$
X70	0.063	1.66	0.07	0.09	0.15	0.15	0.01max	0.01	0.03	Bal	0.162
X80	0.051	1.73		0.18	0.13	0.12	0.21	0.01	0.04	Bal	0.166



Table 4-2. Chemical compositions of filler wires (wt.%).

	C	Mn	Cr	Si	Ni	Cu	Mo	Ti	Zr	Al	Fe	$P_{cm}$
ER70S-6	0.07	1.58	0.01max	0.94	0.01max	0.17	0.01max	0.01max	0.01max	0.01	Bal	0.190
ER70S-2	0.04	1.10	0.06	0.59	0.03	0.21	0.01	0.10	0.03	0.07	Bal	0.129

## 4.2 Welding and monitoring equipment

A typical laser welding set-up is shown in Fig. 4-2. IPG YLS-6000 and YLS-8000 lasers were used, with a maximum power of 6 kW and 8 kW, respectively. Various spot sizes were used, including 111  $\mu\text{m}$ , 300  $\mu\text{m}$ , 600  $\mu\text{m}$  and 1.2 mm. The laser welding heads were positioned by a Fanuc M-710ic six-axis industrial robot system, with repeatability to an accuracy of  $\pm 0.06$  mm. A Lincoln Electric Power Wave L500 power supply was used to preheat and feed the wire in front of the laser, which is a power supply dedicated to hot-wire laser welding applications, capable of restively preheating the wire from 100 to 5000 W, however power levels used in the present work did not exceed 500 W. Beam wobbling was controlled by galvanometer scanners integrated inside an IPG D50 wobble welding head, which can achieve linear, circular, and figure-eight repeating patterns. A side mounted Optris PI640i thermal camera was utilized to monitor the temperature change in the FZ, with a collecting rate of 32 Hz and a temperature range of 200  $^{\circ}\text{C}$  to 925  $^{\circ}\text{C}$ , which covers the  $t_{8/5}$  range during the solidification process.

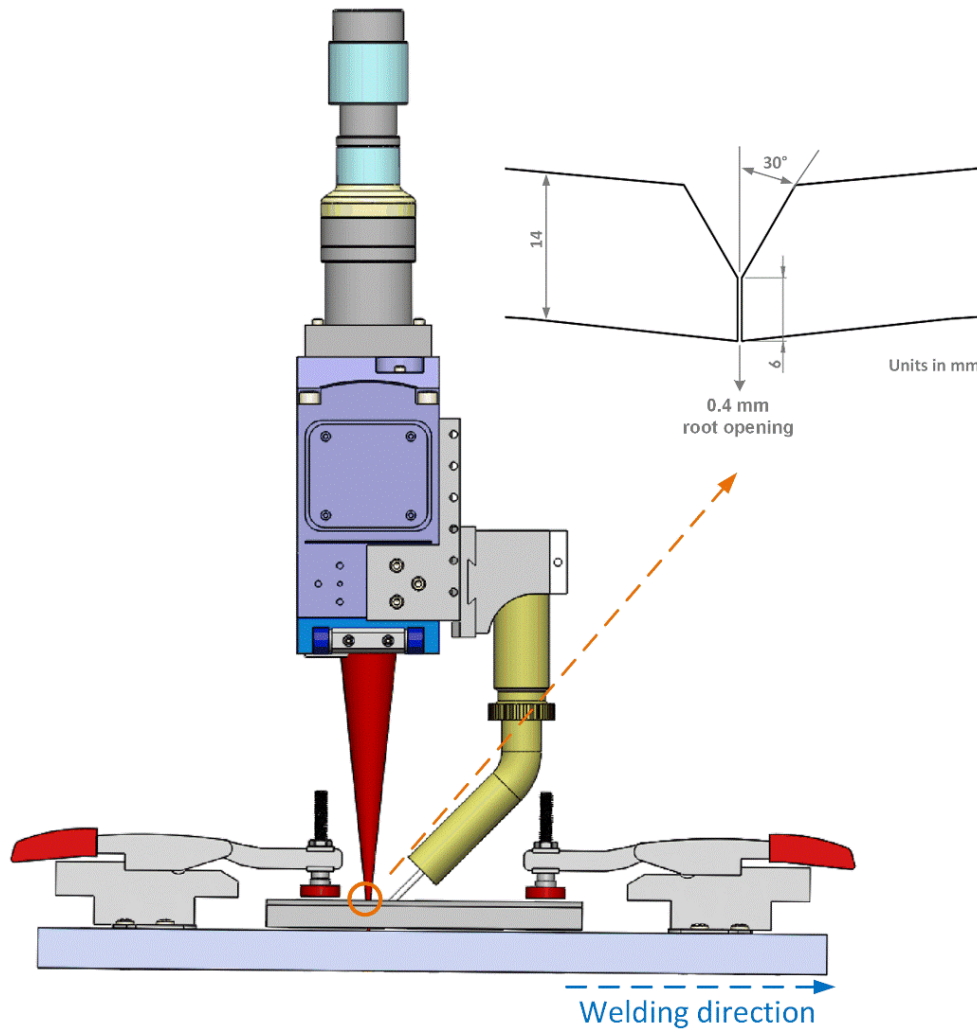


Figure 4-2. A typical experimental set-up for laser welding process

### 4.3 Elements and microstructural analysis

After welding, the cross-sectional samples were cut out and polished for elements and microstructural analysis. The samples were etched with Nital, a mixture of 5% nitric acid and 95% ethanol, for 5 s to reveal the microstructure based on ASTM E407. To identify the weld dimensions, macrographs were taken under a stereoscope. An optical microscope (OM) and a Zeiss Ultra SEM were utilized to characterize the microstructure with various magnifications. EDS was utilized to analyze the chemical composition, with an acceleration voltage of 20 kV. Electron probe microanalysis (EPMA) is a tool to determine the chemical composition of a small volume of solid material with a much higher quantification accuracy (up to 10 times

higher). In this work, EPMA using a JEOL JXA-8530F field-emission electron microprobe was utilized to analyze the elemental distribution. Mapping and line scanning were done with Si being selected as the ‘tracer’ element for EPMA, due to the different Si contents in base metal and ER70S-6 wire.

The volume fraction of microconstituents in the FZ was calculated by point counting according to ASTM E562, with a rectangular counting array consisting of 100 points. The fraction was given by averaging the counting results of 5 micrographs from different locations, with a 95% confidence interval presented. Image processing was also utilized based on the difference in the grayscale of different microconstituents, to help calculate the fraction of MA and grain boundary ferrite. The grain size of base metal and FGHAZ was quantified by the average grain intercept (AGI) method, with the ratio of intercepts to line length (intercepts/ $\mu\text{m}$ ) presented by averaging the results from three calculations.

#### **4.4 Mechanical tests**

##### **4.4.1 Microhardness**

The Vickers microhardness was measured across the weld area using a Clemex instrumented indentation microhardness tester, with a load of 500 gf and a dwell time of 10 s. The hardness map covered half of the joint from the weld centerline to the base metal, with a  $200\ \mu\text{m} \times 250\ \mu\text{m}$  step size. The average values of 5 indentation lines from the weld top surface were calculated for hardness distribution analysis, and the mean weld metal hardness was calculated by averaging the hardness of indents located in the fusion zone, with a 95% confidence interval for statistical analysis. The weld metal hardness distribution along the through-thickness direction was also analyzed by averaging the hardness values of the indentation lines located in the fusion zone. Peak hardness values in the CGHAZ and minimum hardness values in the FGHAZ were also identified to indicate hardening or softening phenomenon in the HAZ.

#### **4.4.2 Instrumented indentation**

Due to the difficulty in extracting all-weld-metal tensile coupons from the narrow laser fusion zone, the instrumented indentation testing was performed, which provides a more realistic way for determining the yield strength of subzones in the weld. A Nanovea M1 instrumented indentation tester was used to perform local indenting and estimate yield strength based on the load-displacement curve. A 50- $\mu\text{m}$ -diameter indenter with a nearly flat contact tip was used, which generates S-shaped indentation curves. The peak load was set to be 8 N, the loading rate was 16 N/min, and the approach speed was 3  $\mu\text{m}/\text{min}$ . The local yield strength was calculated based on the method developed by Midawi et al. [101] in a previous report, which used the same shape indenter and validated for a wide range of pipeline steels and aluminum alloys. Lowess smoothing was utilized to find the best-fit curves and improve the accuracy of the estimation procedure. 5 tests were done in different locations for each interested area, with a 95% confidence interval presented.

#### **4.4.3 Tensile test**

Sub-size tensile samples were extracted from the welded plates, according to ASTM E8. At least 3 tensile tests were performed for each set of parameters, using a Tinius Olsen HK10 tensile tester and loaded at a 1 mm/min crosshead displacement rate. The stress-strain curves are plotted based on the sample best presenting the average tensile strength and elongation, and the average ultimate tensile strength is reported with a 95% confidence interval. The Digital Image Correlation (DIC) technique was also employed using Correlated Solutions VIC-3D software to monitor the fracture behaviour and measure the strain values during the tensile tests. As a non-contact strain measurement technique, DIC provides a more accurate strain measurement and allows local strain measurement by tracking block of pixels at different stages of deformation. The localized strain was automatically calculated by the DIC software with a step size of 29 pixels and a subsize of 7 pixels. The tensile properties of X80 base metal

were tested with the same coupon dimensions and testing procedure, which had a 0.2 % offset yield strength of  $619 \pm 18$  MPa and met the standard of API 5L (with a minimum yield strength of 80 ksi or 555 MPa).

#### **4.4.4 Charpy impact test**

Sub-size Charpy samples with a thickness of 5 mm (according to ASTM E23) and the notch position in the weld metal were extracted from the root laser welds. Charpy impact tests were performed using a Zwick pendulum instrumented impact tester at three temperatures of 0 °C, - 20 °C and - 45 °C, as indicated in CSA Z662. Three repeat Charpy tests were done for each set of parameters at each temperature, and the force-displacement curves were plotted based on the samples with the results closest to the mean. The average Charpy impact toughness values were calculated, and the toughness-temperature curves were plotted with a 95% confidence interval presented as the error bars. SEM examination was conducted close to the notch area and the middle area of the Charpy fracture surfaces.

#### **4.4.5 Bend test**

The semi-guided root bend test was performed at room temperature according to ASTM E290-22, to show if there are any cracks showing up on the weld root after the sample is bended. This is a typical quality assurance test to determine if there are any lack of fusion defects in the weld. The bend test sample had a dimension of 200 mm × 25 mm × 14 mm.

## **Chapter 5: Effect of wire preheat and feed rate in X80 steel laser welds**

### **5.1 Introduction**

In this chapter, the effect of filler material volume and wire preheat on the microstructure and mechanical properties in X80 steel laser welds was studied utilizing a static-spot laser, the results of which could be referred as the basis when laser beam wobbling is applied, and other conditions such as substrate preheating are optimized in the following chapters.

Laser beam welding using a high energy density source is a promising method for joining thick plates due to its deep penetration and high travel speed, enabling low heat input with a minimal HAZ [102]. One of the main drawbacks for autogenous laser welding is the poor gap bridging ability, often requiring a gap of less than 10% of the plate thickness [17,71]. The fast cooling during laser welding leads to the formation of hard and brittle weld metal containing bainite or martensite. Feeding additional wire improves the gap bridging ability and modifies the chemistry and microstructure of the weld metal, which further influences the mechanical properties of the weld. By running an electric current through the wire during hot-wire fed laser welding, the filler material can be preheated to a temperature near the melting point, which increases the deposition rate and reduces the cooling rate [13].

The aim of this part of work is to investigate the effect of wire feed rate and the preheat of the wire on the microstructure and mechanical properties such as microhardness, tensile strength, and Charpy V-notch impact toughness during wire-fed laser keyhole welding of X80 pipeline steel. A much higher productivity is expected compared to the GMAW process. An AF-dominated FZ microstructure, a reduced weld metal hardness and an increased Charpy impact toughness are also expected in the laser weld with hot-wire feeding.

### **5.2 Experimental procedures**

The experimental set-up for the wire-fed laser welding process is shown in Fig. 5-1. An IPG YLS-8000 fiber laser with a maximum power output of 8 kW was used, with a focal length

of 300 mm, a wavelength of 1070 nm, a beam parameter product of 3.5 mm\*mrad, and a focused spot size of 1.2 mm. A Lincoln Electric Power Wave L500 power supply was used to preheat and feed the wire in front of the laser. The base metal was taken from an X80 pipe with dimensions of 250 mm × 120 mm × 14 mm. An ER70S-6 carbon steel welding wire was used with a diameter of 0.9 mm. As shown in Fig. 5-1, the edge of the plate was machined with a 30-degree bevel and a 6 mm root height, the selection of which was based on the penetrating ability with the tested heat input.

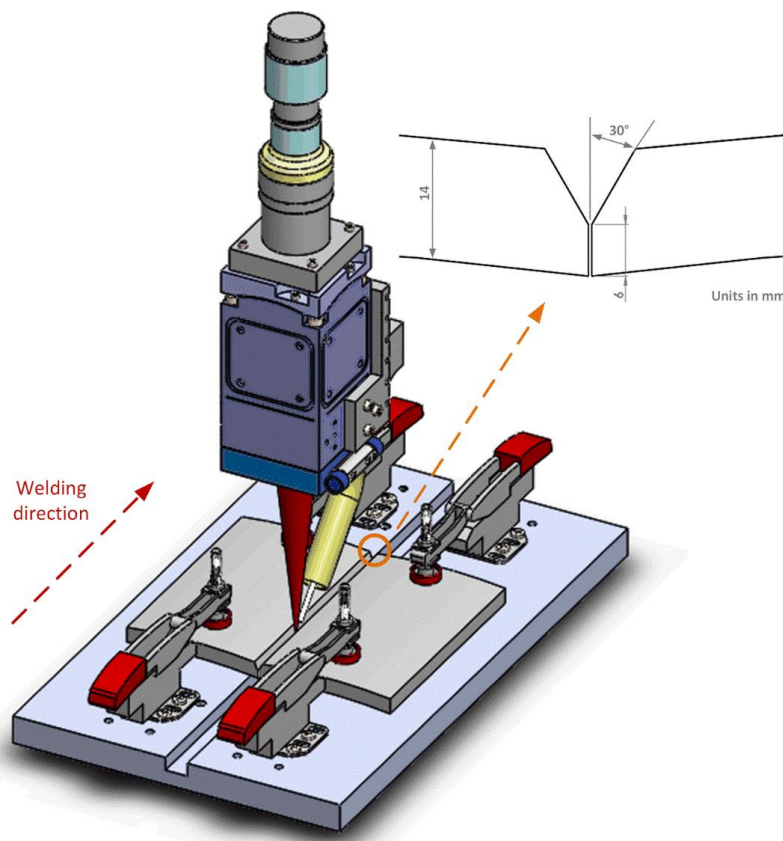


Figure 5-1. Laser welding experimental set-up with wire feed.

Cold- and hot-wire laser welding were performed for the root pass, with the welding parameters listed in Table 5-1. A maximum 8 kW laser power was used to achieve the best penetrating ability. The welding speed of 1 m/min was selected based on the results from a previous report [103], which showed that a welding speed higher than 1 m/min led to an increased solidification cracking sensitivity at a laser power of 8 kW, while a welding speed

lower than 0.5 m/min resulted in melt drop through and an unacceptable weld, based on bead-on-plate welding of carbon steels with a similar chemical composition. Wire feed rates up to 12 m/min were tested, as further increasing the filler material volume led to incomplete penetration. The laser was the only heat source during autogenous laser welding and cold-wire laser welding process. Meanwhile, an external power supply was used to preheat the wire by running an electrical current through it during hot-wire laser welding, such that 0.3 to 0.5 kW were applied to the wire during deposition, depending on the wire feed speed. For the calculated temperature rise based on the wire heat capacity, a 0.3 kW preheat power combined with a WFR of 6 m/min will lead to an estimated temperature increase of around 1200 °C, while a 0.5 kW power combined with a WFR of 12 m/min will lead to a temperature increase of around 1400 °C. With the high WFRs of 6 m/min and 12 m/min, a 0.4 mm root opening was used to help accommodate more filler material. A -3 mm defocused distance was used such that the laser spot was focused below the top of the root face to enhance penetration, a typical approach reported in the literature suggests a focal point to be near mid-thickness. The remaining part of the groove was filled with arc welds with the same ER70S-6 wire, with a travel speed of 0.13 to 0.26 m/min, a welding current of around 143 to 158 A and a welding voltage of 19 to 20 V for the various passes. The shielding gas used for the laser and arc welding processes are pure argon and mixed gas (85% Ar + 15% CO<sub>2</sub>), respectively, with the same flow rate of 18 L/min.

Table 5-1. Welding parameters during static-spot laser welding.

Sample number	Laser power $P$ (kW)	Welding speed $v$ (m/min)	Wire feed rate $WFR$ (m/min)	Hot wire preheat power $P_{wire}$ (kW)	Root opening $d$ (mm)	Defocused distance $D_f$ (mm)	Total linear heat input $HI$ (J/mm)
1	8	1	-	-	0	-3	480
2	8	1	4	-	0	-3	480
3	8	1	6	-	0.4	-3	480
4	8	1	6	0.3	0.4	-3	498
5	8	1	12	-	0.4	-3	480
6	8	1	12	0.5	0.4	-3	510



After welding, OM and SEM were utilized for microstructural analysis. Microhardness tests were done to reveal the differences in hardness across various regions of the FZ and HAZ. Sub-size tensile samples were extracted from the welded plates, with the extraction position and sample dimensions shown in Fig. 5-2a and b, respectively. The sample contained both arc and laser weld metal since the gauge width was 6 mm from the mid-thickness of the pipe wall. The X80 base material has a yield strength of  $619 \pm 18$  MPa and an ultimate tensile strength of  $721 \pm 1$  MPa, as tested with the same procedure. Non-contact DIC measurements were also employed to monitor the fracture behavior and measure the strain values during the tensile tests. Sub-size Charpy samples with a thickness of 5 mm and the notch position in the weld metal were extracted from the root laser welds, with the extraction position and sample dimensions illustrated in Fig. 5-2a and c. Charpy impact tests were performed at three temperatures of 0 °C, - 20 °C and - 45 °C, as indicated in the CSA Z662 standard. EDS was also utilized to analyze the chemical composition of the inclusions found on the fracture surface, with an acceleration voltage of 20 kV and a collection time of 100 s.

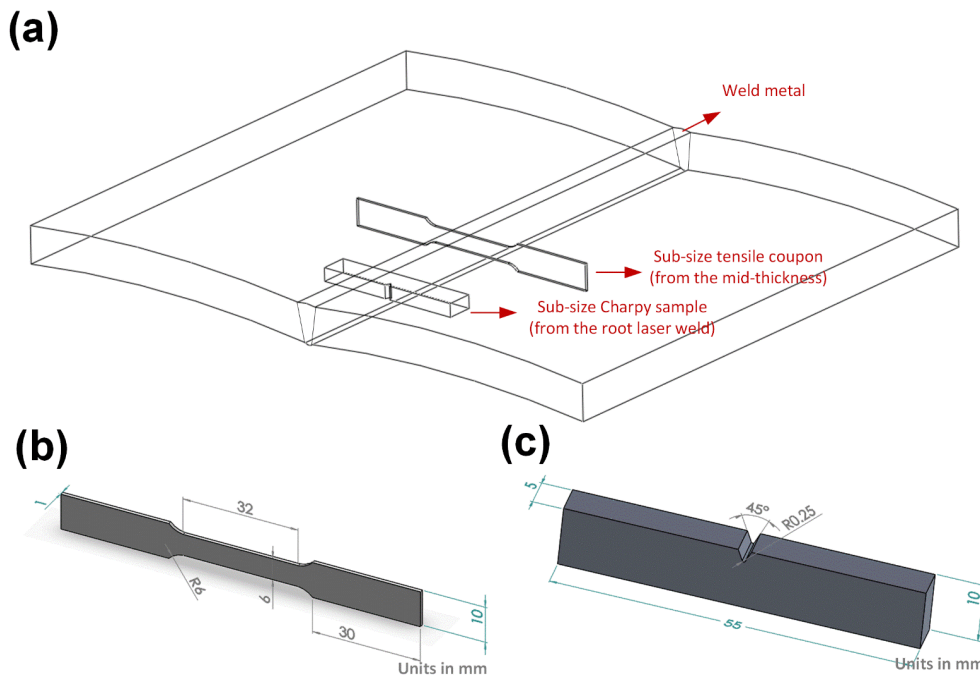


Figure 5-2. (a) Schematic diagram showing the extraction position of tensile and Charpy samples; (b) dimensions of sub-size tensile coupon; (c) dimensions of sub-size Charpy sample.

### 5.3 Weld morphologies

The top and root surfaces of the laser welds and the cap arc weld are shown in Fig 5-3. Crack-free, narrow, and continuous root welds were produced with the laser, in comparison with a much wider cap weld resulting from the lower energy density and larger weld pool from the arc heat source. Cross-section morphologies of the laser welds shown in Fig. 5-4(a-f) clearly demonstrate that the substrates were completely penetrated. The laser welds had high depth to width ratios which is a key feature of laser keyhole mode welding with a high beam power density, and the increase of weld height was found when the wire feed rate increased from 0 to 12 m/min. Five passes of arc welds were required to achieve a comparable weld height with the root laser weld. This demonstrates the significant productivity advantage of laser welding over traditional arc welding techniques.

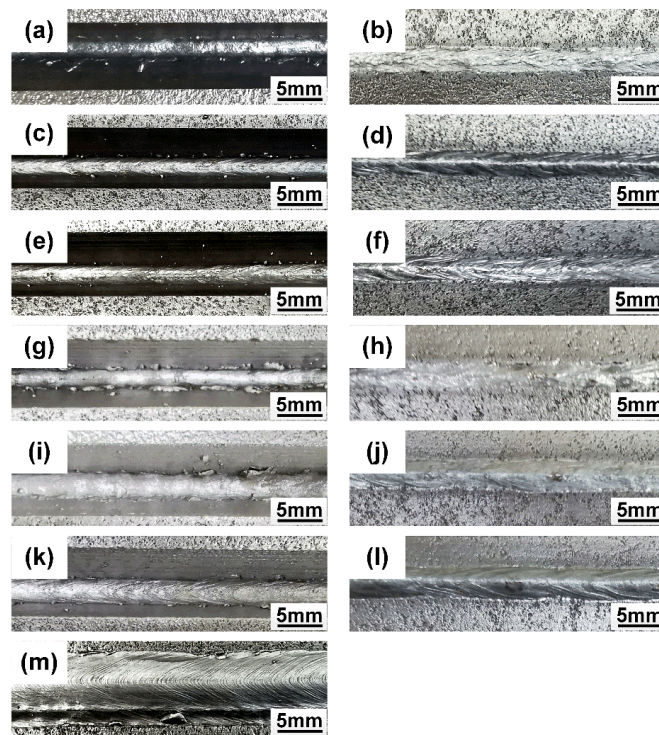


Figure 5-3. Weld surfaces morphologies: (a) and (b) top and bottom surfaces of autogenous laser weld; (c) and (d) top and bottom surfaces of cold-wire laser weld with a WFR of 4 m/min; (e) and (f) top and bottom surfaces of cold-wire laser weld with a WFR of 6 m/min; (g) and (h) top and bottom surfaces of hot-wire laser weld with a WFR of 6 m/min; (i) and (j) top and bottom surfaces of cold-wire laser weld with a WFR of 12 m/min; (k) and (l) top and bottom surfaces of hot-wire laser weld with a WFR of 12 m/min; (m) top surface of cap arc weld.

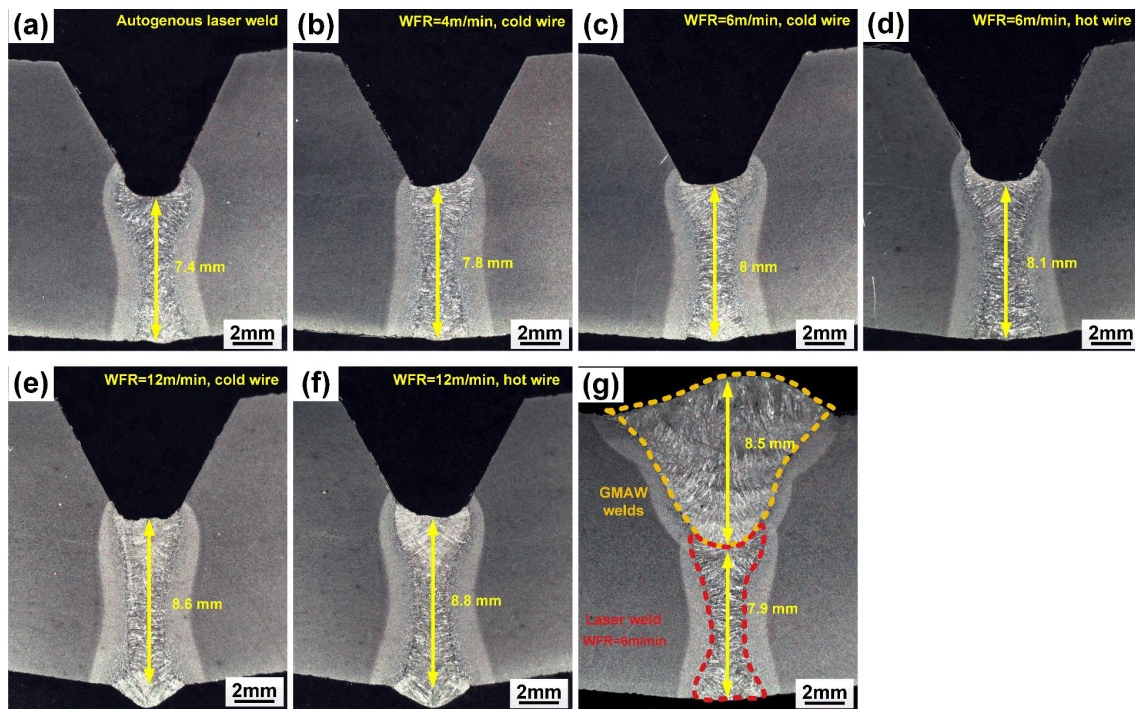


Figure 5-4. Cross-section morphologies: (a) autogenous laser weld; (b) cold-wire laser weld,  $WFR = 4\text{m/min}$ ; (c) cold-wire laser weld,  $WFR = 6\text{m/min}$ ; (d) hot-wire laser weld,  $WFR = 6\text{m/min}$ ; (e) cold-wire laser weld,  $WFR = 12\text{m/min}$ ; (f) hot-wire laser weld,  $WFR = 12\text{m/min}$ ; (g) final joint with root laser weld and filler GMAW welds.

#### 5.4 FZ microstructure

The microstructure of the X80 HSLA steel substrate is shown in Fig. 5-5, which is composed of fine-grained ferrite and MA constituents. During laser welding, the wire was fed from the top side of the root face, which could lead to an uneven distribution of filler material and microstructure inhomogeneity along the through-thickness direction. OM images in Fig. 5-6 show the microstructure of upper region of the laser fusion zone with different welding parameters. The FZ of the autogenous laser weld mainly contained bainite (B), resulting from a high cooling rate, as presented in Fig. 5-6a. In contrast, the feed of wire helped generate acicular ferrite (AF) in the upper region of the FZ. Feeding ER70S-6 filler material may introduce non-metallic inclusions originating from alloying additions and impurities into the weld metal, and some of these provide favorable nucleation sites for the formation of



intragranular AF [104–106]. With a higher WFR, the increasing number of non-metallic inclusions provided more nucleation sites which resulted in the formation of a larger amount of fine-grained AF. On the other hand, preheating the wire reduced the cooling rate [80,107], which limited the formation of bainite. As a result, the upper region of FZ in the hot-wire laser weld with the highest WFR of 12 m/min contained mostly fine AF but little bainite, as shown in Fig. 5-6f.

The microstructure of the lower region of the laser FZ is shown in Fig. 5-7. The lower region of FZ in the autogenous laser weld was mainly made up of bainite, which was similar to the upper region due to a negligible change in the chemical composition, as shown in Fig. 5-7a. Compared to the autogenous laser weld, more AF formed in the lower region of the FZ with a wire feed due to the increased alloying with elements such as silicon, manganese and titanium, which are reported to promote the formation of AF [104,105], and the presence of a root opening which provided a channel for delivery of filler metal to the root region.

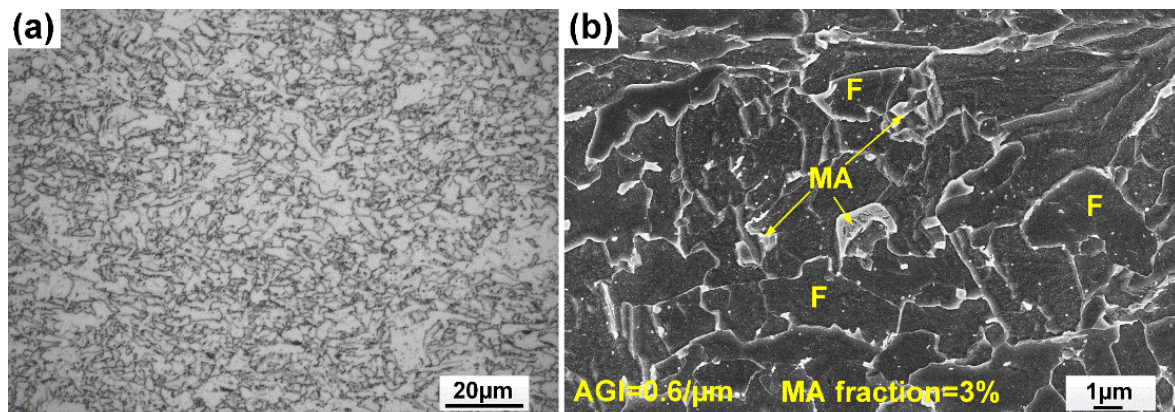


Figure 5-5. Microstructure of the X80 base metal: (a) optical micrograph; (b) SEM micrograph with locations of ferrite (F) and martensite/austenite (MA) indicated.



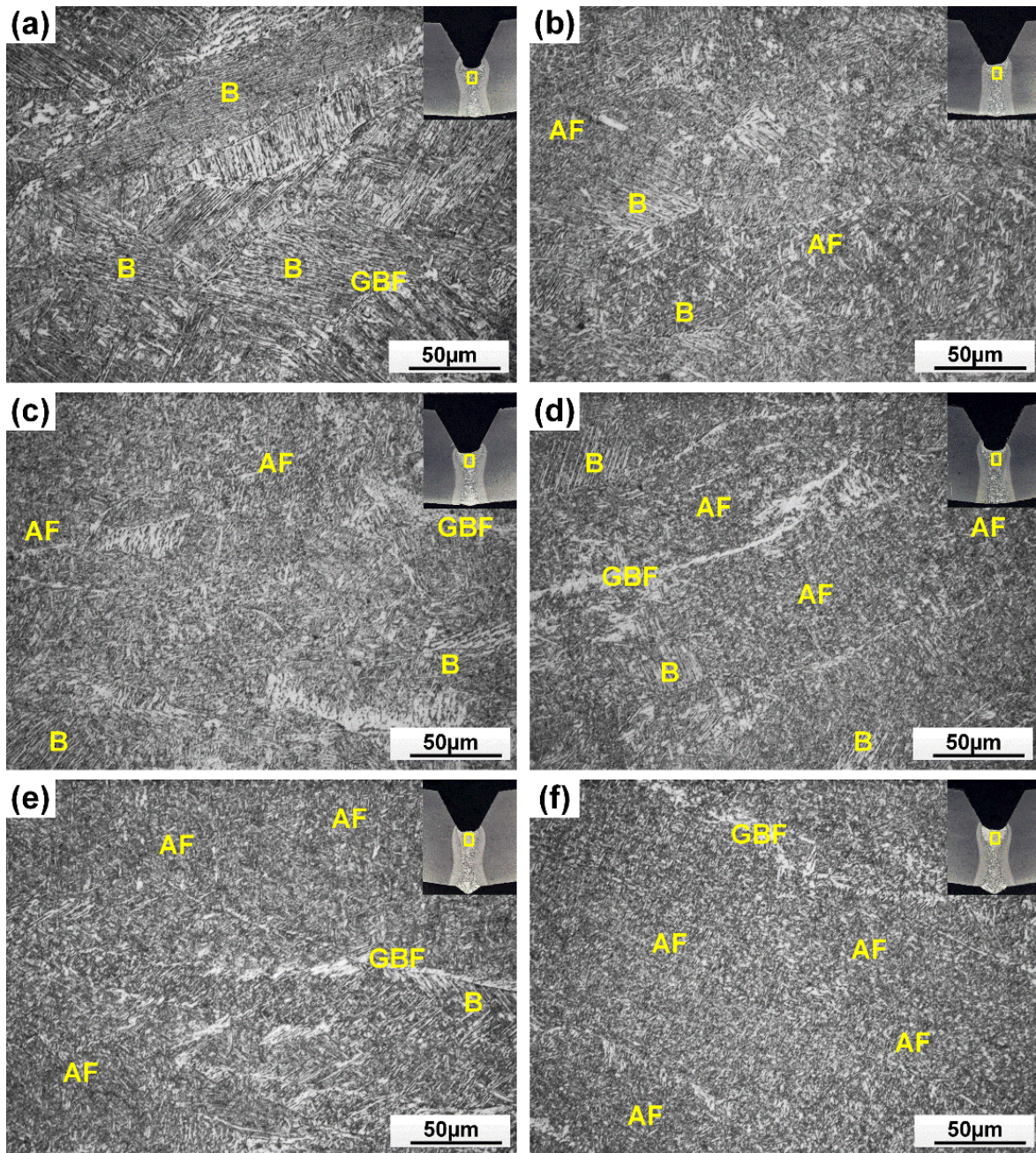


Figure 5-6. Optical micrographs showing the microstructure and locations of acicular ferrite (AF), bainite (B) and grain-boundary ferrite (GBF) in the upper region of the FZ: (a) autogenous laser weld; (b) cold-wire laser weld,  $WFR = 4$  m/min; (c) cold-wire laser weld,  $WFR = 6$  m/min; (d) hot-wire laser weld,  $WFR = 6$  m/min; (e) cold-wire laser weld,  $WFR = 12$  m/min; (f) hot-wire laser weld,  $WFR = 12$  m/min.



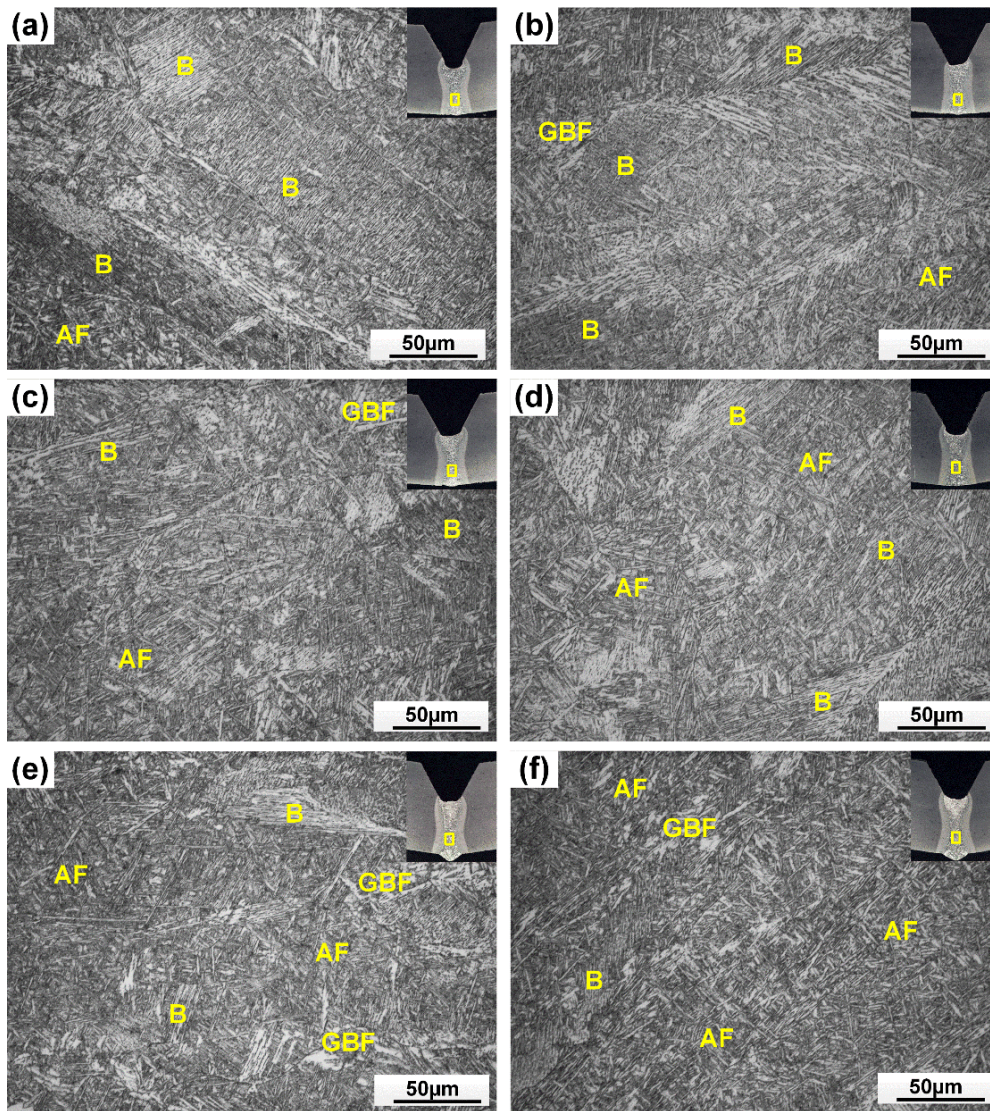


Figure 5-7. Optical micrographs showing the microstructure and locations of acicular ferrite (AF), bainite (B) and grain boundary ferrite (GBF) in the lower region of the FZ; (b) cold-wire laser weld,  $WFR = 4$  m/min; (c) cold-wire laser weld,  $WFR = 6$  m/min; (d) hot-wire laser weld,  $WFR = 6$  m/min; (e) cold-wire laser weld,  $WFR = 12$  m/min; (f) hot-wire laser weld,  $WFR = 12$  m/min.

The high magnification SEM images in Fig. 5-8 provide a clearer view of the FZ microstructure of the autogenous laser weld, and the hot-wire weld with a WFR of 12 m/min. Predominantly bainite was formed in the FZ of the autogenous laser weld, as shown in Fig. 5-8a-d. Meanwhile, the wire additions promoted the formation of acicular ferrite, as shown clearly by the basket-weave morphology of grains in Fig. 5-8e-h. The acicular ferrite in the upper region of FZ was finer than that in the lower region, which might be due to an increase



in nucleation sites available, which would be expected based on reduced mixing and transport of alloying elements to the bottom of the weld pool. Compared to the upper region of FZ, more bainite but less AF was found in the lower region of FZ in the hot-wire weld, which can also be expected from reduced filler material and alloying elements reaching the root region.

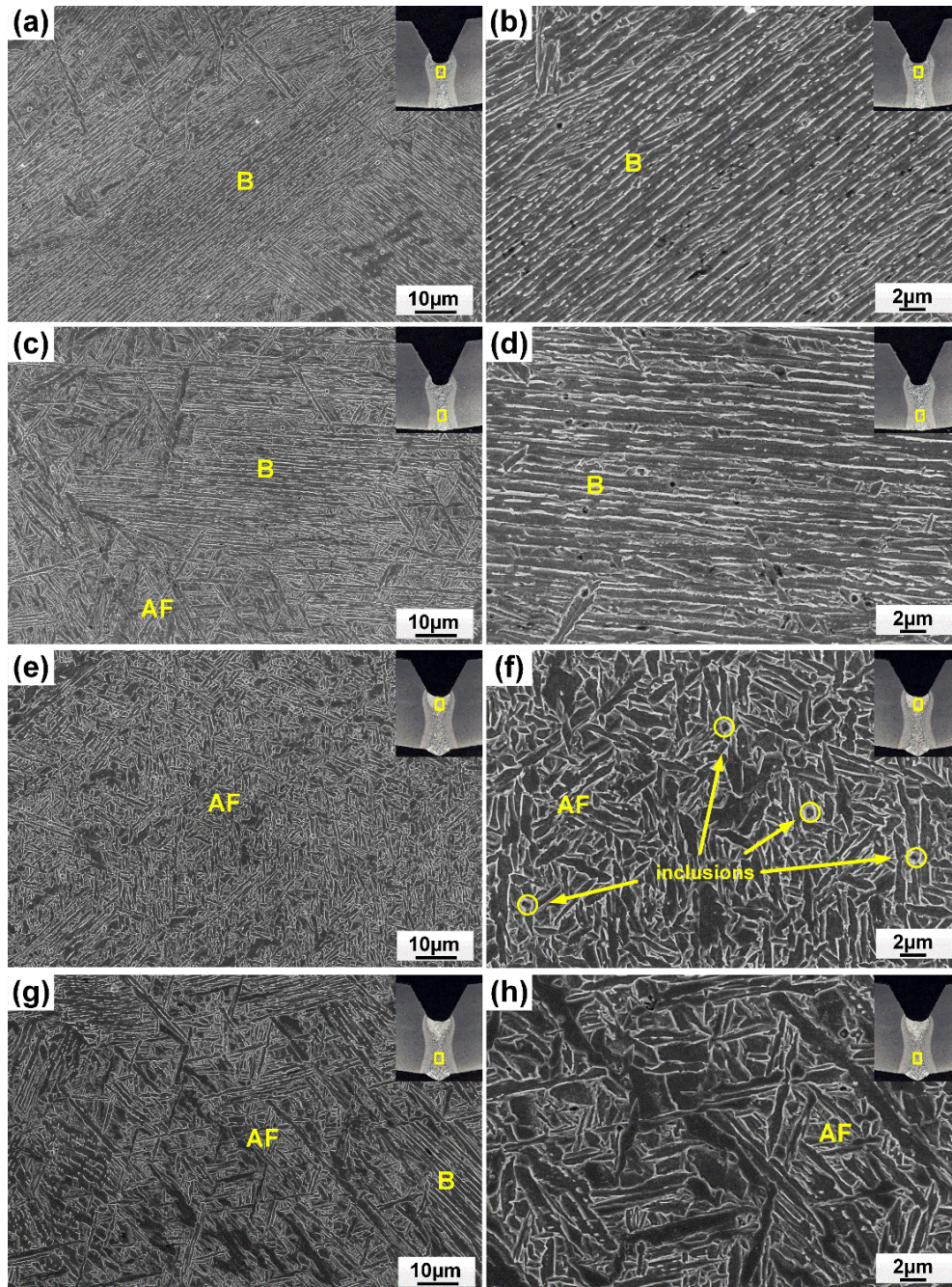


Figure 5-8. SEM micrographs indicating the presence of bainite (B) and acicular ferrite (AF) in: (a) and (b) upper region of the FZ in autogenous laser weld; (c) and (d) lower region of the FZ in autogenous laser weld; (e) and (f) upper region of the FZ in hot-wire laser weld with a WFR of 12 m/min; (g) and (h) lower region of the

FZ in hot-wire laser weld with a WFR of 12 m/min.

## 5.5 HAZ microstructure

Fig. 5-9 and 5-10 show the OM and SEM images of the HAZ of the laser weld, respectively. Sub-zones of the HAZ can be distinguished, which exhibited different grain sizes and microstructures resulting from various peak temperatures and cooling rates, as delineated in Fig. 5-9a, and these were further examined at higher magnification. The CGHAZ mainly consisted of bainite, as shown in Fig. 5-9b and 5-10(a-b). The CGHAZ adjacent to the FZ experienced a high peak temperature that promoted the growth of prior austenite grain, which is beneficial to the formation of low-temperature transformation products like bainite [55,56]. The peak temperature in the FGHAZ was still higher than the  $A_{r3}$ , but lower than the dissolution temperature of most fine precipitates in the base material [56]. The pinning effect from the precipitates would retard the growth of austenite grains, which provided more grain boundaries as favorable nucleation sites for ferrite [55]. As a result, the FGHAZ was made up of fine-grained ferrite, shown in Fig. 5-9c and 5-10(c-d). MA constituents were found in the ICHAZ with a peak temperature between  $A_{r1}$  and  $A_{r3}$  where partial austenization occurred, as presented in Fig. 5-9d and 5-10(e-f). Upon cooling from this temperature range, carbon-enriched austenite was retained to room temperature or partially transformed to martensite below  $M_s$ , thus leading to the formation of MA [57].

The formation of MA was also found in the ICRCGHAZ when a second weld pass was applied over an existing weld pass. The second thermal cycle leads to the formation of multiple reheated HAZ, of which the ICRCGHAZ is often considered the weakest or most brittle region in a multi-pass weldment of pipeline steel due to the bainitic microstructure, large bainite packet size, along with the presence of second phase such as MA [108]. Fig. 5-11 shows the microstructure of CGHAZ formed by a single welding thermal cycle, and ICRCGHAZ formed by double thermal cycles of the arc and laser weld. The lower heat input during laser welding led to finer prior austenite grains and smaller bainite packet size in the CGHAZ, compared to



that in the CGHAZ of the arc weld, as shown in Fig. 5-11a and e. The ICRCGHAZ of the arc weld formed when a second arc weld pass was applied over the existing arc weld pass; meanwhile, the ICRCGHAZ of the laser weld formed when the first pass of arc weld was applied over the root laser weld. Blocky MA constituents were found at the prior austenite grain boundaries in the ICRCGHAZ of both the arc and laser welds, as shown in Fig. 5-11(b-d) and 5-11(f-h), respectively. Compared to GMAW, the deep penetration during laser welding reduced the total number of weld passes required and hence limited the formation of MA within the ICRCGHAZ. A smaller bainite packet size along with less MA in the ICRCGHAZ would be beneficial to the toughness of the HAZ in the laser weld.

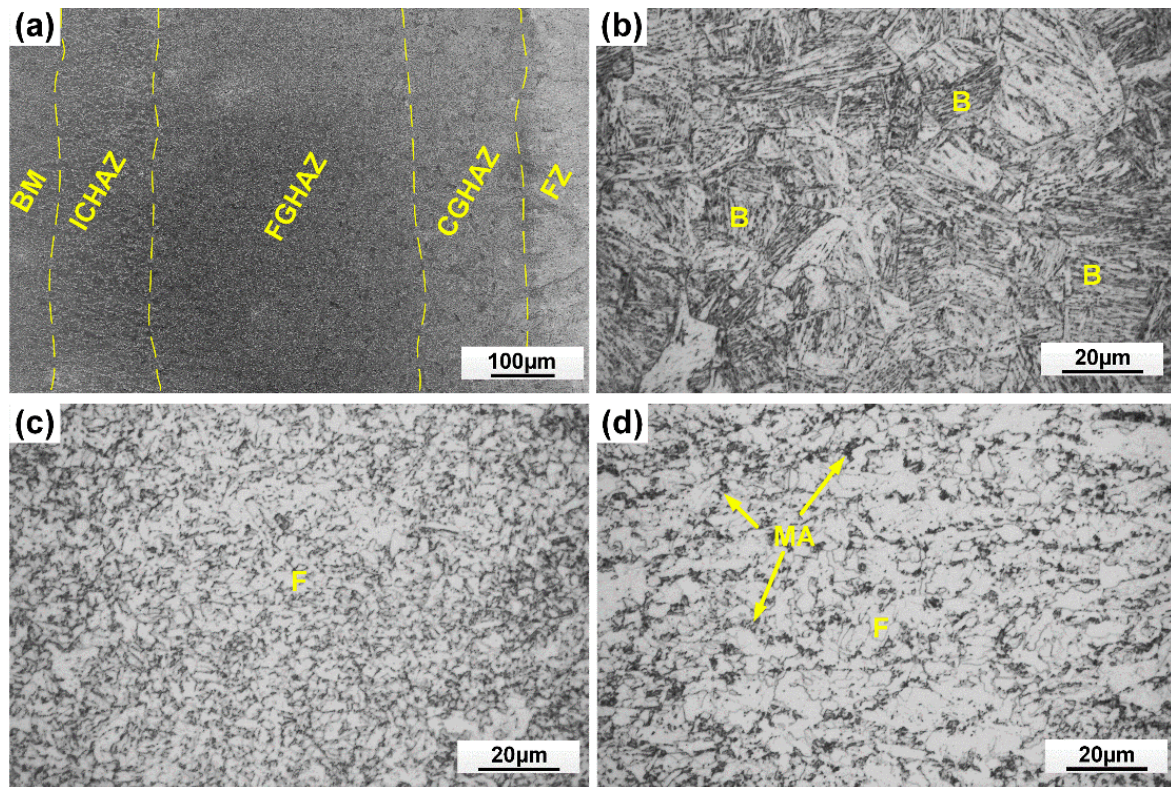


Figure 5-9. (a) Sub-zones in the HAZ of laser weld; (b) optical micrograph of CGHAZ, cold-wire laser weld,  $WFR = 6\text{m/min}$ ; (c) optical micrograph of FGHAZ, cold-wire laser weld,  $WFR = 6\text{ m/min}$ ; (d) optical micrograph of ICHAZ, cold-wire laser weld,  $WFR = 6\text{ m/min}$ .



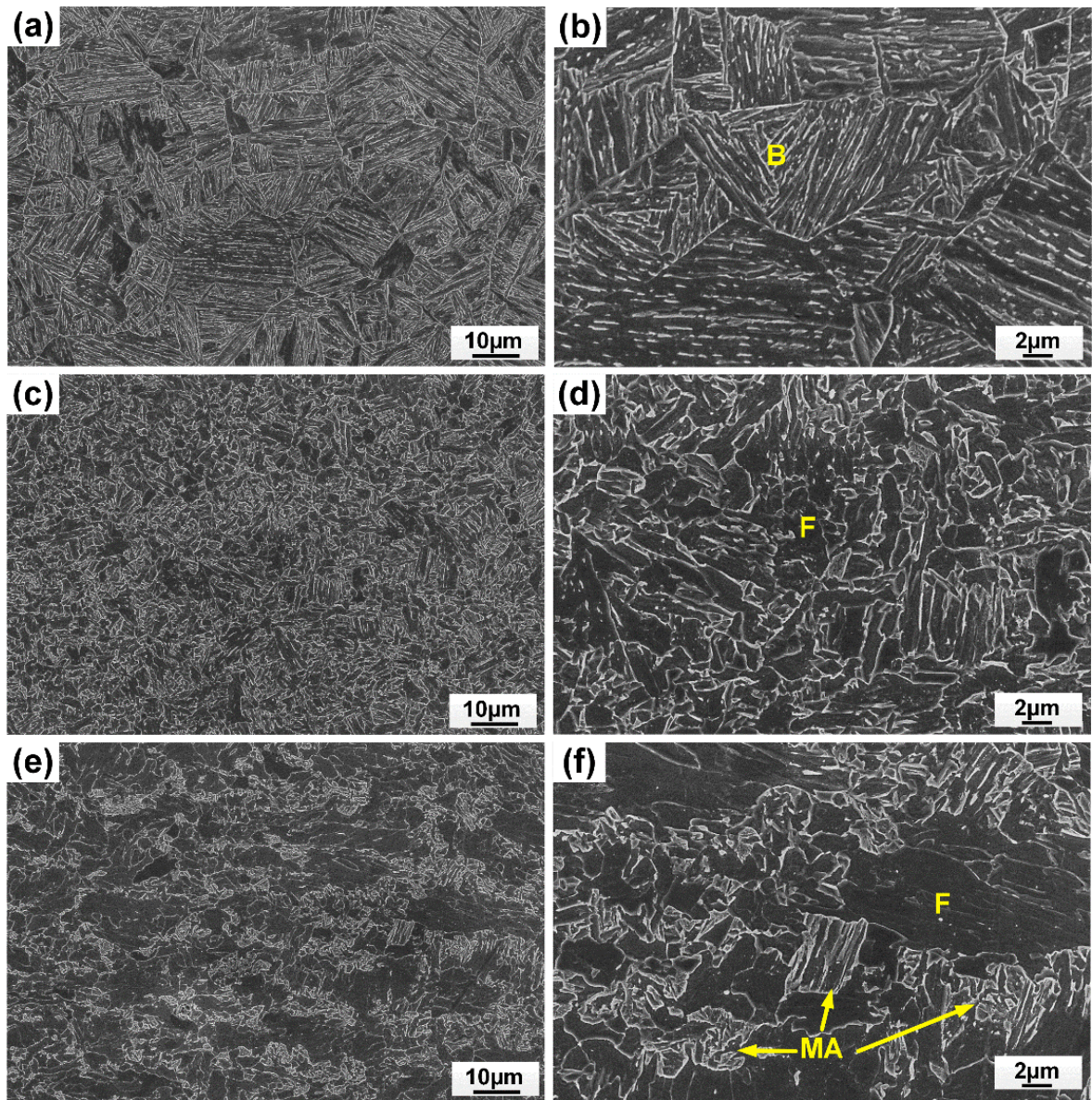


Figure 5-10. SEM micrographs of HAZ of cold-wire laser weld with a WFR of 12 m/min: (a) and (b) CGHAZ; (c) and (d) FGHAZ; (e) and (f) ICHAZ.



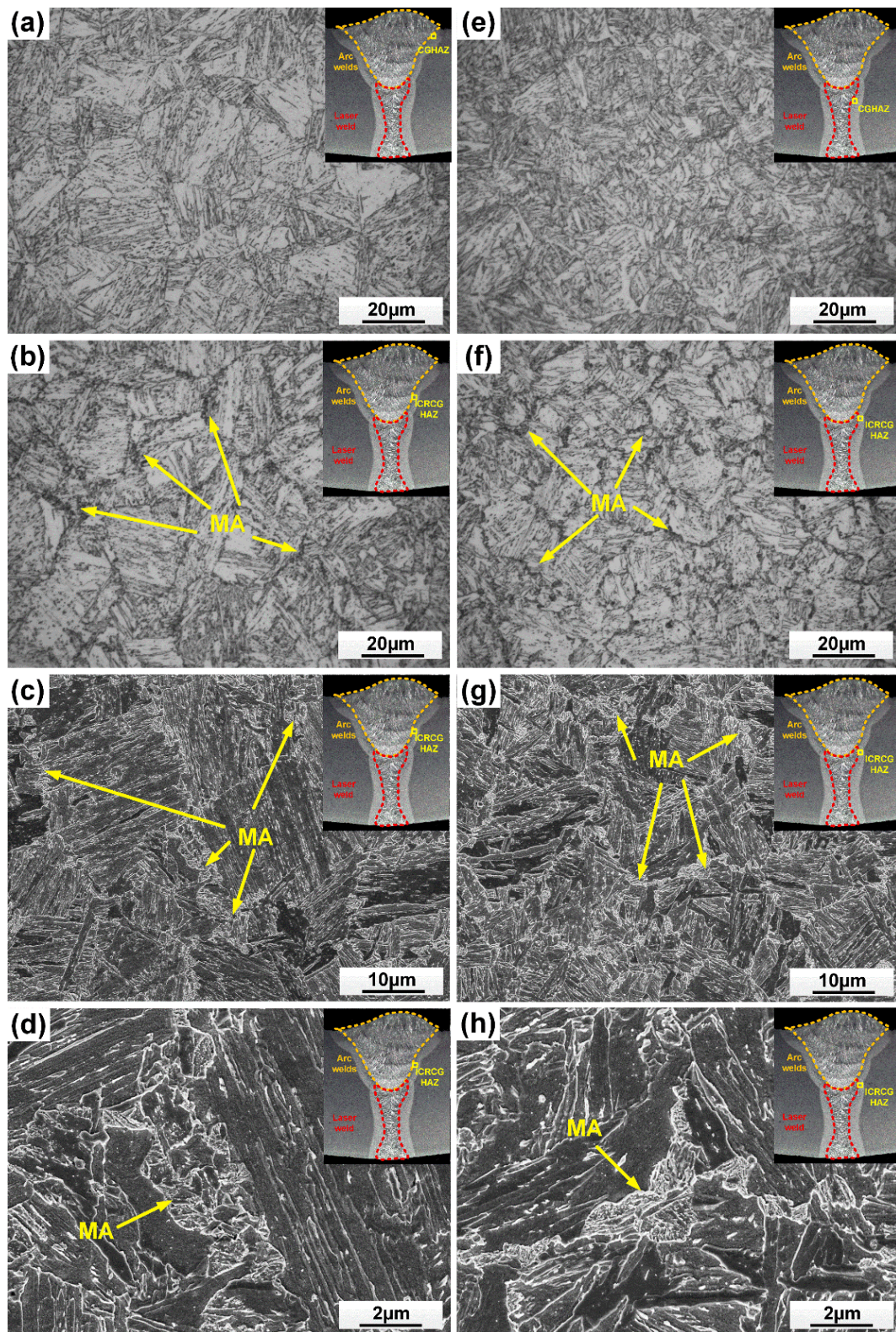


Figure 5-11. (a) Optical micrograph of CGHAZ of arc weld; (b) optical micrograph of ICRCGHAZ of arc weld; (c) and (d) SEM micrographs of ICRCGHAZ of arc weld; (e) optical micrograph of CGHAZ of cold-wire laser weld with a WFR of 6 m/min; (f) optical micrograph of ICRCGHAZ of cold-wire laser weld with a WFR of 6m/min; (g) and (h) SEM micrograph of ICRCGHAZ of cold-wire laser weld with a WFR of 6 m/min.

## 5.6 Microhardness

Fig. 5-12 shows the microhardness maps of the laser welded joints produced with different parameters. The autogenous laser weld exhibited a higher FZ hardness resulting from the bainitic microstructure formed by a high cooling rate during laser welding (as shown in Fig. 5-12a), compared to the welds with more acicular ferrite produced with the addition of filler material. The CGHAZ adjacent to the FZ which experienced a high peak temperature mainly contained bainite and presented a hardness comparable to that of the FZ. A hardness peak was also found in the ICHAZ with a higher hardness than that of the FGHAZ and base metal, due to the presence of MA in this region. Fig. 5-13a provides a more direct comparison of the hardness distribution in the upper region of the joints, meanwhile, Fig. 5-13b shows the FZ hardness distribution along the thickness direction. The mean hardness of the upper region of FZ in the autogenous laser weld, cold-wire laser weld with a WFR of 6 and 12m/min, along with the hot-wire laser weld with a WFR of 12 m/min were averaged to be  $331\pm 4$ ,  $318\pm 3$ ,  $309\pm 3$  and  $305\pm 4$  HV, respectively. Fig 5-13b also clearly demonstrates the difference in the hardness of the upper region of the FZ. The upper region of the FZ in the autogenous laser weld exhibited the highest hardness, and that in the hot-wire laser weld with the high WFR of 12 m/min exhibited the lowest FZ hardness. The reduced hardness observed in the upper region of the FZ in the hot-wire weld with a high WFR is attributed to the decreased bainite content. However, the wire addition had no significant influence on the hardness of the lower region of the FZ, which was due to reduced filler material reaching the root region and less effect on the microstructure compared to the upper region of the FZ.



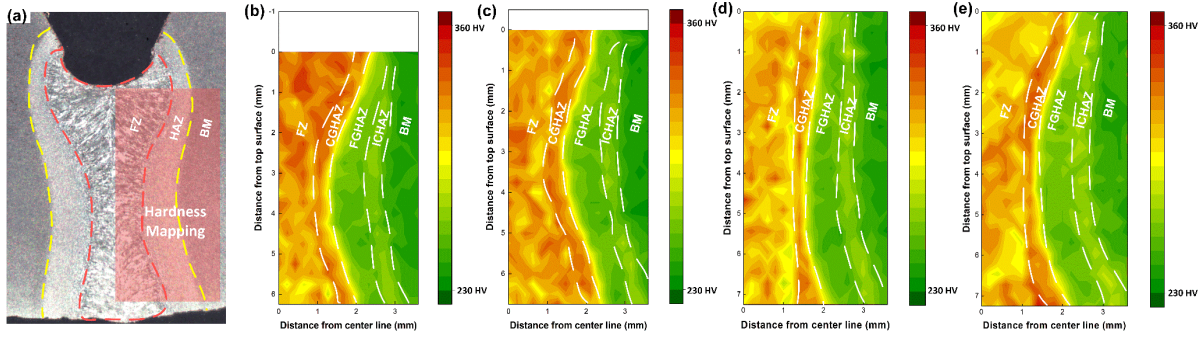


Figure 5-12. (a) Macrograph showing the hardness mapping location; (b) hardness mapping results of autogenous laser weld; (c) hardness mapping results of cold-wire laser weld with a WFR of 6 m/min; (d) hardness mapping results of cold-wire laser weld with a WFR of 12 m/min; (e) hardness mapping results of hot-wire laser weld with a WFR of 12 m/min.

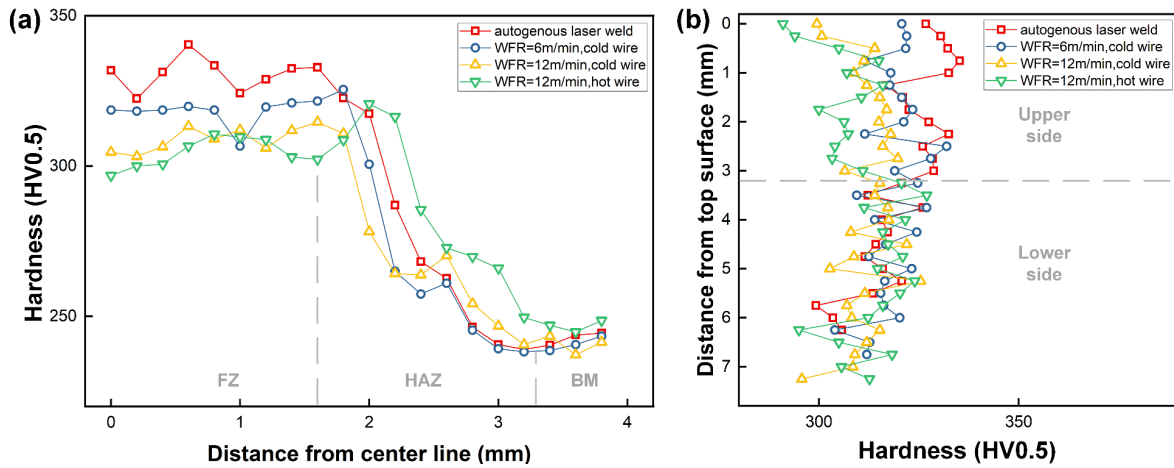


Figure 5-13. (a) Top side hardness distribution of the laser root weld; (b) Weld metal hardness distribution of the laser root weld along the through-thickness direction.

## 5.7 Tensile behavior

Due to the limited total thickness of the plates, only sub-size tensile coupons could be extracted from the welded joints, which contained both laser and arc weld metal, as shown in Fig. 5-14a. DIC strain mapping was utilized to monitor the fracture location and local strain distribution. Fig. 5-14b demonstrates the local strain mapping at a moment after necking happened but before the final failure. Despite the varying welding parameters, fracture occurred in the base metal for all specimens, which indicated that weld metal strength

overmatching was achieved. Bainite and acicular ferrite generated in the weld metal provided a strength higher than that of the base metal. The local strain distribution shown in Fig. 5-14c also confirmed that the strain in the FZ was limited during the tensile test, due to the overmatching of the weld metal. The stress-strain curve of the transverse joint section is shown in Fig. 5-14d, and the ultimate tensile strength is reported in Fig. 5-15, respectively. Since the samples experienced fracture in the base metal material, the ultimate tensile strength reached was comparable and met the requirement for X80 steel listed in API 5L (625 to 825 MPa).

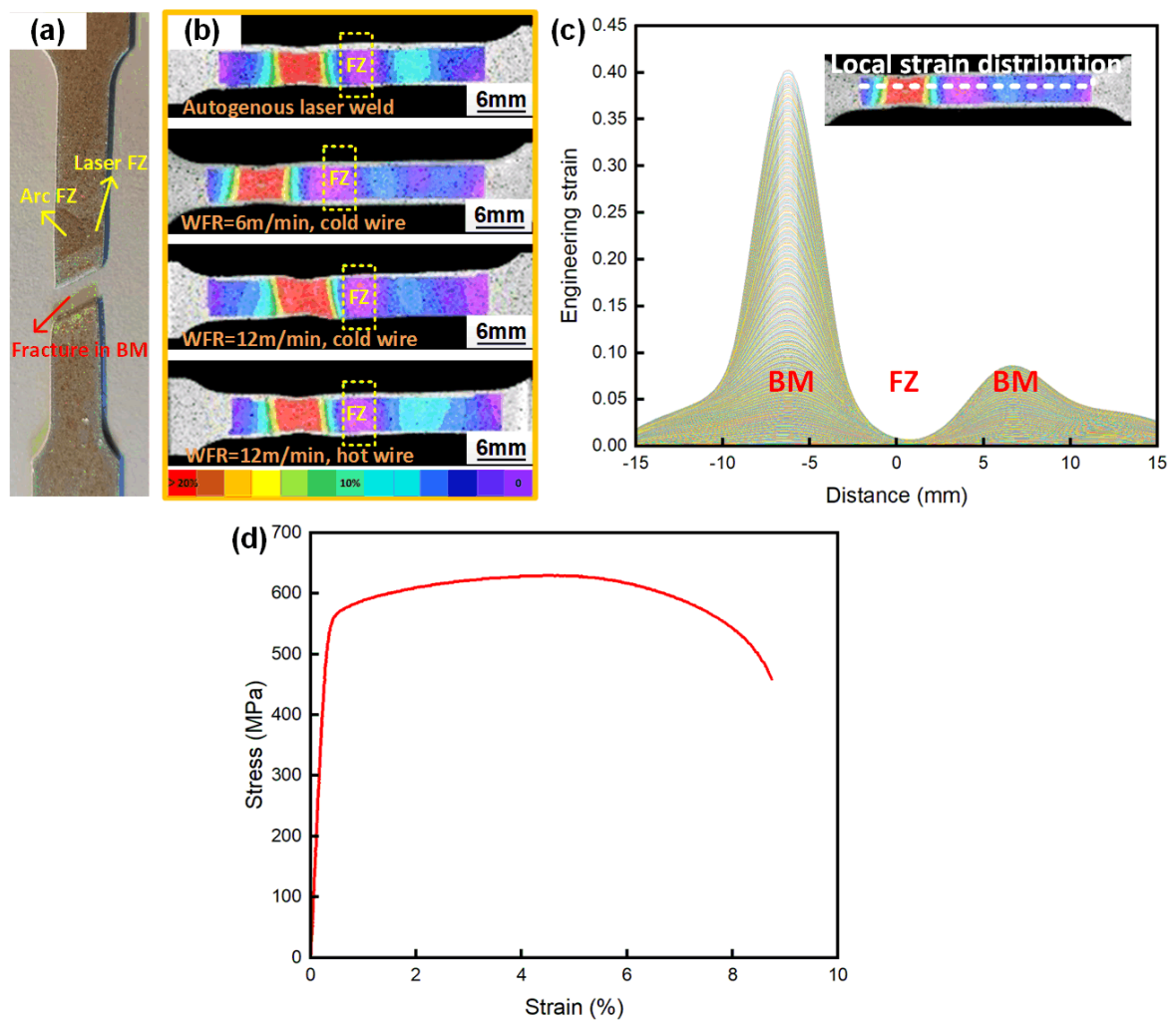


Figure 5-14. (a) Tensile coupon of cold-wire laser weld with a WFR of 6 m/min, showing the fracture in the base metal; (b) DIC strain maps with different welding parameters; (c) local strain distribution of cold-wire laser weld with a WFR of 6 m/min; (d) stress-strain curve of cold-wire laser weld with a WFR of 6 m/min.

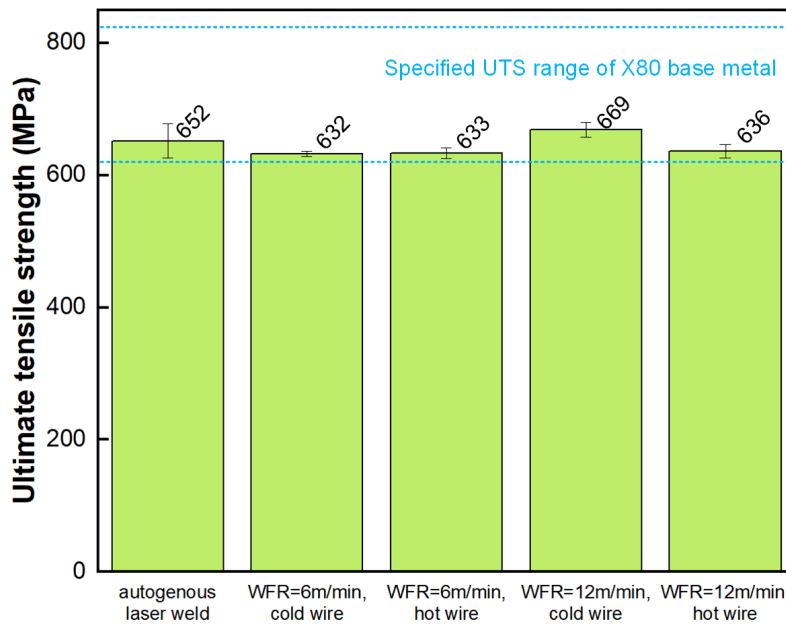


Figure 5-15. Ultimate tensile strength obtained from the transverse tensile tests.

## 5.8 Charpy impact toughness and fracture surfaces

Fig. 5-16 and 5-17 show the force-displacement curves and impact toughness values of laser weld metal at varying Charpy testing temperatures, respectively. Ductile shear fracture occurred at 0 °C, which can be derived from the force-displacement curves shown in Fig. 5-16a, based on the classification by ASTM E23. The trend shown in Fig. 5-17 indicates that the wire addition could increase the upper shelf toughness of the weld metal, where up to a 26% increase in Charpy impact toughness is achieved at the testing temperature of 0 °C by feeding wire with a WFR of 6 to 12 m/min. The presence of acicular ferrite with an interlocking structure formed by wire addition accounts for the improved crack arrest ability of the weld metal, leading to the increase in impact toughness. As the temperature decreased to -20 °C and -45 °C, fast and unstable crack extension occurred (as indicated in Fig. 5-16b-c) as the fracture mechanism changed to cleavage or mixed modes. The ductile to brittle transition appears to occur close to -45 °C, with the impact toughness and final displacement decreased. The dominance of brittle fracture and resulting low impact toughness at this transition temperature range leads to increased scatter in toughness and mostly overlapping toughness values for the

varying weld metals at low temperatures of  $-20\text{ }^{\circ}\text{C}$  and  $-45\text{ }^{\circ}\text{C}$ , as shown in Fig. 5-17. The decreased influence of microstructure on weld metal toughness at low temperatures was also discussed in a previous report [104] investigating GMAW of X80 steel. Even at  $-45\text{ }^{\circ}\text{C}$ , however, the absorbed energy for all the laser welds with varying parameters met the requirement of APL 5L standard for line pipe, which indicates that the average absorbed energy of X80 pipe weld should reach 40 J for full-size test samples, and 20 J for 5 mm-thick sub-size samples at a test temperature of  $0\text{ }^{\circ}\text{C}$  or, if a producer agrees, a lower test temperature.

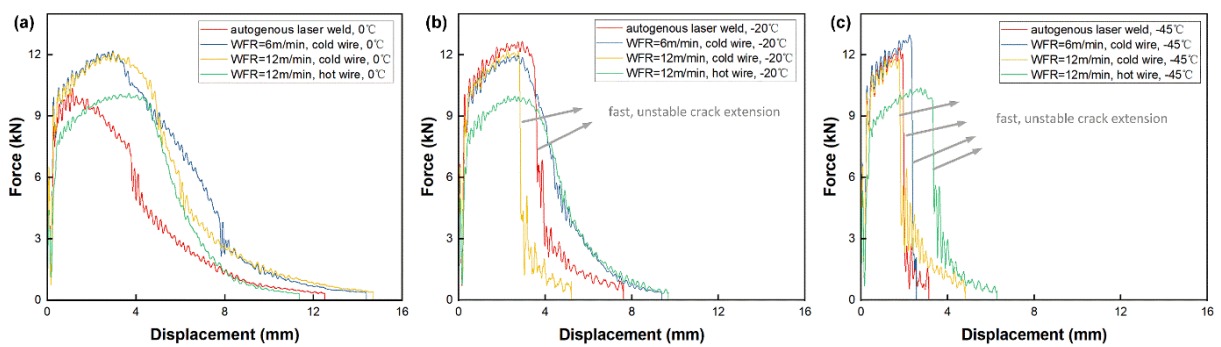


Figure 5-16. Force-displacement curves of Charpy samples at different testing temperatures: (a)  $0\text{ }^{\circ}\text{C}$ ; (b)  $20\text{ }^{\circ}\text{C}$ ; (c)  $-45\text{ }^{\circ}\text{C}$ .

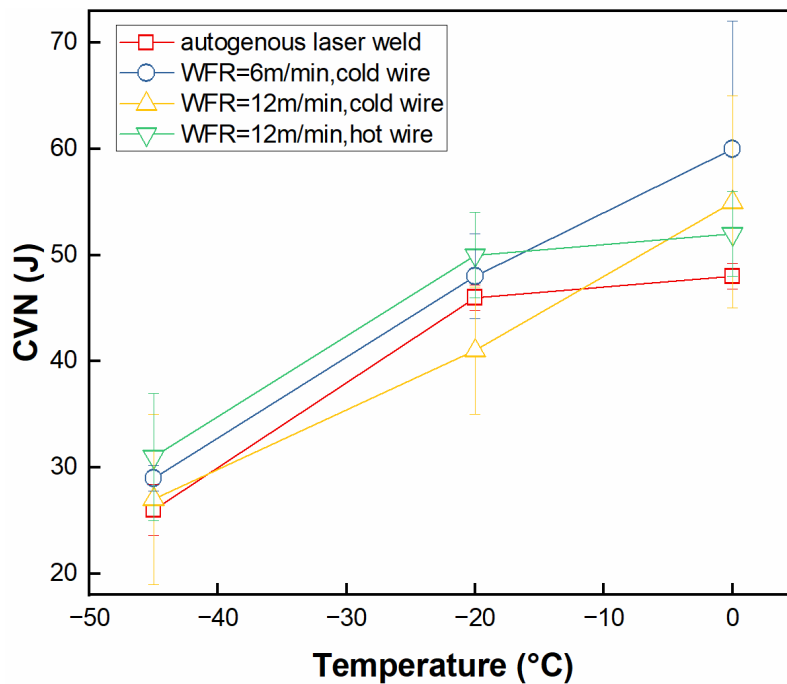


Figure 5-17. Charpy impact toughness of weld metal at different temperatures.



Fig. 5-18 and 5-19 show the SEM images of the Charpy fracture surfaces of the samples tested at 0 °C and -20 °C, respectively. The presence of dimples confirmed that both the autogenous laser weld and the cold-wire laser weld with a WFR of 12 m/min exhibited ductile fracture at 0 °C, as shown in Fig. 5-18. At -20 °C, the ductile fracture was initiated at the root of the notch, as the fracture surfaces close to the notch area exhibited dimple structure, as shown in Fig. 5-19a and c. As the crack propagated towards the middle area, unstable crack extension occurred as the fracture mechanism changed to cleavage mode, which was confirmed by the quasi-cleavage feature of the fracture surfaces shown in Fig. 5-19b and d. This kind of fracture appearance is typical for Charpy tests in the transition-temperature range, according to ASTM E23. Similar Charpy fracture appearances in X80 steel at low testing temperatures were also found in a previous report [108], with the observation close to the notch showing a small ductile layer associated with the crack initiating stage, and the remaining part being cleavage. The SEM fractography also revealed the presence of inclusions in the weld metal of cold-wire laser weld with a WFR of 12 m/min, as shown in Fig. 5-20(a-b). EDS results (in Fig. 5-20c) indicated that the inclusions were mainly manganese, titanium and oxygen based, and most likely correspond to Mn and Ti-based oxide inclusions, which were reported to be effective nucleation sites for AF in carbon steels [104,105,109], and thus explains the formation of acicular ferrite in the weld metal of cold/hot-wire laser weld.

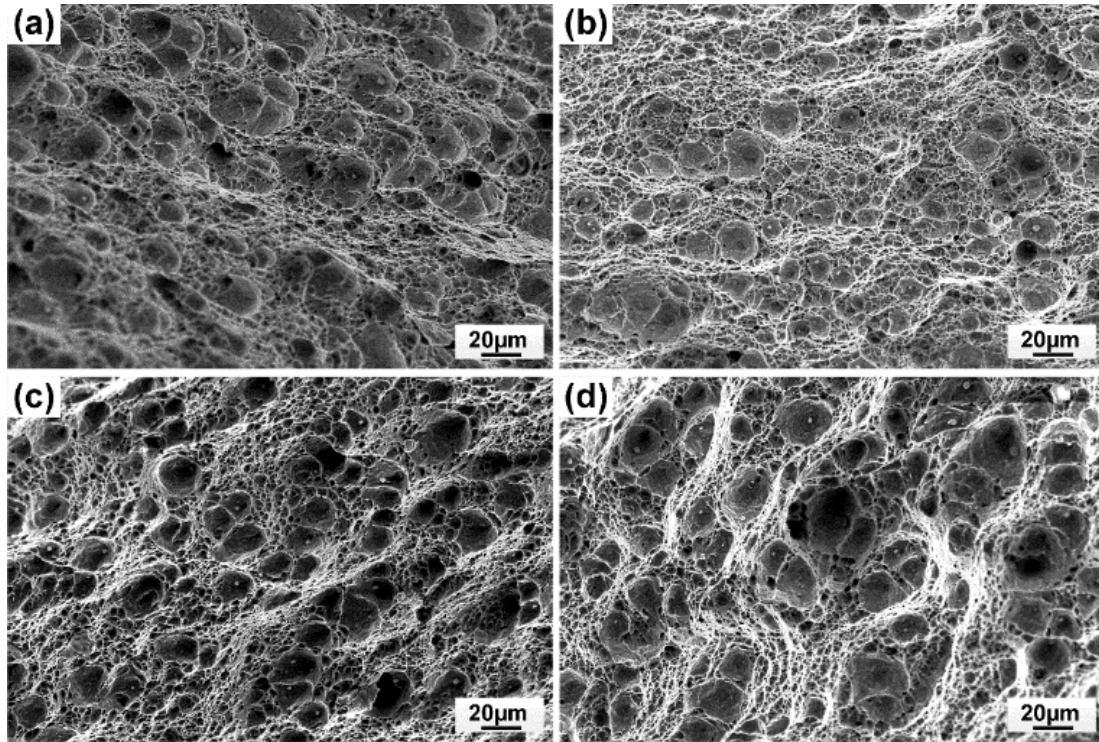


Figure 5-18. SEM images of Charpy fracture surfaces of samples tested at 0 °C: (a) autogenous laser weld, near the notch; (b) autogenous laser weld, towards the middle; (c) cold-wire laser weld with a WFR of 12 m/min, near the notch; (d) cold-wire laser weld with a WFR of 12 m/min, towards the middle.

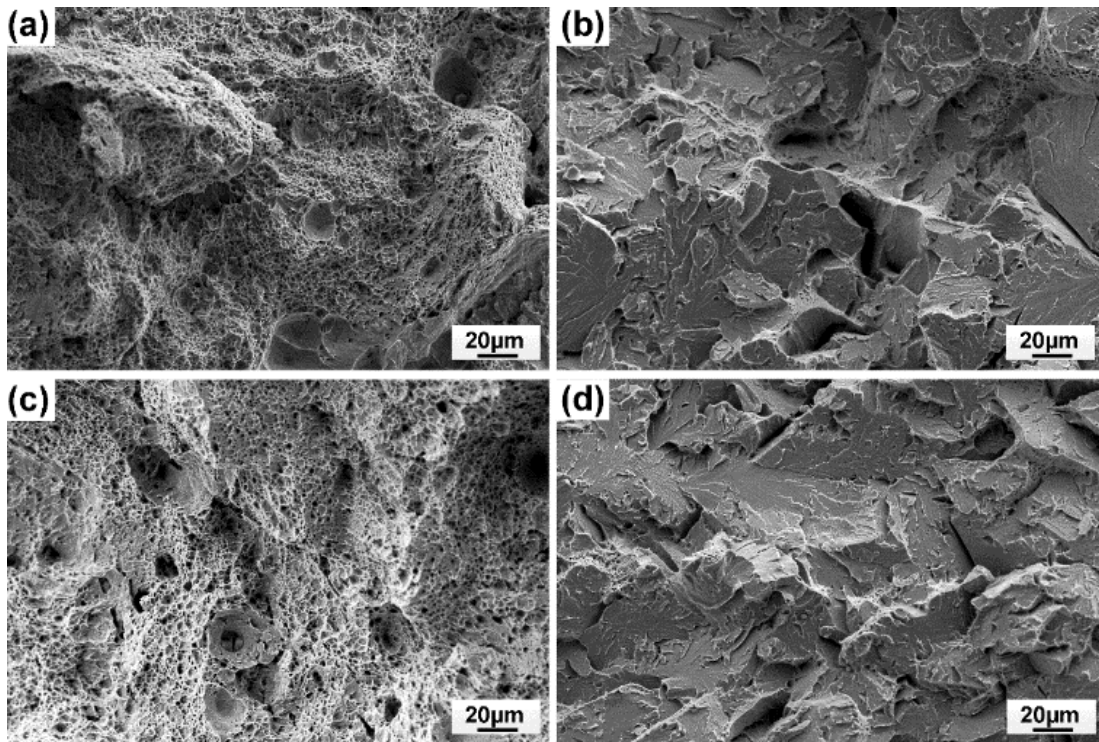


Figure 5-19. SEM images of Charpy fracture surfaces of samples tested at -20 °C: (a) autogenous laser weld, near the notch; (b) autogenous laser weld, towards the middle; (c) cold-wire laser weld with a WFR of 12 m/min, near the notch; (d) cold-wire laser weld with a WFR of 12 m/min, towards the middle.

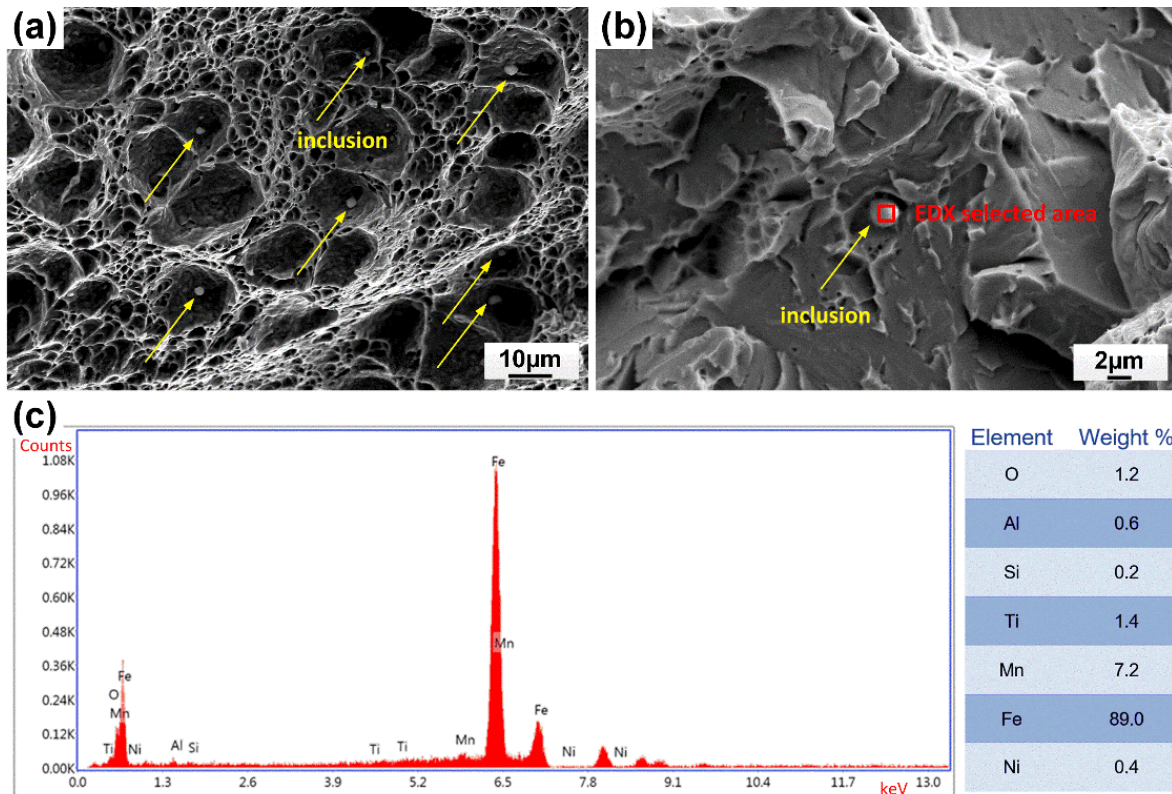


Figure 5-20. (a) SEM image of Charpy fracture surface showing the presence of inclusions in the weld metal of cold-wire laser weld with a WFR of 12 m/min, tested at 0 °C; (b) SEM image of Charpy fracture surface showing the EDS scanning area and the presence of inclusion in the weld metal of cold-wire laser weld with a WFR of 12 m/min, tested at -20 °C; (c) EDS spectrum and chemical composition of the inclusion.

## 5.9 Bend test results

Fig. 5-21 shows the root bend test results for the samples with an autogenous laser weld and a hot-wire-fed laser weld with a WFR of 12 m/min as the root pass. These two welds were selected for the bend tests as they contained the most bainite and the most acicular ferrite in the weld metal, respectively. No visible defects were found after the samples were bent, which met the requirement of API 5L and CSA Z662.

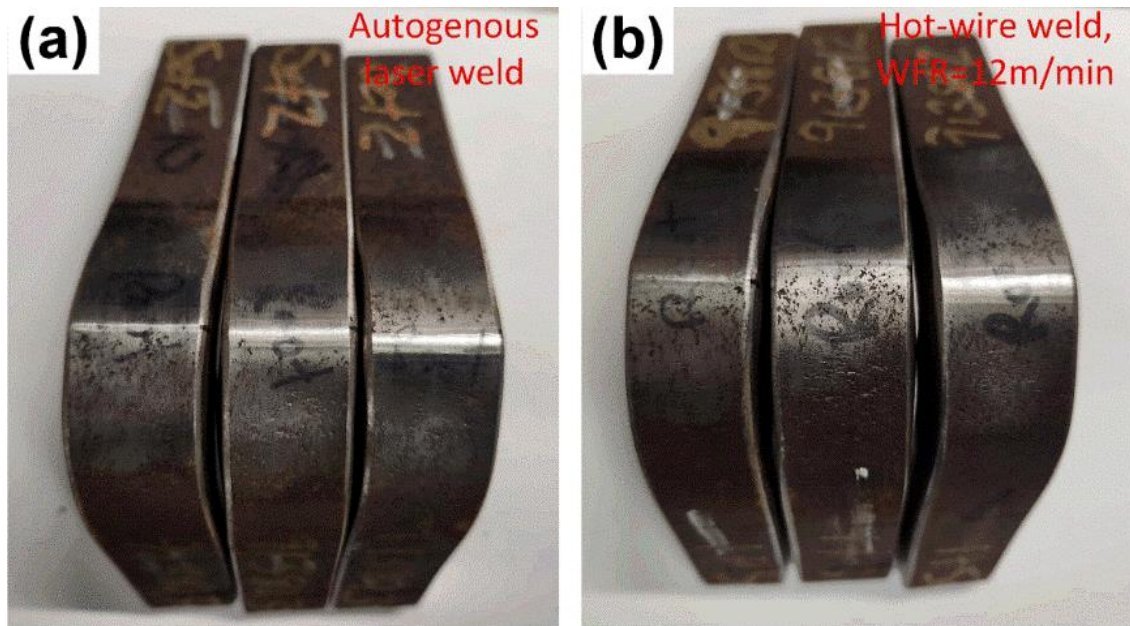


Figure 5-21. Root surfaces of the samples after bend tests, with the root pass of: (a) autogenous laser weld; (b) hot-wire laser weld with a WFR of 12 m/min.

## 5.10 Summary

The findings presented reveal the influence of filler material volume and preheat on the FZ microstructure and mechanical properties during laser welding of X80 pipeline steel. The HAZ microstructure evolution in laser and arc welds was also discussed. In particular:

(1) Introducing ER70S-6 wire at a feed rate of 6 m/min helped generate acicular ferrite in the fusion zone by modifying the chemical composition. The formation of bainite in the weld metal can be limited by increasing the WFR to 12 m/min, along with resistively preheating the wire with a power of 0.5 kW. Compared to the autogenous laser weld with a bainitic microstructure, the upper region of the FZ in the hot-wire weld with a WFR of 12 m/min was mainly composed of acicular ferrite. The acicular ferrite in the upper region of FZ was finer than that in the lower region, which appears to be due to an increase in nucleation sites available. In comparison with GMAW, the deep penetration during laser welding reduced the total number of weld passes required, and hence limited the formation of MA within the ICRCGHAZ.

(2) The addition of ER70S-6 filler wire reduced the hardness of the upper region of FZ but had limited effect on the bottom root of the fusion zone, which was due to the uneven distribution of the filler material and the resulting inhomogeneous microstructure. The hardness of the upper region of the FZ in autogenous laser weld was around 26 HV higher than that in the hot-wire laser weld with a WFR of 12 m/min, due to the presence of more bainite.

(3) Fracture occurred at base metal during the tensile tests, which indicated that weld metal strength overmatch was achieved with the welding parameters tested. Bainite and acicular ferrite generated in the weld metal provided a strength higher than that of the base metal.

(4) Up to a 26% increase in Charpy impact toughness of the weld metal was achieved at 0 °C with wire feed. The presence of acicular ferrite with an interlocking structure formed by wire addition accounts for the improved crack arrest ability of the weld metal. The ductile to brittle transition occurred as the temperature decreased to -20 °C and -45 °C, leading to lower weld metal toughness.

## **Chapter 6: Penetration and microstructural study during bead-on-plate laser welding with beam wobbling**

### **6.1 Introduction**

The static-spot laser welds obtained in chapter 5 had an inhomogeneous weld metal microstructure due to the uneven distribution of filler material, which could be improved utilizing laser beam wobbling technique. Before beam wobbling can be applied onto a Y-shaped groove, bead-on-plate welding tests are worth carrying out to show its effect on the weld penetration, as beam wobbling significantly affects the energy distribution and power density. As a wobble laser usually has a finer focused spot size to achieve better stirring effect, the comparison between a larger-spot static laser and a finer-spot wobble laser with a similar irradiated area would be more meaningful.

Wobble laser welding was first developed in 1997 [16], and requires relatively simple equipment set-up compared with other newly developed technologies like laser arc hybrid welding, vacuum laser welding or dual beam laser welding [14–16,110]. Beam wobbling could change the molten pool size and penetration during laser keyhole welding. However, Grünenwald et al. [111] found that the laser power and welding speed were the most significant factors on FZ dimension, while beam wobbling and focal position were secondary. Since beam wobbling considerably affects the flow of molten pool and temperature gradient, it can help achieve a fine-grained microstructure.

The objective of this phase of work is to study the effect of laser beam wobbling and welding speed on cross-sectional morphologies during wobble laser welding of X70 pipeline steel. The mechanisms behind the microstructure evolution were also discussed in terms of the role of solidification mode and grain nucleation.

### **6.2 Experimental procedures**

The wobble laser welding equipment employed in this work consisted of an IPG YLS-6000



fiber laser with a maximum output power of 6 kW and an IPG D50 Wobble welding head. Beam wobbling is controlled by the galvanometer scanners integrated inside the wobble head which can achieve a variety of wobble patterns, while an oscillation frequency of 160 Hz was applied. The experimental set-up and wobble patterns adopted are shown in Fig. 6-1, with an overall weld length of 140 mm performed as a bead on plate. Circular and figure-eight wobble patterns were employed. To control the laser irradiation area to a similar size, different laser spot sizes and wobble settings were used. The diameters of the focused laser spot used for static-spot and wobble laser welding were 642  $\mu\text{m}$  and 111  $\mu\text{m}$ , respectively.

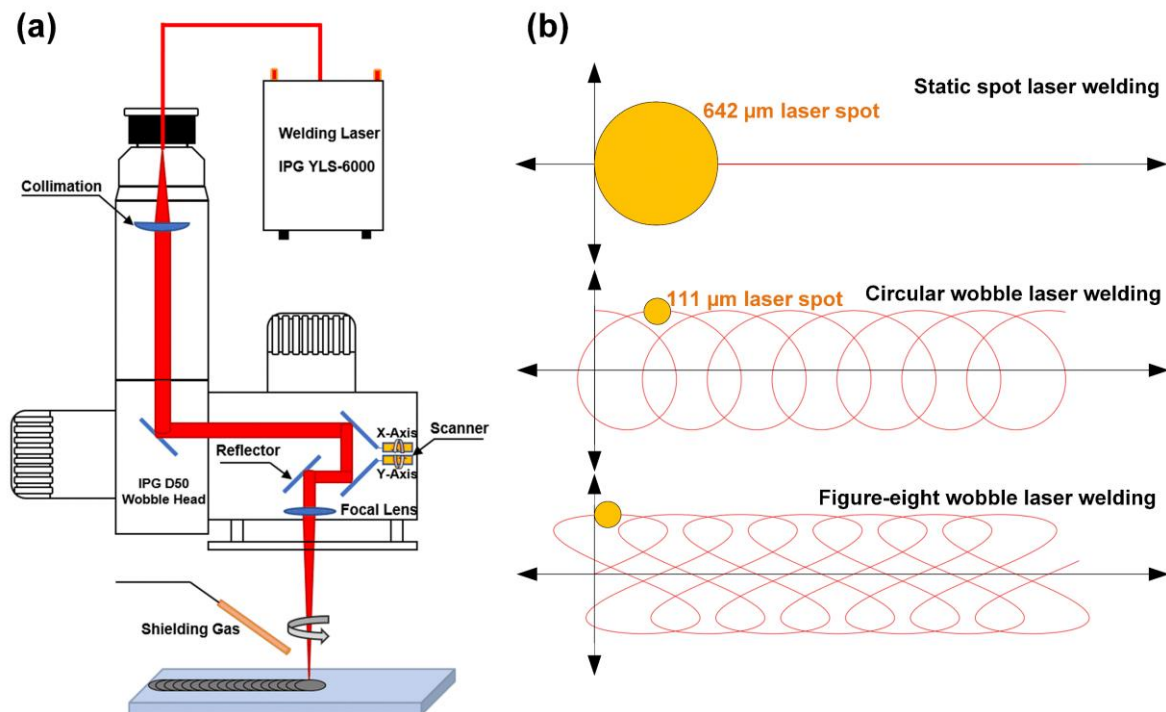


Figure 6-1. Schematic diagram of wobble laser welding: (a) experimental set-up; (b) laser wobble patterns.

The base metal comprised 16-mm-thick X70 HSLA pipeline steel. The welding parameters are listed in Table 6-1. Negative defocusing, i.e. when the laser spot is focused below the plate surface, is beneficial to increase the weld penetration and commonly used during conventional laser welding of thick plate steel, based on previous reports [112,113], thus a defocused distance of -6 mm was used for static-spot laser welding in this work. The focus position for

wobble welding process was modified to the plate surface to achieve a more stable welding process and further reduce spatter. After welding, OM and SEM were utilized for microstructural analysis.

Table 6-1. Welding parameters during bead-on-plate laser welding.

Sample number	Laser power $P$ (kW)	Welding speed $v$ (m/min)	Wobble pattern	Wobble amplitude $A$ (mm)	Wobble frequency $f$ (Hz)	Laser spot size $d$ ( $\mu\text{m}$ )
1	6	1.0	-	-	-	642
2	6	1.0	circle	0.5	160	111
3	6	1.0	circle	1.0	160	111
4	6	1.0	figure-eight	0.5	160	111
5	6	1.5	-	-	-	642
6	6	1.5	circle	0.5	160	111
7	6	1.5	circle	1.0	160	111
8	6	1.5	figure-eight	0.5	160	111

### 6.3 Surface morphologies

The weld surface morphologies of the laser welded beads with different wobble parameters are shown in Fig. 6-2. The welds produced with a static-spot laser had rough surfaces with abundant spatter and undercut defects, as shown in Fig. 6-2a and e. A larger focused laser spot resulted in a weaker plasma recoil pressure and a less stable keyhole [114], which led to more spatters formation. In contrast, all the wobble laser welded beads had smooth top surfaces with almost no spatter or undercut. It is reported that laser beam wobbling can agitate the melt flow within the molten pool, and avoid the excessive evaporation on the edge of base metal such that a more stable welding process is obtained [23,90]. Compared to a larger laser spot used in static-spot laser welding, the stronger plasma recoil pressure from a smaller laser spot during wobble laser welding can lead to a more stable keyhole [114]. Therefore, the formation of spatter was suppressed in the wobble laser condition. In addition, it is obvious that the width



of welded beads with a welding speed of 1.5 m/min were narrower than those at a speed of 1.0 m/min, resulting from a lower heat input.

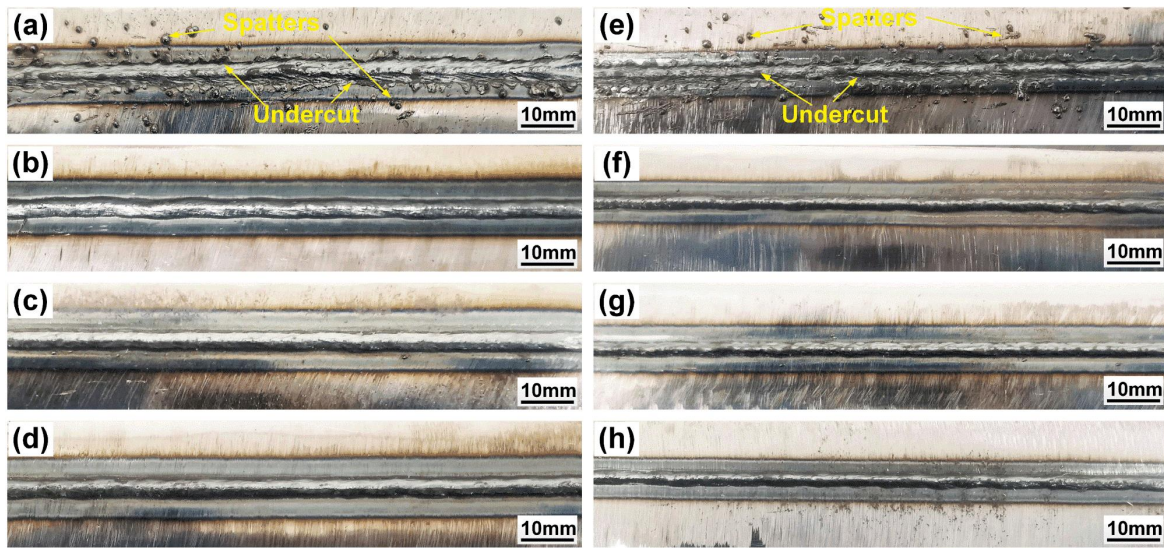


Figure 6-2. Weld surface morphologies with different wobble parameters: (a) without wobble,  $v = 1.0$  m/min; (b) circular wobble,  $A = 0.5$  mm,  $v = 1.0$  m/min; (c) circular wobble,  $A = 1.0$  mm,  $v = 1.0$  m/min; (d) figure-eight wobble,  $A = 0.5$  mm,  $v = 1.0$  m/min; (e) without wobble,  $v = 1.5$  m/min; (f) circular wobble,  $A = 0.5$  mm,  $v = 1.5$  m/min; (g) circular wobble,  $A = 1.0$  mm,  $v = 1.5$  m/min; (h) figure-eight wobble,  $A = 0.5$  mm,  $v = 1.5$  m/min.

#### 6.4 Weld penetration

Fig. 6-3 shows the cross-sections of welds with different wobble parameters. Spatter and undercuts could also be found in the cross-sections of the static spot laser welded joints, as shown in Fig. 6-3a and e. Compared to static-spot laser welds with a spot size of  $642 \mu\text{m}$ , circular wobble laser welding with a spot size of  $111 \mu\text{m}$  and amplitude of  $0.5$  mm resulted in a 15% deeper penetration and a 22% narrower fusion zone, as shown in Figs. 6-3(a-b). This was due to the higher beam energy density with a smaller laser spot size. Increasing the wobble amplitude from  $0.5$  mm to  $1.0$  mm at a welding speed of  $1.0$  m/min leads to a decrease in penetration from  $9.43$  mm to  $8.68$  mm, or a reduction of 8% (Figs. 6-3b and c). With increasing wobble amplitude, the laser beam irradiated a larger area and the energy density decreased, which led to the reduction of penetration. Applying a figure-eight wobble path during welding

also produced a deeper penetration and a narrower FZ compared to static-spot laser welded joint, see Fig. 6-3d. As shown in Figs. 6-3(e-h), increasing the welding speed from 1.0 mm/min to 1.5 mm/min results in a shallower penetration and a narrower FZ due to the lower heat input, while the variation in fusion zone width with varying wobble conditions was less obvious at a higher welding speed.

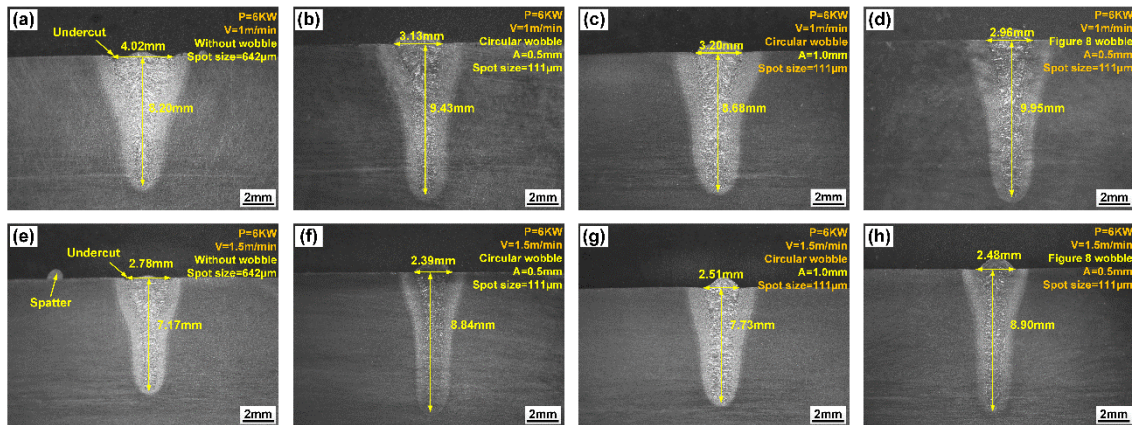


Figure 6-3. Cross-section morphologies with different wobble parameters: (a) without wobble,  $v = 1.0$  m/min; (b) circular wobble,  $A = 0.5$  mm,  $v = 1.0$  m/min; (c) circular wobble,  $A = 1.0$  mm,  $v = 1.0$  m/min; (d) figure-eight wobble,  $A = 0.5$  mm,  $v = 1.0$  m/min; (e) without wobble,  $v = 1.5$  m/min; (f) circular wobble,  $A = 0.5$  mm,  $v = 1.5$  m/min; (g) circular wobble,  $A = 1.0$  mm,  $v = 1.5$  m/min; (h) figure-eight wobble,  $A = 0.5$  mm,  $v = 1.5$  m/min.

## 6.5 FZ microstructure

The pipeline steel substrate consists of ferrite (F) and bainite (B), as presented in Fig. 6-4. The base metal has a carbon fraction below 0.1 wt.% and is classified as a hypoeutectoid steel, and thus at equilibrium solidification, the microstructure is expected to be mainly composed of proeutectoid ferrite and pearlite. However, low temperature transformation products like bainite and martensite are easily formed at fast cooling rates during laser welding. Fig. 6-5 shows that the weld metal mainly contained bainite (B) together with some martensite (M) and grain-boundary ferrite (GBF). The SEM results confirmed the presence of low temperature transformation products including bainite and martensite in weld metal of joints at different welding speeds, as shown in Fig. 6-5(b-d).



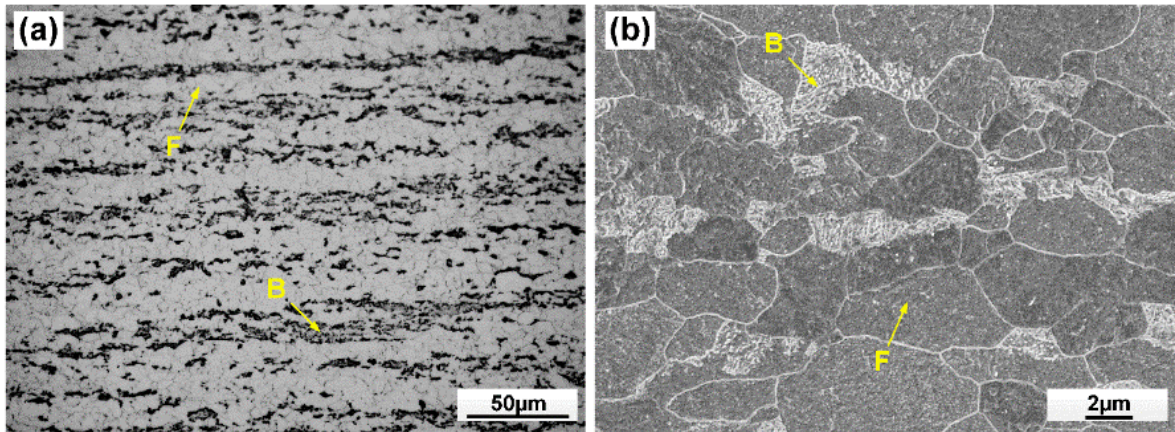


Figure 6-4. Microstructure of the X70 base metal: (a) optical micrograph; (b) SEM micrograph.

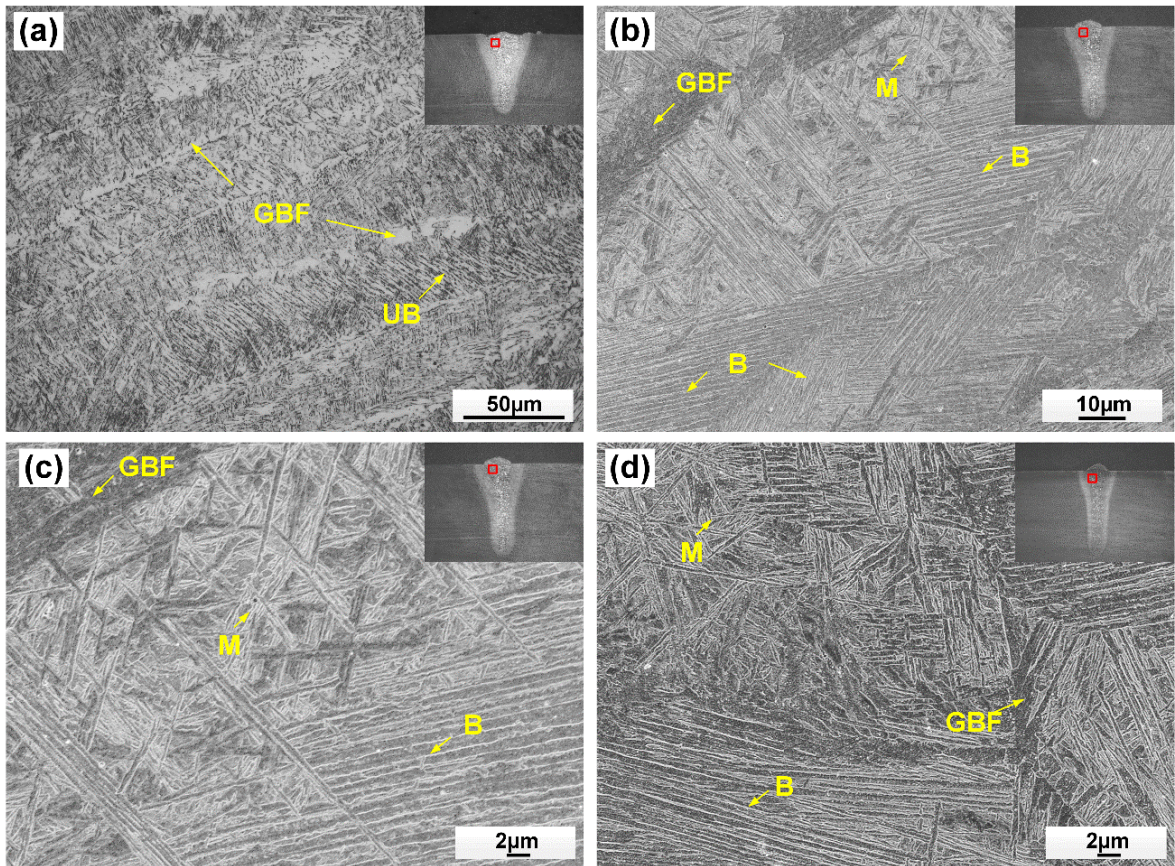


Figure 6-5. Microstructure of weld metal, indicating presence of grain-boundary ferrite (GBF), upper bainite (UB) and martensite (M) in: (a) optical micrograph of static spot laser welded joint at a welding speed of 1.0 m/min; (b) and (c) SEM micrograph of 0.5 mm amplitude wobble laser welded joint at a welding speed of 1.0 m/min with different magnifications; (d) SEM micrograph of 0.5 mm amplitude wobble laser welded joint at a welding speed of 1.5 m/min.

## 6.6 Grain structure

The melt flow behaviour and grain formation process with different beam motion paths are illustrated in Fig. 6-6, prior austenite grains morphologies are also shown in the micrographs taken parallel to the seam top surface. The weld metal in the static-spot laser welded joint consisted of long continuous columnar grains growing parallel to the heat flow direction, which is the typical dendrite morphology for conventional laser welding since the columnar grains grow from fusion line to the center based on the heat flow in keyhole welds, as this corresponds to the direction of the temperature gradient. In contrast, for wobble laser welded joint, the fusion zone mainly contained short broken dendrites and the microstructure was more refined.

During static-spot laser welding, the plasma recoil pressure and Marangoni force would drive the liquid metal to flow from the front of the keyhole to the rear of the molten pool, as shown in Fig. 6-6a. Meanwhile, during wobble laser welding, the beam wobbling would create a vortex flow and drive the melted material rotate with the laser beam. If the melt flow and temperature gradient direction change, this would disrupt the solidification process and change the grain growth direction. In this scenario, small melt flow turbulences would form at the trailing edge of molten pool during wobble laser welding, as illustrated in Fig. 6-6(b-c). Melt flow turbulences would be more likely to initiate when the laser travel path intersects with itself or the traveling direction suddenly changes from backward to forward. These turbulences would penetrate the mushy zone which contains both the growing columnar grains and the liquid metal. The solidifying columnar grains become remelted and broken into small pieces, which leads to a more random and dispersed dendrite grain structure [23,90,92,115]. This kind of melt flow behaviour was also discussed in previous reports [90,92,115], some modelling work [116] and tracer atomic analysis [23] were also done by researchers to reveal the similar melt flow behaviour during laser welding with beam wobbling.



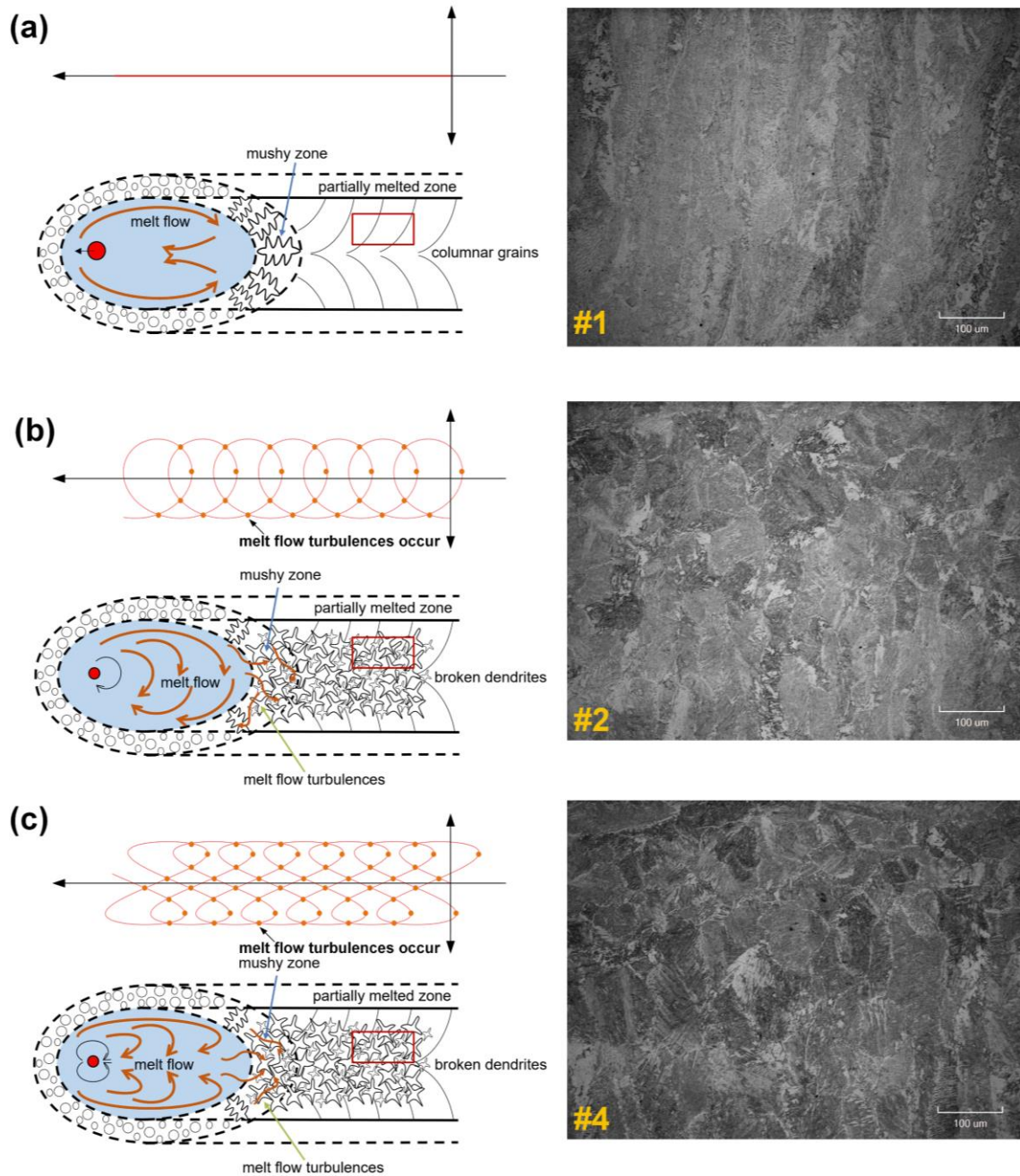


Figure 6-6. Schematics diagram of melt flow and top surface grain structure morphology with different wobble patterns: (a) without wobble; (b) circular wobble; (c) figure-eight wobble.

## 6.7 Summary

The findings presented reveal there are subtle differences in the weld surface morphologies and microstructure imparted by the beam wobbling method compared to conventional laser welding. The following results were obtained:

(1) The formation of spatter or undercuts were suppressed with laser beam wobbling, leading to a smoother bead surface compared to the conventional laser welded beads.

(2) Compared to static-spot laser welding, wobbling beam laser welding with a finer laser spot led to a deeper penetration and a narrower FZ at small amplitudes, resulting from higher beam energy density.

(3) A refined prior austenite grain structure was achieved by a stirring effect of the laser beam wobbling. Beam wobbling would change the melt flow direction, disrupt solidification, and break up the solidifying columnar grains. However, the mechanical properties of carbon steel welds would depend more on the microconstituents in the FZ, and the influence of prior austenite (which is not the final transformation product) grain size could be minor.

## **Chapter 7: Effect of beam wobbling and welding speed in X80 steel wire-fed laser welds**

### **7.1 Introduction**

The study in chapter 6 shows that a finer-spot wobble laser provided a comparable penetration to that obtained with a static-spot laser if the laser irradiation area was similar, which is helpful for determining the wobble parameters when beam wobbling was applied onto the Y-shape groove. Different from autogenous laser welding process, when a wobble laser was combined with a wire feed, it would affect the dilution of the filler material resulting from different volume of melted base metal presenting in the FZ, which is not well studied in the literature. In this chapter, the effect of laser beam wobbling on the filler material dilution, FZ microstructure and mechanical properties in X80 steel laser welds when combined with a cold-wire feed was studied.

The findings in chapter 5 indicate that feeding an ER70S-6 wire during laser keyhole welding led to the formation of acicular ferrite in the weld metal, reduced the fusion zone hardness and improved the toughness while maintaining a high productivity. The results in previous reports showed that beam wobbling improved the elements mixing when an additional wire was introduced into the weld pool, as Wang et al. [96] found that beam wobbling enlarged the transaction angle between the upper and lower molten pool, increased the stirring effect and solute transfer, and mitigated the macro-segregation in laser arc hybrid Al-Si welds. Wu et al. [104] found that beam wobbling could suppress incomplete fusion defects and improve the welding process stability during HLAW of high strength low alloy steel.

In this part of work, the effect of beam wobbling and welding speed on the filler material distribution, fusion zone microstructure, and mechanical properties including hardness and yield strength in X80 steel laser welds is studied. Here the instrumented indentation testing was used for the first time to distinguish the local yield strength values of different regions of the

fine weld zones produced using the novel wobble laser welding method. This allows one for the first time to verify if a critical weld metal strength overmatching is achieved in different regions of the weld metal, which is a key requirement in many industrial standards. The HAZ microstructure and properties are also investigated, and the process-microstructure-properties relationship of the joint is discussed in detail.

## **7.2 Experimental procedures**

The experimental set-up for wire-fed laser welding is shown in Fig. 7-1. An IPG YLS-8000 fiber laser with a maximum power output of 8 kW and a focused spot size of 600  $\mu\text{m}$  was used in this work. Beam wobbling was controlled by galvanometer scanners integrated inside an IPG D50 wobble welding head, which applied a circular repeating pattern at a frequency of 160 Hz. The base metal was taken from an X80 pipe with dimensions of 250 mm  $\times$  120 mm  $\times$  14 mm. An ER70S-6 welding wire was used as the filler material, with a wire diameter of 0.9 mm. As for the groove design, a 30-degree bevel and a 6 mm root height were used, as shown in Fig. 7-1. A 0.4 mm root opening was used during the wire-fed laser welding process to help accommodate the filler material. Argon was used as shielding gas, with a flow rate of 18 L/min. The welding parameters are listed in Table 7-1. The wire feed rate was increased from 6 m/min to 9 m/min as the welding speed increased from 1 m/min to 1.5 m/min, so the same amount of filler material was fed into the groove regardless of changes in travel speed. The wobble parameters and wire feed rates were selected based on the tested penetrating ability of the wobble laser, which will also be discussed in detail in the results section.



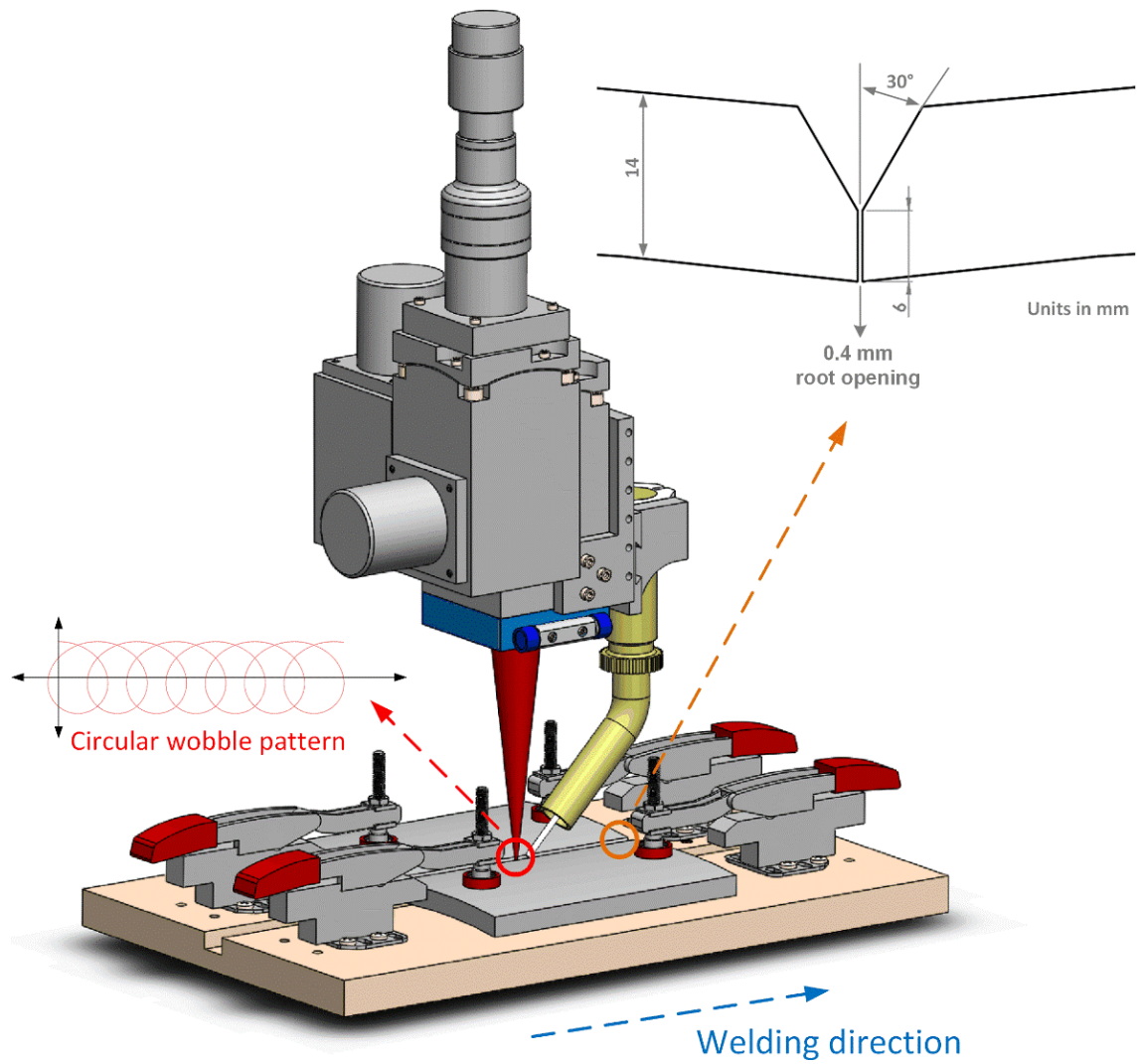


Figure 7-1. Experimental set-up for wire-fed laser welding with beam wobbling, showing wobble pattern and groove design.

Table 7-1. Welding parameters during static-spot and wobble laser welding with cold-wire feeding.

Sample number	Laser power $P$ (kW)	Welding speed $v$ (m/min)	Wire feed rate $WFR$ (m/min)	Wobble amplitude $A$ (mm)	Wobble frequency $f$ (Hz)	Defocused distance $D_f$ (mm)
1	8	1.0	6	-	-	-3
2	8	1.0	6	0.5	160	-3
3	8	1.0	6	1.0	160	-3
4	8	1.5	9	-	-	-3
5	8	1.5	9	0.5	160	-3

Electron probe microanalyzer (EPMA) was utilized to analyze elemental distribution. Silicon was chosen as the tracking element due to the difference in the content in the base metal and filler material. The EPMA maps covered the whole fusion zone, with a step size of 10  $\mu\text{m}$ , a dwell time of 20 ms and a total collecting time of 2.2 h. Line-scanning along the through-thickness direction in the FZ was also done to show the silicon distribution, with a step size of 10  $\mu\text{m}$ , a dwell time of 1 second and a collecting time of 13 minutes per scan. Lowess fit function provided by OriginPro 2023 was utilized to find the best-fit distribution curves, which uses locally weighted linear regression to smooth the data. In this way, the element distribution can be shown more apparently. OM and SEM were utilized for microstructural analysis. Microhardness tests were done to reveal the hardness difference in different regions of FZ and HAZ. A Nanovea M1 instrumented indentation tester was used to perform local indenting and estimate yield strength based on the load-displacement curve. The yield strength of X80 base metal was calculated to be  $559 \pm 14$  MPa using indentation data. Although this represents a 9.7% difference in base metal yield strength compared to the results from a tensile frame ( $619 \pm 18$  MPa), this method provides a reliable means for comparison of local yield strength.

### 7.3 Weld morphologies

With a circular wobble pattern, the travel path of the laser spot can be expressed by:

$$\begin{cases} x(t) = vt + 0.5A\sin(2\pi ft) \\ y(t) = 0.5A\cos(2\pi ft) \end{cases} \quad (7-1)$$

where  $x(t)$  and  $y(t)$  define the laser spot position at a time  $t$ , where  $v$  is the welding speed,  $A$  and  $f$  are the wobble amplitude and frequency, respectively. By taking the derivative of the above equation, an expression for the laser spot velocity can be obtained as follows:

$$\begin{cases} v_x = |v + A\pi f\cos(2\pi ft)| \\ v_y = |A\pi f\sin(2\pi ft)| \\ v_r = \sqrt{v_x^2 + v_y^2} \end{cases} \quad (7-2)$$

where  $v_x$  and  $v_y$  are the moving velocity along  $x$ - and  $y$ -direction, respectively.  $v_r$  is the

actual moving velocity of the laser beam spot. Fig. 7-2 shows the laser travel path with varying welding speeds and wobble amplitudes. With the increase of the wobble amplitude, the laser would irradiate a larger area, leading to a dispersed laser energy over a wider molten pool which reduced the effective heat input, as shown in Fig. 7-2(a-b). A larger wobble amplitude would also result in a higher laser spot velocity and reduce the local penetration. The pitch length of the travel path depends on both the wobble frequency and welding speed along the welding direction, as a 1.5 m/min welding speed led to a larger pitch shown in Fig. 7-2c, which caused less ‘overlapping’ along the path.

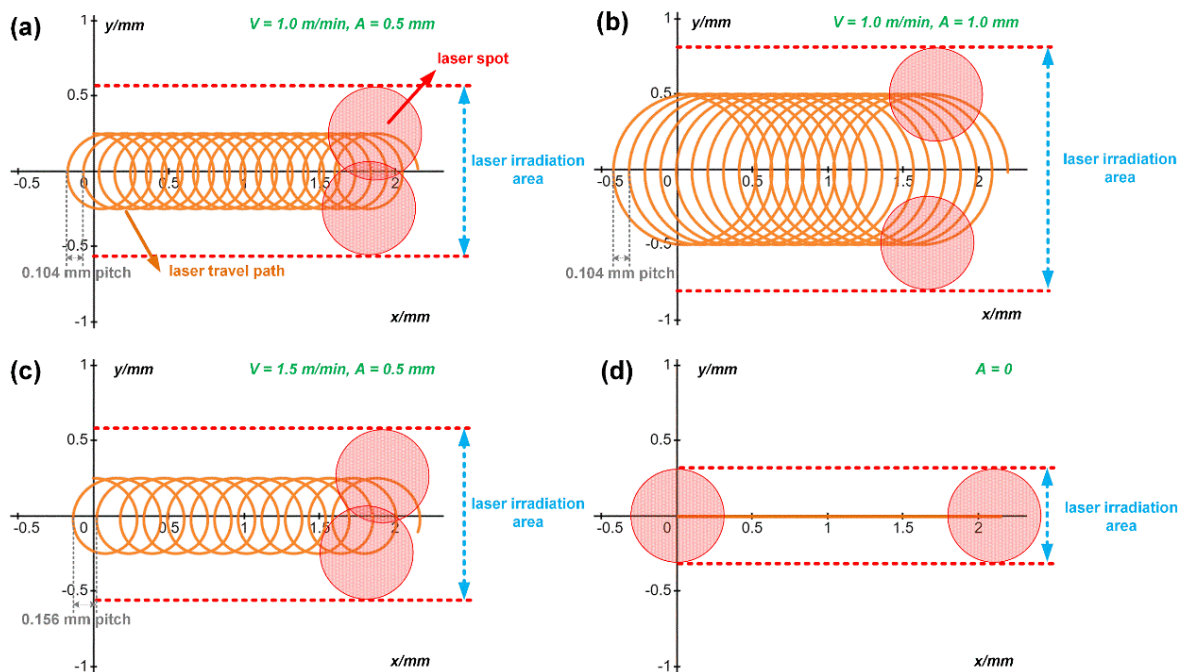


Figure 7-2. Laser travel path and radiation area with varying parameters: (a)  $v = 1.0 \text{ m/min}$ ,  $A = 0.5 \text{ mm}$ ; (b)  $v = 1.0 \text{ m/min}$ ,  $A = 1.0 \text{ mm}$ ; (c)  $v = 1.5 \text{ m/min}$ ,  $A = 0.5 \text{ mm}$ ; (d) static-spot laser welding.

The top and root surfaces of the laser welds are shown in Fig. 7-3. Continuous, crack-free, and full penetration laser welds were obtained. For the 0.5-mm-amplitude wobble laser weld with a welding speed of 1.5 m/min, lack of root fusion can be found due to the decreased heat input, high laser spot velocity and dispersed energy with the beam wobbling, and it can be expected that any further increase in wobble amplitude would not lead to a sound back surface

or sufficient penetration. Fig. 7-4 shows the cross-sectional morphologies of the joints. Beam wobbling enlarged the fusion zone and led to an increase in weld width, which could potentially improve the gap-bridging ability. At a welding speed of 1.0 m/min, the width of the narrowest position in the FZ increased by 31% (from 1.40 mm to 1.84 mm) as the wobble amplitude increased from 0 to 1.0 mm, as shown in Fig. 7-3a and c. Narrower FZ and HAZ were obtained when the welding speed increased from 1.0 m/min to 1.5 m/min, due to the decrease in linear heat input. Although a narrower HAZ is always desired, the associated higher cooling rate may result in the formation of low temperature transformation products like bainite or martensite in the FZ, which will have increased hardness and potentially introduce brittle regions.

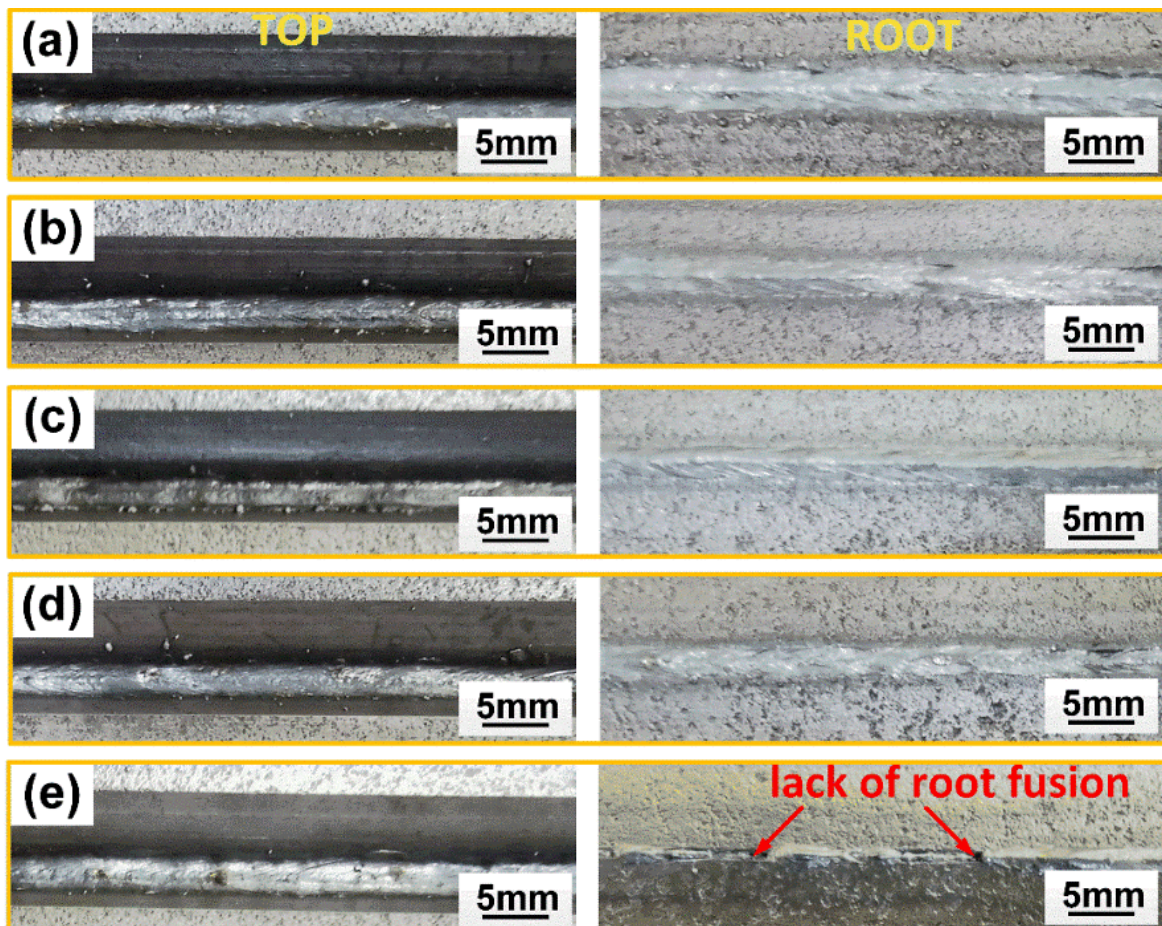


Figure 7-3. Weld surface morphologies on top and back of the welds: (a) static-spot laser weld,  $v = 1.0$  m/min; (b) wobble laser weld,  $v = 1.0$  m/min,  $A = 0.5$  mm; (c) wobble laser weld,  $v = 1.0$  m/min,  $A = 1.0$  mm; (d) static-spot laser weld,  $v = 1.5$  m/min; (e) wobble laser weld,  $v = 1.5$  m/min,  $A = 0.5$  mm.



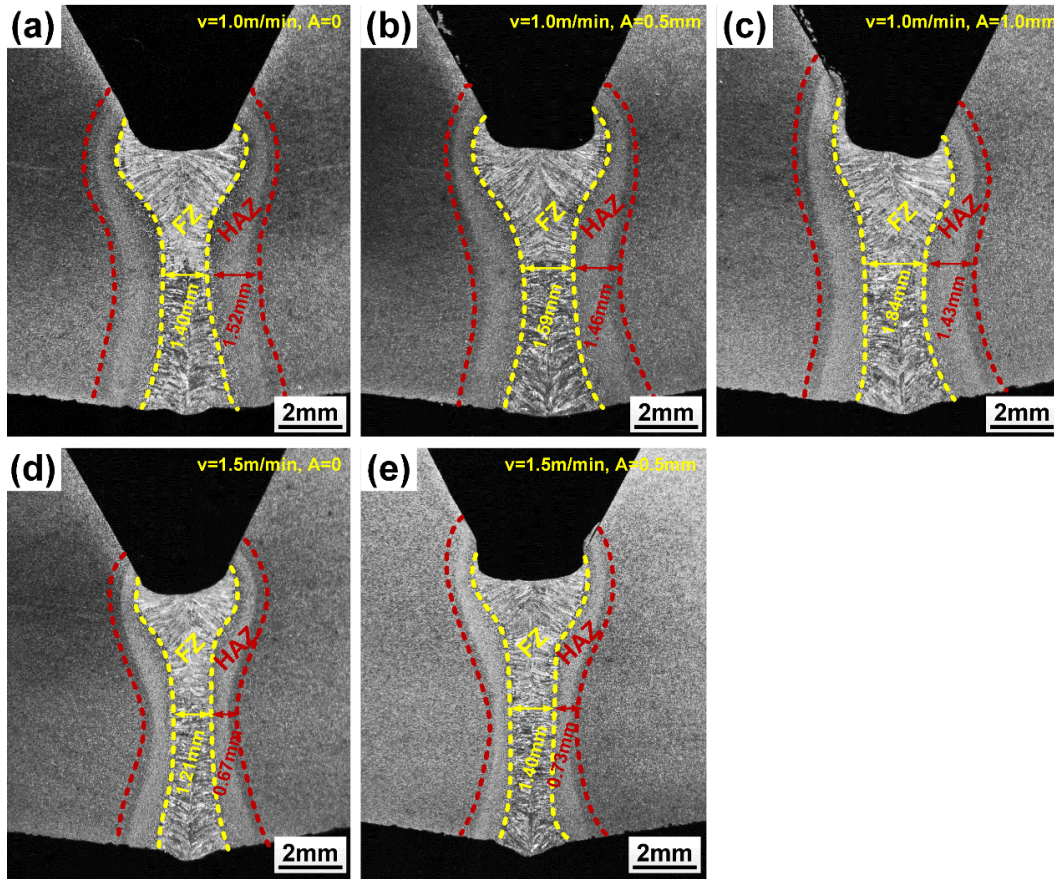


Figure 7-4. Cross-sectional morphologies: (a) static-spot laser weld,  $v = 1.0$  m/min; (b) wobble laser weld,  $v = 1.0$  m/min,  $A = 0.5$  mm; (c) wobble laser weld,  $v = 1.0$  m/min,  $A = 1.0$  mm; (d) static-spot laser weld,  $v = 1.5$  mm; (e) wobble laser weld,  $v = 1.5$  m/min,  $A = 0.5$  mm.

#### 7.4 Alloying element distributions in fusion zones

Silicon was selected as a tracer element for the analysis of the filler material distribution, since the silicon content of the ER70S-6 wire is 5 times higher than that of the X80 base metal. EPMA maps in Fig. 7-5 clearly demonstrate that more filler material stayed in the upper region of the fusion zone, since the wire was fed from the top of the gap. The narrower the FZ was, the higher the silicon content in the upper region of the FZ. On the contrary, increasing the width of the weld zone also increases the volume of melted base material, which increases the consequent dilution of alloying elements from the filler wire. The line-scan results in Fig. 7-6 also confirm that beam wobbling led to the dilution of filler material in the upper region of the FZ due to the increased weld width. A higher welding speed resulted in a reduced dilution effect

due to a decreased FZ width.

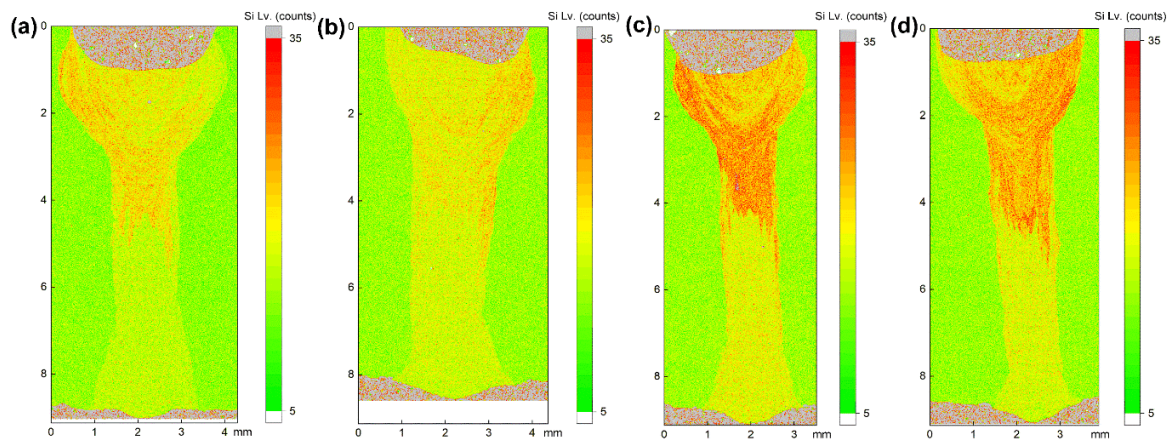


Figure 7-5. EPMA maps showing the Si distribution in the weld metal: (a) static-spot laser weld,  $v = 1.0$  m/min; (b) wobble laser weld,  $v = 1.0$  m/min,  $A = 1.0$  mm; (c) static-spot laser weld,  $v = 1.5$  m/min; (d) wobble laser weld,  $v = 1.5$  m/min,  $A = 0.5$  mm.

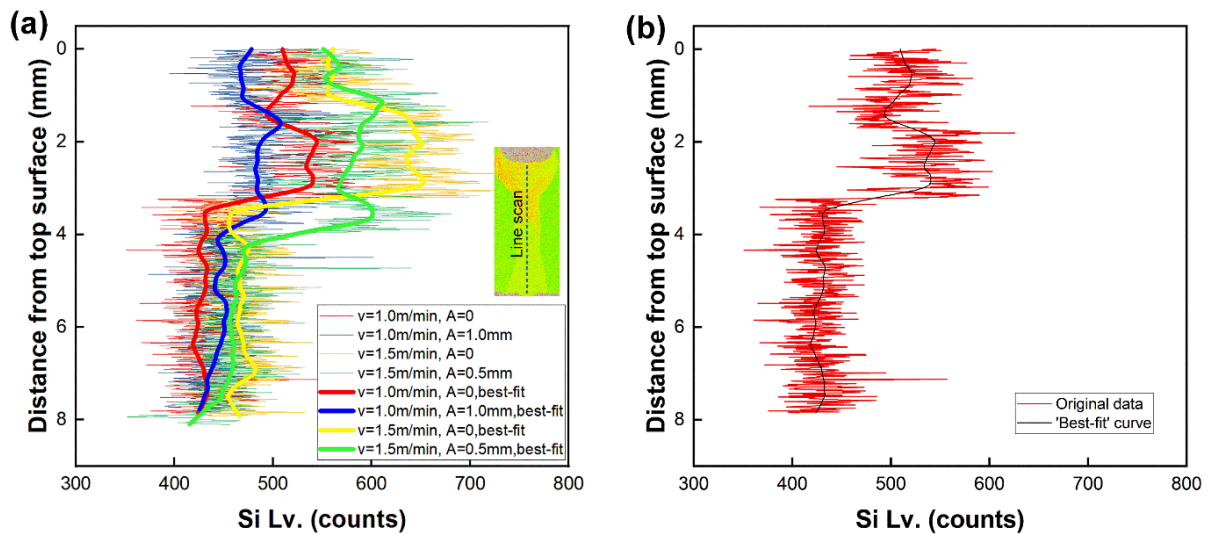


Figure 7-6. (a) EPMA line-scan results showing the Si distribution in the weld metal, with the ‘best-fit’ curves obtained by Lowess fitting highlighted; (b) the comparison between original data and the ‘best-fit’ curve.

## 7.5 Microstructure

Fig. 7-7 and 7-8 show the weld metal microstructure of the upper and lower region of the FZ, respectively. Meanwhile, Fig. 7-9 summarizes the volume fraction of microconstituents in the FZ. Since the upper region of the FZ contained a higher fraction of filler material than the



lower region, the weld metal microstructure is inhomogeneous along the through-thickness direction. The upper region of static-spot laser weld with a welding speed of 1.0 m/min mainly contained acicular ferrite (AF), with a volume fraction of around 87%, as shown in Fig. 7-7a. When using wire-fed laser welding, the ER70S wire promoted formation of non-metallic inclusions in the weld metal, some of which provided preferred nucleation sites for AF. With a wobble amplitude of 1.0 mm, less AF was observed with more bainite (25% compared to 4%) appearing in the weld metal, as a result of the dilution effect caused by beam wobbling which increased the fraction of melted base material, as shown in Fig. 7-7b. As the welding speed increased to 1.5 m/min, the higher cooling rate also resulted in the formation of more bainite (around 32%), as shown in Fig. 7-7c and d.

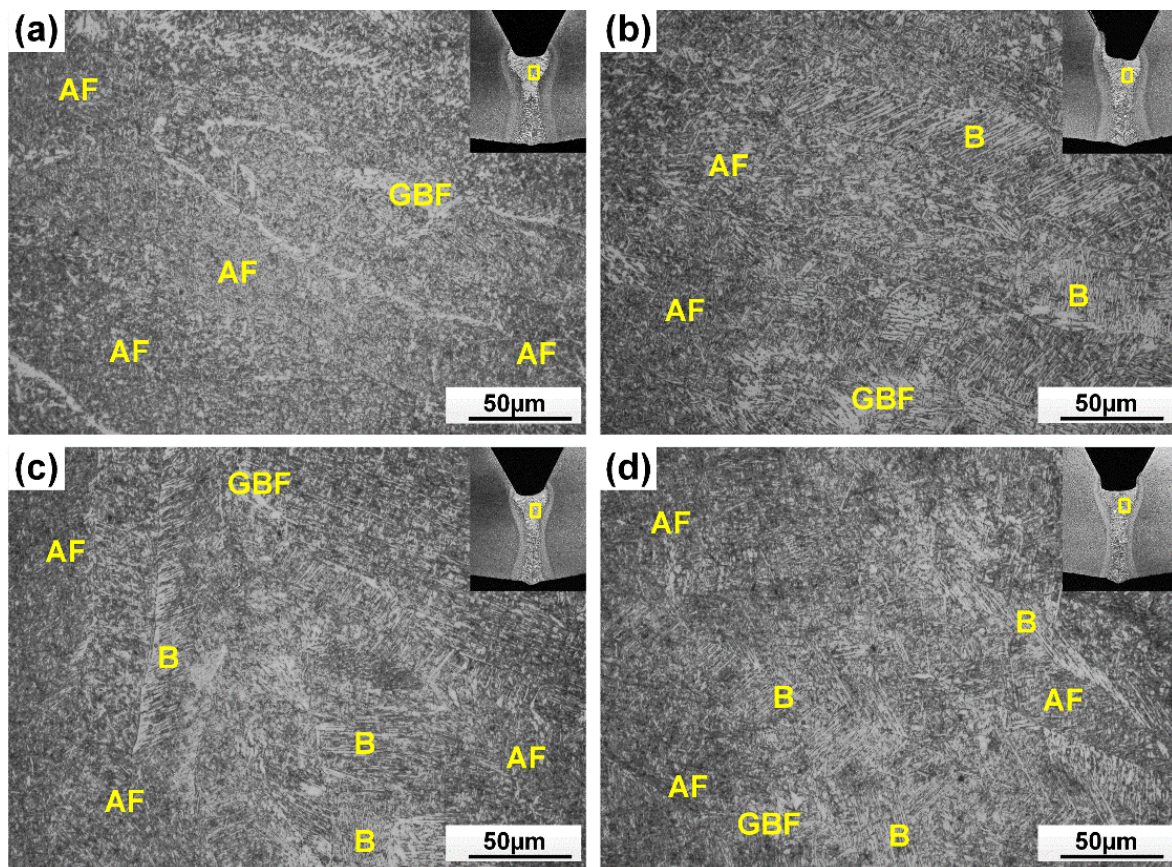


Figure 7-7. Optical micrographs showing the microstructure of upper region of the FZ, indicating the presence of acicular ferrite (AF), grain boundary ferrite (GBF) and bainite (B): (a) static-spot laser weld,  $v = 1.0$  m/min; (b) wobble laser weld,  $v = 1.0$  m/min,  $A = 1.0$  mm; (c) static-spot laser weld,  $v = 1.5$  m/min; (d) wobble laser weld,  $v = 1.5$  m/min,  $A = 0.5$  mm.



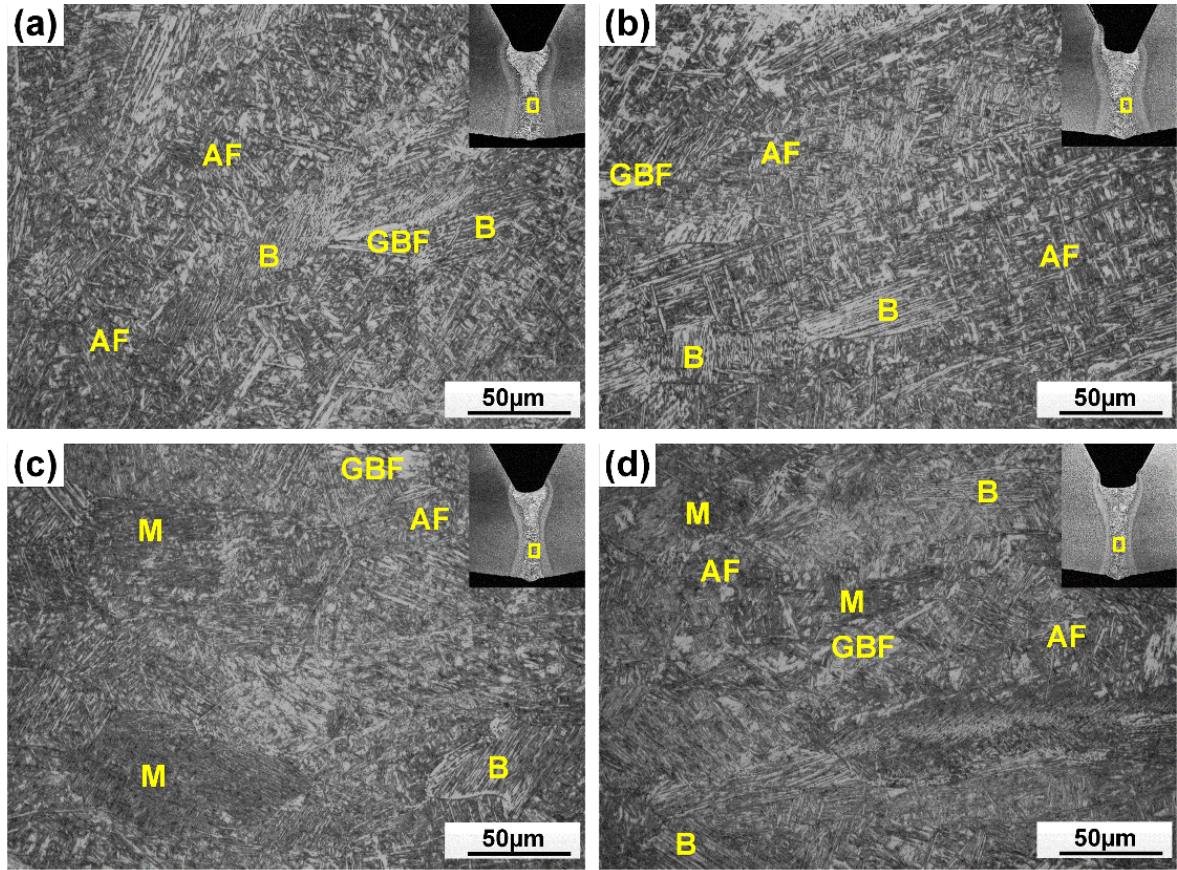


Figure 7-8. Optical micrographs showing the microstructure of lower region of the FZ, indicating the presence of acicular ferrite (AF), grain boundary ferrite (GBF), bainite (B) and martensite (M): (a) static-spot laser weld,  $v = 1.0$  m/min; (b) wobble laser weld,  $v = 1.0$  m/min,  $A = 1.0$  mm; (c) static-spot laser weld,  $v = 1.5$  m/min; (d) wobble laser weld,  $v = 1.5$  m/min,  $A = 0.5$  mm.

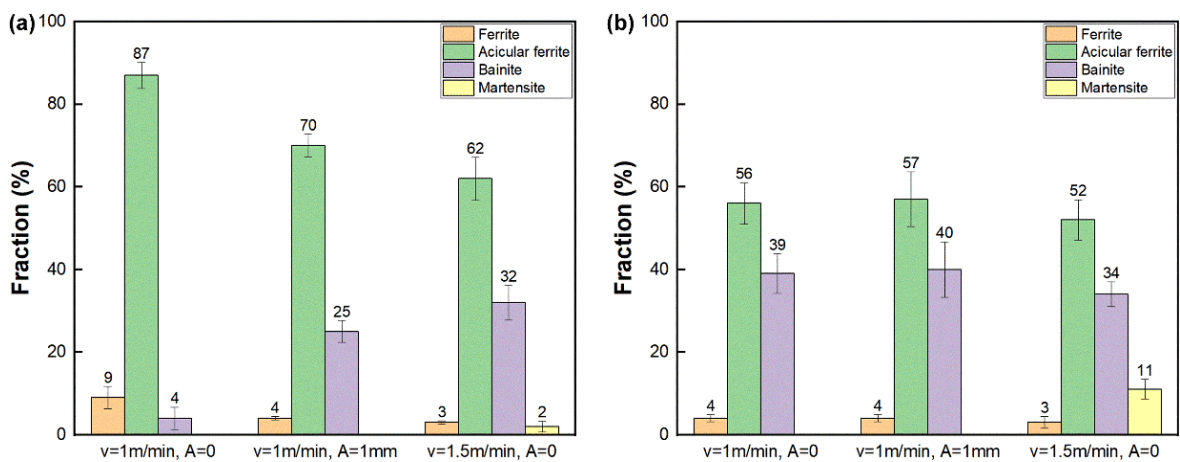


Figure 7-9. Volume fraction of microconstituents within the fusion zone: (a) upper region; (b) lower region.

The lower region of the weld metal with a welding speed of 1.0 m/min was composed of AF and bainite (Fig. 7-8a and b). However, around 11% martensite formed as the welding speed increased to 1.5 m/min, as shown in Fig. 7-8c and d. The high-magnification SEM images in Fig. 7-10 and 7-11 confirmed the presence of AF and bainite in the laser welds with different welding parameters, and martensite with a very fine structure in the lower region of the FZ of the weld with a welding speed of 1.5 m/min, which was resulted from the high cooling rate. The AF in the upper region is finer than that in the lower region, as shown in Fig. 7-10a and 7-11a, which may be attributed to the reduced fraction of filler material reaching the root region of the weld. The increased filler metal near the upper FZ region will provide a higher concentration of nucleation sites, which accounts for the finer AF microstructures there.

Fig. 7-12 shows the CGHAZ and the FGHAZ microstructure of the joints. Meanwhile, the ICHAZ microstructure is shown in Fig. 7-13. Beam wobbling had no significant impact on the HAZ microstructure, which can be expected due to the same overall liner heat input. However, the different heat input resulted from varying welding speeds influenced the grain structure and microconstituents fraction in the HAZ. The CGHAZ adjacent to the FZ was composed of bainite, resulting from the high cooling rate. The prior austenite grains in the CGHAZ were finer with a welding speed of 1.5 m/min due to the lower heat input, compared to those with a welding speed of 1.0 m/min, as shown in Fig. 7-12a and c. The FGHAZ which experienced a lower peak temperature mainly contained fine-grain ferrite. As shown in Fig. 7-12(d-f), the lower heat input with a welding speed of 1.5 m/min limited the growth of the grains, leading to the formation of finer ferrite grains ( $AGI = 1.3 / \mu\text{m}$ ) in the FGHAZ, compared to that with a welding speed of 1.0 m/min ( $AGI = 0.9 / \mu\text{m}$ ). MA constituents were formed in the ICHAZ that experienced a peak temperature between  $A_{c1}$  and  $A_{c3}$ . The higher heat input with a welding speed of 1.0 m/min led to the formation of more MA, which was also coarser, as shown in Fig. 7-13.



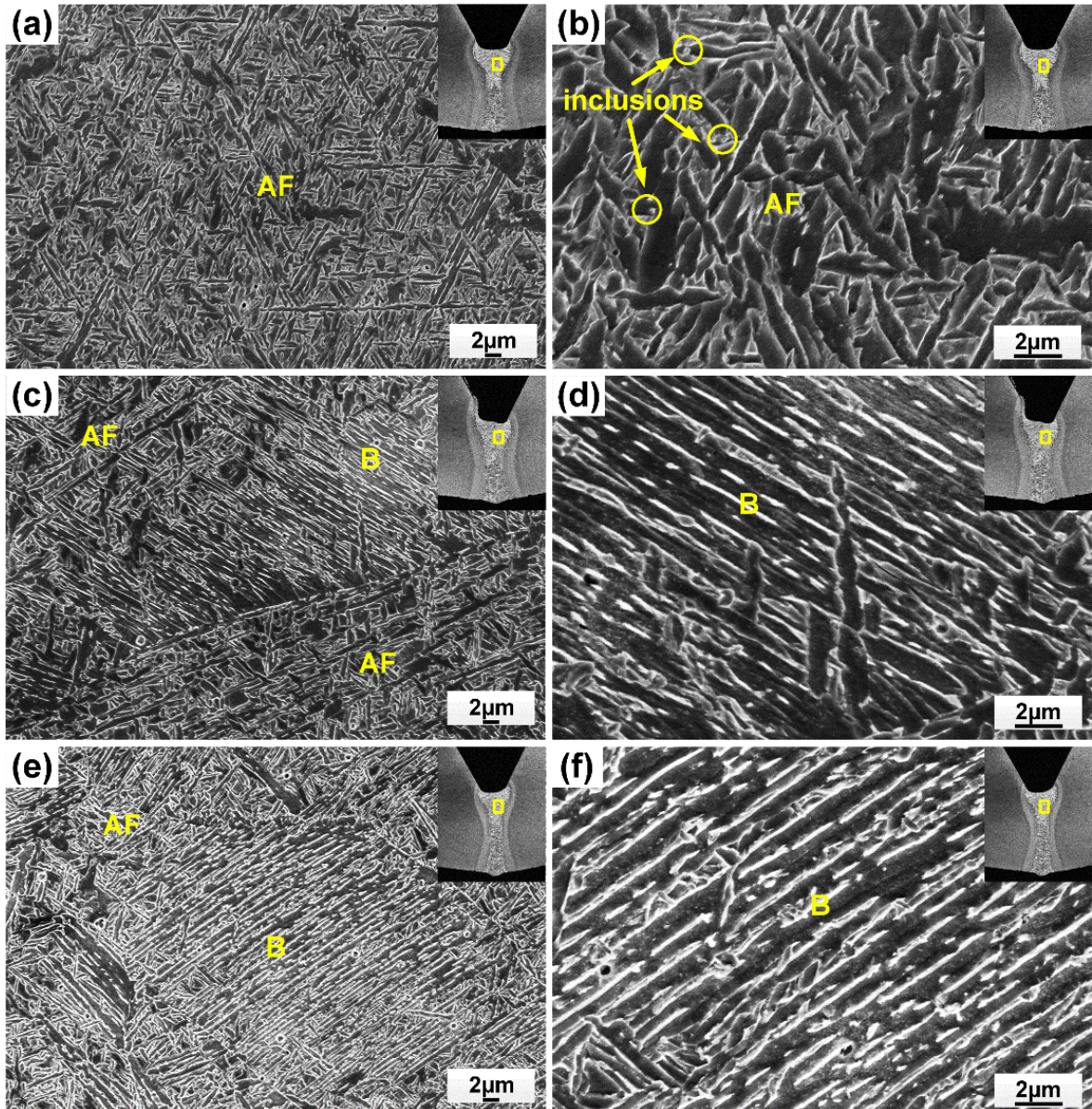


Figure 7-10 SEM micrographs indicating the presence of acicular ferrite (AF) and bainite (B) in the upper region of the fusion zone: (a) and (b) static-spot laser weld,  $v = 1.0$  m/min; (c) and (d) wobble laser weld,  $v = 1.0$  m/min;  $A = 1.0$  mm; (e) and (f) static-spot laser weld,  $v = 1.5$  m/min.



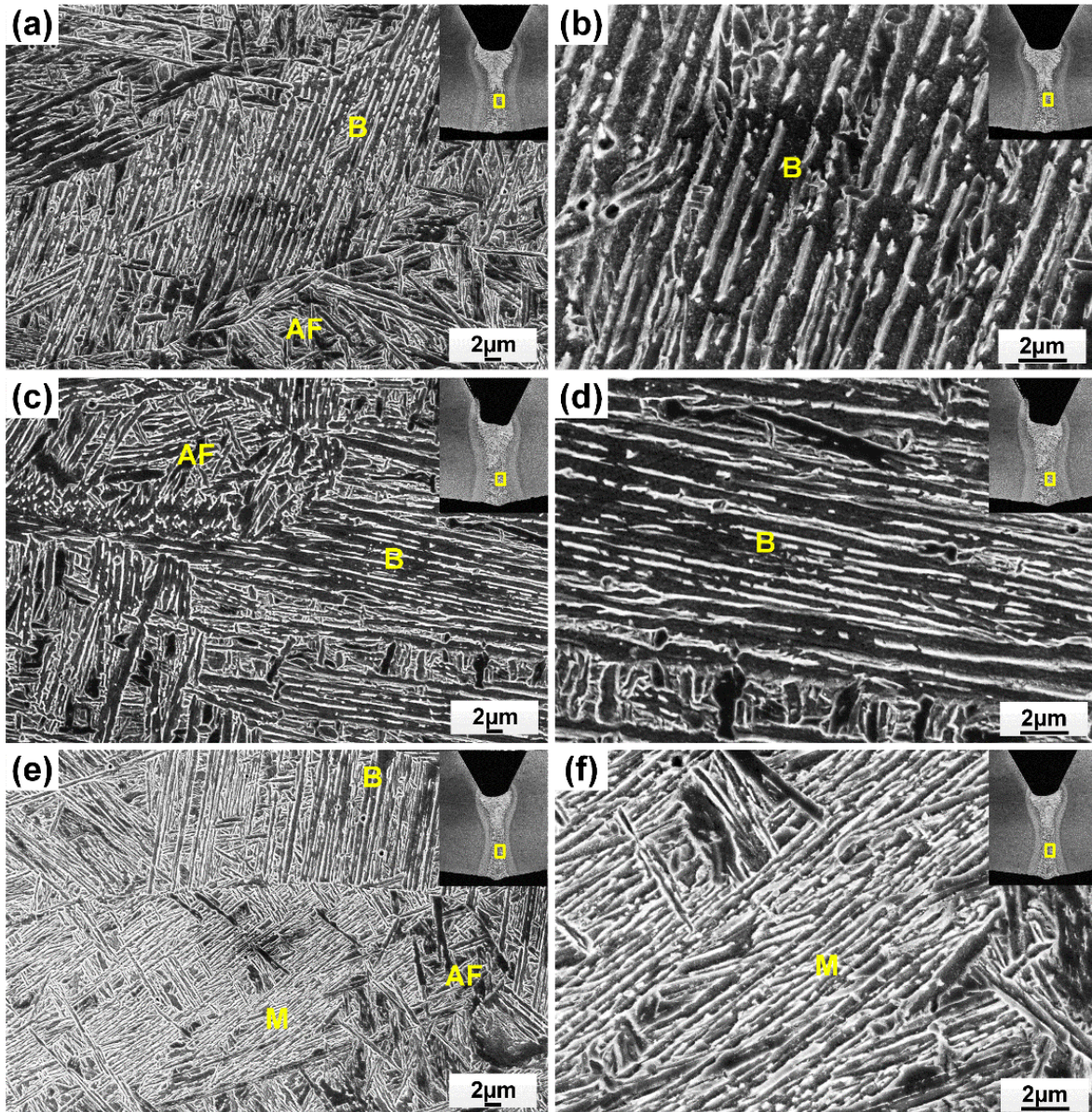


Figure 7-11. SEM micrographs indicating the presence of acicular ferrite (AF), bainite (B) and martensite (M) in the lower region of the fusion zone: (a) and (b) static-spot laser weld,  $v = 1.0$  m/min; (c) and (d) wobble laser weld,  $v = 1.0$  m/min;  $A = 1.0$  mm; (e) and (f) static-spot laser weld,  $v = 1.5$  m/min.



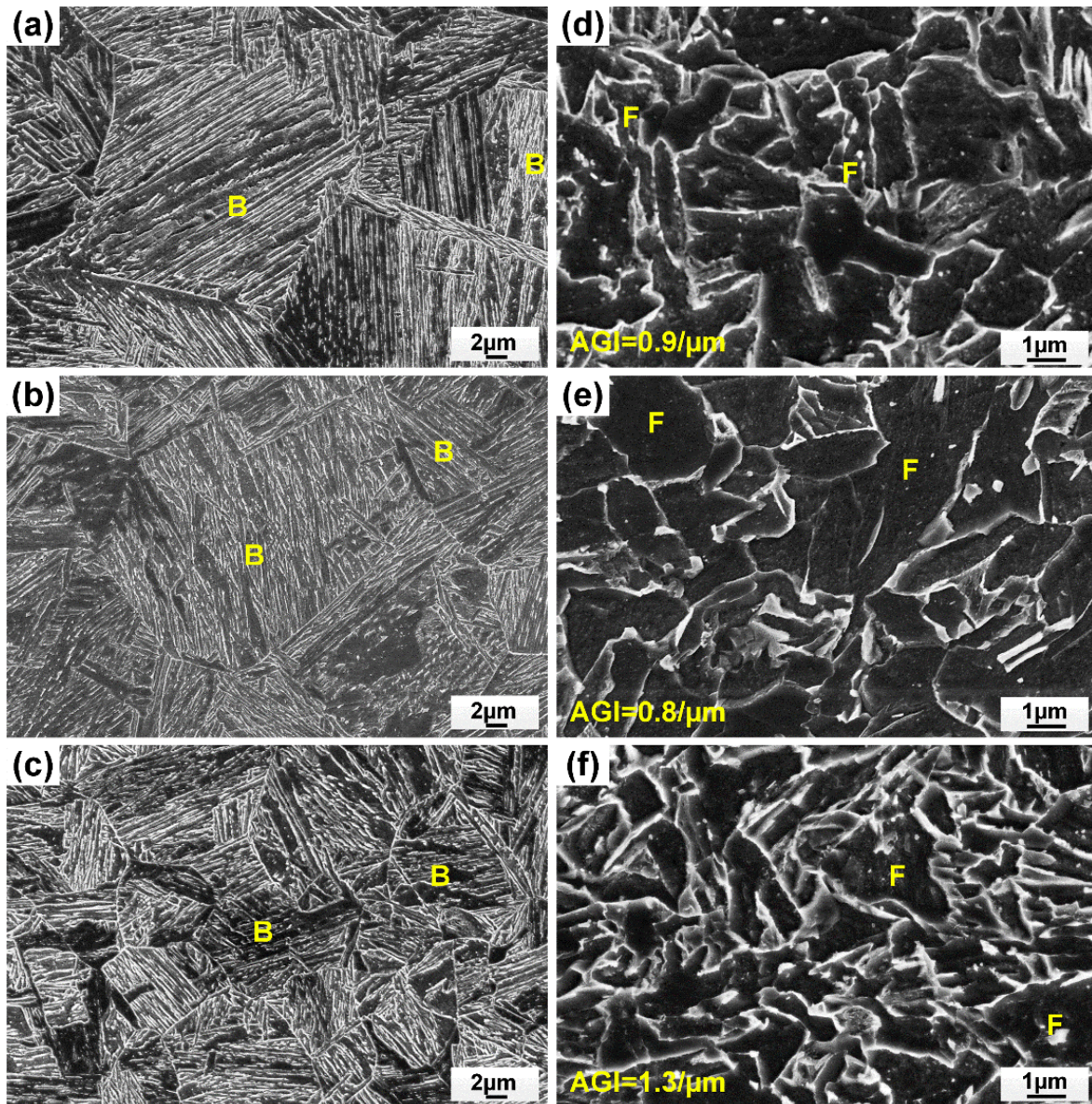


Figure 7-12. SEM micrographs showing the presence of bainite (B) and ferrite (F) in the HAZ, and the ferrite grain size was evaluated by average grain intercept (AGI) method: (a) CGHAZ of the static-spot laser weld with a welding speed of 1.0 m/min; (b) CGHAZ of the wobble laser weld with a welding speed of 1.0 m/min and a wobble amplitude of 1.0 mm; (c) CGHAZ of the static-spot laser weld with a welding speed of 1.5 m/min; (d) FGHAZ of the static-spot laser weld with a welding speed of 1.0 m/min; (e) FGHAZ of the wobble laser weld with a welding speed of 1.0 m/min and a wobble amplitude of 1.0 mm; (f) FGHAZ of the static-spot laser weld with a welding speed of 1.5 m/min.



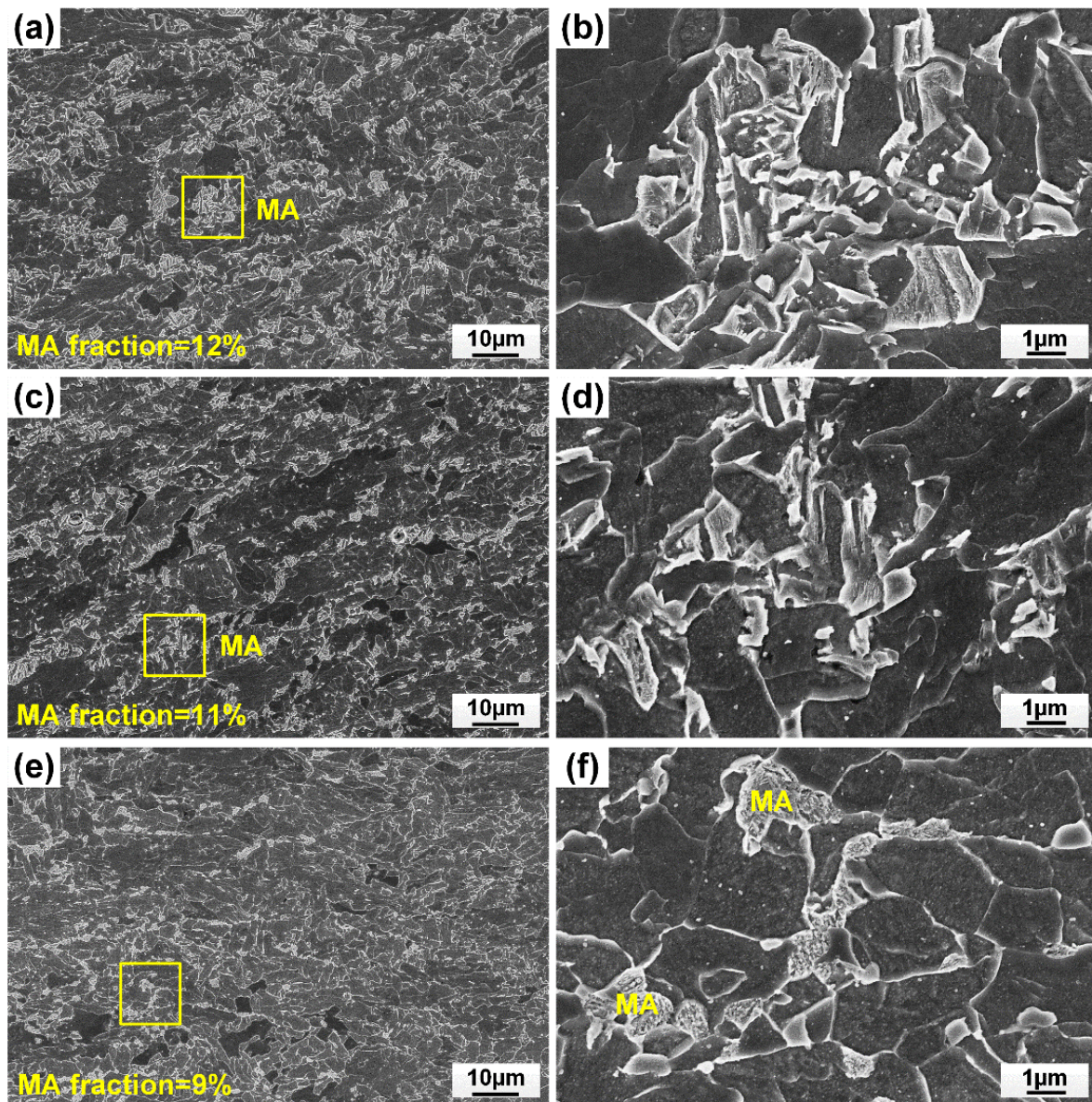


Figure 7-13. SEM micrographs showing the ICHAZ microstructure, indicating the presence of martensite-austenite (MA) island: (a) and (b) static-spot laser weld with a welding speed of 1.0 m/min; (c) and (d) wobble laser weld with a welding speed of 1.0 m/min and a wobble amplitude of 1.0 mm; (e) and (f) static-spot laser weld with a welding speed of 1.5 m/min.

## 7.6 Role of beam wobbling and travel speed on microhardness distribution

The microhardness maps of the joints with different welding parameters are shown in Fig. 7-14. For the static-laser weld with a welding speed of 1.0 m/min, the upper region of the FZ with an AF-dominated microstructure exhibited a lower hardness compared to the lower region



which contained more bainite, as shown in Fig. 7-14a. Beam wobbling led to a higher hardness in the upper region of the FZ, due to the formation of more bainite but less AF caused by the dilution of filler material, as shown in Fig. 7-14b. As the welding speed increased to 1.5 m/min, the higher cooling rate resulted in the formation of more low temperature transformation products including bainite and martensite, which led to a higher FZ hardness, as seen in Fig. 7-14c and d.

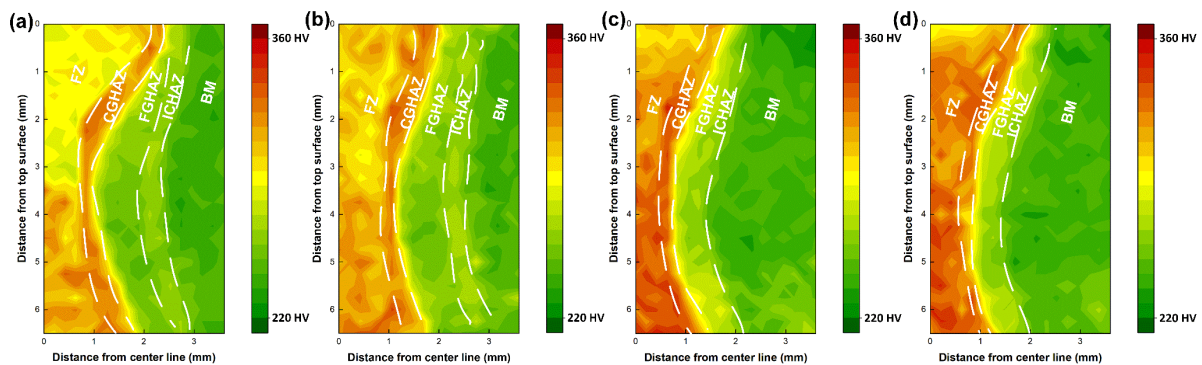


Figure 7-14. Microhardness mapping results: (a) static-spot laser weld,  $v = 1.0$  m/min; (b) wobble laser weld,  $v = 1.0$  m/min,  $A = 1.0$  mm; (c) static-spot laser weld,  $v = 1.5$  m/min; (d) wobble laser weld,  $v = 1.5$  m/min,  $A = 0.5$  mm.

The CGHAZ exhibited a hardness comparable to that of the FZ, resulting from the bainitic microstructure. At a welding speed of 1.0 m/min, a hardness peak was found in the ICHAZ with a hardness higher than that of the FGHAZ, due to the formation of MA in this region. Interestingly, as the welding speed increased to 1.5 m/min, no hardness peak in the location around 2 to 2.5 mm was found in the ICHAZ, which may be due to the formation of finer ferrite grains that led to a higher hardness in the FGHAZ.

Fig. 7-15a shows the weld metal hardness distribution along the through-thickness direction, which clearly demonstrates the hardness difference between the upper and lower regions of the FZ. The average weld metal hardness of the joints was summarized in Table 7-2. Beam wobbling increased the hardness of the upper region of the FZ at a constant welding speed. At a welding speed of 1.0 m/min, a 1.0 mm wobble amplitude led to a hardness increase

of around 15 HV in the upper region of the fusion zone. Meanwhile, an increased welding speed leads to higher FZ hardness, although within a penetration range of 0.5 mm, no significant changes were found in the FZ hardness which might be due to the wider molten pool width and slower cooling rate in this region. As the welding speed increased from 1.0 m/min to 1.5 m/min, the hardness of upper region of the FZ increased by around 26 HV. The hardness distribution of the upper side of the joints shown in Fig. 7-15b also confirmed the influence of beam wobbling and welding speed on the FZ hardness. Hardness peaks in the CGHAZ and ICHAZ can also be found on the curves shown in Fig. 7-15b.

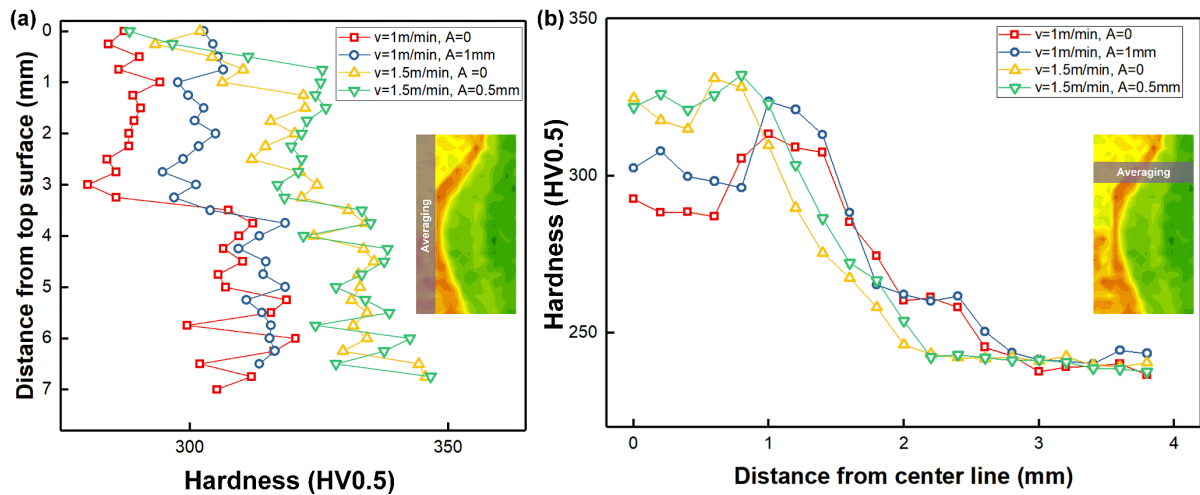


Figure 7-15. (a) Weld metal hardness distribution along the through-thickness direction; (b) Top side hardness distribution.

Table 7-2. Average hardness of the weld metal with different welding speeds and wobble conditions.

Welding speed $v$ (m/min)	Wobble amplitude $A$ (mm)	Hardness of upper region of the FZ (HV)	Hardness of lower region of the FZ (HV)
1.0	-	$287 \pm 2$	$308 \pm 2$
1.0	1.0	$302 \pm 2$	$313 \pm 1$
1.5	-	$313 \pm 3$	$333 \pm 2$
1.5	0.5	$317 \pm 3$	$333 \pm 2$

## 7.7 Local yield strength estimation

The all-weld-metal tensile test for different regions of the FZ in a laser weld would be extremely difficult due to the limited weld width, and the difficulty in distinguishing between upper and lower regions of the FZ during the sample extracting process. Instead, Midawi et al. [101] developed an evaluation method to estimate the yield strength of materials including X80 pipeline steel using a nearly flat instrumented indenter, which helped estimate the local yield strength of different regions in the FZ and HAZ of the welds. The yield strength  $\sigma_y$  can be estimated using [101]:

$$\sigma_y = F_s / (3.28\pi a^2) \quad (7-3)$$

where  $a$  is the radius of the indenter,  $F_s$  is load corresponding to the point on the obtained load-depth curve when the highest plastic strain is concentrated at the edge of the indenter and can be identified by constructing a tangent line to the curve. Fig. 7-16 shows the  $F_s$  determined for X80 base metal and the fusion zone, with the 50- $\mu\text{m}$ -diameter nearly flat indenter profile and the round-shape indentations presented. The estimated local yield strength of the upper and lower regions of the fusion zone in different laser welds is shown in Fig. 7-17. Regardless of the welding parameters, the lower region of the FZ always exhibited consistently higher yield strength, due to the presence of more bainite and martensite as shown in Fig. 7-9. At a welding speed of 1.0 m/min, beam wobbling with a 1.0 mm amplitude led to a yield strength increase of around 40 MPa in the upper region of the FZ, which is due to the formation of more bainite. As the welding speed increased from 1.0 to 1.5 m/min, the presence of more low temperature transformation products resulting from a higher cooling rate led to a 70 MPa higher yield strength in the upper region of the FZ. The yield strength of the FZ in all the welds overmatched that of the X80 base material, which met the CSA Z662 pipeline welding standard.

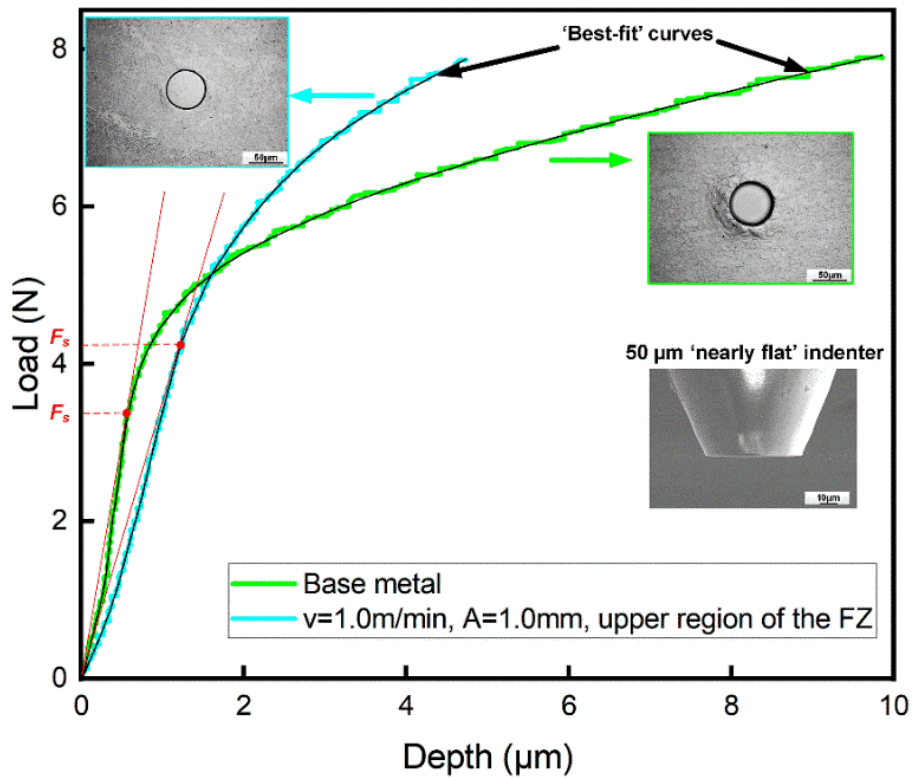


Figure 7-16. Load - depth curves obtained through indentation tests, showing the load when the highest plastic strain is concentrated at the edge of the indenter ( $F_s$ ). The indenter profile and indentation location were also presented.

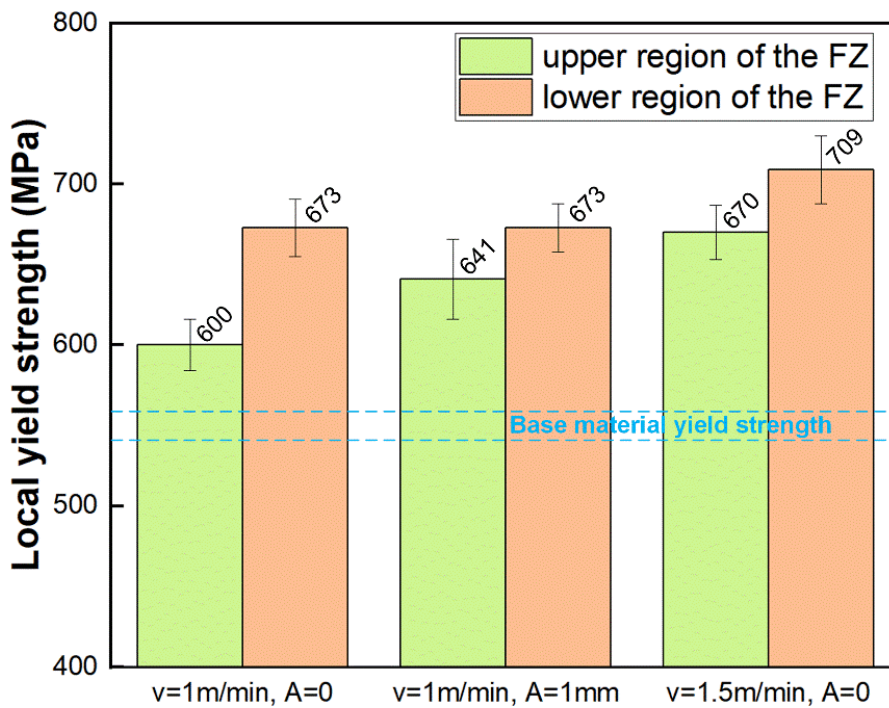


Figure 7-17. Local yield strength estimation of the FZ in the laser welds. The error bars represent a 95% confidence interval from the mean yield strength value of 5 tests.

## 7.8 Summary

The findings presented in this part of work reveal the effect of laser beam wobbling and heat input on the filler material distribution, microstructure, and mechanical properties in X80 steel laser welds. In particular:

(1) Laser beam wobbling increased the width of the fusion zone. At a welding speed of 1.0 m/min, the width of the narrowest position in the FZ increased by 31% with a wobble amplitude of 1.0 mm, compared to that of the static-laser weld.

(2) Beam wobbling increased the fraction of bainite due to the dilution effect with more melted base material in the fusion zone, and this led to an increase in the hardness of the upper region of the FZ at a constant welding speed. A hardness increase of around 26 HV in the upper region of the FZ was observed as the welding speed increased from 1.0 to 1.5 m/min, due to the formation of more low temperature transformation products.

(3) The use of beam wobbling with a 1.0 mm amplitude led to a yield strength increase of around 40 MPa in the upper region of the FZ due to the formation of more bainite. As the welding speed increased from 1.0 to 1.5 m/min, the presence of more low temperature transformation products led to a 70 MPa higher yield strength in the upper region of the FZ.



## **Chapter 8: Study in hot-wire-fed laser welding of X80 steel using beam wobbling**

### **8.1 Introduction**

The results from previous chapters show that the FZ hardness of the X80 laser welds can be reduced by feeding an ER70S-6 wire into the weld pool. However, more filler material stayed at the upper region of the FZ, leading to an inhomogeneous weld metal microstructure and an uneven hardness distribution along the through-thickness direction. Although a hot-wire-feed further reduced the FZ hardness, the hardness still exceeds the maximum value required by most industrial standards.

The wobble laser welds with cold-wire addition obtained in chapter 7 showed even higher weld metal hardness due to the dilution of filler material in the FZ, compared to static-spot laser welds. The FZ hardness of a wobble laser weld could be reduced when combined with a hot-wire feed, and the joint configuration is optimized to reduce the volume of melted base metal in the FZ. A larger root gap can be used during wobble laser welding, which is reported to enhance the filler material delivery by providing a channel to the root bottom of the molten pool and reduced the flowing resistance [29,30]. Preheating of the substrates is a common strategy for reducing the cooling rate and hardness in the FZ and HAZ of pipeline welds [117,118]. However, the softening in the fine-grained HAZ by excessive preheating could limit its application [117].

In this part of work, a wobble laser was utilized for the first time in combination with a hot-wire feed when laser welding X80 steel. The effect of substrates preheating on the cooling rate, FZ and HAZ microstructure, and hardness variation was investigated. The influence of varying root gaps on the weld metal chemistry, microstructure and hardness was also studied.

### **8.2 Experimental procedures**

An IPG YLS-8000 fiber laser was used in this part of work, with a maximum output power

of 8 kW, a focused spot size of 300  $\mu\text{m}$  and a divergence angle of around 3.3  $^\circ$ . A circular wobble pattern was achieved by an IPG D50 Wobble Head, with a wobble amplitude of 1.2 mm and a frequency of 300 Hz. A Lincoln Electric Power Wave L500 power supply was used to feed a hot-wire in front of the laser, with a wire feed rate of 12 m/min and a preheating power of 0.5 kW. A side mounted Optris PI640i thermal camera was utilized to monitor the temperature change in the FZ, with a collecting rate of 32 Hz and a temperature range of 200  $^\circ\text{C}$  to 925  $^\circ\text{C}$ . Laser welding was performed on the API 5L X80 pipeline steel, with dimensions of 250 mm  $\times$  120 mm  $\times$  14 mm. A 0.9-mm-diameter ER70S-6 wire was fed into a Y-shape groove with a 6 mm root height and a 30  $^\circ$  bevel. Varying gaps from 0.4 mm to 0.8 mm were tested to investigate the effect of root opening. Negative defocusing of -3 mm (i.e., the laser spot was focused 3 mm below the top surface) was used to enhance the penetration. Prior to welding, preheating with two temperatures (80  $^\circ\text{C}$  and 120  $^\circ\text{C}$ ) was applied to the groove area, in comparison to the welding process with no preheating. Argon was used as the shielding gas, with a flow rate of 18 L/min. The welding parameters are summarized in Table 8-1. Here, a wire feed rate of 12 m/min was used, which is the optimized parameter for the hot-wire welding process tested in chapter 5. A 300 Hz wobble frequency was selected to achieve a strong stirring effect and a stable weld pool.

Table 8-1. Welding parameters during hot-wire-fed laser welding with beam wobbling.

Sample number	Laser power $P$ (kW)	Welding speed $v$ (m/min)	Wire feed rate $WFR$ (m/min)	Wobble amplitude $A$ (mm)	Wobble frequency $f$ (Hz)	Hot-wire preheat power $P_{wire}$ (kW)	Preheat temperature $T$ ( $^\circ\text{C}$ )	Root gap $d$ (mm)
1	8	1.0	12	1.2	300	0.5	-	0.4
2	8	1.0	12	1.2	300	0.5	-	0.8
3	8	1.0	12	1.2	300	0.5	80	0.4
4	8	1.0	12	1.2	300	0.5	80	0.8
5	8	1.0	12	1.2	300	0.5	120	0.4
6	8	1.0	12	1.2	300	0.5	120	0.8

After welding, EPMA was done to analyze the elemental distribution, with a map covering the FZ, which had a step size of 10  $\mu\text{m}$ , a dwell time of 40 ms and a total collecting time of around 4.5 h. EPMA line-scanning was also done across the joint to show the silicon distribution, with a step size of 10  $\mu\text{m}$ , a dwell time of 10000 ms and a collecting time of 2 h. Microstructural analysis was done under OM and SEM. The volume fraction of the microconstituents in the FZ was calculated by point counting. Microhardness mapping was done, and the mean FZ hardness value was calculated by averaging all the indentation points (around 100 points) located in the FZ, with a 95% confidence interval presented. Peak hardness value in the CGHAZ and minimum hardness value in the FGHAZ were also identified to indicate hardening or softening phenomenon in the HAZ.

### **8.3 Cross-sectional morphologies**

Compared to a static-spot laser, a wobble laser irradiates a larger area and generates a wider molten pool, leading to an improved gap-bridging ability. As shown in Fig. 8-1, with a 0.8 mm root gap, a static-spot laser would not irradiate the base material due to the highly focused character of the laser beam, in comparison to a 1.2-mm-amplitude wobble laser which still irradiated the substrates. Less base material was melted by the laser as the root gap increased from 0.4 mm to 0.8 mm, which resulted in the reduction of weld height and less dilution of the filler material. The cross-sectional morphologies of the laser welds are shown in Fig. 8-2. Full penetration was achieved with varying root gaps, indicating good gap-bridging ability by the hot-wire fed laser welding process using beam wobbling.

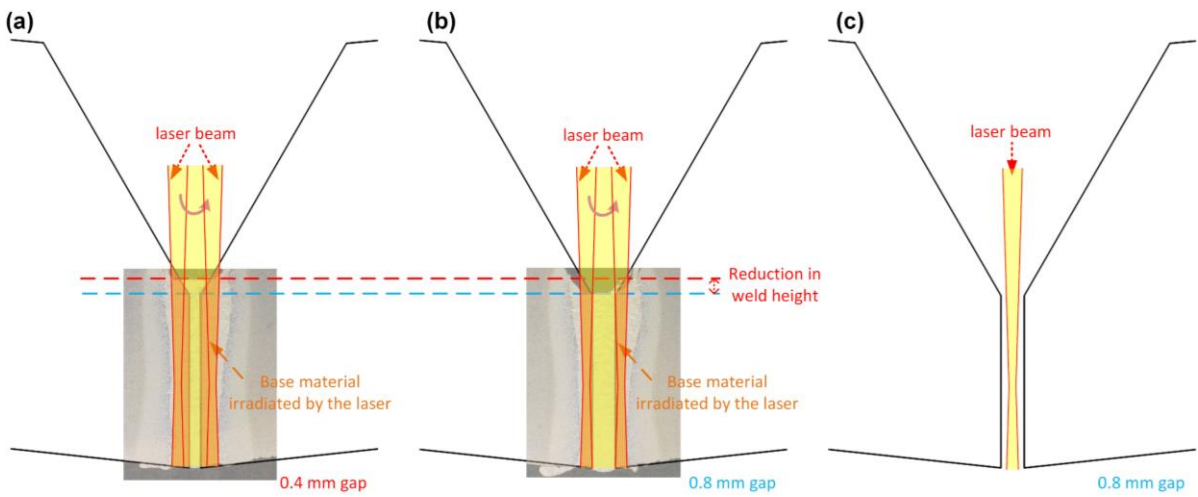


Figure 8-1. Schematics of laser-base metal interactions with different root gaps and wobbling conditions: (a) wobble laser, 0.4 mm gap; (b) wobble laser, 0.8 mm gap; (c) static laser, 0.8 mm gap.

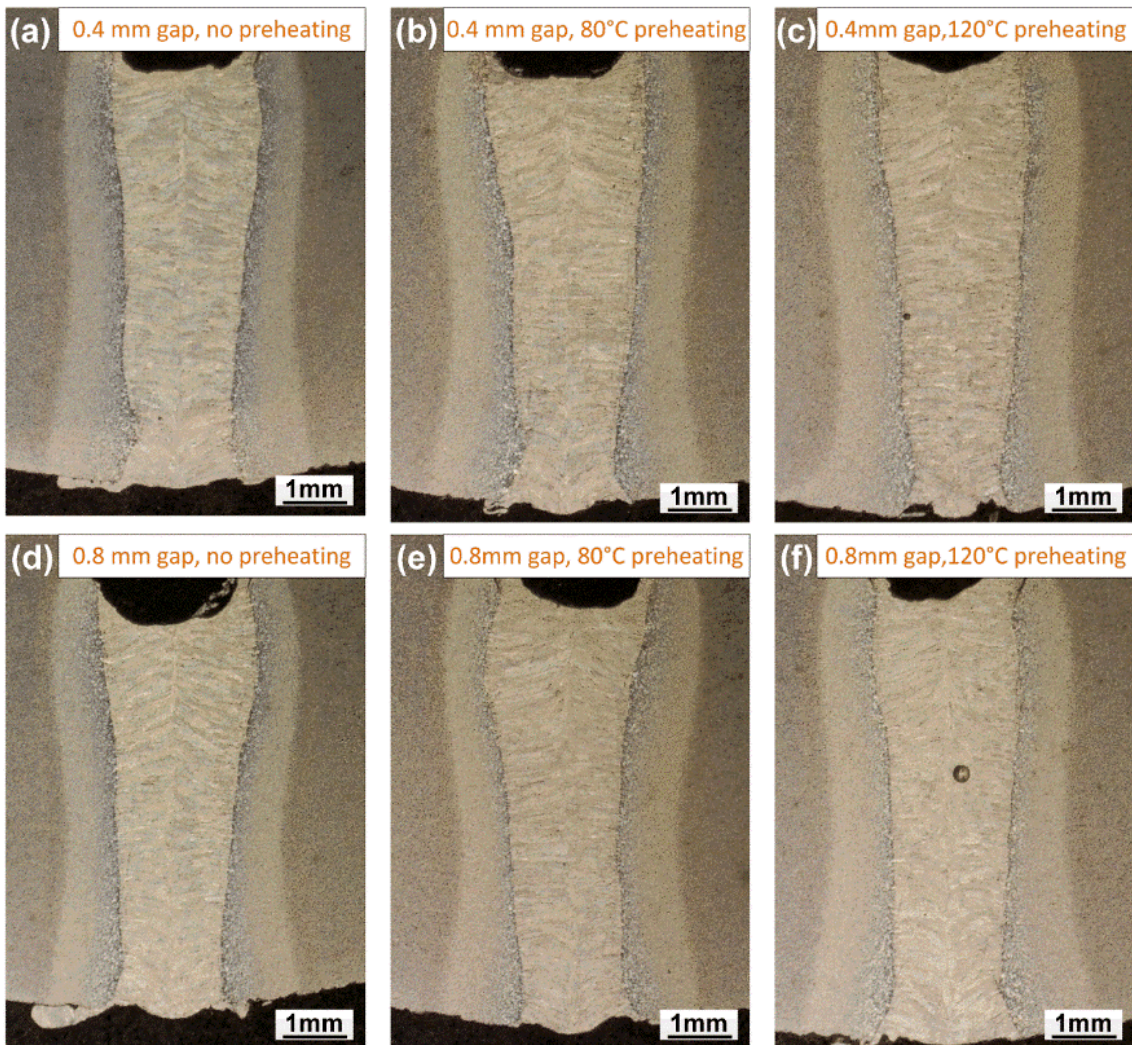


Figure 8-2. Cross-sectional morphologies of laser welds with varying gaps and preheat temperatures.

## 8.4 Elements distribution

Silicon was chosen as the ‘tracer’ element due to the different contents in the base metal and filler wire. As shown in the EPMA maps in Fig. 8-3a and b, the silicon content increased with the root gap increasing from 0.4 mm to 0.8 mm. A larger root gap reduced the volume of melted base material, and hence led to less dilution and increased the fraction of filler material in the FZ. The upper region of the FZ contained slightly more filler material since the welding wire was fed from the top of the gap. Line-scanning results in Fig. 8-3c also confirm that an increasing root gap led to a higher filler material fraction in the FZ.

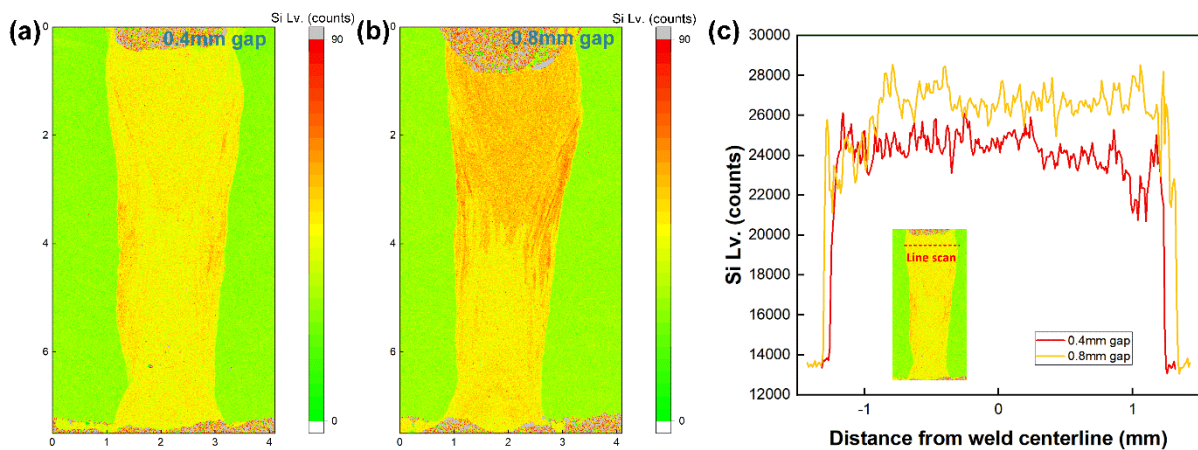


Figure 8-3. (a) EPMA map showing the distribution of Si in the weld with a 0.4 mm gap (without preheating); (b) EPMA map showing the distribution of Si in the weld with a 0.8 mm gap (without preheating); (c) EPMA line-scan results showing the distribution of Si in the welds without preheating.

## 8.5 Microstructure

SEM images in Fig. 8-4 shows the microstructure of different regions in the FZ produced with varying preheating conditions and root gaps. The weld metal had an AF dominated microstructure, along with grain-boundary ferrite (GBF), polygonal ferrite (PF) and bainite (B). Feeding an ER70S wire introduced non-metallic inclusions originating from the reaction of alloying additions including silicon, manganese, and titanium with residual oxygen in the molten pool as shown in Fig. 8-4(g-h), some of which provide favorable nucleation sites for AF [105,119]. Lower magnification OM images in Fig. 8-5 provide a clearer view of the



difference in grain-boundary ferrite or polygonal ferrite and bainite fractions between the welds with different welding parameters. Meanwhile, the volume fraction of microconstituents in the weld metal are summarized in Fig. 8-6. Preheating with a temperature of 120 °C led to the formation of more ferrite (13%) instead of low temperature transformation products, as shown in Fig. 8-5a and e. With a preheating temperature of 120 °C, the  $t_{8/5}$  (the time to cool from 800 °C to 500 °C, which determines the most important phase transformations in steels) increased by 57% (from 1.20 s to 1.88 s) compared to that with no preheating, as shown in Fig. 8-7, indicating a lower cooling rate in the FZ. Compared to a 0.4 mm root gap, a larger gap of 0.8 mm helped generate more AF but less bainite (5% compared to 12%) in the FZ, which is promoted by having less dilution of the hot-wire filler material.

The microstructures in subzones of the HAZ are shown in Fig. 8-8. The CGHAZ near the fusion line contained bainite and ferrite, which experienced a temperature above  $A_{c3}$  when complete retransformation to austenite occurred. Preheating led to the growth of prior austenite grains and the formation of more ferrite in this region, as shown in Fig. 8-8a and b. The FGHAZ also formed at a temperature above  $A_{c3}$  and was composed of fine ferrite grains. Preheating at a temperature of 120 °C resulted in the formation of coarser ferrite grains due to the slower cooling, as shown in Fig. 8-8c and d. MA was found in the ICHAZ formed between  $A_{c1}$  and  $A_{c1}$ , where partial austenization occurs and carbon enriched austenite transformed to a mixture of martensite and retained austenite, as shown in Fig. 8-8e and f.



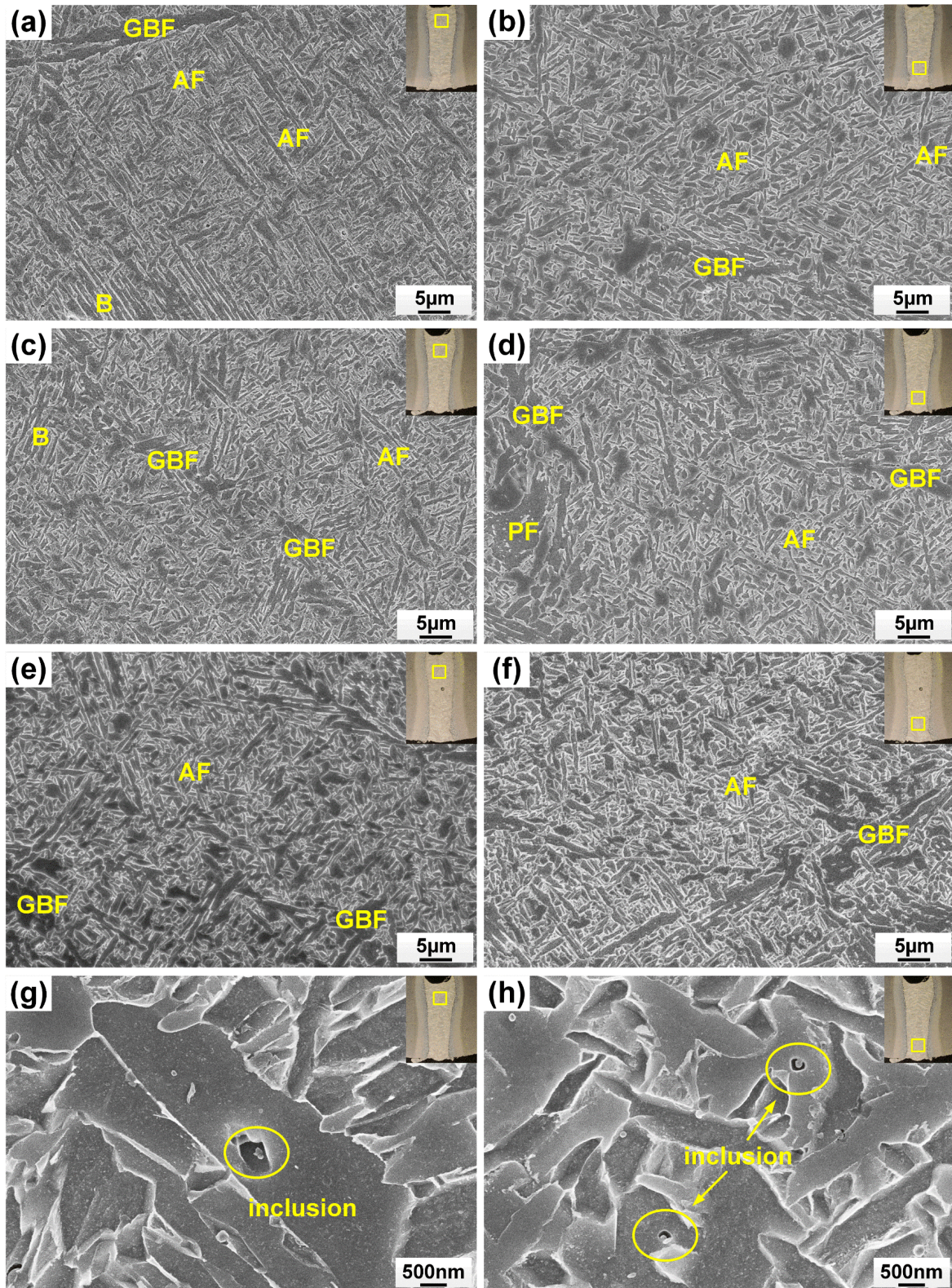


Figure 8-4. SEM images showing the microstructure in the FZ, indicating the presence of acicular ferrite (AF), bainite (B), polygonal ferrite (PF) and gran boundary ferrite (GBF): (a) and (b) 0.4 mm gap, without preheating; (c) and (d) 0.8 mm gap, without preheating; (e) and (f) 0.8 mm gap, with a preheat temperature of 120 °C; (g) and (h) 0.8 mm gap, without preheating, indicating the presence of inclusions.



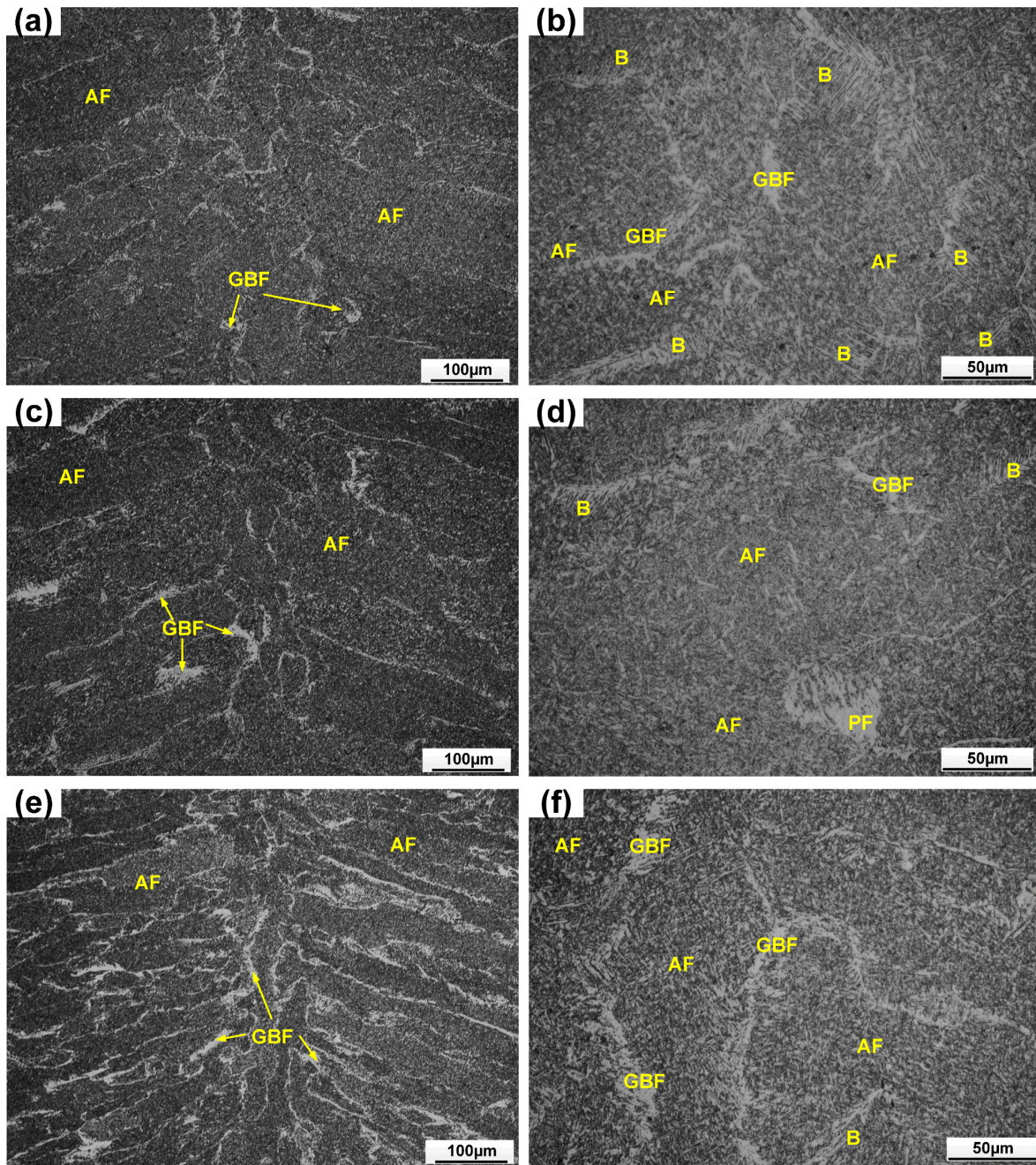


Figure 8-5. OM images showing the microstructure in the FZ, indicating the presence of acicular ferrite (AF), bainite (B), polygonal ferrite (PF) and gran boundary ferrite (GBF): (a) and (b) 0.4 mm gap, without preheating; (c) and (d) 0.8 mm gap, without preheating; (g)-(i) 0.8 mm gap, with a preheat temperature of 120 °C.

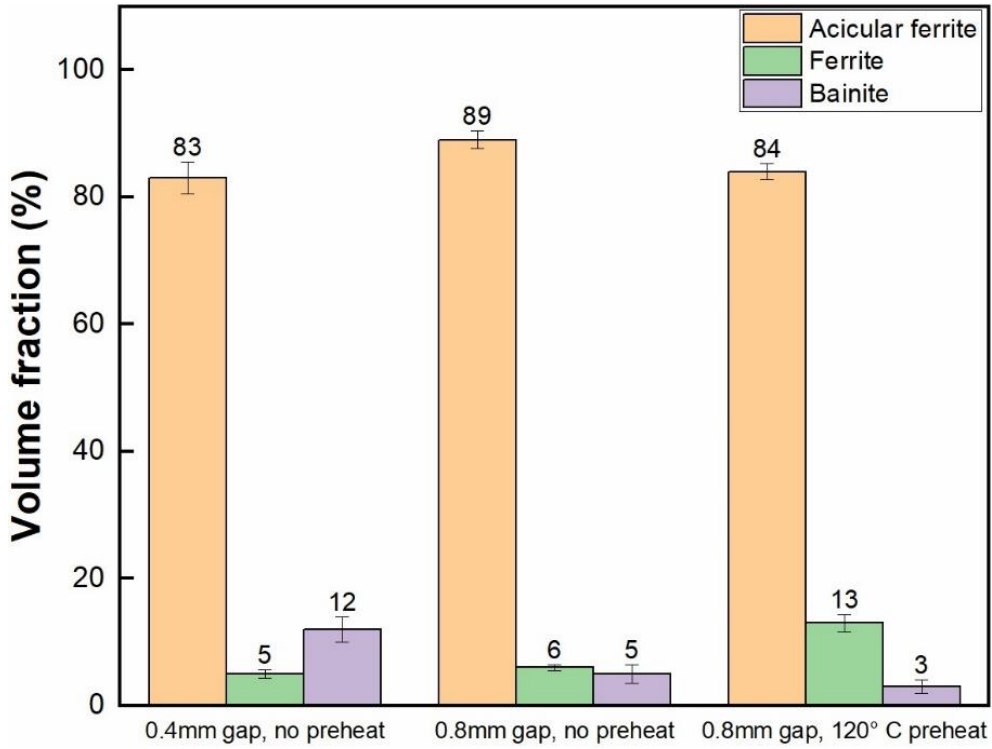


Figure 8-6. Volume fraction of microconstituents in weld metal produced using different preheats and gaps.

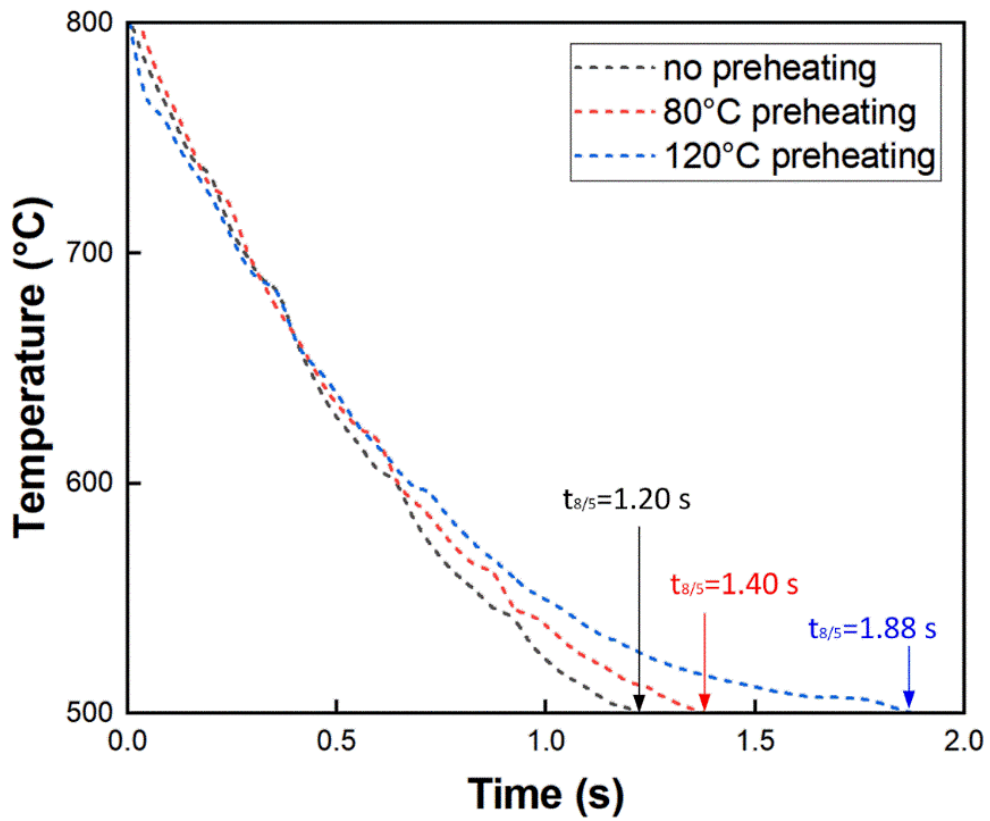


Figure 8-7. Cooling curves in the FZ with varying preheat temperatures, showing the  $t_{8/5}$  values.



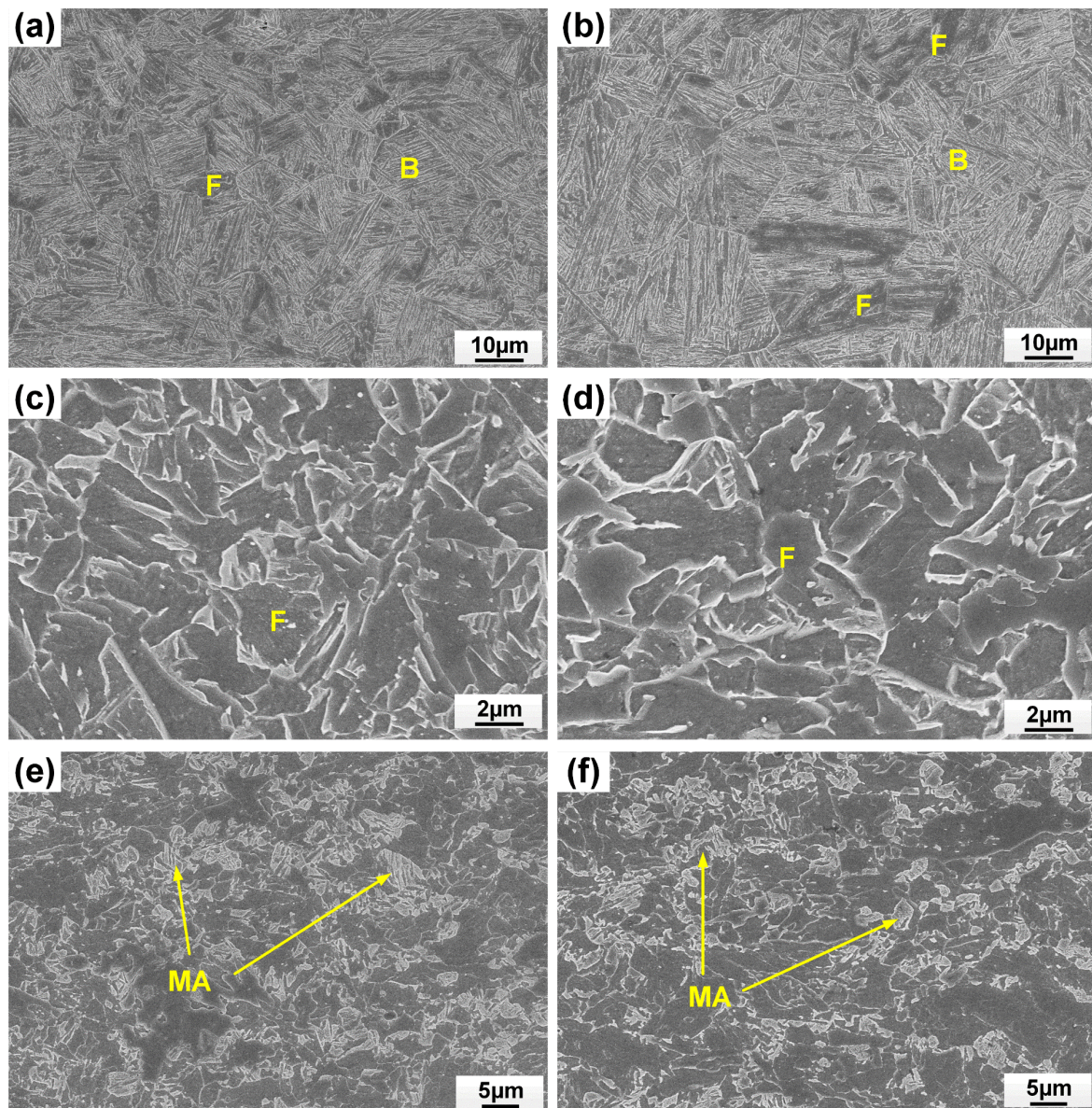


Figure 8-8. SEM images showing the HAZ microstructure, indicating the presence of ferrite (F), bainite (B) and martensite-austenite (MA) islands: (a) CGHAZ, 0.4 mm gap, without preheating; (b) CGHAZ, 0.4 mm gap, with a preheat temperature of 120 °C; (c) FGHAZ, 0.4 mm gap, without preheating; (d) FGHAZ, 0.4 mm gap, with a preheat temperature of 120 °C; (e) ICHAZ, 0.4 mm gap, without preheating; (f) ICHAZ, 0.4 mm gap, with a preheat temperature of 120 °C.

## 8.6 Microhardness

The microhardness maps are shown in Fig. 8-9, meanwhile, the mean hardness values in the FZ and subzones of HAZ are summarized in Table 8-2 and 8-3, respectively. The weld metal hardness was lower than 300 HV, which met the requirement for non-sour service pipes.



Hardness maps in Fig. 8-9 clearly show that preheating and increasing the root gap promote a reduction in FZ hardness. The all-weld-metal hardness distribution along the through-thickness direction in Fig. 8-10 also confirmed that the welds with a preheat temperature of 120 °C always exhibited a lower FZ hardness regardless of root gaps, the mean value of which is around 13 HV lower compared to those without preheating, due to the formation of more ferrite but less low temperature transformation products. As shown in Fig. 8-11, the welds with a root gap of 0.8 mm always showed a lower FZ hardness, due to the presence of less bainite resulting from less dilution of the filler material. Preheating with a temperature of 120 °C also reduced the hardness of CGHAZ by 17 HV (Fig. 8-12a) due to the formation of more ferrite, and the hardness of FGHAZ by 12 HV (Fig. 8-12b) due to the growth of ferrite grains. It should be noted that a softened region was found in the FGHAZ with a preheat temperature of 120 °C, the hardness of which is lower than that of the base metal, as shown in Fig. 8-12b. Although this small, softened zone might not affect the large-scale properties, caution is required when choosing a preheat temperature higher than 120 °C.

Table 8-2. Mean hardness values in the FZ with different preheat temperatures and root gaps (HV).

	<i>d</i> =0.4 mm	<i>d</i> =0.8 mm
<i>T</i> =0	296±1	290±2
<i>T</i> =80 °C	290±2	282±1
<i>T</i> =120 °C	284±2	277±1

Table 8-3. Mean hardness values in the HAZ with different preheat temperatures (HV).

	CGHAZ	FGHAZ
<i>T</i> =0, <i>d</i> =0.4 mm	332±3	260±2
<i>T</i> =80 °C, <i>d</i> =0.4 mm	325±3	254±2
<i>T</i> =120 °C, <i>d</i> =0.4 mm	315±3	248±2

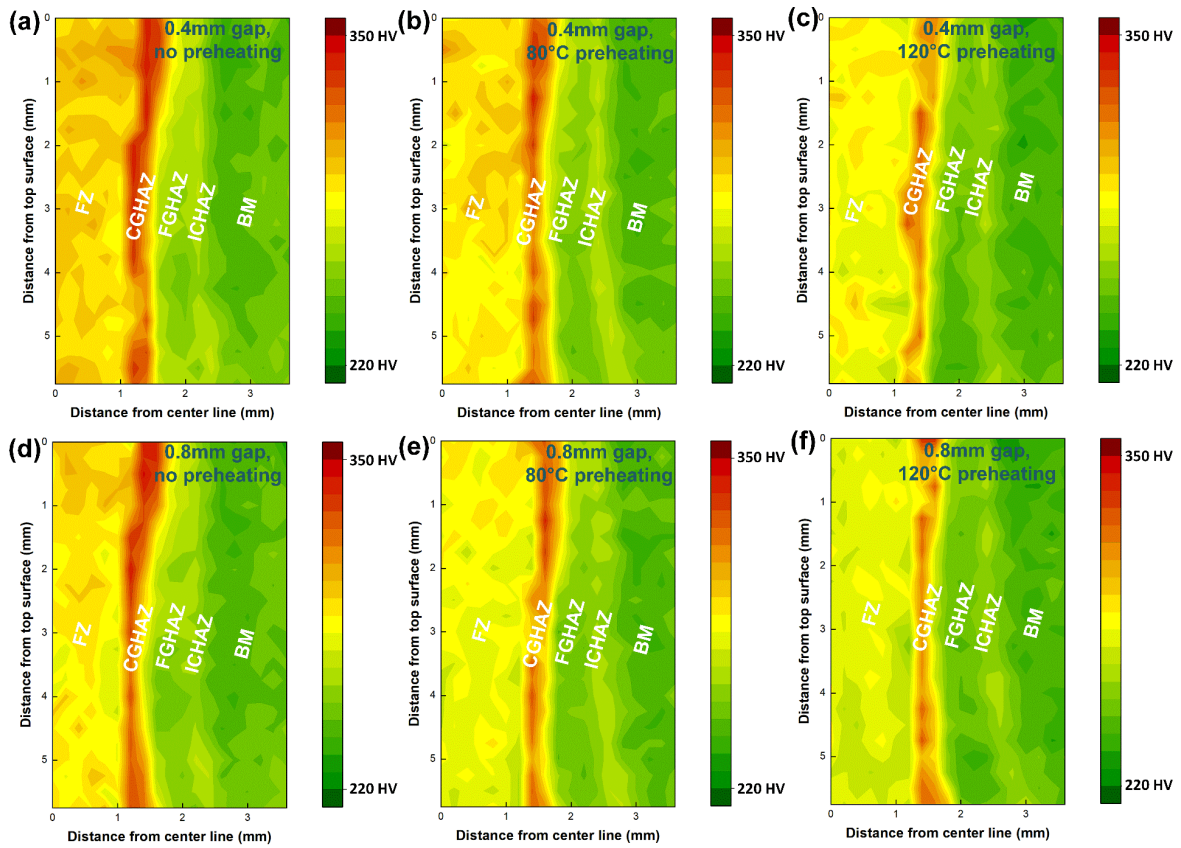


Figure 8-9. Microhardness maps of the welds with varying root gaps and preheat temperatures.

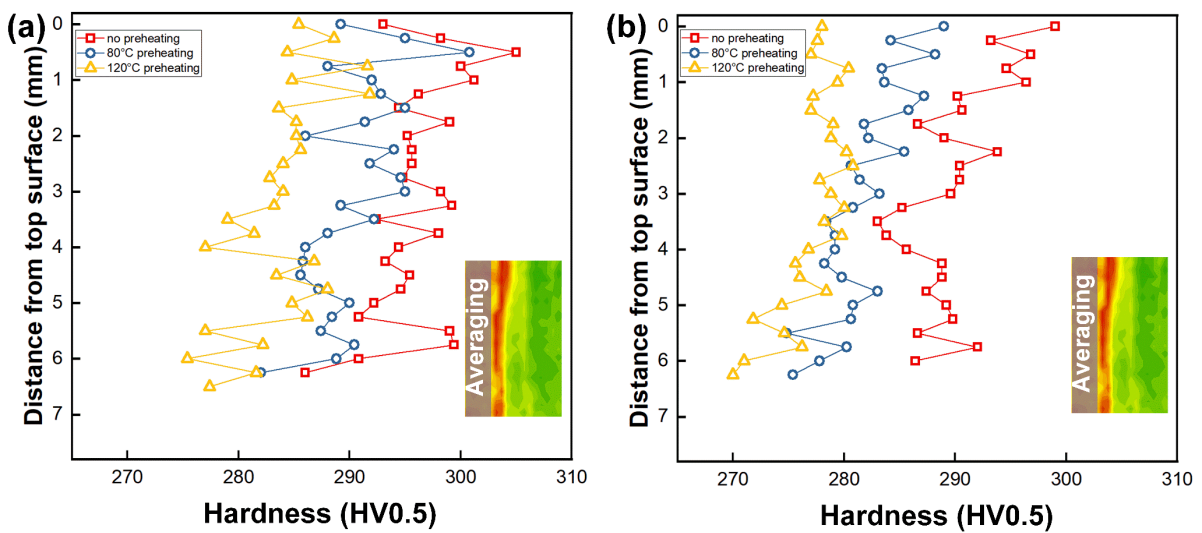


Figure 8-10. FZ hardness changes with preheat temperature: (a) welds with a 0.4 mm gap; (b) welds with a 0.8 mm gap.

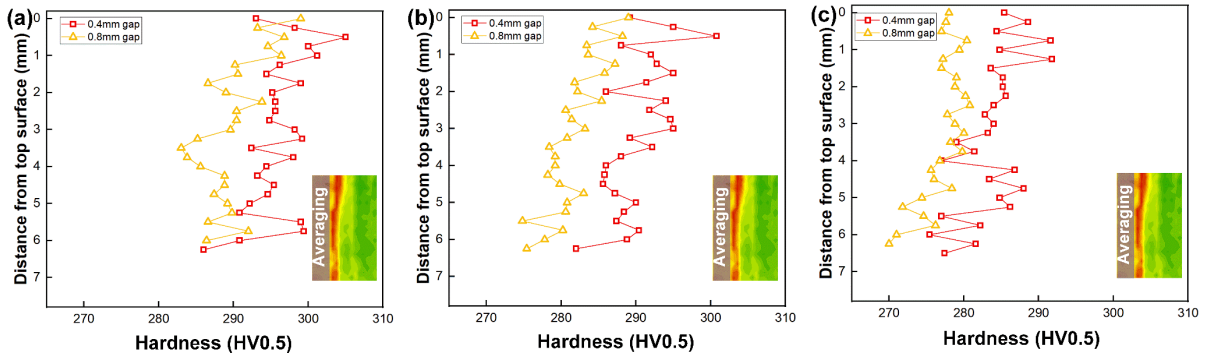


Figure 8-11. FZ hardness changes with root gap: (a) welds without preheating; (b) welds with a preheat temperature of 80 °C; (c) welds with a preheat temperature of 120 °C.

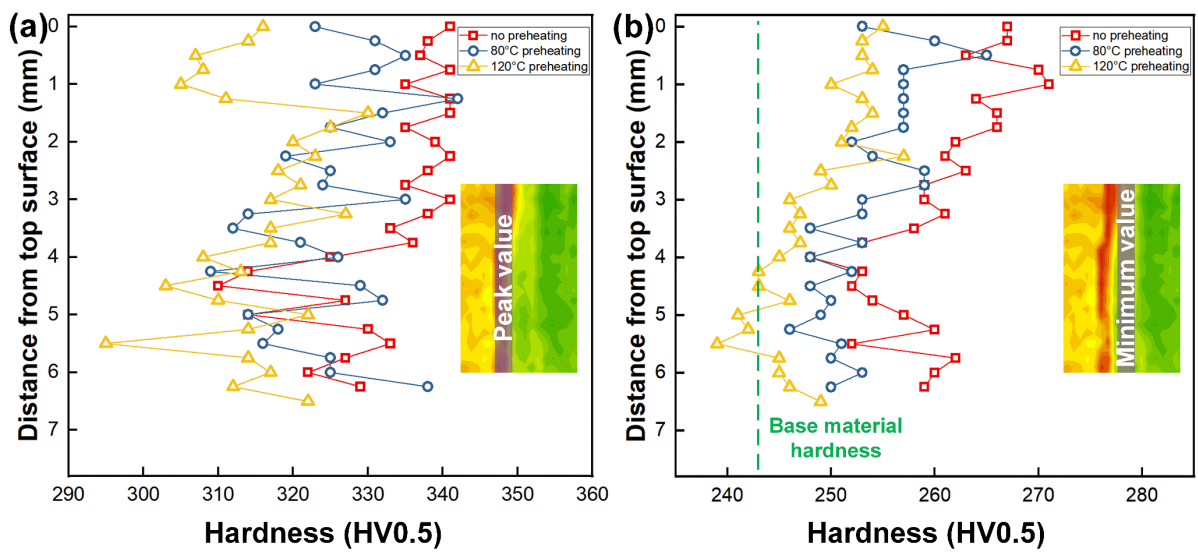


Figure 8-12. HAZ hardness distribution of the welds with a 0.4 mm root gap: (a) CGHAZ; (b) FGHAZ.

## 8.7 Conclusions

The findings presented in this part of work reveal the effect of substrates preheating and varying root gaps on the microstructure and hardness during a hot-wire-fed laser welding of X80 steel using beam wobbling. It has been shown that:

- (1) Preheating with a temperature of 120 °C reduced the cooling rate in the FZ and decreased the  $t_{8/5}$  by 57%, which led to the formation of more ferrite and reduced the weld metal hardness by around 13 HV.

(2) A preheat temperature of 120 °C limited the hardness of CGHAZ with a reduction of 17 HV, due to the formation of more ferrite in this region. It also reduced the FGHAZ hardness by 12 HV resulting from the growth of the ferrite grains.

(3) Compared to a smaller root gap of 0.4 mm, a gap of 0.8 mm limited the dilution of alloying elements from the filler wire, due to the reduced volume of melted base metal. This helped limit the formation of bainite and reduce the weld metal hardness.

(4) The laser welds obtained in this chapter met the hardness requirement for non-sour service pipeline, which is targeted to be lower than 300 HV.

## **Chapter 9: Effect of filler wire composition on weld metal in X80 steel laser welds**

### **9.1 Introduction**

The hot-wire-fed wobble laser welds obtained in chapter 8 exhibited a FZ hardness that met the requirement for non-sour service pipeline, while the hardness still exceeded the maximum value required for sour-service pipes, which are filled with substances that contains hydrogen sulfide and thus prone to hydrogen induced cracking or sulfide stress cracking [5]. The microstructure and mechanical properties of the laser welds depends on both the thermal history and the alloying composition of the weld metal. Diluting the alloying elements in the FZ by feeding a wire with a lower carbon equivalent could further lower down the FZ hardness with the optimized welding procedures developed in previous chapters.

Autogenous laser welding of thick carbon steel presents certain technical difficulties, notably a reduced capability for bridging gaps effectively, especially when using a fine laser spot size ( $< 1\text{mm}$ ), and the high cooling rate which may promote formation of hard and brittle microstructures in the fusion zone. These limitations can be overcome by adding a filler wire into the weld pool. However, the majority of commercial wires are developed and optimized for conventional arc welding processes like GMAW and SAW. The results from previous chapters show that introducing an ER70S-6 wire during laser welding of X80 pipeline steel led to the formation of acicular ferrite and bainite in the weld metal, with a higher hardness than that required by API standard for pipes used in sour gas applications (not exceed 275 HV). Midawi et al. [104] investigated the influence of wire chemistry in X80 steel GMAW welds, and showed that in the case of mechanized narrow-gap joints, they are particularly sensitive to the higher carbon equivalent since this will promote higher weld metal hardness.

Previous results showed that the deep and narrow FZ geometry of a laser weld led to an uneven distribution in filler metal alloy elements along the through-thickness direction. It has been shown that a nickel-based wire can be used to trace the filler material distribution during



hybrid laser-arc welding of 20-mm-thick steel plates [120], and the homogeneity and dilution of the filler wire can be revealed by utilizing EDS. In addition, nickel can promote solid solution hardening of ferrite, and influence the microstructure by suppressing the  $\gamma$  to  $\alpha$  transformation [121]. Mao et al. [122] found that 2% to 6% Ni promoted the formation of more low temperature transformation products, including acicular ferrite and lath martensite instead of polygonal ferrite. For example, the weld metal contained up to 75% martensite with a nickel content of 6% [122].

In the first part of this chapter, a pure iron wire was fed during static-spot laser welding of X80 steel to dilute the alloying elements from the base metal plate in the fusion zone. A pure nickel wire was also used to help indicate the dilution of filler material in the fusion zone. These filler wires were also compared to an autogenous and an ER70S-wire-fed laser weld to provide a comprehensive comparison of the role of FZ chemistry. In the second part, two ER70S steel wires with different carbon equivalents were used during hot-wire-fed wobble laser welding, with the optimized parameters obtained in chapter 8. The influence of wire chemistry on the microstructure and mechanical properties was studied, and the process-structure-property relationships are discussed in detail.

## **9.2 Experimental procedures**

All the welds were performed on X80 steel, with a laser power of 8 kW and a travel speed of 1 m/min. A 'Y'-shaped groove design was chosen with a 30-degree bevel and a 6 mm root height. A -3 mm defocused distance was used such that the laser beam focused below the top surface. The shielding gas used was pure argon, with a flow rate of 18 L/min.

For static-spot laser welding, a 1.2-mm-diameter laser spot was used. No root gap was used during autogenous laser welding, while a 0.4 mm gap was used for wire-fed laser welding process. An ER70S-6 steel, a 99.95% pure iron and a 99% pure nickel wire were used, and the diameter of the welding wires was 0.9 mm for all wires used here. The welding parameters are

summarized in Table 9-1. EDS was done to show the elements distribution in the FZ. SEM was utilized for microstructural analysis. Microhardness tests were done to reveal the hardness difference in different regions of FZ.

Table 9-1. Welding parameters during static-spot laser welding with different wires.

Sample number	Laser power $P$ (kW)	Welding speed $v$ (m/min)	Wire feed rate $WFR$ (m/min)	Wire type	Wire diameter $d$ (mm)	Defocused distance $D_f$ (mm)
1	8	1.0	-	-	-	-3
2	8	1.0	6	ER70S-6	0.9	-3
3	8	1.0	6	Pure iron (99.95%)	0.9	-3
4	8	1.0	6	Pure nickel (99%)	0.9	-3

For the wobble laser welding process, a 0.3-mm-diameter laser spot was used. A 0.8 mm root gap was used based on the optimized conditions obtained in Chapter 8. The X80 substrates were preheated to 120 °C prior to welding. A laser power of 8 kW and a welding speed of 1 m/min were used. Two types of carbon steel wires (ER70S-6 and ER70S-2) with a diameter of 0.9 mm were fed in front of the laser, with a WFR of 12 m/min and a wire-preheat power of 0.5 kW. After welding, the FZ microstructure was compared under SEM, microhardness and Charpy impact tests (at 0 °C, -20 °C and -45 °C) were done to reveal the differences in mechanical properties.

### 9.3 Effect of feeding pure iron and nickel wires

#### 9.3.1 Cross-sectional morphologies

The morphologies of the weld cross-sections are shown in Fig. 9-1. Deep and narrow laser welds were obtained, and full penetration was achieved. Fig. 9-2 provides a clearer view of the weld with nickel wire, showing the presence of fine centerline crack in the upper region of the FZ. A high nickel fraction (> 25%) could lead to a fully austenite microstructure based on the Schaeffler diagram [123], which increases the hot cracking sensitivity in steels due to its poor

thermal conductivity and high coefficient of thermal expansion, and the lower solubility for sulfur, phosphorus, silicon and boron elements in austenite which form a low melting point eutectic liquid along grain boundaries that leads to solidification cracking under shrinkage strain [124]. The high welding speed during laser welding leads to a rapid solidification and imposes thermal tensile strains on the residual liquid due to solidification shrinkage. If the strain exceeds the ductility of the liquid containing solidifying grain boundaries, they would be pulled apart and cracks form in the FZ during solidification [125,126].

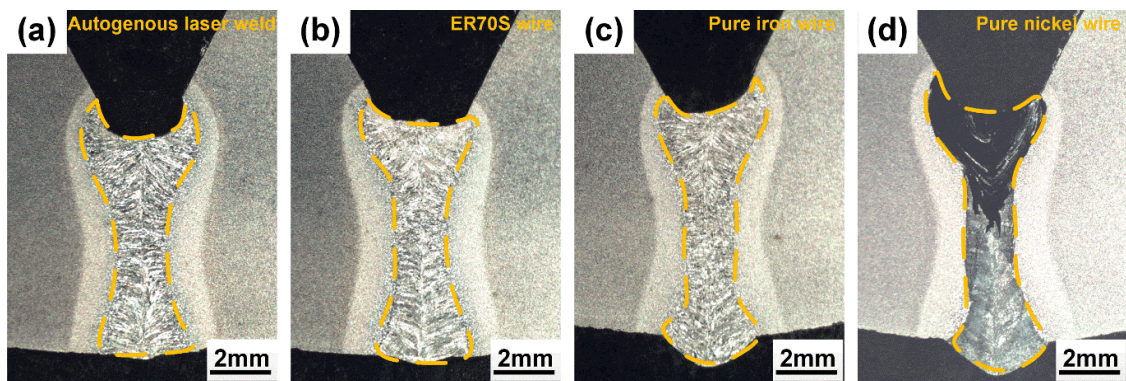


Figure 9-1. Cross-section morphologies: (a) autogenous laser weld; (b) laser weld with ER70S wire; (c) laser weld with pure iron wire; (d) laser weld with nickel wire.

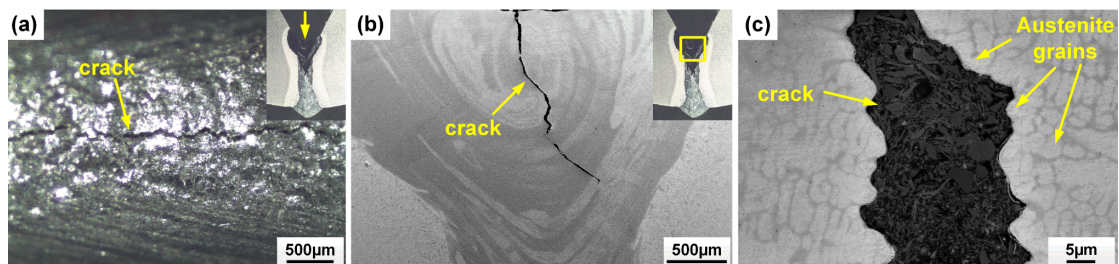


Figure 9-2. (a) top surface of the laser weld with pure nickel wire, showing the presence of crack; (b) and (c) SEM images of cross-sectional morphology of the laser weld with pure nickel wire, showing the presence of crack in the upper region of the FZ.

### 9.3.2 Filler material distribution and FZ microstructure

The nickel distribution along the through-thickness direction in the laser weld with pure nickel wire, as shown in Fig. 9-3, demonstrates the filler material dilution in the laser welds. A

higher nickel fraction was found in the upper region of the FZ, compared to the lower region, indicating an uneven distribution of the filler material. The upper and lower region of the FZ contained around 34% and 11% of the filler material, respectively. In this case, the expected element fractions can be evaluated by

$$C = 34\% C_{wire} + 66\% C_{BM} \quad (9-1)$$

in the upper region of the FZ, and

$$C = 11\% C_{wire} + 89\% C_{BM} \quad (9-2)$$

in the lower region of the FZ, where  $C_{wire}$  is the weight fraction of the element in the filler wire, and  $C_{BM}$  is the fraction in the X80 base material. The above calculated dilutions might have deviation for other steel wires due to different melting point, viscosity, and surface tension, but they provided a guideline for estimating and understanding dilution during laser welding.

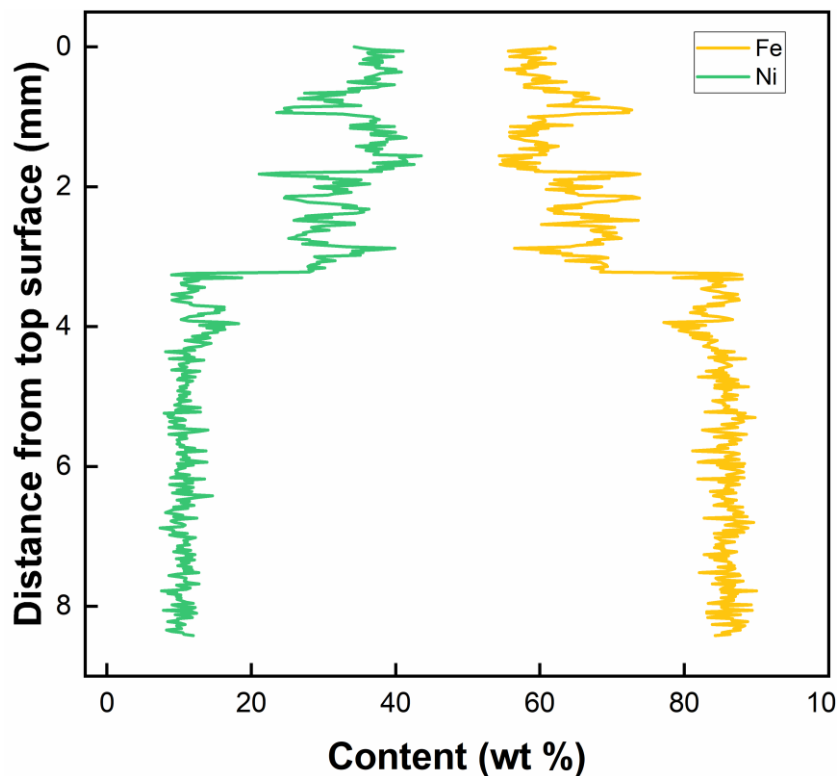


Figure 9-3. EDS results showing the distribution of Ni and Fe in the laser weld with pure nickel wire.

Fig. 9-4 shows the microstructure of upper and lower regions of FZ in the welds with different filler material. Meanwhile, the volume fraction of microconstituents in the FZ is

summarized in Fig. 9-5. Resulting from a high cooling rate of laser welding, the weld metal in the autogenous laser weld had a bainite dominated microstructure (with a volume fraction of around 66%), as shown in Fig. 9-4a and b. The addition of ER70S wire helped to generate more AF in the weld metal (Fig. 9-4c and d), which is generally considered the preferred microstructure in pipeline welds due to the high toughness, high strength, and ductility attributed to the fine interlocking grain structure [104,106]. Specifically designed for carbon steels, ER70S wire can introduce non-metallic inclusions like silicon-, titanium- or manganese-based oxides into the weld metal, which act as the favorable nucleation sites for forming intragranular AF [48,105].

As shown in Fig. 9-4e and f, the addition of pure iron wire diluted the alloying elements in the FZ, and led to the formation of more polygonal and coarse-grained ferrite in the weld metal. Compared to low temperature transformation products, these constituents in the FZ will reduce the weld metal hardness and strength. However, coarse-grained ferrite may deteriorate low temperature toughness due to the decreased density of grain boundaries that promote crack deviation during brittle fracture [127]. A possible approach to mitigate the formation of coarse-grained ferrite may be to utilize a wobble laser, which is able to effectively refine the grain structure and improve the intermixing of elements in the molten pool [23,24,26,102].

Fig. 9-4g shows that a high nickel fraction (34%) in the upper region of the FZ in the laser weld with nickel wire led to the formation of austenite, as nickel is a strong austenite stabilizer in steels. Columnar grains formed near the fusion line side, which grew along the direction of the temperature gradient. In contrast, equiaxed grains formed near the weld centerline, due to the decreased temperature gradient in this region. For the lower region of the FZ, the presence of 11% nickel was not sufficient to form austenite but would still lower the austenite to ferrite transformation temperature, and led to the formation of lath martensite (LM). One can expect a considerable difference in the local mechanical properties between the upper and lower



regions of the FZ when using nickel filler wire.

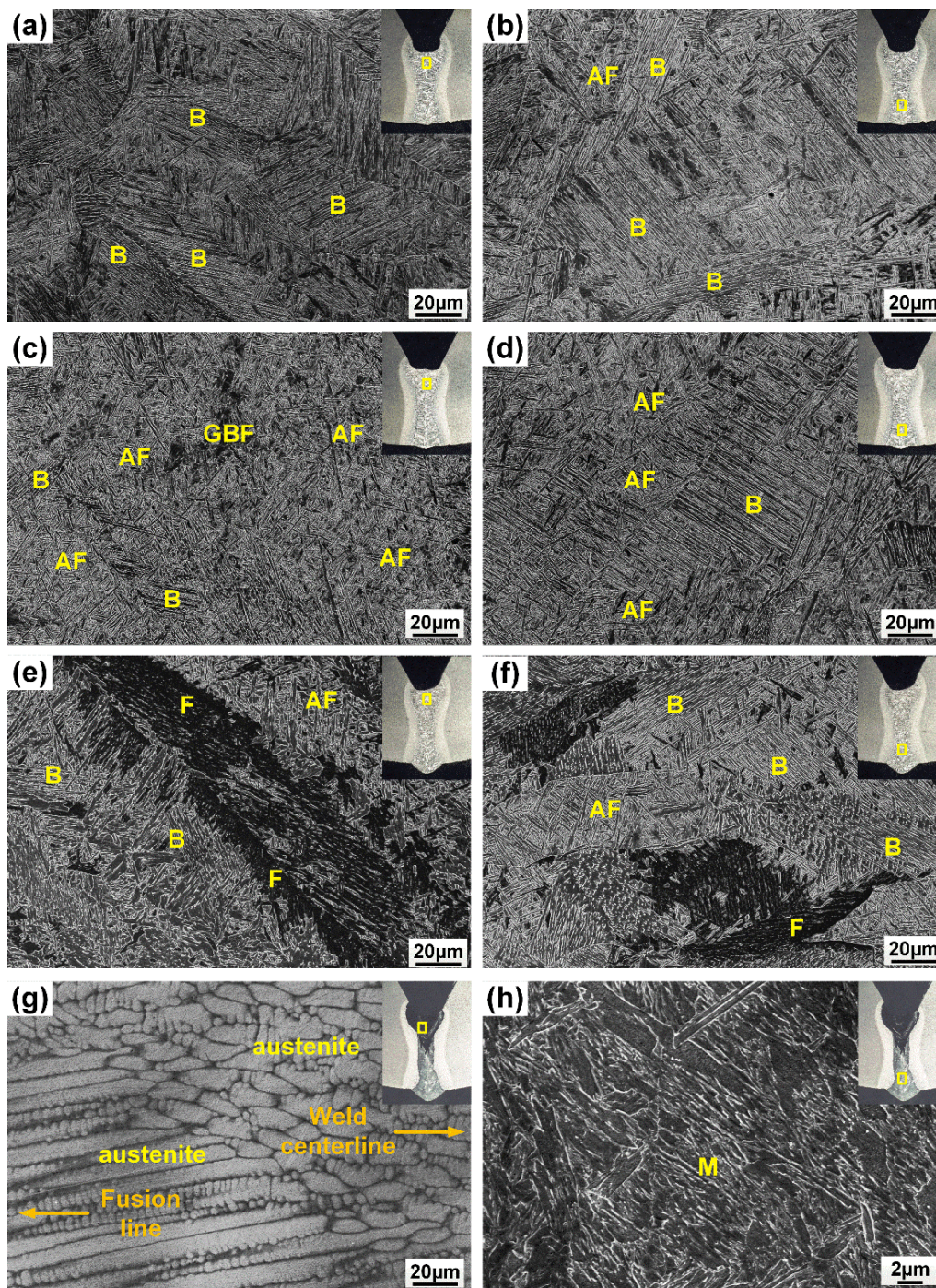


Figure 9-4. SEM images showing the microstructure and locations of acicular ferrite (AF), ferrite (F), bainite (B), austenite and martensite (M) in: (a) upper region of the FZ in autogenous laser weld; (b) lower region of the FZ in autogenous laser weld; (c) upper region of the FZ in the laser weld with ER70S wire; (d) lower region of the FZ in the laser weld with ER70S wire; (e) upper region of the FZ in the laser weld with pure iron wire; (f) lower region of the FZ in the laser weld with pure iron wire; (g) upper region of the FZ in the laser weld with pure nickel wire; (h) lower region of the FZ in the laser weld with pure nickel wire



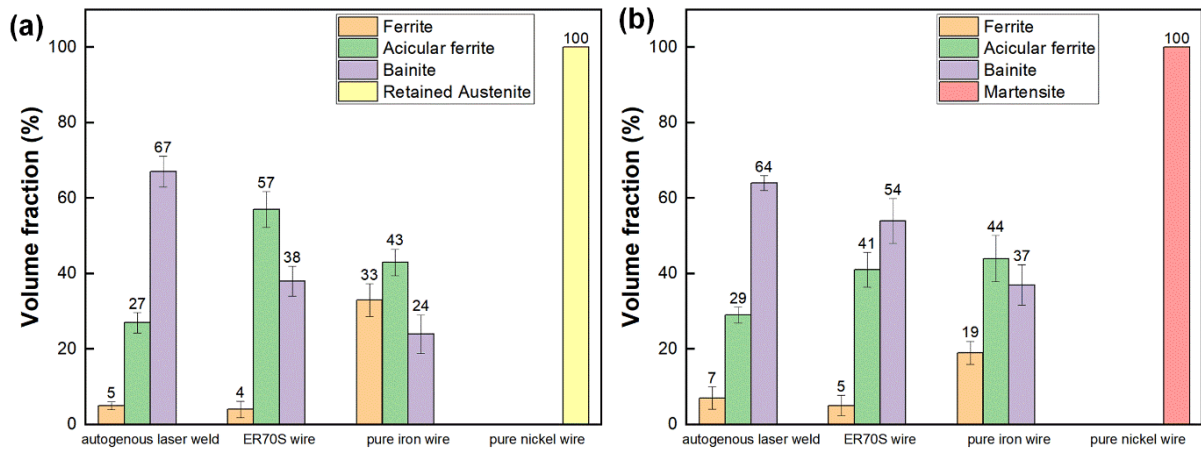


Figure 9-5. Volume fraction of microconstituents within the fusion zone: (a) upper region; (b) lower region.

### 9.3.3 FZ hardness

The hardness maps and weld metal hardness distribution along the through-thickness direction are shown in Fig. 9-6 and 9-7, respectively. Meanwhile, the average hardness values in different locations of the welds are also summarized in Table 9-2. Compared to the autogenous laser weld, the addition of ER70S wire led to a minor decrease in the hardness of upper region of the FZ, and both the autogenous and ER70S-wire-fed laser welds exhibited a hardness higher than the maximum value required by API 5L for sour-service pipes (275 HV). It is worth noting that no preheat was applied here in order to achieve a high productivity. However, preheat may help reduce the FZ hardness and is a common strategy in pipeline industry. As shown in Fig. 9-6c and d, uneven hardness distribution along the through-thickness direction was found in the welds with iron and nickel wire addition, due to the inhomogeneous microstructure. Introducing pure iron wire into the FZ reduced the weld metal hardness from an average of 328 HV to 237 HV in the upper region and an average from 314 HV to 267 HV in the lower region, due to the formation of more ferrite. The reduced carbon equivalent caused by the dilution of the elements could also contribute to the decreased weld metal hardness. In comparison with other welds, the weld with iron wire exhibited a hardness closer to that of the X80 base metal and does not exceed the maximum value limited by the API standard.

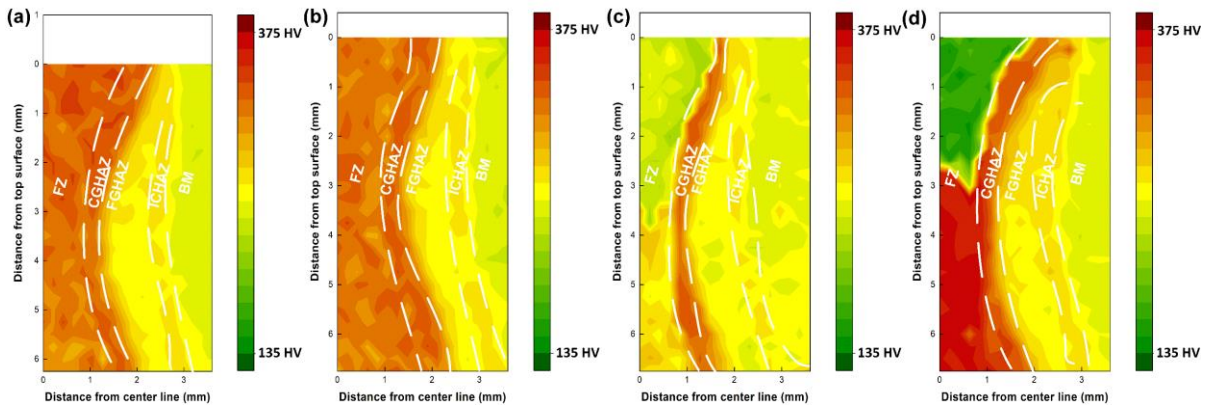


Figure 9-6. Hardness mapping results of: (a) autogenous laser weld; (b) laser weld with ER70S wire; (c) laser weld with pure iron wire; (d) laser weld with nickel wire.

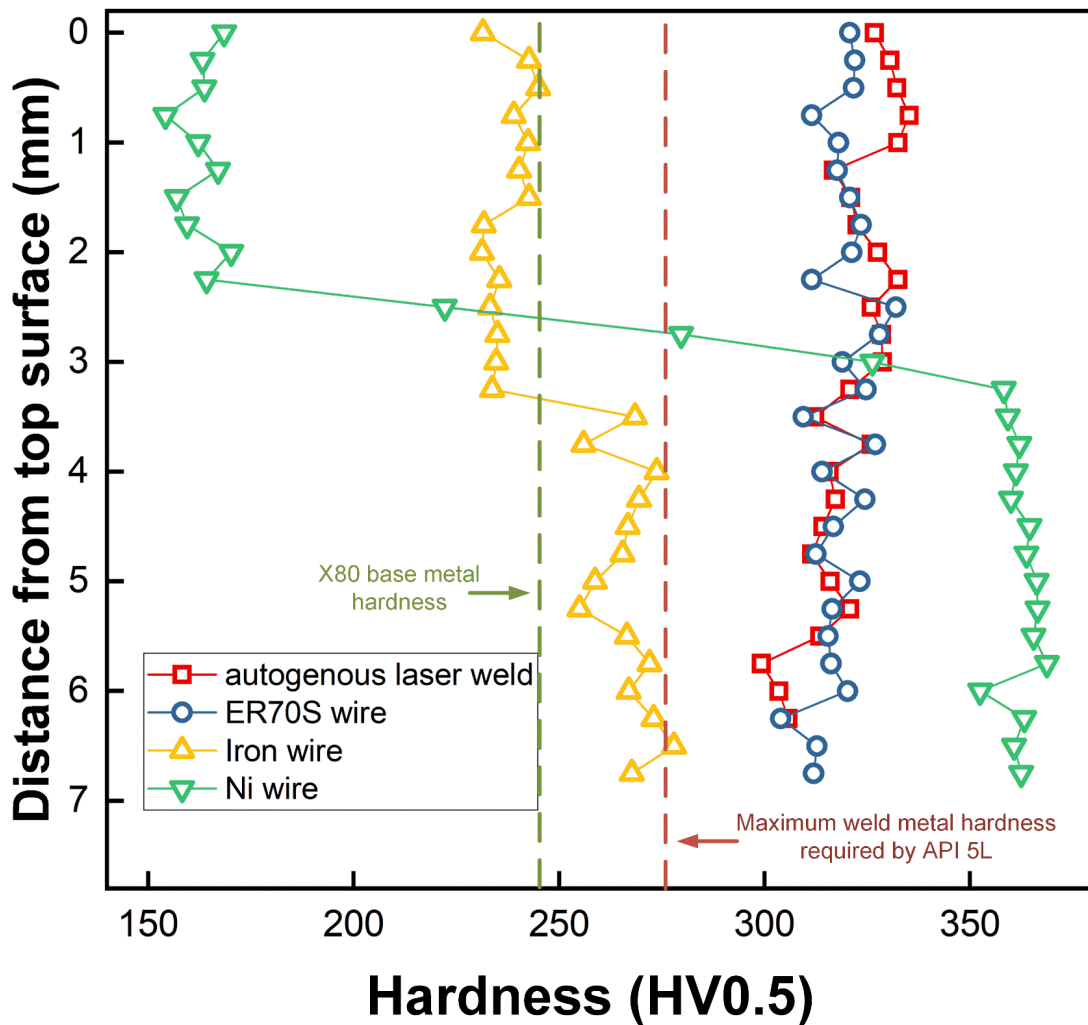


Figure 9-7. Weld metal hardness distribution along the through-thickness direction.

Table 9-2. Average hardness in different locations of the joints.

	Upper region of the fusion zone	Lower region of the fusion zone	Base metal
Autogenous laser weld	328 ± 1 HV	314 ± 2 HV	-
Laser weld with ER70S wire	321 ± 1 HV	317 ± 2 HV	-
Laser weld with pure iron wire	237 ± 1 HV	267 ± 2 HV	-
Laser weld with pure nickel wire	163 ± 1 HV	362 ± 1 HV	-
X80 base metal	-	-	243 ± 1 HV

The upper region of the fusion zone in the weld with nickel wire had an average hardness of 163 HV, which is 165 HV lower than that of the autogenous laser weld, resulting from the formation of soft austenite. However, the presence of martensite in the lower region of the FZ in the weld with nickel wire led to a much higher hardness of 362 HV (which is 52 HV higher than that of the autogenous laser weld). The large difference in the hardness of different locations in the FZ, together with the high sensitivity of hot cracking indicates that with a high wire feed rate, pure nickel wire is not suitable for the welding of pipeline steels. However, it still provides a simple and useful way for quantifying the filler material dilution. Although the wire chemistry significantly affected the weld metal hardness, the HAZ of the welds exhibited similar hardness due to the same thermal cycle, with the CGHAZ presenting a higher hardness than the FGHAZ and ICHAZ due to a faster cooling. In addition, the microhardness test examined the local properties of the welds and helped determine the feasibility of feeding different wires during laser welding process, however, further joint property testing would not be meaningful unless the weld metal softening can be resolved in the iron-wire fed welds, and cracking can be mitigated in the nickel-wire fed welds.

## 9.4 Effect of feeding ER70S wires with different carbon equivalents

### 9.4.1 FZ microstructure

Fig. 9-8 shows the FZ microstructure in the weld made with different carbon steel wires. The addition of an ER70S-2 wire led to the formation of a coarser microstructure with more ferrite, compared to the ER70S-6 wire. The ER70S-2 wire has a significantly lower carbon

equivalent (with a  $P_{cm}$  of 0.129 compared to 0.190), which indicates a lower hardenability and generates less carbides and non-metallic inclusions in the weld metal, and thus promoted the formation of more ferrite instead of acicular ferrite or bainite.

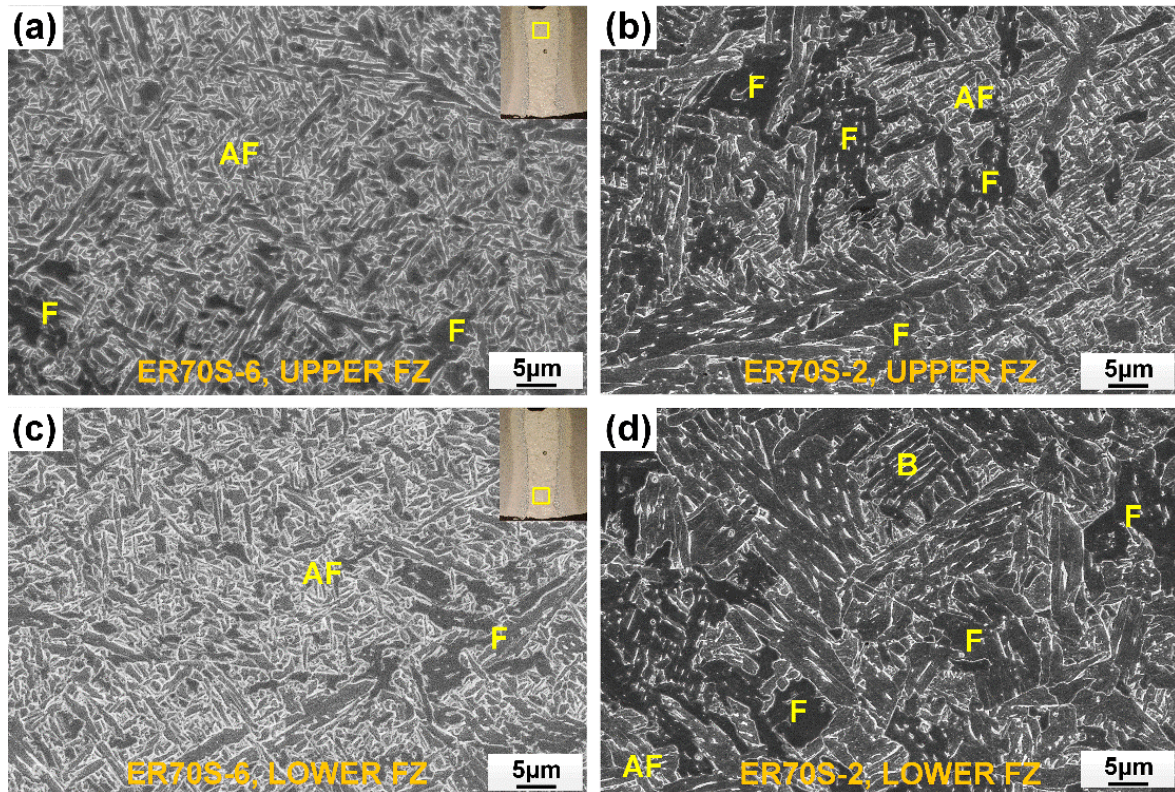


Figure 9-8. SEM images showing the FZ microstructure, indicating the presence of acicular ferrite (AF), ferrite (F) and bainite (B): (a) with ER70S-6 wire, upper region; (b) with ER70S-2 wire, upper region; (c) with ER70S-6 wire, lower region; (d) with ER70S-2 wire, lower region.

#### 9.4.2 FZ hardness

Fig. 9-9 shows the hardness distribution of the welds made with the two different carbon steel wires. The feeding of ER70S-2 wire resulted in a lower FZ hardness, due to the coarser microstructure and the presence of more ferrite. The mean FZ hardness of the welds made with an ER70S-6 and an ER70S-2 wire were  $277 \pm 1$  HV and  $251 \pm 1$  HV, respectively. A hardness decrease of 26 HV was found when using the ER70S-2 wire, and the FZ hardness met the requirement of API 5L, which indicates the maximum hardness for sour service pipes should not exceed 275 HV. The weld metal strength overmatch should also be maintained, as the FZ



hardness was still higher than that of the base material (243 HV).

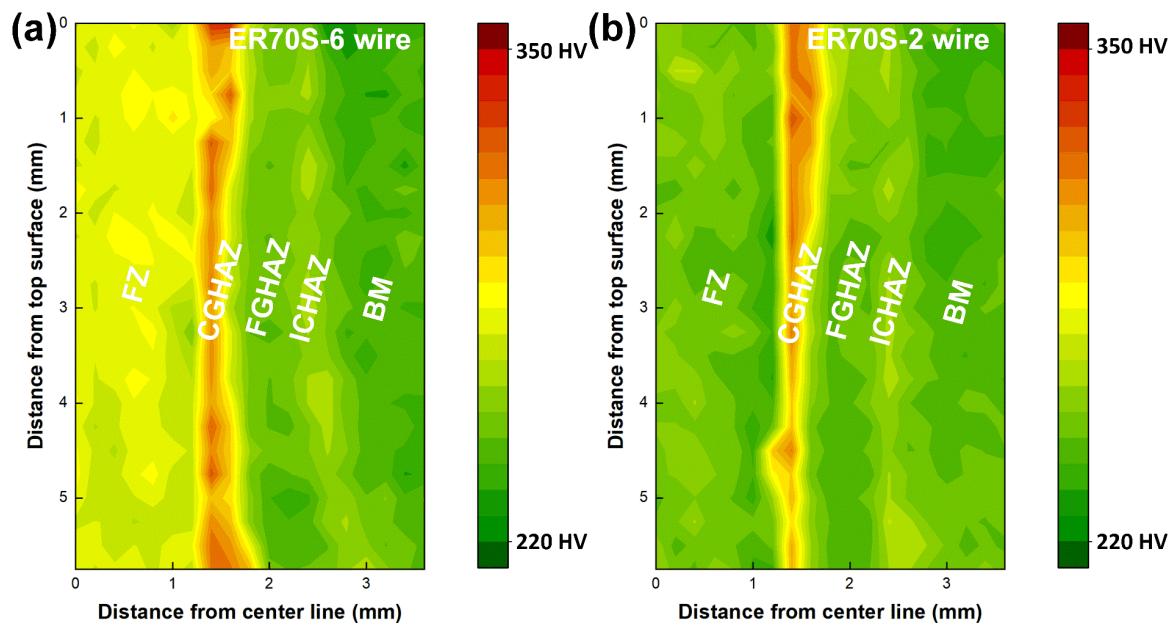


Figure 9-9. Microhardness maps of the welds made with: (a) ER70S-6 wire; (b) ER70S-2 wire.

### 9.4.3 Charpy impact toughness and fracture surfaces

Fig. 9-10a and b show the impact toughness values and the force-displacement curves of the laser weld metal with the ER70S-2 wire at varying Charpy testing temperatures, respectively. The absorbed energy at the test temperatures met the requirement of API 5L, which is 20 J for 5 mm-thick sub-size samples at a test temperature of 0 °C or, if a producer agreed, a lower test temperature. The sharp drop on the force-displacement curves at low temperatures of -20 °C and -45 °C indicates that unstable crack extension occurred, and the fracture mechanism might change to cleavage or mixed modes. The areas under the force-displacement curves in Fig. 9-10b also indicate that the absorbed energy decreased with decreasing test temperature. Interestingly, compared to the ER70S-6 wire-fed laser welds obtained in Chapter 5, the laser weld with the addition of ER70S-2 wire exhibited a lower weld metal toughness, although the FZ hardness was lower and met the API 5L standard. This might be resulted from the coarser microstructure with less AF, as an AF-dominated microstructure provides both high strength and toughness at the same time. The presence of dimples on the

fracture surface shown in Fig. 9-11a indicates that the weld metal exhibited ductile fracture at the testing temperature of 0 °C. As the temperature decreased to -20 °C, the fracture mechanism changed to cleavage mode, which was confirmed by the quasi-cleavage feature of the fracture surface in Fig. 9-11b, indicating that the transition-temperature range is close to this temperature.

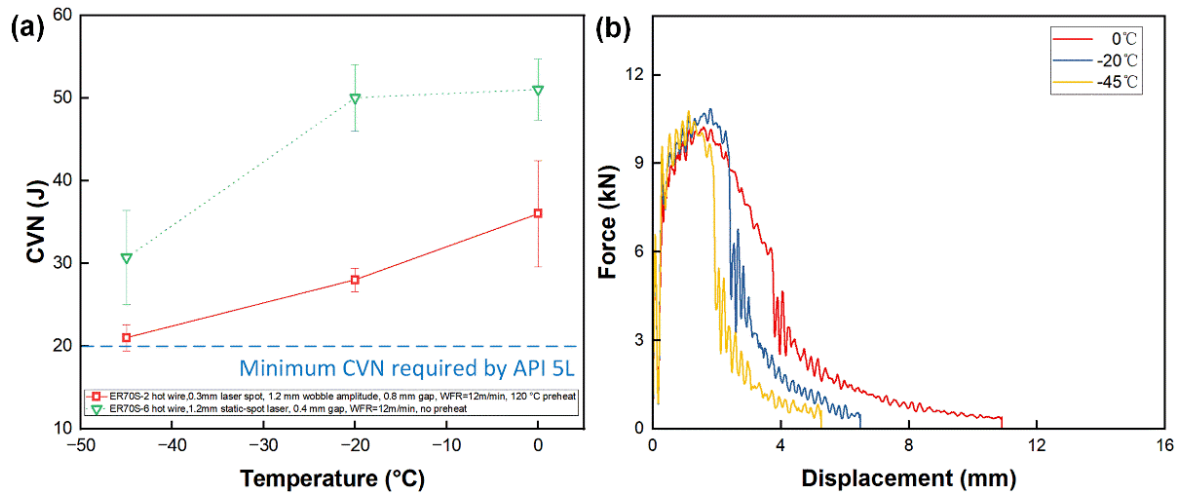


Figure 9-10. (a) Charpy impact toughness of weld metal with ER70S wires addition at different temperatures; (b) force-displacement curves of Charpy samples with ER70S-2 wire addition at different testing temperatures.

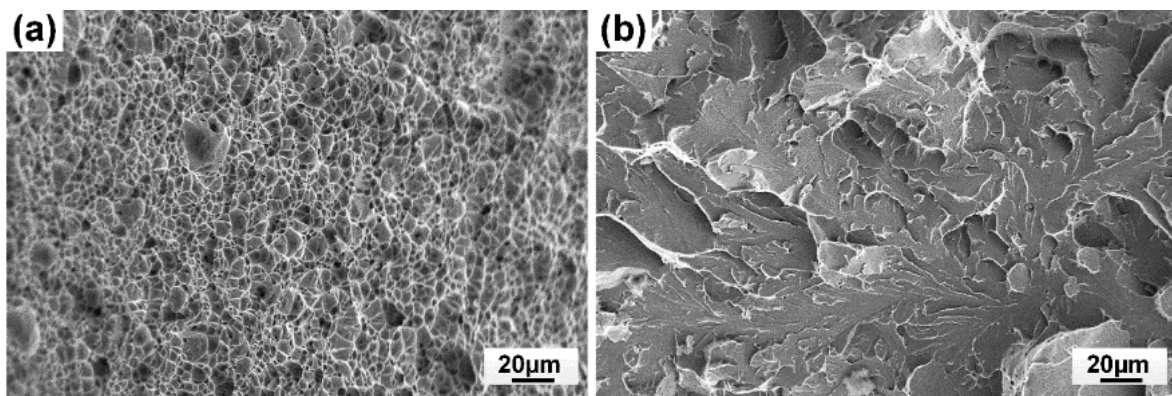


Figure 9-11. SEM images of Charpy fracture surfaces of ER70S-2-wire-fed weld samples tested at: (a) 0 °C; (b) -20 °C.

## 9.5 FZ hardness comparison of the laser welds obtained in this work

Fig. 9-12 compared the FZ hardness values of the laser welds obtained in this work. The

use of substrates preheating and a larger gap, together with applying a hot-wire feed and beam wobbling technique provided the ability to reduce the weld metal hardness. Meanwhile, the feed of an ER70S-2 wire with a lower carbon equivalent further reduced the hardness, compared to the addition of an ER70S-6 wire. An 80 HV decrease in FZ hardness was achieved in the ER70S-2-wire-fed wobble laser weld with a preheat temperature of 120 °C and a root gap of 0.8 mm, compared to the autogenous laser weld. The pipeline industry uses hardness as an indicator for cracking sensitivity under sour conditions, which normally increases with the hardness and strength of carbon steels. The API 5L pipeline standard requires that the weld metal hardness should not exceed 275 HV for sour service pipes, however this criterion is based on conventional arc welding methods. The ER70S-2 wire-fed laser weld with the optimized welding procedures developed in this work exhibited a satisfactory FZ hardness lower than 275 HV and met the requirement for sour-service pipes, compared to the reported values usually higher than 300 HV in previous literature working on hybrid laser arc welding of X80 steel [7,97–100].

For laser welding which typically has a higher cooling rate, the very fine AF-dominated microstructure could lead to a hardness higher than 275 HV, but also remain a good crack-arrest ability due to the interlocking structure, as confirmed by the Charpy impact tests results showing the toughness of the laser welds met the API 5L requirements. For non-sour service pipes, the weld metal hardness limit can be relaxed, which is 300 HV. Considering the high productivity associated with a 7-mm-weld height with a single pass, a relatively high welding speed, a minimal HAZ resulting from a low heat input, and the satisfactory mechanical properties, the laser welding procedure proposed by this work show strong potential for utilizing laser welding for more applications in the pipeline industry.

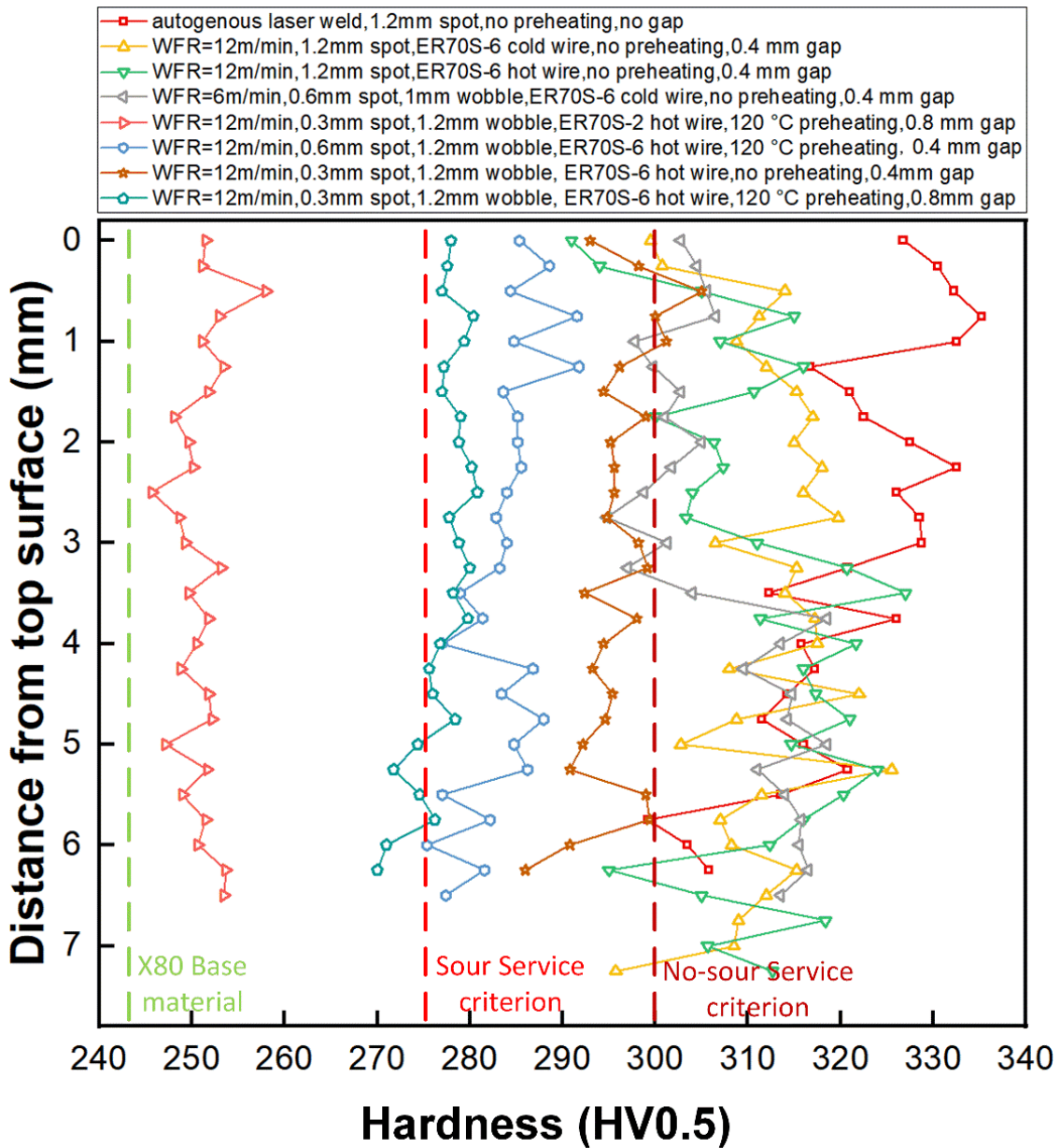


Figure 9-12. FZ hardness comparison of the welds obtained in this work.

## 9.6 Summary

The findings presented in this part of work reveal the influence of wire chemistry and elements dilution on the microstructure and hardness in X80 steel laser welds. The following conclusions can be drawn:

- (1) The addition of pure iron wire led to the formation of more ferrite in the fusion zone and reduced the weld metal hardness due to the dilution of alloying elements. Compared to the

autogenous laser weld, the hardness of the upper region of the FZ was reduced by around 90 HV, while that of the lower region was reduced by approximately 50 HV. Weld metal softening was found in the upper region of the FZ, with a hardness lower than that of the base material.

(2) Feeding a pure nickel wire helped demonstrate the filler material dilution in the FZ, with the finding that the upper region of the FZ contained 34% of the filler material, and the lower region contained 11% of the wire material. The cracking sensitivity and uneven hardness distribution makes feeding nickel wire not suitable for laser welding of X80 steel.

(3) Compared to feeding an ER70S-6 wire, introducing an ER70S-2 wire with a lower carbon equivalent during laser welding of X80 steel promoted the formation of more ferrite and generated a coarser FZ microstructure. This led to a FZ hardness lower than 275 HV which met the API standard for sour service pipes and a sufficient toughness higher than 20 J for 5-mm-thick sub-size Charpy samples.



## Chapter 10: Conclusions

In conclusion, this work focused on developing a state-of-the-art laser welding process as a root pass for the welding of HSLA pipeline steels with improved weld quality, mechanical properties, and increased productivity. Laser beam wobbling and hot-wire feeding techniques were utilized to improve the gap-bridging ability, enhance the filler material intermixing, and optimize the fusion zone microstructure. The influence of joint configuration, filler material composition and welding parameters on the microstructure and mechanical properties are discussed in detail.

Introducing an ER70S-6 wire into the weld pool helped generate acicular ferrite in the fusion zone by modifying the chemical composition. The formation of bainite in the weld metal can be further limited by preheating the wire to a temperature near the melting point. A higher wire feed rate reduced the hardness of the upper region of the fusion zone but had limited effect on the bottom root of the fusion zone, which was due to the uneven distribution of the filler material and the resulting inhomogeneous microstructure during static-spot laser welding. The strength and toughness of the weld metal met the API industrial standard, although the weld metal hardness exceeded the maximum value required.

During the wire-fed laser welding process, applying laser beam wobbling enabled better control of filler metal dilution, which determined the weld metal microstructure and the resulting mechanical properties. Beam wobbling increased the fraction of bainite in the fusion zone due to the dilution effect with more melted base material, and this led to an increase in the hardness and strength of the weld metal.

Utilizing a wobble laser with a finer spot in combination with a hot-wire feed improved the fusion zone microstructure homogeneity and reduced the weld metal hardness. Preheating the substrates to a temperature of 120 °C reduced the cooling rate in the fusion zone, which led to the formation of more grain boundary ferrite and reduced the weld metal hardness. HAZ

hardness was also reduced with preheating. Compared to a smaller root gap of 0.4 mm, a gap of 0.8 mm limited the dilution of alloying elements from the filler wire, due to the reduced volume of melted base metal, and helped limit the formation of bainite and reduce the weld metal hardness.

Introducing an ER70S-2 wire with a lower carbon equivalent during laser welding of X80 steel generated a coarser fusion zone microstructure and promoted the formation of more ferrite. The significantly reduced content of carbon, manganese and silicon limited the hardenability, leading to a fusion zone hardness lower than 275 HV which met the requirement for sour-service pipes by API 5L standard. A sufficient toughness was achieved at varying temperatures, which is targeted to be higher than 20 J for the 5-mm-thick sub-size Charpy samples tested in this work. The ER70S-2 hot-wire addition together with the optimized wobble laser welding conditions (with a wire feed rate of 12 m/min, a root gap of 0.8 mm, and a preheat temperature of 120 °C) led to the best overall mechanical performance with satisfactory weld metal hardness and toughness according to API 5L standard.

Compared to conventional arc welding methods, the laser welding procedure developed in the current work significantly increased productivity by producing a 7-mm-height weld with a single pass. The low heat input and limited reheating is beneficial to the HAZ properties by avoiding the grain growth and the formation of MA constituents. Satisfactory mechanical properties including hardness, weld metal strength and toughness were obtained for the laser welds with optimized groove design, wire chemistry and welding parameters. By applying novel technologies including beam wobbling and hot-wire feeding, the laser welding procedure proposed by this work show strong potential for utilizing laser welding for more applications in the pipeline industry.

## **Recommendations and opportunities for future work**

The feasibility of welding procedures developed in the current study for other steels with a higher alloying level can be tested. For instance, HY80 steel is popular in naval and nuclear industries; however, the relatively high carbon equivalent limits the application of laser welding of this material. The dilution of alloying elements by feeding an ER70S-6 or ER70S-2 wire provides the potential to limit the brittleness of the weld metal, and the effectiveness is expected to be enhanced with a hot-wire feed, a larger root gap, preheating of the substrates and laser beam wobbling.

Introducing an ER70S-6 wire led to a FZ hardness slightly higher than the maximum value allowed by API 5L. Meanwhile, the addition of an ER70S-2 filler wire reduced the weld metal hardness to a level close to that of the base material. It would be interesting to feed these two types of steel wires with varying volume fractions into the same weld pool, so that the relationship between the carbon equivalent and the hardness can be detailly understood. This would potentially provide a way to control the properties of weld metal more precisely.

There is a research gap in the numerical modelling on wire-fed laser welding of thick steels with laser beam wobbling technique. The hot-wire feeding, beam wobbling and varying defocusing positions increased the complexity of the modelling. A substrate thickness of 14 mm and a laser spot size of 100 to 300  $\mu\text{m}$  would dramatically increase the required simulation time. Despite these difficulties, it would be interesting to study the effect of beam wobbling on the local heat input and the flow behaviour of the molten pool during wire-fed laser welding. Additionally, the modelling can also help estimate the feasibility of the optimized welding procedures obtained in the lab for actual industrial applications, where much larger pipe sections are welded together, as unaware results may show up when the technique was applied for industrial applications. For example, in pipeline industry, the residual stresses resulted from welded coupons are very difficult to correlate directly to residual stresses in complete girth

welds, where the welding is performed on a whole section of pipe which is much bigger than the coupons welded in a laboratory, since the residual stresses depend greatly on the level of constrain.

# Letters of Copyright Permission

Fig. 2-1

1/23/24, 3:55 PM

RightsLink Printable License

## JOHN WILEY AND SONS LICENSE TERMS AND CONDITIONS

Jan 23, 2024

---

This Agreement between University of Waterloo -- Hanwen Yang ("You") and John Wiley and Sons ("John Wiley and Sons") consists of your license details and the terms and conditions provided by John Wiley and Sons and Copyright Clearance Center.

License Number	5714950035026
License date	Jan 23, 2024
Licensed Content Publisher	John Wiley and Sons
Licensed Content Publication	Wiley Books
Licensed Content Title	Welding Metallurgy, 3rd Edition
Licensed Content Author	Sindo Kou
Licensed Content Date	Oct 1, 2020
Licensed Content Pages	1
Type of use	Dissertation/Thesis
Requestor type	University/Academic
Format	Print and electronic
Portion	Figure/table



Number of figures/tables	1
Will you be translating?	No
Title of new work	Advanced hybrid laser welding of pipeline steels using novel technologies
Institution name	University of Waterloo
Expected presentation date	Apr 2024
Portions	Figure 9.21-Continuous-cooling transformation diagram for weld metal of lowcarbon steel
Requestor Location	University of Waterloo 203 Deacon Wood Pl Waterloo, ON N2T 2S1 Canada Attn: University of Waterloo
Publisher Tax ID	EU826007151
Total	0.00 CAD

Fig. 2-2

ELSEVIER LICENSE  
TERMS AND CONDITIONS

Jan 23, 2024

---

This Agreement between University of Waterloo -- Hanwen Yang ("You") and Elsevier ("Elsevier") consists of your license details and the terms and conditions provided by Elsevier and Copyright Clearance Center.

License Number	5714960187404
License date	Jan 23, 2024
Licensed Content Publisher	Elsevier
Licensed Content Publication	Elsevier Books
Licensed Content Title	Introduction to the Physical Metallurgy of Welding
Licensed Content Author	Kenneth Easterling
Licensed Content Date	Jan 1, 1992
Licensed Content Pages	65
Start Page	126
End Page	190
Type of Use	reuse in a thesis/dissertation
Portion	figures/tables/illustrations

Number of figures/tables/illustrations	1
Format	both print and electronic
Are you the author of this Elsevier chapter?	No
Will you be translating?	No
Title of new work	Advanced hybrid laser welding of pipeline steels using novel technologies
Institution name	University of Waterloo
Expected presentation date	Apr 2024
Portions	HAZ figure3.1
	University of Waterloo 203 Deacon Wood Pl
Requestor Location	Waterloo, ON N2T 2S1 Canada Attn: University of Waterloo
Publisher Tax ID	GB 494 6272 12
Total	0.00 CAD

Fig. 2-3

ELSEVIER LICENSE  
TERMS AND CONDITIONS

Jan 24, 2024

---

This Agreement between University of Waterloo -- Hanwen Yang ("You") and Elsevier ("Elsevier") consists of your license details and the terms and conditions provided by Elsevier and Copyright Clearance Center.

License Number	5715530270631
License date	Jan 24, 2024
Licensed Content Publisher	Elsevier
Licensed Content Publication	Anaesthesia & Intensive Care Medicine
Licensed Content Title	Basic principles of lasers
Licensed Content Author	Daniel Haley, Oliver Pratt
Licensed Content Date	Dec 1, 2017
Licensed Content Volume	18
Licensed Content Issue	12
Licensed Content Pages	3
Start Page	648
End Page	650
Type of Use	reuse in a thesis/dissertation

Portion	figures/tables/illustrations
Number of figures/tables/illustrations	1
Format	both print and electronic
Are you the author of this Elsevier article?	No
Will you be translating?	No
Title of new work	Advanced hybrid laser welding of pipeline steels using novel technologies
Institution name	University of Waterloo
Expected presentation date	Apr 2024
Portions	Fig1
Requestor Location	University of Waterloo 203 Deacon Wood Pl
Publisher Tax ID	Waterloo, ON N2T 2S1 Canada Attn: University of Waterloo
Publisher Tax ID	GB 494 6272 12
Total	0.00 CAD



Fig. 2-4



Canonical URL : <https://creativecommons.org/licenses/by-nc-nd/4.0/>


[See the legal code](#)


### You are free to:


**Share** — copy and redistribute the material in any medium or format

The licensor cannot revoke these freedoms as long as you follow the license terms.

### Under the following terms:

 **Attribution** — You must give appropriate credit, provide a link to the license, and indicate if changes were made. You may do so in any reasonable manner, but not in any way that suggests the licensor endorses you or your use.

 **NonCommercial** — You may not use the material for commercial purposes.

 **NoDerivatives** — If you remix, transform, or build upon the material, you may not distribute the modified material.

**No additional restrictions** — You may not apply legal terms or technological measures that legally restrict others from doing anything the license permits.

### Notices:

You do not have to comply with the license for elements of the material in the public domain or where your use is permitted by an applicable exception or limitation.

No warranties are given. The license may not give you all of the permissions necessary for your intended use. For example, other rights such as publicity, privacy, or moral rights may limit how you use the material.

Fig. 2-5

**SPRINGER LINK** Login

---

Find a journal | Publish with us | Track your research | Search Cart


---

Home > The International Journal of Advanced Manufacturing Technology > Article

## Absorbance measurement for in situ process regime identification in laser processing


ORIGINAL ARTICLE | [Open access](#) | Published: 22 February 2023  
Volume 126, pages 103–115, (2023) [Cite this article](#)



[Download PDF](#) You have full access to this [open access](#) article




**The International Journal of Advanced Manufacturing Technology**

[Aims and scope](#) →  
[Submit manuscript](#) →

Moritz Wittmer , [Jonas Grünewald](#) & [Katrin Wudy](#)

 1256 Accesses  1 Citation [Explore all metrics](#) →

[Use our pre-submission checklist](#) →  
Avoid common mistakes on your manuscript. 

Absorbance measurement for in situ process regime identification in laser processing

## Rights and permissions

**Open Access** This article is licensed under a Creative Commons Attribution 4.0 International License, which permits use, sharing, adaptation, distribution and reproduction in any medium or format, as long as you give appropriate credit to the original author(s) and the source, provide a link to the Creative Commons licence, and indicate if changes were made. The images or other third party material in this article are included in the article's Creative Commons licence, unless indicated otherwise in a credit line to the material. If material is not included in the article's Creative Commons licence and your intended use is not permitted by statutory regulation or exceeds the permitted use, you will need to obtain permission directly from the copyright holder. To view a copy of this licence, visit <http://creativecommons.org/licenses/by/4.0/>.

Fig. 2-6

ELSEVIER LICENSE  
TERMS AND CONDITIONS

Jan 24, 2024

---

This Agreement between University of Waterloo -- Hanwen Yang ("You") and Elsevier ("Elsevier") consists of your license details and the terms and conditions provided by Elsevier and Copyright Clearance Center.

License Number	5715510721432
License date	Jan 24, 2024
Licensed Content Publisher	Elsevier
Licensed Content Publication	Optics and Lasers in Engineering
Licensed Content Title	Laser hot-wire cladding of Co-Cr-W metal cored wire
Licensed Content Author	Zhe Zhang,Fanrong Kong,Radovan Kovacevic
Licensed Content Date	May 1, 2020
Licensed Content Volume	128
Licensed Content Issue	n/a
Licensed Content Pages	1
Start Page	105998
End Page	0

Type of Use	reuse in a thesis/dissertation
Portion	figures/tables/illustrations
Number of figures/tables/illustrations	1
Format	both print and electronic
Are you the author of this Elsevier article?	No
Will you be translating?	No
Title of new work	Advanced hybrid laser welding of pipeline steels using novel technologies
Institution name	University of Waterloo
Expected presentation date	Apr 2024
Portions	Fig1
Requestor Location	University of Waterloo 203 Deacon Wood Pl  Waterloo, ON N2T 2S1 Canada Attn: University of Waterloo
Publisher Tax ID	GB 494 6272 12
Total	0.00 CAD

Fig. 2-7; 2-8

ELSEVIER LICENSE  
TERMS AND CONDITIONS

Jan 24, 2024

---

---

This Agreement between University of Waterloo -- Hanwen Yang ("You") and Elsevier ("Elsevier") consists of your license details and the terms and conditions provided by Elsevier and Copyright Clearance Center.

License Number	5715520643574
License date	Jan 24, 2024
Licensed Content Publisher	Elsevier
Licensed Content Publication	Optics & Laser Technology
Licensed Content Title	Hybrid laser arc welding: State-of-art review
Licensed Content Author	Bappa Acherjee
Licensed Content Date	Feb 1, 2018
Licensed Content Volume	99
Licensed Content Issue	n/a
Licensed Content Pages	12
Start Page	60
End Page	71
Type of Use	reuse in a thesis/dissertation



Portion	figures/tables/illustrations
Number of figures/tables/illustrations	2
Format	both print and electronic
Are you the author of this Elsevier article?	No
Will you be translating?	No
Title of new work	Advanced hybrid laser welding of pipeline steels using novel technologies
Institution name	University of Waterloo
Expected presentation date	Apr 2024
Portions	Fig1,2
Requestor Location	University of Waterloo 203 Deacon Wood Pl  Waterloo, ON N2T 2S1 Canada Attn: University of Waterloo
Publisher Tax ID	GB 494 6272 12
Total	0.00 CAD

Fig. 2-9

CCC RightsLink Sign in/Register ⓘ 🔗

---

**Hybrid laser arc welding of X80 and X120 steel grade**

**S Sage** Author: S. Gook, A. Gumenyuk, M. Rethmeier  
Publication: Science and Technology of Welding and Joining  
Publisher: SAGE Publications  
Date: 2014-01-01  
Copyright © 2014, © SAGE Publications

---

**Gratis Reuse**

Permission is granted at no cost for use of content in a Master's Thesis and/or Doctoral Dissertation, subject to the following limitations. You may use a single excerpt or up to 3 figures tables. If you use more than those limits, or intend to distribute or sell your Master's Thesis/Doctoral Dissertation to the general public through print or website publication, please return to the previous page and select 'Republish in a Book/Journal' or 'Post on intranet/password-protected website' to complete your request.

BACK CLOSE WINDOW

Fig. 2-10

CCC RightsLink Sign in/Register ?

---

**Weld microstructure and shape of laser-arc hybrid welding**

**Sage** Author: M. Gao, X. Y. Zeng, Q. W. Hu, J. Yan  
Publication: Science and Technology of Welding and Joining  
Publisher: SAGE Publications  
Date: 2008-02-01  
Copyright © 2008, © SAGE Publications

---

**Gratis Reuse**

Permission is granted at no cost for use of content in a Master's Thesis and/or Doctoral Dissertation, subject to the following limitations. You may use a single excerpt or up to 3 figures tables. If you use more than those limits, or intend to distribute or sell your Master's Thesis/Doctoral Dissertation to the general public through print or website publication, please return to the previous page and select 'Republish in a Book/Journal' or 'Post on Intranet/password-protected website' to complete your request.

BACK CLOSE WINDOW

Fig. 2-11

ELSEVIER LICENSE  
TERMS AND CONDITIONS

Jan 24, 2024

---

---

This Agreement between University of Waterloo -- Hanwen Yang ("You") and Elsevier ("Elsevier") consists of your license details and the terms and conditions provided by Elsevier and Copyright Clearance Center.

License Number	5715450190188
License date	Jan 24, 2024
Licensed Content Publisher	Elsevier
Licensed Content Publication	Materials & Design
Licensed Content Title	Single pass hybrid laser-arc welding of 25mm thick square groove butt joints
Licensed Content Author	M. Wahba,M. Mizutani,S. Katayama
Licensed Content Date	5 May 2016
Licensed Content Volume	97
Licensed Content Issue	n/a
Licensed Content Pages	6
Start Page	1
End Page	6

Type of Use	reuse in a thesis/dissertation
Portion	figures/tables/illustrations
Number of figures/tables/illustrations	1
Format	both print and electronic
Are you the author of this Elsevier article?	No
Will you be translating?	No
Title of new work	Advanced hybrid laser welding of pipeline steels using novel technologies
Institution name	University of Waterloo
Expected presentation date	Apr 2024
Portions	Fig1
Requestor Location	University of Waterloo 203 Deacon Wood Pl  Waterloo, ON N2T 2S1 Canada Attn: University of Waterloo
Publisher Tax ID	GB 494 6272 12
Total	0.00 CAD



Fig. 2-12

CCC RightsLink Sign in/Register ⓘ 🔒

---

**Numerical investigation of asymmetric weld fusion geometry in laser welding of aluminium alloy with beam oscillation**

**S Sage** Author: Xi Chen, Nan Jiang, Meng Jiang, Yang Du, et al.  
Publication: Science and Technology of Welding and Joining  
Publisher: SAGE Publications  
Date: 2022-11-01  
Copyright © 2022. © SAGE Publications

---

**Gratis Reuse**

Permission is granted at no cost for use of content in a Master's Thesis and/or Doctoral Dissertation, subject to the following limitations. You may use a single excerpt or up to 3 figures tables. If you use more than those limits, or intend to distribute or sell your Master's Thesis/Doctoral Dissertation to the general public through print or website publication, please return to the previous page and select 'Republish in a Book/Journal' or 'Post on intranet/password-protected website' to complete your request.

[BACK](#)

[CLOSE WINDOW](#)

Fig.2-13

ELSEVIER LICENSE  
TERMS AND CONDITIONS

Jan 24, 2024

---

---


This Agreement between University of Waterloo -- Hanwen Yang ("You") and Elsevier ("Elsevier") consists of your license details and the terms and conditions provided by Elsevier and Copyright Clearance Center.

License Number	5715450432222
License date	Jan 24, 2024
Licensed Content Publisher	Elsevier
Licensed Content Publication	Journal of Materials Processing Technology
Licensed Content Title	Weld formation mechanism of fiber laser oscillating welding of austenitic stainless steel
Licensed Content Author	Kangda Hao,Geng Li,Ming Gao,Xiaoyan Zeng
Licensed Content Date	Nov 1, 2015
Licensed Content Volume	225
Licensed Content Issue	n/a
Licensed Content Pages	7
Start Page	77
End Page	83

Type of Use	reuse in a thesis/dissertation
Portion	figures/tables/illustrations
Number of figures/tables/illustrations	1
Format	both print and electronic
Are you the author of this Elsevier article?	No
Will you be translating?	No
Title of new work	Advanced hybrid laser welding of pipeline steels using novel technologies
Institution name	University of Waterloo
Expected presentation date	Apr 2024
Portions	Fig2
Requestor Location	University of Waterloo 203 Deacon Wood Pl  Waterloo, ON N2T 2S1 Canada Attn: University of Waterloo
Publisher Tax ID	GB 494 6272 12
Total	0.00 CAD

Fig. 2-14

CC BY RightsLink 🔍 📄



**Reduction of pores by means of laser beam oscillation during remote welding of AlMgSi**

Author: Florian Fatzer, Martin Sommer, Rudolf Weber, Jan-Philipp Weierpals, Thomas Graf

Publication: Optics and Lasers in Engineering

Publisher: Elsevier

Date: September 2018

© 2018 The Authors. Published by Elsevier Ltd.

**Creative Commons**

This is an open access article distributed under the terms of the Creative Commons CC-BY license, which permits unrestricted use, distribution, and reproduction in any medium, provided the original work is properly cited.

You are not required to obtain permission to reuse this article.

To request permission for a type of use not listed, please contact Elsevier Global Rights Department.

Are you the author of this Elsevier journal article?

Fig. 2-15, 2-16

ELSEVIER LICENSE  
TERMS AND CONDITIONS

Jan 24, 2024

---

---

This Agreement between University of Waterloo -- Hanwen Yang ("You") and Elsevier ("Elsevier") consists of your license details and the terms and conditions provided by Elsevier and Copyright Clearance Center.

License Number	5715510224818
License date	Jan 24, 2024
Licensed Content Publisher	Elsevier
Licensed Content Publication	Materials & Design
Licensed Content Title	Effect of beam oscillating pattern on weld characterization of laser welding of AA6061-T6 aluminum alloy
Licensed Content Author	Lei Wang,Ming Gao,Chen Zhang,Xiaoyan Zeng
Licensed Content Date	Oct 15, 2016
Licensed Content Volume	108
Licensed Content Issue	n/a
Licensed Content Pages	11
Start Page	707
End Page	717



Type of Use	reuse in a thesis/dissertation
Portion	figures/tables/illustrations
Number of figures/tables/illustrations	2
Format	both print and electronic
Are you the author of this Elsevier article?	No
Will you be translating?	No
Title of new work	Advanced hybrid laser welding of pipeline steels using novel technologies
Institution name	University of Waterloo
Expected presentation date	Apr 2024
Portions	Fig.9 and 17
Requestor Location	University of Waterloo 203 Deacon Wood Pl Waterloo, ON N2T 2S1 Canada Attn: University of Waterloo
Publisher Tax ID	GB 494 6272 12
Total	0.00 CAD

Fig. 2-17

ELSEVIER LICENSE  
TERMS AND CONDITIONS

Jan 24, 2024

---

This Agreement between University of Waterloo -- Hanwen Yang ("You") and Elsevier ("Elsevier") consists of your license details and the terms and conditions provided by Elsevier and Copyright Clearance Center.

License Number	5715450860361
License date	Jan 24, 2024
Licensed Content Publisher	Elsevier
Licensed Content Publication	Materials Letters
Licensed Content Title	Improving fusion zone microstructure inhomogeneity in dissimilar-metal welding by laser welding with oscillation
Licensed Content Author	Zhenguo Jiang,Xi Chen,Kun Yu,Zhenglong Lei,Yanbin Chen,Shibo Wu,Zhijun Li
Licensed Content Date	Feb 15, 2020
Licensed Content Volume	261
Licensed Content Issue	n/a
Licensed Content Pages	1
Start Page	126995
End Page	0

Type of Use	reuse in a thesis/dissertation
Portion	figures/tables/illustrations
Number of figures/tables/illustrations	1
Format	both print and electronic
Are you the author of this Elsevier article?	No
Will you be translating?	No
Title of new work	Advanced hybrid laser welding of pipeline steels using novel technologies
Institution name	University of Waterloo
Expected presentation date	Apr 2024
Portions	Fig3
Requestor Location	University of Waterloo 203 Deacon Wood Pl  Waterloo, ON N2T 2S1 Canada Attn: University of Waterloo
Publisher Tax ID	GB 494 6272 12
Total	0.00 CAD

Fig. 2-18

ELSEVIER LICENSE  
TERMS AND CONDITIONS

Jan 24, 2024

---

---

This Agreement between University of Waterloo -- Hanwen Yang ("You") and Elsevier ("Elsevier") consists of your license details and the terms and conditions provided by Elsevier and Copyright Clearance Center.

License Number	5715450995284
License date	Jan 24, 2024
Licensed Content Publisher	Elsevier
Licensed Content Publication	International Journal of Heat and Mass Transfer
Licensed Content Title	A pathway to mitigate macrosegregation of laser-arc hybrid Al-Si welds through beam oscillation
Licensed Content Author	Lei Wang,Ming Gao,Zhongqi Hao
Licensed Content Date	Apr 1, 2020
Licensed Content Volume	151
Licensed Content Issue	n/a
Licensed Content Pages	1
Start Page	119467
End Page	0

Type of Use	reuse in a thesis/dissertation
Portion	figures/tables/illustrations
Number of figures/tables/illustrations	1
Format	both print and electronic
Are you the author of this Elsevier article?	No
Will you be translating?	No
Title of new work	Advanced hybrid laser welding of pipeline steels using novel technologies
Institution name	University of Waterloo
Expected presentation date	Apr 2024
Portions	Fig7
Requestor Location	University of Waterloo 203 Deacon Wood Pl
Publisher Tax ID	Waterloo, ON N2T 2S1 Canada Attn: University of Waterloo
Total	GB 494 6272 12
	0.00 CAD



## References

- [1] BP p.l.c. BP Statistical Review of World Energy 71th edition. 2022.
- [2] Yong S, Hwang B, Kim S, et al. Fracture toughness analysis in transition temperature region of API X70 pipeline steels. 2006;429:196–204.
- [3] Komizo Y. Overview of Recent Welding Technology Relating to Pipeline Construction. Trans JWRI. 2008;37:1–5.
- [4] Okaguchi S, Makino H, Hamada M, et al. Development and mechanical properties of X120 linepipe. Int J Offshore Polar Eng. 2004;14:29–35.
- [5] Hudson MG. Welding of X100 linepipe [dissertation]. Cranfield university; 2004.
- [6] Liu C, Bhole SD. Challenges and developments in pipeline weldability and mechanical properties. Sci Technol Weld Join. 2013;18:169–181.
- [7] Zhenglong L, Caiwang T, Yanbin C, et al. Microstructure and mechanical properties of fiber laser-metal active gas hybrid weld of X80 pipeline steel. J Press Vessel Technol Trans ASME. 2013;135:1–7.
- [8] Dawes CT. Laser Welding: A Practical Guide. New York: Abington Publishing; 1992.
- [9] Katayama S. Introduction: Fundamentals of laser welding. Handb Laser Weld Technol. Cambridge: Woodhead Publishing Limited; 2013: 3–16.
- [10] Hao K, Li G, Gao M, et al. Weld formation mechanism of fiber laser oscillating welding of austenitic stainless steel. J Mater Process Technol. 2015;225:77–83.
- [11] Matsunawa A, Mizutani M, Katayama S, et al. Porosity formation mechanism and its prevention in laser welding. Weld Int. 2003;17:431–437.

- [12] Moore PL, Howse DS, Wallach ER. Microstructures and properties of laser/arc hybrid welds and autogenous laser welds in pipeline steels. *Sci Technol Weld Join*. 2004;9:314–322.
- [13] Wei H, Zhang Y, Tan L, et al. Energy efficiency evaluation of hot-wire laser welding based on process characteristic and power consumption. *J Clean Prod*. 2015;87:255–262.
- [14] Shen J, Li B, Hu S, et al. Comparison of single-beam and dual-beam laser welding of Ti–22Al–25Nb/TA15 dissimilar titanium alloys. *Opt Laser Technol*. 2017;93:118–126.
- [15] Jiang M, Tao W, Chen Y. Laser welding under vacuum: A review. *Appl Sci Switz*. 2017;7(9): 909.
- [16] Rubben K, Mohrbacher H, Leirman E. Advantages of using an oscillating laser beam for the production of tailed blanks. *Lasers Mater Process*. 1997;3097:228–241.
- [17] Salminen A. The filler wire - Laser beam interaction during laser welding with low alloyed steel filler wire. *Mechanika*. 2010;84:67–74.
- [18] Li S, Xu W, Xiao G, et al. Weld formation in laser hot-wire welding of 7075 aluminum alloy. *Metals*. 2018; 8(11): 909.
- [19] Phillips R, Metzbowler E. Laser beam welding of HY80 and HY100 steels using hot welding wire addition. *Weld J*. 1992;71:201s–208s.
- [20] Näsström J, Frostevarg J, Silver T. Hot-wire Laser Welding of Deep and Wide Gaps. *Phys Procedia*. 2015;78:247–254.
- [21] Fetzer F, Sommer M, Weber R, et al. Reduction of pores by means of laser beam oscillation during remote welding of AlMgSi. *Opt Lasers Eng*. 2018;108:68–77.

- [22] Zhang C, Yu Y, Chen C, et al. Suppressing porosity of a laser keyhole welded Al-6Mg alloy via beam oscillation. *J Mater Process Technol.* 2020;278:116382.
- [23] Li J, Sun Q, Liu Y, et al. Melt flow and microstructural characteristics in beam oscillation superimposed laser welding of 304 stainless steel. *J Manuf Process.* 2020;50:629–637.
- [24] Jiang Z, Chen X, Li H, et al. Grain refinement and laser energy distribution during laser oscillating welding of Invar alloy. *Mater Des.* 2020;186:108195.
- [25] Shah LH, Khodabakhshi F, Gerlich A. Effect of beam wobbling on laser welding of aluminum and magnesium alloy with nickel interlayer. *J Manuf Process.* 2019;37:212–219.
- [26] Jiang Z, Chen X, Yu K, et al. Improving fusion zone microstructure inhomogeneity in dissimilar-metal welding by laser welding with oscillation. *Mater Lett.* 2020;261:126995.
- [27] Acherjee B. Hybrid laser arc welding: State-of-art review. *Opt Laser Technol.* 2018;99:60–71.
- [28] Gook S, Gumenyuk A, Rethmeier M. Hybrid laser arc welding of X80 and X120 steel grade. *Sci Technol Weld Join.* 2014;19:15–24.
- [29] Bunaziv I, Wenner S, Ren X, et al. Filler metal distribution and processing stability in laser-arc hybrid welding of thick HSLA steel. *J Manuf Process.* 2020;54:228–239.
- [30] Gao M, Zeng XY, Hu QW, et al. Weld microstructure and shape of laser-arc hybrid welding. *Sci Technol Weld Join.* 2008;13:106–113.

- [31] API. API Specification 5L, 46th edition. 2018.
- [32] ASM International. ASM Handbook: Alloy phase diagrams. Volume 3. A S M International; 1992.
- [33] Trench CJ, Kiefner JF. Oil Pipeline Characteristics and Risk Factors: Illustrations from the Decade of Construction. American Petroleum Institute; 2001: 2–6.
- [34] Kumar S, Mondal N, Arora A. Metallurgical Perspective of Line Pipe Steel. Res J Eng Technol. 2017;8:225.
- [35] Yoo JY, Ahn SS, Seo DH, et al. New development of high grade X80 to X120 pipeline steels. Mater Manuf Process. 2011;26:154–160.
- [36] Liu B, Liu XJ, Zhang H. Strain-based design criteria of pipelines. J Loss Prev Process Ind. 2009;22:884–888.
- [37] Reichert JM. Structure and properties of complex transformation products in Nb/Mo-microalloyed steels [dissertation]. The university of British columbia; 2016.
- [38] Dearden J, O'Neill H, Association BWR. A Guide to the Selection and Welding of Low Alloy Structural Steels. Welding Research Council of the Institute of Welding; 1940.
- [39] Ito Y, Bessyo K. Cracking Parameter of High Strength Steels related to heat Affected zone Cracking. J Jpn Weld Soc. 1968;37:983-991.
- [40] Nishioka K, Ichikawa K. Progress in thermomechanical control of steel plates and their commercialization. Sci Technol Adv Mater. 2012;13:1–20.
- [41] Endo S, Nakata N. Development of Thermo-Mechanical Control Process (TMCP) and high performance steel in JFE Steel. JFE Tech Rep. 2015;20:1–7.

- [42] Petch NJ. The cleavage strength of polycrystals. *J Iron Steel Inst*. 1953;174:25-28.
- [43] Cuddy LJ, Raley JC. Austenite grain coarsening in microalloyed steels. *Metall Trans A*. 1983;14:1989-1995.
- [44] Krauss G, Thompson SW. Ferritic Microstructures in Continuously Cooled Low- and Ultralow-carbon Steels. *ISIJ Int*. 1995;35:937–945.
- [45] Kou S. *Welding Metallurgy*, 3rd Edition. New York: Wiley; 2020.
- [46] Yang JR, Bhadeshia HKDH. Acicular ferrite transformation in alloy-steel weld metals. *J Mater Sci*. 1991;26:839–845.
- [47] Sarma DS, Karasev AV, Jönsson PG. On the role of non-metallic inclusions in the nucleation of acicular ferrite in steels. *ISIJ Int*. 2009;49:1063–1074.
- [48] Zhang Z, Farrar RA. Role of non-metallic inclusions in formation of acicular ferrite in low alloy weld metals. *Mater Sci Technol*. 1996;12:237–260.
- [49] Evans GM. The Effect of Titanium in SMA C-Mn Steel Multipass Deposits. *Weld J*. 1992;71:447–454.
- [50] Gregg JM, Bhadeshia HKDH. Bainite nucleation from mineral surfaces. *Acta Metall Mater*. 1994;42:3321–3330.
- [51] Zhou Y, Jia T, Zhang X, et al. Investigation on tempering of granular bainite in an offshore platform steel. *Mater Sci Eng A*. 2015;626:352–361.
- [52] Shchyglo O, Du G, Engels JK, et al. Phase-field simulation of martensite microstructure in low-carbon steel. *Acta Mater*. 2019;175:415–425.
- [53] Akselsen OM, Grong Ø, Solberg JK. Structure-property relationships in intercritical heat

- affected zone of low-carbon microalloyed steels. *Mater Sci Technol.* 1987;3:649–655.
- [54] Davis CL, King JE. Effect of cooling rate on intercritically reheated microstructure and toughness in high strength low alloy steel. *Mater Sci Technol.* 1993;9:8–15.
- [55] Lan L, Chang Z, Fan P. Exploring the difference in bainite transformation with varying the prior austenite grain size in low carbon steel. *Metals.* 2018;8:1-3.
- [56] Toloui M. Microstructural evolution in the HAZ of X80 linepipe steel phase field modelling [dissertation]. The University of British Columbia; 2015.
- [57] Huda N. Effect of Martensite-Austenite (MA) on Mechanical Properties of X80 Linepipe Steel [dissertation]. University of Waterloo; 2018.
- [58] Easterling K. *Introduction to the Physical Metallurgy of Welding.* 2nd ed. Elsevier; 1992.
- [59] Gould RG. The LASER, light amplification by stimulated emission of radiation. *Ann Arbor Conf Opt Pump Univ Mich.* 1959; 92.
- [60] Näsström J. Phenomena in wire based multi-layer laser welding and hybrid deposition [dissertation]. Luleå University of Technology; 2019.
- [61] Haley D, Pratt O. Basic principles of lasers. *Anaesth Intensive Care Med.* 2017;18:648–650.
- [62] Long C, Loveday P, Forbes A. Piezoelectric deformable mirror for intra-cavity laser adaptive optics. *Proc SPIE - Int Soc Opt Eng.* 2008;6930.
- [63] Ballal NV, Kundabala M, Bhat KS. Lasers general principles: A review. *Clin Dent Res Compend.* 2013;133–146.
- [64] Akselsen OM, Ren X, Aas SK. Review of laser and hybrid laser-arc welding. *Proc Int*



- Offshore Polar Eng Conf. 2014;3:278–285.
- [65] Ostrowski R, Cywiński A, Strzelec M. Electronic warfare in the optical band: Main features, examples and selected measurement data. *Def Technol.* 2021;17:1636–1649.
- [66] Einstein A. Zur Quantentheorie der Strahlung. *Phys Z.* 1917;18:121–128.
- [67] Maiman TH. Stimulated optical radiation in ruby. *Nature.* 1960;187:493–494.
- [68] Martukanitz RP. A critical review of laser beam welding. *Crit Rev Ind Lasers Appl.* 2005;5706:11–24.
- [69] Wittemer M, Grünewald J, Wudy K. Absorbance measurement for in situ process regime identification in laser processing. *Int J Adv Manuf Technol.* 2023;126:103–115.
- [70] Quintino L, Assunção E. Conduction laser welding. *Handb Laser Weld Technol.* 2013;139–162.
- [71] Lehner C, Reinhart G, Schaller L. Welding of die-casted magnesium alloys for production. *J Laser Appl.* 1999;11:206–210.
- [72] Lampa C. Practical and Theoretical Aspects of Laser Welding [dissertation]. Luleå University of Technology; 1995.
- [73] Tsukamoto T, Kawanaka H, Maeda Y. Laser narrow gap welding of thick carbon steels using high brightness laser with beam oscillation. 30th Int Congr Appl Lasers Electro-Opt ICALEO 2011. 2011;141:141–146.
- [74] Ramakrishna R VSM, Amrutha PHSLR, Rahman Rashid RA, et al. Narrow gap laser welding (NGLW) of structural steels—a technological review and future research recommendations. *Int J Adv Manuf Technol.* 2020;111:2277–2300.

- [75] Guo W, Li L, Dong S, et al. Comparison of microstructure and mechanical properties of ultra-narrow gap laser and gas-metal-arc welded S960 high strength steel. *Opt Lasers Eng.* 2017;91:1–15.
- [76] Zhang Z, Kong F, Kovacevic R. Laser hot-wire cladding of Co-Cr-W metal cored wire. *Opt Lasers Eng.* 2020;128:105998.
- [77] Nurminen J, Riihimäki J, Näkki J, et al. Comparison of laser cladding with powder and hot and cold wire techniques. *ICALEO 2006 - 25th Int Congr Appl Laser Electro-Opt Congr Proc.* 2006;1006:634–637.
- [78] Ohnishi T, Kawahito Y, Mizutani M, et al. Butt welding of thick, high strength steel plate with a high power laser and hot wire to improve tolerance to gap variance and control weld metal oxygen content. *Sci Technol Weld Join.* 2013;18:314–322.
- [79] Sun Z, Kuo M. Bridging the joint gap with wire feed laser welding. *J Mater Process Technol.* 1999;87:213–222.
- [80] Metzbower EA, Bhadeshia HKDH, Phillips RH. Microstructures in hot wire laser beam welding of HY 80 steel. *Mater Sci Technol U K.* 1994;10:56–59.
- [81] Steen WM. Arc augmented laser processing of materials. *J Appl Phys.* 1980;51:5636–5641.
- [82] Petring D, Fuhrmann C. Recent progress and innovative solutions for laser-arc hybrid welding. *1st Pac Int Conf Appl Laser Opt.* Melbourne, Australia; 2004;7–10.
- [83] Liu W, Ma J, Yang G, et al. Hybrid laser-arc welding of advanced high-strength steel. *J Mater Process Technol.* 2014;214:2823–2833.

- [84] Bagger C, Olsen FO. Review of laser hybrid welding. *J Laser Appl.* 2005;17:2–14.
- [85] Liu L, Huang R, Song G, et al. Behavior and spectrum analysis of welding arc in low-power YAG-laser-MAG hybrid-welding process. *IEEE Trans Plasma Sci.* 2008;36:1937–1943.
- [86] Churiaque C, Chludzinski M, Porrua-Lara M, et al. Laser hybrid butt welding of large thickness naval steel. *Metals.* 2019;9(1):100.
- [87] Wahba M, Mizutani M, Katayama S. Single pass hybrid laser-arc welding of 25 mm thick square groove butt joints. *Mater Des.* 2016;97:1–6.
- [88] Chen X, Jiang N, Jiang M, et al. Numerical investigation of asymmetric weld fusion geometry in laser welding of aluminium alloy with beam oscillation. *Sci Technol Weld Join.* 2022;27:595–605.
- [89] Mahrle A, Beyer E. Control of the Energy Deposition during Laser Beam Welding by Oscillation Techniques. *Proceeding 4th Int WLT Conf Lasers Manuf.* 2007; 97-103.
- [90] Wang L, Gao M, Zhang C, et al. Effect of beam oscillating pattern on weld characterization of laser welding of AA6061-T6 aluminum alloy. *Mater Des.* 2016;108:707–717.
- [91] Schweier M, Heins JF, Haubold MW, et al. Spatter formation in laser welding with beam oscillation. *Phys Procedia.* 2013;41:20–30.
- [92] Hao K, Wang H, Gao M, et al. Laser welding of AZ31B magnesium alloy with beam oscillation. *J Mater Res Technol.* 2019;8:3044–3053.
- [93] Sabir T. *Laser Welding Characterization of 5083 Aluminum Alloys [dissertation].*

Ankara Yildirim Beyazit University; 2019.

- [94] Liu T, Mu Z, Hu R, et al. Sinusoidal oscillating laser welding of 7075 aluminum alloy: Hydrodynamics, porosity formation and optimization. *Int J Heat Mass Transf.* 2019;140:346–358.
- [95] StJohn DH, Prasad A, Easton MA, et al. The Contribution of Constitutional Supercooling to Nucleation and Grain Formation. *Metall Mater Trans Phys Metall Mater Sci.* 2015;46:4868–4885.
- [96] Wang L, Gao M, Hao Z. A pathway to mitigate macrosegregation of laser-arc hybrid Al-Si welds through beam oscillation. *Int J Heat Mass Transf.* 2020;151:1–8.
- [97] Turichin G, Kuznetsov M, Sokolov M, et al. Hybrid Laser Arc Welding of X80 Steel: Influence of Welding Speed and Preheating on the Microstructure and Mechanical Properties. *Phys Procedia.* 2015;78:35–44.
- [98] Zheng B, Li Y, Ao S, et al. Narrow Gap Welding of X80 Steel Using Laser-CMT Hybrid Welding with Misaligned Laser and Arc. *Crystals.* 2022;12:832.
- [99] Yan C, Li C, Kan C, et al. Experimental investigation of hybrid laser arc welding of X80 pipeline steel. *IOP Conf Ser Mater Sci Eng.* 2018;452:022021.
- [100] Kaplan A, Höfemann M, Vaamonde E, et al. Microstructures from wire-fed laser welding of high strength steel grades. *J Laser Appl.* 2020;32:022050.
- [101] Midawi ARH, Simha CHM, Gerlich AP. Novel techniques for estimating yield strength from loads measured using nearly-flat instrumented indenters. *Mater Sci Eng A.* 2016;675:449–453.

- [102] Yang H, Chen J, Huda N, et al. Effect of beam wobbling on microstructure and hardness during laser welding of X70 pipeline steel. *Sci Technol Weld Join.* 2022;27:326–338.
- [103] Nielsen SE. High Power Laser Hybrid Welding – Challenges and Perspectives. *Phys Procedia.* 2015;78:24–34.
- [104] Midawi ARH, Santos EBF, Huda N, et al. Microstructures and mechanical properties in two X80 weld metals produced using similar heat input. *J Mater Process Technol.* 2015;226:272–279.
- [105] Beidokhti B, Koukabi AH, Dolati A. Influences of titanium and manganese on high strength low alloy SAW weld metal properties. *Mater Charact.* 2009;60:225–233.
- [106] Babu SS. The mechanism of acicular ferrite in weld deposits. *Curr Opin Solid State Mater Sci.* 2004;8:267–278.
- [107] Li S, Xu W, Xiao G, et al. Effects of Sc on laser hot-wire welding performance of 7075 aluminum alloy. *Mater Res Express.* 2020;7:106506.
- [108] Huda N, Midawi A, Gianetto JA, et al. Continuous cooling transformation behaviour and toughness of heat-affected zones in an X80 line pipe steel. *J Mater Res Technol.* 2021;12:613–628.
- [109] Prokić-Cvetković RM, Milosavljević AJ, Sedmak AS, et al. Formation Of Acicular Ferrite on Non-Metallic Inclusion In Low-Alloy Welded Joints. 10th Int Res Conf Trends Dev Mach Assoc Technol. 2006;1315–1318.
- [110] Casalino G, Dal Maso U, Angelastro A, et al. Hybrid Laser Welding: A Review. *DAAAM Int Sci Book 2010.* 2010;38:413–430.

- [111] Grünenwald S, Unt A, Salminen A. Investigation of the influence of welding parameters on the weld geometry when welding structural steel with oscillated high-power laser beam. *Procedia CIRP*. Elsevier B.V.; 2018;74:461–465.
- [112] Li S, Chen G, Zhou C. Effects of welding parameters on weld geometry during high-power laser welding of thick plate. *Int J Adv Manuf Technol*. 2015;79:177–182.
- [113] Li S, Chen G, Katayama S, et al. Relationship between spatter formation and dynamic molten pool during high-power deep-penetration laser welding. *Appl Surf Sci*. 2014;303:481–488.
- [114] Zou J, Zhu B, Zhang G, et al. Power density effect on the laser beam-induced eruption of spatters in fiber laser keyhole welding. *Opt Laser Technol*. 2022;147:107651.
- [115] Li S, Mi G, Wang C. A study on laser beam oscillating welding characteristics for the 5083 aluminum alloy: Morphology, microstructure and mechanical properties. *J Manuf Process*. 2020;53:12–20.
- [116] Li L, Gong J, Xia H, et al. Influence of scan paths on flow dynamics and weld formations during oscillating laser welding of 5A06 aluminum alloy. *J Mater Res Technol*. 2021;11:19–32.
- [117] Bunaziv I, Langelandsvik G, Ren X, et al. Effect of preheating and preplaced filler wire on microstructure and toughness in laser-arc hybrid welding of thick steel. *J Manuf Process*. 2022;82:829–847.
- [118] Turichin G, Kuznetsov M, Pozdnyakov A, et al. Influence of heat input and preheating on the cooling rate, microstructure and mechanical properties at the hybrid laser-arc welding of API 5L X80 steel. *Procedia CIRP*. 2018;74:748–751.



- [119] Zhang D, Terasaki H, Komizo Y. In situ observation of the formation of intragranular acicular ferrite at non-metallic inclusions in C-Mn steel. *Acta Mater.* 2010;58:1369–1378.
- [120] Üstündağ Ö, Avilov V, Gumenyuk A, et al. Improvement of filler wire dilution using external oscillating magnetic field at full penetration hybrid laser-arc welding of thick materials. *Metals.* 2019;9(5):9.
- [121] Zhang Z, Farrar RA. Influence of Mn and Ni on the microstructure and toughness of C-Mn-Ni weld metals. *Weld J.* 1997;76:183s-196s.
- [122] Mao G, Cao R, Yang J, et al. Effect of Nickel Contents on the Microstructure and Mechanical Properties for Low-Carbon Bainitic Weld Metals. *J Mater Eng Perform.* 2017;26:2057–2071.
- [123] Schaeffler AL. Constitution Diagram for Stainless Steel Weld Metal. *Met Prog.* 1949;56:680.
- [124] Ramon J, Basu R, Voort GV, et al. A comprehensive study on solidification (hot) cracking in austenitic stainless steel welds from a microstructural approach. *Int J Press Vessels Pip.* 2021;194:104560.
- [125] Lippold JC, Kiser SD, DuPont JN. *Welding Metallurgy and Weldability of Nickel-Base Alloys.* Hoboken, New Jersey: John Wiley & Sons; 2011.
- [126] Lippold JC, Kotecki DJ. *Welding Metallurgy and Weldability of Stainless Steels.* Weld. Metall. Weldability Stainl. Steels. Hoboken, New Jersey: John Wiley & Sons; 2005.
- [127] Yan H, Zhao D, Qi T, et al. Relationship of the Microstructure and Toughness of the

Coarse Grain Heat-Affected Zone of TiNbV Microalloyed Steels Based on Electron Backscatter Diffraction Analysis. *J Mater Eng Perform.* 2022;31:201–210.